TECHNISCHE UNIVERSITÄT MÜNCHEN

Lehrstuhl für Aerodynamik und Strömungsmechanik

Towards an Improved Lattice-Boltzmann Methodology for the Simulation of Turbulent Flows

Patrick Nathen

Vollständiger Abdruck der von der Fakultät für Maschinenwesen der Technischen Universität München zur Erlangung des akademischen Grades eines

Doktor-Ingenieurs

genehmigten Dissertation.

Vorsitzender:		Prof. Dr.-Ing. Florian Holzapfel
Prüfer der Dissertation:	1.	Prof. Dr.-Ing. Nikolaus A. Adams
	2.	Prof. Dr.-Ing. Stefan Hickel
	3.	Prof. Dr. Barbara Wohlmuth

Die Dissertation wurde am 07.05.2018 bei der Technischen Universität München eingereicht und durch die Fakultät für Maschinenwesen am 16.05.2019 angenommen.

Patrick Nathen
Steinheilstraße 16
80333 München
Germany

patrick.nathen@lilium.com

Released July 18, 2019
Typesetting LaTeX

ABSTRACT

In this work, the suitability of the Lattice Boltzmann Method (LBM) for the simulation of turbulent flows is systematically analyzed. So far, no analysis has pointed out, which closure for the collision term is most suitable for the simulation of turbulent flows. With respect to turbulence modeling in the Large-Eddy Simulation (LES) framework, it is of essential interest to validate different collision models to obtain proper stability and accuracy characteristics. A detailed analysis of turbulent flows in real and spectral space is provided for three commonly used collision models. Namely the Bhatnagar-Gross-Krook (BGK), the multi-relaxation time (MRT) and the regularized BGK (RLB) model are discussed and one of the main conclusions is, that the BGK scheme is the most suitable closing approach regarding the simulation of homogeneous isotropic turbulence and wall-bounded turbulent flows. It is demonstrated, that the MRT scheme does not achieve mesh convergence in the incompressible limit for the investigated turbulent flows and it's applicability is limited to under resolved test cases only. The regularized BGK scheme suffers from excessive numerical dissipation, which prohibits the application to LES, since the subgrid-scale turbulence closure is dominated by numerical dissipation emerging from he collision model.

On the basis of these findings, a novel subgrid-scale closure is derived based on a selective viscosity filter approach. As opposed to increasing the filter stencil to achieve high accuracy, the filter strength is modified by considering the resolved turbulent scales. The novel approach is compared to a explicit subgrid-scale closure employed by Navier-Stokes equation based LES simulations. We find, that the explicit filter as well as the consistent approach lead to superior results compared to a naive model. Beyond that, it is demonstrated, how the new subgrid-closure overcomes the stability issues of common explicit eddy-viscosity closures by suppressing non-linear instabilities. Common turbulence models in the Lattice Boltzmann framework take non-linear instabilities into account for the estimation of a turbulent viscosity, which is circumvented completely by the new approach. From a computational point of view, the selective filtering approach is very efficient, since high-order stencils are avoided and the local criterion allows for high accuracy with low-order explicit filter stencils.

ZUSAMMENFASSUNG

In der vorliegenden Arbeit wird eine systematische Analyse für die Simulation von turbulenten Strömungen mit der Lattice Boltzmann Methode vorgestellt. Bis zum jetzigen Zeitpunkt wurde keine Analyse vorgestellt in der gezeigt wird, welche Lösung des Kollisionsoperator für die Simulation von turbulenten Strömungen am besten geeignet ist. Hinsichtlich der Modellierung von Turbulenz im Rahmen von Grobstruktursimulationen, ist es essentiel verschiedene Lösungen unter Stabilitäts und Genauigkeitsaspekten zu validieren. Aus diesem Grund wird eine detaillierte Analyse präsentiert, welche darstellt wie turbulente Strömungen im Real- und Spektralraum abgebildet werden. Als Basis dienen hierzu drei häufig benutzte Modellierungsansätze welche unter dem BGK, dem MRT und dem regularisierten BGK Ansatz bekannt sind. Der Rückschluss, dass das singulär relaxierte BGK Verfahren sich am besten für die Simulation von isotrop homogener Turbulenz und turbulenten wandgebundenen Strömungen eignet, wird geschlossen. Als neue Erkenntnis wird gezeigt, dass für die untersuchten numerischen Testfälle keine Gitterkonvergenz mit dem MRT Verfahren im Grenzfall der Inkompressibilität erreicht werden kann und nur unteraufgelöste Testfälle zu zuverlässigen Ergebnissen führt. Das regularisierte BGK Modell erzeugte bei den untersuchten Testfällen zuviel numerische Dissipation, was die Anwendbarkeit im Rahmen der LES unterbindet, da zwischen der Dissipation aus dem Feinskalen Modell und dem Kollisionsoperator nicht mehr unterschieden werden kann.

Auf Basis dieser Ergebnisse wird ein neues, auf einer expliziten Filterung beruhendes Feinstruktur Modell vorgestellt. Um eine möglichst hohe Genauigkeit zu gewährleisten wird mit dem neuen Ansatz die Filterstärke an die aufgelösten turbulenten Skalen angepasst anstatt die Filterordnung zu erhöhen. Das Modell wird mit einer konsistenten Wirbelviskositätshypothese für die Lattice Boltzmann Methode und einem Smagorinsky Ansatz aus der Navier-Stokes Theorie verglichen. Im Detail wird gezeigt, wie das neue LES Modell nicht-lineare Instabilitäten unterdrückt ohne dabei künstlich die Viskosität zu erhöhen wie es bei den gängigen Turbulenz Modellen für LES basierte Simulationen mit der Lattice Boltzmann Methode üblich ist. Durch die lokale Anpassung der Filterstärke reichen "low-order stencil" um bei gleich bleibender Genauigkeit die Rechenzeit niedrig zu halten und somit eine hohe Effizienz zu erreichen.

DANKSAGUNG

To my parents ...

"Ever tried. Ever failed.
No matter.
Try Again. Fail again.
Fail better."

\- Samuel Beckett

Table of contents

CHAPTER 1

Introduction

The need to shorten the turn-around times for development processes has raised the demand for efficient numerical algorithms in industrial fluid flow analysis. Experimental studies are still an indispensable tool to develop and optimize aerodynamic concepts, e.g., in aviation or automotive industry. Nevertheless, the extreme high costs, the insufficient reproducibility and the large validation time limits the process of fast and efficient development across different industries based on pure experimental studies. Therefore, Computational Fluid Dynamics (CFD) takes a huge part in the development process of aerodynamic concepts nowadays. Especially with growing computational resources, CFD is increasingly used for challenging tasks in aerodynamics, like full scale aircraft simulations, the investigations of complex turbo machinery flow, thermal management processes or aero-acoustic analysis in near- and far-field.

The flows in industrial applications are dominated by complex three dimensional turbulent structures and therefore the numerical investigation and the subsequent optimization of aerodynamic features depends crucially on the available numerical tools and their underlying loop-timing and accuracy. The applied turbulence models, the treatment of complex moving geometries as well as the underlying numerical accuracy of the tool determine the efficiency for aerodynamic design studies in any industry. Commonly these tools rely on the Navier-Stokes equations (NSE), a macroscopic description of mass, momentum and energy conversation. In this work an alternative approach is chosen and an open-source CFD code based on the Lattice Boltzmann Method (LBM) is extended by a novel turbulence model, which allows for the correct prediction of turbulent structures at high Reynolds numbers. In order to gain deeper understanding of the interaction between turbulence model and numerical scheme, a detailed analysis outlines the possibilities and limitations of commonly applied Boltzmann models in order to represent turbulent flow structures. Based on these findings, a single-relaxation-time scheme will be extended by an adaptive filter approach in the Large-Eddy Simulation (LES) framework for the LBM.

1.1. THE LATTICE BOLTZMANN METHOD AS AN ALTERNATIVE FOR FLUID FLOW SIMULATIONS

Common CFD tools for the numerical investigation of fluid flows are based on the macroscopic transport equations for mass and momentum, namely the Navier-Stokes equations, which read

$$\frac{\partial u_i}{\partial t} + u_j \frac{\partial u_i}{\partial x_j} = -\frac{1}{\rho}\frac{\partial p}{\partial x_i} + \nu \frac{\partial^2 u_i}{\partial x_j^2} \tag{1.1a}$$

$$\frac{\partial u_i}{\partial x_i} = 0 \tag{1.1b}$$

for an incompressible fluid without body forces, constant viscosity and constant density, which is assumed throughout this work. Commercial and academic CFD codes discretize the incompressible NSE on a mesh on which Equations (1.1a)-(1.1b) are approximated numerically by finite volumes (FVM), finite differences (FDM) oder finite elements (FEM) methods. The equations are transformed into a set of algebraic equations and solved numerically. Depending on the method and the applied numerical scheme, the computational effort differs significantly. For further details, the interested reader is referred to Ferziger and Peric (2002) and Versteeg and Malalasekra (2007). It should be noted, that for the incompressible NSE, the pressure has no thermodynamic properties and is function of the velocity (and fluid properties) only. To keep the fluids volume conserved given by Equation (1.1b), a pressure projection is necessary for the incompressible case. Pressure correction steps, e.g., with fractional steps methods are executed each discrete physical time step and based on the pressure correction method, $65 - 80\%$ of the computational time is necessary to maintain the velocity field solenoidal. Although spectral methods do not need a pressure correction step for solving the incompressible NSE, they are limited to rather simple geometries in order to avoid tremendous implementation efforts. FEM methods using solenoidal basis functions do not require an additional pressure correction step for the incompressible NSE as well, but require in depth analysis with respect to the correct turbulent flow representation on unstructured grids. With respect to compressible flows, conditionally stable explicit time-stepping leads time steps which are proportional to the Mach number. This leads to tremendous computational times especially for rather low Mach numbers. In order to cope more efficiently with low Mach numbers in a compressible fluid flow solver, low-Mach approximations and weakly compressible formulations of Equations (1.1a)-(1.1b) can be used, see also Versteeg and Malalasekra (2007). Thus, efficient algorithms are a premise for the simulation of complex aerodynamic problems in industrial aerodynamic applications.

For dilute gases, LBM is often presented as a very efficient and accurate alternative to conventional CFD tools based on the NSE, see Chen and Doolen (1998); He and Luo (1997); Guo et al. (2000); Waldrow (2000); Sukop and Thorne (2006); Guo and Shu (2013); Succi (2001) and Hänel (2004) among others. In contrast to the NSE, LBM is based on a mesoscopic description of the flow field in terms of discrete velocity distribution functions $f(x_i, \boldsymbol{\xi}, t)$, which describes the probability to find molecules at position x_i at time t with molecular velocity $\boldsymbol{\xi}$. The continuous Boltzmann equation can be written as

$$\frac{\partial f}{\partial t} + \boldsymbol{\xi} \cdot \nabla_i f + f \cdot \nabla_{\boldsymbol{\xi}} = \int_V \int_{\boldsymbol{\xi}} Q(f,f) d\boldsymbol{\xi} dV. \tag{1.2}$$

Equation (1.2) closes the gap between the description of fluid motion on a microscopic level and the continuous description given by Equations (1.1a)-(1.1b). Non-linear interactions of the fluid, like turbulent motion, as well as damping characteristics emerging from the viscosity are described by the right hand side of equation 1.2, namely the collision term. In the NSE the linear $\nu \frac{\partial^2 u_i}{\partial x_j^2}$ and non-linear terms $u_j \frac{\partial u_i}{\partial x_j}$ are separated, which is a major difference to the underlying equation of Lattice Boltzmann based methods. The analytical form of the collision term is not suitable for numerical simulations since huge computational effort is necessary to estimate it exactly. Therefore, different approaches to simplify the right hand side of equation 1.2 have been developed. All approaches employed in this work are based on a linearization of the collision term

$$\int_V \int_{\boldsymbol{\xi}} Q(f,f) d\boldsymbol{\xi} dV \approx g(f, f^{eq}) \ , \tag{1.3}$$

with a functional g around an equilibrium f^{eq}, which is only valid for small Mach numbers and thus under the assumption of weak compressibility, which will be further outlined in Chapter 2. Special emphasis will be given on the physics of different collision models, namely the Bhatnagar-Gross-Krook (BGK) or single-relaxation time (SRT),see Chen and Doolen (1998); Waldrow (2000), the multi-relaxation time (MRT), see d'Humiéres et al. (2002); Yu et al. (2006) and Yu and Girimaji (2005), and the regularized lattice Boltzmann (RLB) model, see Latt (2007); Latt and Chopard (2006) and Latt et al. (2008), will be analyzed for simulation of turbulent flows. To the authors knowledge, no attention was paid on the interaction between the applied collision model and the resolved turbulent scales so far. Thus, a detailed analysis of the interaction between a collision model, the resolution of the numerical setup and the Reynolds number Re will be given to understand the predictability of turbulent flow structures with LBM.

1.2. Direct Turbulent Flow Simulation with the Lattice Boltzmann Method

Although the LBM has been applied to a wide range of fluid-dynamics applications, turbulence modeling in the LBM framework still requires considerable research and has not reached the level of maturity as seen for Navier-Stokes-based methods, see, e.g., Ricot et al. (2009, 2002) and Sagaut (2010). Recent advances have been made by Sagaut (2010) and Malaspinas and Sagaut (2012, 2011). Malaspinas and Sagaut (2011) proposed an approach which is based on the Approximate Deconvolution Method (ADM), see Stolz and Adams (1999). The Boltzmann equations are filtered and subsequently deconvoluted by a regular filter and inverse filter operation respectively, in order to reconstruct the proper macroscopic equations for LES within the kinetic theory. The ADM as implemented in Malaspinas and Sagaut (2011) is based on the simplest collision operator modeling, namely the BGK approach. It is crucial to understand the properties in terms of stability and accuracy of the pure BGK approach, when used for the simulation of turbulent flows before methods like the ADM approach can be adapted directly to the BGK Boltzmann equations. Moreover, these properties have to be taken into account when adapting turbulence models to LBM schemes.

To the author's knowledge, a comparison of the stability and accuracy properties of different discrete LBM schemes without turbulence models when applied to three-dimensional turbulent flows of varying Reynolds number has not been outlined so far. In this context stability refers to the tendency of the LBM to diverge at high Reynolds number flow simulations and accuracy describes the representation of turbulent scales compared to reference DNS data. As the Lattice Boltzmann algorithm corresponds to a finite difference scheme with spatial accuracy $\mathcal{O}(\Delta x^2)$ and a temporal accuracy $\mathcal{O}(\Delta t)$, see Succi (2001), this work aims to investigate the underlying stability and accuracy features of different discrete collision schemes for the LBM by carrying out resolved and under-resolved Direct Numerical Simulations (DNS) of Homogeneous Isotropic Turbulence at varying Reynolds numbers. Since no turbulence models will be employed, the observed dissipation can be related to viscous effects and numerical dissipation of the respective collision operator. For the type of flow considered in this work some of the recently presented LBM schemes showed improved stability and accuracy properties, which were not considered, yet for completion should be mentioned. Among others, the Karlin-Bösch-Chikatamarla (KBC) model, see Karlin et al. (2014), uses an entropy collision operation, which lead to significantly increased stability properties. This model was additionally enhanced by Dorschner et al. (2016a) and Dorschner et al. (2016b). Geller et al. (2013) and Geier et al. (2015) introduced another advanced LB model, which allowed for improved stability properties for the simulation of turbulent flows. So far, no in-depth mesh convergence analysis was outlined for these models. Since these models also do not make use of an explicit turbulence closure, yet demonstrate excellent stability behavior at very high Reynolds numbers, they are mistakingly referred as implicit LES closures.

1.3. TURBULENCE MODELING IN THE LATTICE BOLTZMANN FRAMEWORK

As already mentioned, turbulence modeling in the LBM framework still has not reached a level of maturity as seen for Navier-Stokes based methods, see Ricot et al. (2009, 2002) and Sagaut (2010). The concept of turbulence modeling in the LBM framework is primarily based on simple extrapolations of Large Eddy Simulation (LES) models as used for simulations based on the filtered Navier-Stokes equations. These models employ an effective relaxation rate that can be interpreted as an effective viscosity concept. Models that use this technique were presented and applied to varying benchmarks in Hou et al. (1996); Dong and Sagaut (2008); Dong et al. (2008); Filippova et al. (2002) and Yu et al. (2005) among others. Recent improvements for LES based simulations in the LBM framework were made by Sagaut (2010); Malaspinas and Sagaut (2012, 2011). They showed that the concept of an effective relaxation rate adopted from the Navier-Stokes based LES does not necessarily lead to the correct macroscopic equations, that is, the filtered Navier-Stokes equations. Consequently, the underlying equations for LES in the framework of LBM do not resemble the filtered macroscopic equations. Recently, Sagaut (2010) and Malaspinas and Sagaut (2011) presented a novel turbulence model for LES in the LBM framework, which is based on the Approximate Deconvolution Model (ADM), see Stolz and Adams (1999) and Stolz et al. (2001). ADM exploits the underesolved range of scales in order to partially mimic energy transfer in the subfilter-range, see Adams (2011) and Layton (2010). An implementation of the ADM algorithm in a DNS LBM code was demonstrated in Malaspinas and Sagaut (2011), where the discrete Boltzmann equations are filtered with an explicit filter stencil and subsequently deconvolved with a regularized inverse filter operation in order to reconstruct the proper macroscopic equations for LES within the kinetic theory.

Tam et al. (1993) introduced a set of stencils, known as selective viscosity filters, where a constant filter intensity is related directly to the filter operation. This class of filters was also the underlying ADM approach of Malaspinas and Sagaut (2011), which was also successfully applied in previous work by Ricot et al. (2009) and Ricot et al. (2002). Fauconnier et al. (2013) employed this class of filters for the simulation of Homogeneous Isotropic Turbulence (HIT) in the context of Navier-Stokes equations based simulations of fluid flows. They outlined that the accuracy of the numerical results strongly depends on the artificial viscosity, which needs to be adapted according to the mesh resolution, the order of the filter stencil and under consideration of stability issues. Similar results were found in Malaspinas and Sagaut (2011) by computing a turbulent shear layer. Only for very well resolved numerical test cases satisfying agreement with reference data was achieved while showing a minor influence of the filters artificial viscosity. For rather under resolved setups the development of turbulent structures strongly depends on the filter stencil and the applied artificial viscosity constant. In conclusion, no general strategy can be found in the literature for employing selective viscosity filters of Tam et al. (1993) for the simulation of turbulent flows within the ADM theory for LBM. Depending on the test case and under consideration of the resolution, the artificial viscosity as well as the filter stencil have to be tuned with care.

Our goal is to improve the prediction of turbulent flows in the the LBM-LES framework by extending an existing ADM approach to self-adapting filter stencils. By doing so, we aim for less mesh-sensitivity for a given Reynolds number in order to derive a more general framework for the simulation of turbulent flows with LBM. A connection between spatial and temporal resolution and locally resolved scales has to be made and incorporated into the self-adaptive filter.

1.4. Structure of this Work

This work is structured as followed: First, the LBM is introduced in Chapter 2 and different lattice schemes are introduced. A detailed quantitative and qualitative analysis of different lattice schemes with DNS-like setups will be presented in the first publication attached in Section B.1 to demonstrate the applicability of lattice schemes for turbulent flows, considering different mesh resolutions and Reynolds numbers from a stability and accuracy point of view. The next part of this work is devoted to the development of an accurate explicit low-pass filtering subgrid-scale approach in Section B.2, which is consistent with the hydrodynamic limit of the filtered NSE in the LES-LBM framework. The supportive work, which triggered the content of the main publication are attached in C.1 and C.2. Final conclusions and an outlook for future research will be given in Chapter 4.

CHAPTER 2

The Lattice Boltzmann Method

This chapter presents the mathematical background of the LBM. The Boltzmann equation will be derived from the kinetic theory of gases and he origin of the Lattice Boltzmann Method will derived in Section 2.1. Properties of the Boltzmann equation will be discussed in Section 2.2. In Section 2.2.3, the approximation of the Boltzmann equation in terms a Hermite polynomial expansion will be presented and afterwards the reconstruction of the weakly compressible Navier-Stokes Equations (NSE) will be shown in Section 2.3. Different modeling approaches for the collision operator, see the right hand side of Equation (1.2), will be introduced in Section 2.4.

2.1. KINETIC THEORY OF GASES

Starting from a microscopic point of view, the motion of a fluid can be modeled by particle motion. Considering a 1 cm^3 large cube filled with air, which corresponds to $\approx 2.5 * 10^{19}$ molecules, it is easy to understand that even with Newtonian mechanics the simulation of a real flow problem becomes unrealistic in microscopic space. Even if the degrees of freedom (DOF) are limited to 6, this problem is not reduced noticeably, see the $6-N$ theory in Hänel (2004). These many-particle systems are generally described by the Newton-Hamilton equations emerging from classical mechanics. Due to the complexity of these systems a single particle motion described by

$$\begin{aligned} \frac{d\boldsymbol{x}_i}{dt} &= \frac{\boldsymbol{p}_i}{m_p} \\ \frac{d\boldsymbol{p}_i}{dt} &= \boldsymbol{F}_i \end{aligned} \tag{2.1}$$

is not suitable. In Equations (2.1), $\boldsymbol{x}_i$ is the position vector of the i^{th} particle, $\boldsymbol{p}_i$ the momentum and $\boldsymbol{F}_i$ the force acting on the i^{th} particle for $i = 1..N$. Considering the aforementioned $6-N$ DOF system, six functions of time, namely $\boldsymbol{x}$ and $\boldsymbol{p}$, need to be solved for every $i = 1..N$ particle. The associated computational effort for solving an industrial engineering problem based on single particle motions becomes proportional to the considered number of particles (neglection of interaction), which is impracticable.

Another level of describing fluid motions is not on a microscopic level, but rather on a mesoscopic one. Here, the many particle system is described in terms of velocity distribution functions in phase space. The aim is to provide an equation for the spatial and temporal probability to find particles around $x_i + \Delta x_i$, with velocity ranges $\boldsymbol{\xi} + \Delta\boldsymbol{\xi}$ at time t. The superposition of the Euclidean space and the velocity space is known as the phase space. The underlying equation, named after *Liouville* will be the starting point to derive the Boltzmann equation. The initial idea is to decrease the particle count $i = 1..N$ drastically compared to the approach given in Equation (2.1). This leads to the velocity distribution function $f_N(\boldsymbol{x}_1, \boldsymbol{p}_1, ..., \boldsymbol{x}_N, \boldsymbol{p}_N, t)$ in phase space $[\boldsymbol{x}_1, \boldsymbol{x}_1 + d\boldsymbol{x}_1] \times [\boldsymbol{p}_1, \boldsymbol{p}_1 + d\boldsymbol{p}_1] \times ... \times [\boldsymbol{p}_N, \boldsymbol{p}_N + d\boldsymbol{p}_N] \times [\boldsymbol{p}_N, \boldsymbol{p}_N + d\boldsymbol{p}_N]$, which bridges classical and statistical mechanics. All statistical information is captured by f_N and according to *Liouville*, see Schwabl (2006), f_N evolves as:

$$\frac{\partial f_N}{\partial t} - \sum_{j=1}^{3N} \left(\frac{\partial H_N}{\partial x_j} \frac{\partial f_N}{\partial p_j} - \frac{\partial H_N}{\partial p_j} \frac{\partial f_N}{\partial x_j} \right) = 0, \tag{2.2}$$

where H_N describes the Hamiltonian of the underlying dynamic system. By integrating Equation (2.2) over a reduced density space, see Lammers (2004) and Illnera and Pulvirentib (1987), the *BBGKY* hierarchy of equations named after the scientists *Bogoljubov*, *Born*, *Greenwood*, *Kirkwood* and *Yvon* can be derived. This reduced density system F_s can be written as

$$F_s(\boldsymbol{x}_1, \boldsymbol{p}_1, ..., \boldsymbol{x}_s, \boldsymbol{p}_s, t) \propto \int f_N(\boldsymbol{x}_1, \boldsymbol{p}_1, ..., \boldsymbol{x}_N, \boldsymbol{p}_N, t) d\boldsymbol{x}_{s+1} d\boldsymbol{p}_{s+1} ... d\boldsymbol{x}_N d\boldsymbol{p}_N. \tag{2.3}$$

In Equation (2.3) the one-particle probability density function F_s depends on the two-particle probability density function $f_1 = G(f_1, f_2)$ and so on. $f_1 = G(f_1, f_2)$ gives the probability to find particles in two different phase spaces. Even estimating the reduced density system numerically is, from a numerical point of view, too expensive and thus an appropriate truncation for F_s must be found. Assuming only local, two body collisions with uncorrelated velocities in diluted gases one can write Equation (2.3) as an integro-differential equation

$$\begin{gathered} \frac{\partial f}{\partial t} + \boldsymbol{\xi} \cdot \nabla_i f + \frac{\boldsymbol{F}}{m} \cdot \nabla_{\boldsymbol{\xi}} f = \int_V \int_{\boldsymbol{\xi}} Q(f, f^{'}) d\boldsymbol{\xi} dV = \\ \int d\boldsymbol{\xi}_1 \int d\sigma(\Omega) |\boldsymbol{\xi} - \boldsymbol{\xi}_1| (f(\boldsymbol{\xi}^{'}) f(\boldsymbol{\xi}_1^{'}) - f(\boldsymbol{\xi}) f(\boldsymbol{\xi}_1)) \end{gathered} \tag{2.4}$$

known as the Boltzmann equation. $Q(f, f^{'})$ is the non-linear collision operator, $\boldsymbol{F}$ are the body forces and m are the particles mass. At this point the *Boltzmann'sche Stoßzahlansatz* Succi (2001) was used, which is defined by

$$f(\boldsymbol{\xi}^{'}, \boldsymbol{\xi}_1^{'}) = f(\boldsymbol{\xi}^{'}) f(\boldsymbol{\xi}_1^{'}). \tag{2.5}$$

Equation (2.5) is fairly plausible for diluted gases and decorrelated collisions. In Equation (2.4) $\boldsymbol{\xi}$ and $\boldsymbol{\xi}_1$ are the ingoing velocities within the differential collision cross section $d\sigma(\Omega)$, by which the velocities are redistributed to $\boldsymbol{\xi}^{'}$ and $\boldsymbol{\xi}_1^{'}$ for a two-body particle collision model.

In order to perform fluid simulations by applying Equation (2.4) mass, momentum and energy need to be conserved. Thus, for an incompressible formulation without presence of thermal energy, five (ρ, u_i and e_{kin}) collision invariants need to be conserved by the collision integral, see Cercignani (1988). The collision integral satisfies

$$\int Q(f,f^{'})\Psi_k(\boldsymbol{\xi})d\boldsymbol{\xi} = 0 \tag{2.6}$$

with $k = 1..5$. The collision invariants $|\Psi\rangle = (\rho, \xi^x, \xi^y, \xi^z, \frac{1}{2}\boldsymbol{\xi}^2)$ are related to the mass, momentum and energy. In Section 2.2.1 an analytical solution for the collision integral will be derived and the invariance of the collision operator will be demonstrated in Section 2.2.2.

2.2. THE BOLTZMANN BGK APPROACH

In Section 2.1 the Boltzmann equation was derived. The underlying assumption, namely low Mach numbers, diluted gases and uncorrelated collisions are applied in order to derive the temporal evolution of the velocity density probability function $f(\boldsymbol{x}, \boldsymbol{\xi}, t)$ as

$$\begin{gathered}(\partial_t + \boldsymbol{\xi}\cdot\nabla_x + \boldsymbol{g}\cdot\nabla_{\boldsymbol{\xi}})\, f(x_i, \boldsymbol{\xi}, t) = Q(f,f^{'}) = \\ \int d\boldsymbol{\xi}_1 \int d\sigma(\Omega)|\boldsymbol{\xi} - \boldsymbol{\xi}_1|(f(\boldsymbol{\xi}^{'})f(\boldsymbol{\xi}_1^{'}) - f(\boldsymbol{\xi})f(\boldsymbol{\xi}_1)).\end{gathered} \tag{2.7}$$

As stated before, the collision operator needs to be expressed appropriate in terms of mass, momentum and energy conservation. Throughout this thesis an athermal flow is considered and thus, the macroscopic moments of fluid motion, namely the density ρ, the momentum $\rho\boldsymbol{u}$ and the stress field $\boldsymbol{Q}$ can be reconstructed by taking the velocity moments of the velocity density probability function $f(x_i, \boldsymbol{\xi}, t)$.

$$\rho = \int d\boldsymbol{\xi} f(x_i, \boldsymbol{\xi}, t), \tag{2.8a}$$

$$\rho\boldsymbol{u} = \int d\boldsymbol{\xi}\boldsymbol{\xi} f(x_i, \boldsymbol{\xi}, t) \tag{2.8b}$$

$$\boldsymbol{Q} = \int d\boldsymbol{c}\ \boldsymbol{\xi}\boldsymbol{\xi} f(x_i, \boldsymbol{\xi}, t) \tag{2.8c}$$

where $\boldsymbol{c} = \boldsymbol{\xi} - \boldsymbol{u}$ is the microscopic velocity of a particle in a reference mean flow with velocity $\boldsymbol{u}$. The most established way to represent the collision operator is the Bhatnagar-

Gross-Krook (BGK) model, see Bhatangar et al. (1954), where the velocity distribution function is relaxed towards a local low Mach number truncated Maxwell-Boltzmann distribution function $f^{eq}(x_i, \boldsymbol{\xi}, t)$. This approach is also known as single-relaxation time (SRT) and in absence of an external body force this model reads

$$(\partial_t + \boldsymbol{\xi} \cdot \nabla_x) f(x_i, \boldsymbol{\xi}, t) = -\frac{1}{\tau} \left(f(x_i, \boldsymbol{\xi}, t) - f^{eq}(x_i, \boldsymbol{\xi}, t) \right) \tag{2.9}$$

The relaxation time τ is related to the physical viscosity as $\nu = c_s^2(\tau - 0.5)\Delta_t$. Here, c_s is the lattice speed of sound and Δ_t the discrete time step. In the next Section, design and properties of the equilibrium distribution function $f^{eq}(x_i, \boldsymbol{\xi}, t)$ are discussed. Properties of the discrete BGK Boltzmann approach are shown in Section 2.4.

2.2.1. Derivation and Properties of the Maxwell Distribution Function

The collision operator in the Boltzmann equation is crucial for the representation of the dynamics of fluid flow. Linear as well as non-linear dynamics of fluid motion are modeled by the collision term. This is a major difference compared to NSE based methods, where viscous effects are represented by the diffusive term $\nu \frac{\partial^2 u_i}{\partial x_j}$ and non-linear effects are taken into account by the convective term $u_j \frac{\partial u_i}{\partial x_j}$. The question: *"How are non-linear effects taken into account, using the linearization shown in Equation* (2.9)*? And how can non-linear effects like those of turbulent fluid motion be represented by this linearization?* arises.

The linear relaxation towards a local equilibrium distribution function needs to fulfill certain requirements, including mass, momentum and energy conservation. Using the Maxwell distribution function as an approach to design the equilibrium distribution function, the positivity of the entropy s is fulfilled, which is shown in the next subsection.

Generally, the Maxwell distribution can be written as

$$f^{eq}(x_i, \boldsymbol{\xi}, t) = \frac{\rho(x_i, t)}{(2\pi k_b T(x_i, t))^{D/2}} \exp\left\{ \left(-\frac{(\boldsymbol{\xi} - \boldsymbol{u}_{ref}(x_i, t))^2}{2 k_b T(x_i, t)} \right) \right\}, \tag{2.10}$$

where k_b is the Boltzmann constant, $\rho(x_i, t)$ is the density at point $\boldsymbol{x}$ and time t and $T(x_i, t)$ is the temperature of the current thermodynamic state assumed to be constant in an athermal flow. ρ is the local density and $\boldsymbol{u}_{ref}$ is the local reference velocity of the fluid. Equation (2.10) gives the probability to find particles in thermodynamic equilibrium with a momentum $\rho(\boldsymbol{u} - \boldsymbol{\xi})$ at an ambient temperature T. The reference state around $\boldsymbol{u}_{ref}$ and T is called thermodynamic equilibrium. In order to understand the Maxwellian distribution for the particle velocity better, Figure 2.1 shows the probability $P(v)$ to find particles with a velocity v at ambient temperature $T = 298.15K$ for three different gases, namely Air, Hydrogen and Helium. The probability $P(v)$ shown in Figure 2.1 refers to a Maxwellian distribution given by Equation (2.10).

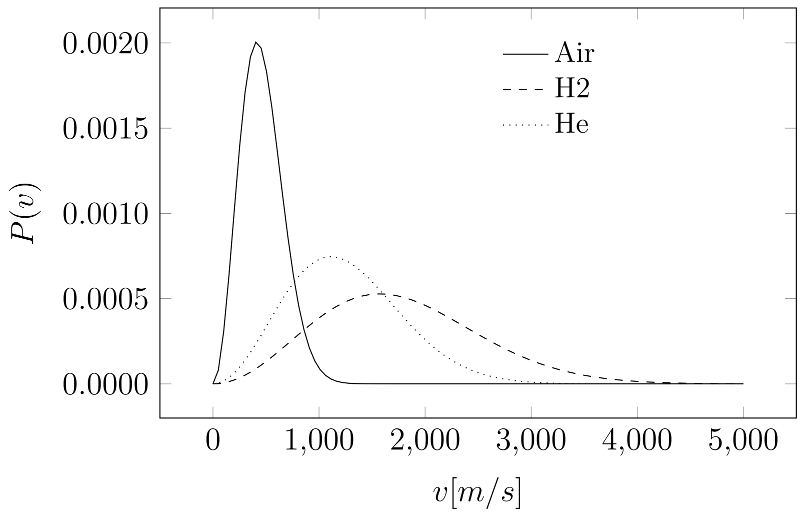

Figure 2.1.: Maxwell-Boltzmann distribution of different gases at $T = 293,15K$.

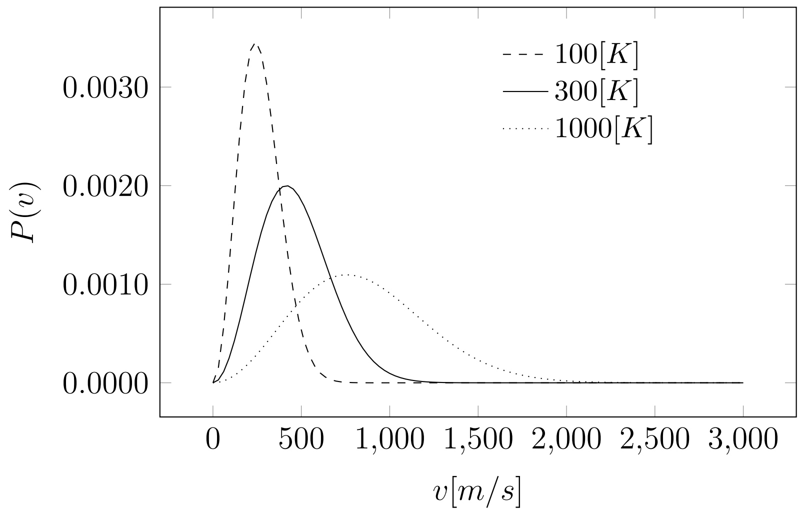

Figure 2.2.: Maxwell-Boltzmann distribution for dry air at different temperatures.

By varying the temperature for a given gas like air, see Figure 2.2, the probability is distributed over a wider range of velocities for increasing temperature.

Following the work of Hänel (2004), the derivation of Equation (2.10) will be shown based on the limiting case of a continuous flow at a Knudsen number $Kn = \frac{\lambda_f}{L_{ref}} \to 0$. If $Kn \ll 1$ the flow can be called continuous, since the mean free molecule path λ_f is much smaller than the reference length L_{ref}. For $Kn \gg 1$ the underlying physics are considered as a free particle flow. The right hand side of Equation (2.4), needs to be zero in order to fulfill $Kn \to 0$ in order to have a continuous fluid in thermodynamic equilibrium. Thus,

$$\begin{gathered}\int_V \int_{\boldsymbol{\xi}} Q(f,f) d\boldsymbol{\xi} dV = \\ \int d\boldsymbol{\xi}_1 \int d\sigma(\Omega) |\boldsymbol{\xi} - \boldsymbol{\xi}_1| (f(\boldsymbol{\xi}') f(\boldsymbol{\xi}_1') - f(\boldsymbol{\xi}) f(\boldsymbol{\xi}_1)) = 0\end{gathered} \tag{2.11}$$

which leads to

$$f(\boldsymbol{\xi}^{'})f(\boldsymbol{\xi}_1^{'}) - f(\boldsymbol{\xi})f(\boldsymbol{\xi}_1) = 0. \tag{2.12}$$

Equation (2.11) states, that during a collision process $f(\boldsymbol{\xi})f(\boldsymbol{\xi}_1)$ particles are leaving phase space $\boldsymbol{\xi} + \Delta\boldsymbol{\xi}$, where the collision took place and an inverse collision described by $f(\boldsymbol{\xi}^{'})f(\boldsymbol{\xi}_1^{'})$ is redistributing particles back from $\boldsymbol{\xi}^{'} + \Delta\boldsymbol{\xi}^{'}$ in the original phase space. This can be considered as conservation of mass, momentum and energy in phase space. Equation (2.12) leads to

$$\ln\Big(f(\boldsymbol{\xi}^{'})\Big) + \ln\Big(f(\boldsymbol{\xi}_1^{'})\Big) = \ln(f(\boldsymbol{\xi})) + \ln(f(\boldsymbol{\xi}_1)) \tag{2.13}$$

for $Kn \to 0$, by assuming a local thermodynamic equilibrium. In order to proof that Equation (2.12) leads to a correct solution of the Boltzmann equation, we rewrite the terms of the aforementioned collision invariants as in Equation (2.12)

$$m + m_1 = m^{'} + m_1^{'} \tag{2.14a}$$

$$m\boldsymbol{\xi} + m_1\boldsymbol{\xi}_1 = m^{'}\boldsymbol{\xi}^{'} + m_1^{'}\boldsymbol{\xi}_1^{'} \tag{2.14b}$$

$$\frac{m}{2}\boldsymbol{\xi}^2 + \frac{m_1}{2}\boldsymbol{\xi}_1^2 = \frac{m^{'}}{2}\boldsymbol{\xi}^{'2} + \frac{m_1^{'}}{2}\boldsymbol{\xi}_1^{'2}. \tag{2.14c}$$

Comparing Equation (2.14a)-(2.14c) with Equation (2.13), we see that $\ln\big(f(\boldsymbol{\xi}^{'})\big)$ is an additive collision invariant and, thus, the microscopic properties do not change after the collision, see Succi (2001).

Thus, Equation (2.13) can be rewritten in terms of additive invariance

$$\ln(f(\boldsymbol{\xi})) = A + Bu_i + \frac{1}{2}Cu_iu_i \Rightarrow \; f(\boldsymbol{\xi}) = \exp(A)\exp(Bu_i)\exp\left(\frac{1}{2}Cu_iu_i\right) \tag{2.15}$$

where A, B and C are constants, fitted to reconstruct density, momentum and energy properly, leading to Equation (2.10).

The connection to the H-theorem, which states the positivity of the entropy for the Boltzmann equation, will be shown in the next section based on the findings of the Maxwell distribution function.

2.2.2. THE H-THEOREM

The incorporation of the entropy in the Boltzmann equation, leading to the *H-theorem*, will be outlined. The specific entropy s is a fundamental physical property of thermodynamic systems and regarding the second law of thermodynamics, it satisfies $s = 0$ for flows in thermodynamic equilibrium and positivity $s > 0$ for flows apart from equilibrium state.

In order to represent the entropy in a closed thermodynamic flow system described by the Boltzmann equation, we define the H value as a moment of the equilibrium velocity distribution function as

$$H = -\int_{\boldsymbol{\xi}} f^{eq}(\boldsymbol{\xi}) \ln(f^{eq}(\boldsymbol{\xi}))d\boldsymbol{\xi}. \tag{2.16}$$

The change of entropy in a thermodynamic closed system is defined as

$$T \cdot dS = dE + pdV \geq 0, \tag{2.17}$$

where E is the energy and p the constant pressure. Following Hänel (2004), Equations (2.16) and (2.17) correlate corresponding to

$$\frac{\partial \Delta S}{\partial t} \propto \frac{\partial H}{\partial t}. \tag{2.18}$$

If Equation (2.16) can be applied to a system with underlying Boltzmann dynamics, Equation (2.18) would close the gap between the temporal growth of entropy and the Boltzmann equation. Assuming a closed system, where all spatial derivatives vanish, Equation (2.4) can be rewritten as

$$\frac{\partial f(\boldsymbol{\xi})}{\partial t} = \int d\boldsymbol{\xi}_1 \int d\sigma(\Omega)|\boldsymbol{\xi} - \boldsymbol{\xi}_1|(f(\boldsymbol{\xi}')f(\boldsymbol{\xi}_1') - f(\boldsymbol{\xi})f(\boldsymbol{\xi}_1)). \tag{2.19}$$

From Equation (2.16) follows

$$\frac{\partial H}{\partial t} = -\int_{\boldsymbol{\xi}} \frac{f^{eq}(\boldsymbol{\xi}) \ln(f^{eq}(\boldsymbol{\xi}))}{\partial t} d\boldsymbol{\xi} = -\int_{\boldsymbol{\xi}} \frac{f^{eq}(\boldsymbol{\xi})}{\partial t}(1 + \ln(f^{eq}(\boldsymbol{\xi})))d\boldsymbol{\xi}. \tag{2.20}$$

By replacing the temporal derivative of $f^{eq}(\boldsymbol{\xi})$ in Equation (2.20) with $\frac{f(\boldsymbol{\xi})}{\partial t}$ of Equation (2.19), an expression for the algebraic sign of the temporal evolution of the H value can be derived. After algebraic transformations taking the particle exchange between $f(\boldsymbol{\xi})f(\boldsymbol{\xi}_1)$ and $f(\boldsymbol{\xi}')f(\boldsymbol{\xi}_1')$ into consideration, we find

$$(f(\boldsymbol{\xi}')f(\boldsymbol{\xi}_1') - f(\boldsymbol{\xi})f(\boldsymbol{\xi}_1)) \ln\left(\frac{f(\boldsymbol{\xi})f(\boldsymbol{\xi}_1)}{f(\boldsymbol{\xi}')f(\boldsymbol{\xi}_1')}\right) \geq 0 \tag{2.21}$$

and therefore

$$\frac{\partial H}{\partial t} \geq 0. \tag{2.22}$$

If $f(\boldsymbol{\xi}')f(\boldsymbol{\xi}_1') - f(\boldsymbol{\xi})f(\boldsymbol{\xi}_1) < 0$, it follows subsequently that $\ln\left(\frac{f(\boldsymbol{\xi})f(\boldsymbol{\xi}_1)}{f(\boldsymbol{\xi}')f(\boldsymbol{\xi}_1')}\right) < 0$ is negative and vice versa.

Thus, the entropy s can be expressed within the framework of the Boltzmann equation in terms of an arbitrary velocity moment of the velocity distribution function. The temporal evolution of the *H-theorem* corresponds to $\frac{\partial H}{\partial t} \geq 0$. Therefore the entropy is monotonically increasing for systems described by the Boltzmann equation.

2.2.3. HERMITE POLYNOMIAL EXPANSION OF THE BGK BOLTZMANN EQUATION AND THE HYDRODYNAMIC LIMIT: THE LATTICE BOLTZMANN METHOD

In order to derive a numerical model for Equation (2.9), the macroscopic limit of the BGK Boltzmann equation needs to converge to the NSE. To show that the Boltzmann BGK approach stands up to the Navier-Stokes equations we use *Grad's* approach, see Grad (1949a) and Grad (1949b). The idea is to project the velocity distribution function on a Hermite polynomial basis. As we see later, this is a very convenient approach, since the moments of the Hermite polynomial expansion are equal to the velocity moments of the Boltzmann equation. It will be shown, that a low order approximation of the BGK Boltzmann equation in terms of the Hermite polynomial expansion leads to the correct macroscopic equations of fluid motion. First, some basic properties of Hermite polynomials will be discussed. Second, the Boltzmann BGK approach is projected onto a Hermite basis and the key aspects of deriving the Navier-Stokes equations will be introduced. Next, a numerical model based on the Hermite basis will be introduced, leading to a complete numerical model for the simulation of fluid flows, known as the Lattice Boltzmann BGK approach. The next section examines the exact derivation of the NSE applying the Chapman Enskog multi-scale expansion to the lattice Boltzmann BGK method.

As already stated, the expansion coefficients of Hermite polynomials correspond exactly to the velocity moments up to a desired order N. Therefore, a projection of the BGK Boltzmann equation on a Hermite basis leads to the desired equation at the hydrodynamic limit, see Chen and Doolen (1998).

Assuming a D dimensional space, Hermite polynomials are defined by the n^{th} derivative of a generic weight function, written as

$$\omega(\boldsymbol{\xi}) \propto A \exp\big(\boldsymbol{\xi}^2\big) \tag{2.23}$$

where $A = \frac{1}{(2\pi)^{D/2}}$. The Hermite polynomial of order n is defined in tensorial form as

$$\Upsilon(\boldsymbol{\xi}) = \frac{(-1)^n}{\omega(\boldsymbol{\xi})} \nabla^n \omega \boldsymbol{\xi}, \tag{2.24}$$

which implies a n^{th} rank symmetric tensor of the n^{th} order polynomial.

The first four polynomials $n = 3$ are written out explicitly in tensorial form, since they are used for consistent turbulence modeling later. Introducing the Kronecker delta $\boldsymbol{\delta}$ with the properties $\boldsymbol{\delta}_{i=j} = 1$ and $\boldsymbol{\delta}_{i\neq j} = 0$ we define the Hermite polynomials $\Upsilon^{(n)}(\boldsymbol{\xi})$ with $n = 0..3$ as

$$\Upsilon^{(0)}(\boldsymbol{\xi}) = 1, \tag{2.25a}$$

$$\Upsilon^{(1)}(\boldsymbol{\xi}) = \boldsymbol{\xi}, \tag{2.25b}$$

$$\Upsilon^{(2)}(\boldsymbol{\xi}) = \boldsymbol{\xi}\boldsymbol{\xi} - \boldsymbol{\delta}, \tag{2.25c}$$

$$\Upsilon^{(3)}(\boldsymbol{\xi}) = \xi_i\xi_j\xi_k - (\xi_i\delta_{jk} + \xi_j\delta_{ki} + \xi_k\delta_{ij}). \tag{2.25d}$$

By applying Equation (2.24) we can project the Boltzmann equation on a Hermite basis leading to

$$f(x_i, \boldsymbol{\xi}, t) = \omega(\boldsymbol{\xi}) \sum_{n=0}^{\infty} \frac{1}{n!} \boldsymbol{a}^{(n)}(x_i, t) \Upsilon^{(n)}(\boldsymbol{\xi}). \tag{2.26}$$

For the truncation of the series at N^{th} order we define

$$f(x_i, \boldsymbol{\xi}, t) = \omega(\boldsymbol{\xi}) \sum_{n=0}^{N} \frac{1}{n!} \boldsymbol{a}^{(n)}(x_i, t) \Upsilon^{(n)}(\boldsymbol{\xi}), \tag{2.27}$$

where the coefficients $\boldsymbol{a}^{(n)}(x_i, t)$ are defined as

$$\boldsymbol{a}^{(n)}(x_i, t) = \int f(x_i, \boldsymbol{\xi}, t) \Upsilon^{(n)}(\boldsymbol{\xi}) d\boldsymbol{\xi}. \tag{2.28}$$

In Equation (2.27), the product $\boldsymbol{a}^{(n)}(x_i, t)\ \Upsilon^{(n)}(\boldsymbol{\xi})$ can be interpreted as a full summation, since both terms are n^{th} rank tensors. The full summation will be denoted as $\boldsymbol{a} : \boldsymbol{a}$, which can be rewritten as $a_{ij}a_{ji}$ using the *Einstein'sche Summenkonvention.* Equation (2.28) already implies the necessity of Hermite polynomials for designing a numerical scheme for the Boltzmann BGK approach, since the moments in Equation (2.8c) correspond to the coefficients of the Hermite basis. The Hermite coefficients are written as

$$\boldsymbol{a}^{(0)} = \rho, \tag{2.29a}$$

$$\boldsymbol{a}^{(1)} = \rho \boldsymbol{u}, \tag{2.29b}$$

$$\boldsymbol{a}^{(2)} = \boldsymbol{\Pi} + \rho(\boldsymbol{u}\boldsymbol{u} - \boldsymbol{\delta}), \tag{2.29c}$$

$$\boldsymbol{a}^{(3)} = \int \boldsymbol{\xi}\boldsymbol{\xi}\boldsymbol{\xi} f(x_i, \boldsymbol{\xi}, t) d\boldsymbol{\xi} + 3\boldsymbol{u}\boldsymbol{a}^{(2)} - 2\rho\boldsymbol{u}\boldsymbol{u}\boldsymbol{u}. \tag{2.29d}$$

Here, Θ is the kinetic temperature, which will be set to $\Theta = 1$ for all simulations, since an athermal Boltzmann scheme is used. The corresponding Hermite coefficients for the equilibrium distribution function are defined as

$$\boldsymbol{a}_0^{(0)} = \rho, \tag{2.30a}$$

$$\boldsymbol{a}_0^{(1)} = \rho \boldsymbol{u}, \tag{2.30b}$$

$$\boldsymbol{a}_0^{(2)} = \rho \boldsymbol{u}\boldsymbol{u} + \rho(\Theta - 1)\boldsymbol{\delta}, \tag{2.30c}$$

$$\boldsymbol{a}_0^{(3)} = \rho u_i u_j u_k - \rho(\Theta - 1)^2 (u_i \delta_{jk} + u_j \delta_{ki} + u_k \delta_{ij})\ . \tag{2.30d}$$

So far, the conceptual design of the velocity distribution function based on Hermite bases was shown. To derive the Euler equations, we use the Hermite truncated Boltzmann equation. Inserting Equations (2.27), (2.29a)-(2.29d) and (2.30a)-(2.30d) in the BGK approach, given by Equation (2.9), one obtains

$$\frac{\partial}{\partial t} \boldsymbol{a}^{(n)} + \nabla_x \cdot \boldsymbol{a}^{(n+1)} + \boldsymbol{\delta} \cdot \nabla_x \cdot \boldsymbol{a}^{(n-1)} \boldsymbol{\delta} = -\frac{1}{\tau}(\boldsymbol{a}^{(n)} - \boldsymbol{a}_0^{(n)}). \tag{2.31}$$

By assuming a thermodynamic equilibrium, Equation (2.31) leads to the Euler equation by replacing the velocity distribution function by its equilibrium projected Boltzmann BGK equation

$$\frac{\partial}{\partial t}\boldsymbol{a}_0^{(n)} + \nabla_x \cdot \boldsymbol{a}_0^{(n+1)} + \boldsymbol{\delta} \cdot \nabla_x \cdot \boldsymbol{a}_0^{(n-1)}\boldsymbol{\delta} = -\frac{1}{\tau}(\boldsymbol{a}_0^{(n)} - \boldsymbol{a}_0^{(n)}). \tag{2.32}$$

For $n = 0$ the continuity equation

$$\frac{\partial \rho}{\partial t} + \nabla \cdot (\rho \boldsymbol{u}) = 0 \tag{2.33}$$

is obtained and for $n = 1$ Equation (2.32) leads to the desired inviscid momentum equation

$$\frac{\partial \rho \boldsymbol{u}}{\partial t} + \nabla \cdot (\rho \boldsymbol{u}\boldsymbol{u} + p\boldsymbol{\delta}) = 0 \ . \tag{2.34}$$

In order to derive the NSE we allow small disturbances of the thermodynamic equilibrium for the velocity distribution function

$$f(x_i, \boldsymbol{\xi}, t) = f^{eq}(x_i, \boldsymbol{\xi}, t) + f^{neq}(x_i, \boldsymbol{\xi}, t) \ . \tag{2.35}$$

Using Equation (2.35) we write the Hermite truncated BGK Boltzmann equation at non-equilibrium state as

$$\frac{\partial}{\partial t}\boldsymbol{a}_0^{(n)} + \nabla_x \cdot \boldsymbol{a}_0^{(n+1)} + \boldsymbol{\delta} \cdot \nabla_x \cdot \boldsymbol{a}_0^{(n-1)}\boldsymbol{\delta} = -\frac{1}{\tau}\boldsymbol{a}_1^{(n)} \tag{2.36}$$

with

$$\boldsymbol{a}_1^{(n)}(x_i, t) = \int f^{neq}(x_i, \boldsymbol{\xi}, t)\Upsilon^{(n)}(\boldsymbol{\xi})d\boldsymbol{\xi} \tag{2.37}$$

and

$$f^{neq}(x_i, \boldsymbol{\xi}, t) = \sum_{n=0}^{N} \frac{1}{n!}\Upsilon^{(n)}(\boldsymbol{\xi})\boldsymbol{a}_1^{(n)}(x_i, t) \ . \tag{2.38}$$

In Equation 2.36 τ is the relaxation time, which is related to the viscosity as $\nu = c_s^2(\tau - \frac{1}{2})$. Assuming small disturbances from the local thermodynamic equilibrium in Equation (2.36), leads for $n = 1$ to

$$\frac{\partial \rho \boldsymbol{u}}{\partial t} + \nabla \cdot (\rho \boldsymbol{u}\boldsymbol{u} + p\boldsymbol{\delta} - \boldsymbol{\Pi}) = 0 \ , \tag{2.39}$$

see Bespalko (2011); Lammers (2004) and Peng (2014). A proper expression for $\boldsymbol{a}_1^{(n)}$ in order to describe the momentum flux tensor $\boldsymbol{\Pi}$ needs to be derived now. It can be shown, e.g., in Waldrow (2000), that in an athermal flow $\boldsymbol{a}_1^{(2)}$ is defined by

$$\boldsymbol{a}_1^{(2)}(x_i, t) = -\tau\rho(2\nabla\boldsymbol{u} - 2/3(\nabla \cdot \boldsymbol{u})\boldsymbol{\delta}), \tag{2.40}$$

which directly connects $\boldsymbol{a}_1^{(2)}$ to the strain-field and following Peng (2014), $\boldsymbol{\Pi}$ can subsequently be expressed as

$$\boldsymbol{\Pi} = 2\mu\boldsymbol{S} \ . \tag{2.41}$$

$\boldsymbol{S}$ is the strain-rate. In consideration with Equation (2.39), this leads to the NSE. Note, that Equation (2.39) implies the second order truncated equilibrium distribution function

$$f^{neq}(x_i, \boldsymbol{\xi}, t) = \omega(\boldsymbol{\xi}) \left(1 + \boldsymbol{\xi} \cdot \boldsymbol{u} + \frac{(\boldsymbol{\xi} \cdot \boldsymbol{u})^2}{2} - \frac{1}{2}\boldsymbol{u}^2\right). \tag{2.42}$$

Thus, a second order approximation of the velocity distribution function in terms of a Hermite polynomial expansion leads to the NSE using the BGK Boltzmann approach. At this point, only the derivation of the macroscopic equations has been shown, without commenting on the actual accuracy of this approximation. Aspects regarding the accuracy will be discussed later in Section 2.3.

Now, the numerical discretization of the velocity distribution function will be introduced, based on the previous derivations. The numerical discretization of the BGK Boltzmann equation leads to the LBM. An appropriate numerical model for Equation (2.9), is found by defining a finite set of discrete lattice links at each numerical node. The definition of discrete lattice links at each spatial node is based on the velocity distribution function, which is defined in phase space. Thus, $f(x_i, \boldsymbol{\xi}, t)$ is discretized in space, time and velocity space. A pure space and time discretization would lead to a very expensive estimation of the velocity moments. Furthermore, the phase space discretization is essential for the evaluation of the velocity moments since a Gauß-Hermite quadrature allows the evaluation of the macroscopic moments based on the Hermite truncated Boltzmann equation. Therefore, a discrete set of finite velocities is defined in space, which is described by voxels. On each voxel the discrete lattice links are defined and the Gauss-Hermite quadrature is performed based on the Hermite projection of the Boltzmann BGK equation. Throughout this work we use the discrete $D3Q19$ model, which implies 19 discrete velocities in a three-dimensional space. Common velocity sets are the $D3Q13$, the $D3Q15$ and the $D3Q27$ for three- dimensional problems, or the well-known $D2Q5$ and $D2Q9$ model for two-dimensional flow problems. They all have different advantages and disadvantages, which will not be discussed here but are analyzed in detail in Hänel (2004); Waldrow (2000) or Geier (2006).

The discrete lattice for the $D3Q19$ model applied in this work is shown in figure 2.3.

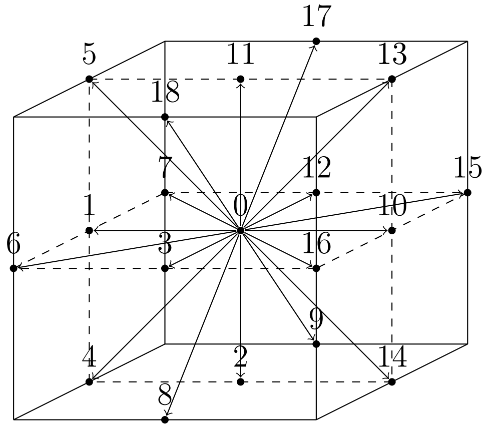

Figure 2.3.: Discrete $D3Q19$ lattice links.

The numbering of the lattice links differs from the common way in literature, but is rather efficient regarding the implementation of boundary conditions within *OpenLB*.

It has been shown, that the macroscopic moments of the velocity distribution functions are identical to the weighting coefficients of the Hermite polynomials. Thus, a discrete velocity field $\boldsymbol{c}_\alpha$ with $\alpha = 0...q-1$ is introduced, see Figure 2.3, where q is the number of discrete lattice links. The Gauß-Hermite quadrature for the reconstruction of the macroscopic moments is written as

$$\int_{\boldsymbol{\xi}} \omega(\boldsymbol{\xi}) f(x_i, \boldsymbol{\xi}, t) = \sum_{\alpha=0}^{q-1} \omega_\alpha f(x_i, \boldsymbol{c}_\alpha, t), \tag{2.43}$$

where $\boldsymbol{c}_\alpha$ is the discrete lattice velocity of the corresponding model, α is the discrete direction, q is the number of discrete lattice velocities and ω_α are the weights of the quadrature formula.

The macroscopic moments are consequently

$$\rho = \int d\boldsymbol{\xi} f(x_i, \boldsymbol{\xi}, t) = \sum_{\alpha=0}^{q-1} f_\alpha(x_i, \boldsymbol{c}_\alpha, t), \tag{2.44a}$$

$$\rho \boldsymbol{u} = \int d\boldsymbol{\xi} \boldsymbol{\xi} f(x_i, \boldsymbol{\xi}, t) = \sum_{\alpha=0}^{q-1} f_\alpha(x_i, \boldsymbol{c}_\alpha, t) \boldsymbol{c}_\alpha, \tag{2.44b}$$

$$\boldsymbol{Q} = \int d\boldsymbol{\xi}\ \boldsymbol{\xi}\boldsymbol{\xi} f^{neq}(x_i, \boldsymbol{\xi}, t) = \sum_{\alpha=0}^{q-1} f_\alpha^{neq}(x_i, \boldsymbol{c}_\alpha, t) \boldsymbol{c}_\alpha \boldsymbol{c}_\alpha, \tag{2.44c}$$

where ρ is the density, $\rho\boldsymbol{u}$ the momentum and $\boldsymbol{Q}$ the stress.

Before the numerical procedure is explained, the lattice properties and the discretized version of the velocity distribution function are summarized. Tabular 2.1 gives an overview of the discrete directions for the $D3Q19$ lattice links used in this work. Discretization

q	0	1	2	3	4	5	6	7	8
ω_α	1/3	1/18	1/18	1/18	1/36	1/36	1/36	1/36	1/36
c_x	0	−1	0	0	−1	−1	−1	−1	0
c_y	0	0	−1	0	−1	1	0	0	−1
c_z	0	0	0	−1	0	0	−1	1	−1

q	9	10	11	12	13	14	15	16	17	18
ω_α	1/36	1/18	1/18	1/18	1/36	1/36	1/36	1/36	1/36	1/36
c_x	0	1	0	0	1	1	1	1	0	0
c_y	−1	0	1	0	1	−1	0	0	1	1
c_z	1	0	0	1	0	0	1	−1	1	−1

Table 2.1.: Discrete lattice directions and the corresponding weights for quadrature formula.

of Equation (2.9) onto a lattice with the demonstrated properties leads to the evolution equation for the lattice BGK model:

$$\frac{f_\alpha(x_i+\boldsymbol{c}_\alpha\Delta t,\boldsymbol{c}_\alpha,t+\Delta t)-f_\alpha(x_i,\boldsymbol{c}_\alpha,t)}{\Delta t}=-\frac{1}{\tau}(f_\alpha(x_i,\boldsymbol{c}_\alpha,t)-f_\alpha^{eq}(x_i,\boldsymbol{c}_\alpha,t)). \tag{2.45}$$

Defining $\Delta t=1$, as well as, $c_x=c_y=c_z=\frac{\Delta x}{\Delta t}=1$ in lattice units on an equidistant grid, the typical LBM algorithm consisting of the two elementary steps:

1. Collide: $\tilde{f}_\alpha(x_i,\boldsymbol{c}_\alpha,t)=-\frac{1}{\tau}(f_\alpha(x_i,\boldsymbol{c}_\alpha,t)-f_\alpha^{eq}(x_i,\boldsymbol{c}_\alpha,t))$.
2. Stream: $f_\alpha(x_i+\boldsymbol{c}_\alpha t,\boldsymbol{c}_\alpha,t+\Delta t)-f_\alpha(x_i,\boldsymbol{c}_\alpha,t)=\tilde{f}_\alpha(x_i,\boldsymbol{c}_\alpha,t)$.

can be introduced.

$f_\alpha^{eq}(x_i,\boldsymbol{c}_\alpha,t)$ is the discrete approximation of the low Mach number expanded Maxwell distribution given in Equation (2.10). A Taylor series approximation for small Mach numbers at a constant $\boldsymbol{x}$ leads to

$$f_\alpha^{eq}(x_i,\boldsymbol{c}_\alpha,t)=\rho\omega_\alpha\left[1+\frac{\boldsymbol{c}_\alpha u_i}{c_s^2}+\frac{1}{2c_s^4}(u_iu_j-c_s^2\boldsymbol{\delta})u_iu_j\right]. \tag{2.46}$$

In Equation (2.46), $c_s=\frac{1}{\sqrt{3}}$ is the lattice speed of sound, leading to the Mach number $Ma=\frac{|\boldsymbol{c}|}{c_s}$ defined in lattice space. To finalize the discussion, we close the gap between Equation (2.46), Equation (2.10) and the Hermite quadrature, to show that the discrete Maxwellian equation conserves mass, momentum and energy in the same way as its continuous definition. First, we rewrite Equation (2.10) with the discrete lattice velocity $\boldsymbol{c}$, using ideal gas formulations for the isothermal speed of sound $c_s=\sqrt{RT}$ and $D=3$

$$f^{eq}(x_i,\boldsymbol{\xi},t)=\frac{\rho(x_i,t)}{(2\pi RT(x_i,t))^{3/2}}\exp\left\{\left(-\frac{(\boldsymbol{\xi}-\boldsymbol{u}_{ref})^2}{2RT(x_i,t)}\right)\right\}=\frac{\rho(x_i,t)}{(2\pi c_s^2)^{3/2}}\exp\left\{\left(-\frac{(\boldsymbol{c}_\alpha-\boldsymbol{u}_{ref})^2}{2c_s^2}\right)\right\}. \tag{2.47}$$

Separating the exponential part of Equation (2.47), leads to different Mach number dependencies

$$\exp\left\{\left(-\frac{(\boldsymbol{c}_\alpha-\boldsymbol{u}_{ref})^2}{2c_s^2}\right)\right\}=\underbrace{\exp\left\{\left(-\frac{\boldsymbol{c}_\alpha^2}{2c_s^2}\right)\right\}}_{\mathcal{O}(1)}\underbrace{\exp\left\{\left(-\frac{u_{ref,i}\boldsymbol{c}_\alpha}{c_s^2}\right)\right\}}_{\mathcal{O}(Ma)}\underbrace{\exp\left\{\left(-\frac{u_{ref,i}u_{ref,i}}{2c_s^2}\right)\right\}}_{\mathcal{O}(Ma^2)}. \tag{2.48}$$

Equation (2.48) is now expanded in terms of a Taylor series around small Mach numbers leading to the equivalent of Equation (2.46)

$$f^{eq}(x_i,\boldsymbol{c}_\alpha,t)=\frac{\rho(x_i,t)}{(2\pi c_s^2)^{3/2}}\exp\left\{\left(-\frac{\boldsymbol{c}_\alpha^2}{2c_s^2}\right)\right\}\exp\left\{\left(1+\frac{u_i\boldsymbol{c}_\alpha}{c_s^2}+\frac{u_iu_i}{2c_s^2}+\frac{u_i\boldsymbol{c}_\alpha u_j\boldsymbol{c}_\beta}{2c_s^4}\right)\right\}, \tag{2.49}$$

where the first two terms on the right hand side are the underlying weighting coefficients of ω_α, see Table 2.1, of the Hermite quadrature. These weights satisfy

$$\sum_\alpha\omega_\alpha=1,\ \sum_\alpha\omega_\alpha c_{i\alpha}c_{j\alpha}=c_s^2\boldsymbol{\delta} \tag{2.50}$$

for $f_\alpha^{eq}(x_i, \boldsymbol{c}_\alpha, t)$. This section introduced the Hermite projection of the BGK Boltzmann approach and its discretization on a lattice with discrete velocity links. It was shown, that the discrete BGK Boltzmann approach conserves the macroscopic moments by using a truncated Hermite polynomial expansion of the velocity distribution function up to order 2 for the weakly compressible limit of the NSE.

2.3. From the Kinetic Level to the Navier-Stokes Equations: The Chapman Enskog Expansion

In order to reconstruct the macroscopic equations of fluid motion, a Chapman Enskog expansion is used, see Chen and Doolen (1998). The velocity distribution functions are expanded with a multi-scale expansion factor ϵ, which is directly related to the Knudsen number $\epsilon = Kn$. For the discrete distribution functions, this expansion reads

$$f_\alpha = f_\alpha^{(0)} + \epsilon f_\alpha^{(1)} + \epsilon^2 f_\alpha^{(2)} + \; ..., \tag{2.51}$$

where $f_\alpha^{(0)}$ corresponds to f_α^{eq}. For the time and space derivatives one obtains

$$\frac{\partial}{\partial t} = \epsilon \frac{\partial}{\partial t_0} + \epsilon^2 \frac{\partial}{\partial t_1}, \quad \frac{\partial}{\partial x_i} = \frac{\partial}{\partial x_i^{(0)}} + \epsilon \frac{\partial}{\partial x_i^{(1)}}, \tag{2.52}$$

where the indices 0 and 1 indicate different scales of the corresponding unit. The starting point is Equation (2.45), which is approximated by a second order Taylor series with respect to $\boldsymbol{c}_\alpha$ and x_i, leading to

$$\frac{\partial f_\alpha}{\partial t} + \frac{\partial f_\alpha}{\partial x_i} \boldsymbol{c}_\alpha + 2 \frac{\partial^2 f_\alpha}{\partial x_i \partial t} \boldsymbol{c}_\alpha + \frac{\partial^2 f_\alpha}{\partial^2 t} + \frac{\partial^2 f_\alpha}{\partial x_i \partial x_j} \boldsymbol{c}_\alpha \boldsymbol{c}_\alpha = -\frac{1}{\tau} f_\alpha^{neq}. \tag{2.53}$$

Taking Equations (2.53) and inserting Equations (2.52) and (2.51) one obtains a set of equations, which separated by order ϵ^n, leads to

$$\mathcal{O}(\epsilon^0): \qquad -\frac{1}{\tau}(f_\alpha - f_\alpha^{eq}) = 0 \tag{2.54a}$$

$$\mathcal{O}(\epsilon^1): \qquad \frac{\partial f_\alpha^{eq}}{\partial t_0} + \boldsymbol{\delta c}_\alpha \frac{\partial f_\alpha^{eq}}{\partial x_i^{(1)}} = -\frac{1}{\tau} f_\alpha^{neq} \tag{2.54b}$$

Multiplication of Equation (2.54a) and (2.54b) by $\boldsymbol{c}_\alpha$ leads with subsequent integration to mass and momentum conservation up to order $\mathcal{O}(\epsilon^1)$. The continuity equation as well as the Euler momentum equations can be written as

$$\frac{\partial \rho}{\partial t_0} + \nabla_i^{(0)}(\rho u_i) = 0 \tag{2.55a}$$

$$\frac{\partial \rho u_i}{\partial t_0} + \nabla_j^{(0)}\Pi_{ij}^{(0)} = 0 \tag{2.55b}$$

with $\Pi_{ij}^{(0)} = \sum_\alpha \boldsymbol{c}_\alpha \boldsymbol{c}_\alpha f_\alpha^{eq} = \rho u_i u_j + p\boldsymbol{\delta}$ being the zeroth-order momentum flux tensor, see Section 2.2.3.

This is similar to the procedure based on Grad's approach. For $\mathcal{O}(\epsilon^2)$ one obtains

$$\mathcal{O}(\epsilon^2): \qquad \frac{\partial f_\alpha^{eq}}{\partial t_1} + \left(1 - \frac{1}{2\tau}\right)\left(\frac{\partial f_\alpha^{neq}}{\partial t_0} + \frac{\partial f_\alpha^{neq}}{\partial x_i^{(1)}}\boldsymbol{\delta c}_\alpha\right) = -\frac{1}{\tau} f_\alpha^{(2)}. \tag{2.56}$$

Following the same procedure as for Equations (2.54a) and (2.54b), Equation (2.56) leads to

$$\frac{\partial \rho}{\partial t_1} = 0 \tag{2.57a}$$

$$\frac{\partial \rho u_i}{\partial t_1} + \left(1 - \frac{1}{2\tau}\right)\nabla_j^{(0)}\Pi_{ij}^{(1)} = 0. \tag{2.57b}$$

In Equation (2.57b) $\Pi_{ij}^{(1)} = \sum_\alpha \boldsymbol{c}_\alpha \boldsymbol{c}_\alpha f_\alpha^{neq}$ is the first order off-equilibrium momentum flux tensor. An expression for this term is found by multiplying Equation (2.54b) by $\boldsymbol{c}_\alpha \boldsymbol{c}_\alpha = c_{i\alpha} c_{j\alpha}$. The summation over all discrete links α, corresponding to a velocity space integration, leads to

$$-\frac{1}{\tau}\sum_\alpha c_{i\alpha} c_{j\alpha} f_\alpha^{neq} = \sum_\alpha \frac{c_{i\alpha} c_{j\alpha} \partial f_\alpha^{eq}}{\partial t_0} + \sum_\alpha \frac{c_{i\alpha} c_{j\alpha} c_{k\alpha} \partial f_\alpha^{eq}}{\partial x_k^{(1)}}. \tag{2.58}$$

After some algebra, we obtain

$$\Pi_{ij}^{(1)} = \frac{\rho}{c_s^2}\left(\frac{\partial u_j}{\partial x_i^{(1)}} + \frac{\partial u_i}{\partial x_j^{(1)}}\right) + \mathcal{O}(Ma^3). \tag{2.59}$$

Neglecting high-order terms on the Mach number and applying Equation (2.59) to Equation (2.57b) the hydrodynamic equation of fluid motion can be finally written as

$$\frac{\partial \rho u_i}{\partial t} + \nabla_j\left(p\delta_{ij} + \frac{\partial \rho u_i}{\partial x_j} - \frac{\rho}{c_s^2}\left(\frac{1}{\tau} - \frac{1}{2}\right)\frac{\partial u_i}{\partial x_j}\right) = 0\ . \tag{2.60}$$

2.4. Modeling of the Collision Operator

LBM solves a set of kinetic equations in terms of discrete velocity distribution functions $f_\alpha(x_i, \boldsymbol{c}_\alpha, t)$ numerically. The discrete Boltzmann equation, see section 2.2.3, can be written as

$$f_\alpha(x_i, x_i + \boldsymbol{c}_\alpha \Delta t, t + \Delta t) = f_\alpha(x_i, \boldsymbol{c}_\alpha, t) + \Omega_\alpha(f_\alpha(x_i, \boldsymbol{c}_\alpha, t), f_\alpha^{'}(x_i, \boldsymbol{c}_\alpha, t)) \tag{2.61}$$

where $\boldsymbol{c}_\alpha$ is the discrete velocity set of the applied lattice structure. The discrete collision operator $\Omega_\alpha(f_\alpha(x_i, \boldsymbol{c}_\alpha, t), f_\alpha^{'}(x_i, \boldsymbol{c}_\alpha, t))$, represents non-linear and viscous effects, similar to those of the NSE.

This work deals with high Reynolds number flows and it has been observed, that the discretization of the right-hand side of Equation (2.61) influences the numerical stability, as well as the statistics of the investigated turbulent flow. In order to derive a sufficient accurate turbulence model for LES in the LBM framework, it is mandatory to understand the pure LBM schemes in order to develop turbulence models that not only increase the stability of LBM methods but also treat the energy transfer and the statistics of turbulent flows correctly. Three different schemes are part of the investigation in Chapter 3, namely the BGK, the MRT and the RLB.

So far, only the BGK approach for modeling the collision term has been introduced shortly but the properties of this model have not been discussed yet. This will be done in Section 2.4.1. In Section 2.4.2, the well-known MRT scheme will be introduced and major characteristics will be discussed. Finally, the regularized BGK approach will be introduced and the differences between the schemes will be outlined shortly.

Depending on the applied discrete scheme, the collision term is modeled in a different manner. The reconstruction of macroscopic moments based on a Gauss-Hermite quadrature of the velocity distribution function on a discrete lattice is the same for all models. The first two moments of the velocity distribution functions are density ρ and the momentum $\rho\boldsymbol{u}$, that is,

$$\rho = \sum_\alpha f_\alpha, \;\; \rho\boldsymbol{u} = \sum_\alpha \boldsymbol{c}_\alpha f_\alpha. \tag{2.62}$$

The momentum flux is the second-order off-equilibrium moment of the velocity distribution functions, defined as

$$\boldsymbol{\Pi} = \sum_\alpha f_\alpha^{neq} \boldsymbol{c}_\alpha \boldsymbol{c}_\alpha. \tag{2.63}$$

There are several other approaches for modeling for the collision operator like the cascaded Lattice Boltzmann scheme of Martin Geier, see Geier (2006) and Geller et al. (2013). This approach applies central moments instead of uncentered moments and low-order velocity moments are used in a cascaded process to estimate high-order velocity moments. An essential part of the Boltzmann theory is to hold a positive definiteness of the entropy. Explicit formulations of entropy are enhanced in the entropic LBM (ELBM), which can be divided in two different approaches. The first one is based on the weighted discrete version of the H-theorem, see Section 2.2.2, developed by Ansumali and Karlin, see, e.g., Ansumali and Karlin (2002, 2000) and Chikaarla and Karlin (2013). The second approach is based on a *Tsallis* entropy function, derived and demonstrated in Boghosian et al. (2001) and Boghosian et al. (2003). Another possibility to design the collision operator is similar to the BGK approach, known as the two relaxation time (TRT) model. As shown later, the discrete velocity distribution functions can be related to macroscopic moments by a linear transformation matrix. The TRT approach differs between odd order moments, which are relaxed separately from the even order ones. This approach is outlined by Ginzburg et al. (2008).

2.4.1. The Lattice BGK Approach Revised

The most common applied approach is called the BGK approach, see He and Luo (1997); Guo et al. (2000); Guo and Shu (2013); Sukop and Thorne (2006), which models the collision term as a linear relaxation towards a Maxwellian equilibrium. The BGK approach was already introduced for the continuous Boltzmann equation in Section 2.2. The discrete BGK Boltzmann approach is described by

$$\begin{aligned}\Omega_\alpha(f_\alpha(x_i,\boldsymbol{c}_\alpha,t),f_\alpha^{'}(x_i,\boldsymbol{c}_\alpha,t)) = f_\alpha(x_i,x_i+\boldsymbol{c}_\alpha\Delta t,t+\Delta t) - f_\alpha(x_i,\boldsymbol{c}_\alpha,t) = \\ -\frac{1}{\tau}\left(f_\alpha(x_i,\boldsymbol{c}_\alpha,t) - f_\alpha^{eq}(x_i,\boldsymbol{c}_\alpha,t)\right),\end{aligned} \tag{2.64}$$

where $f_\alpha^{eq}(t,\boldsymbol{x})$ is a low Mach number truncated Maxwell-Boltzmann distribution, which is adjusted in such a way, that Equation (2.63) is fulfilled and mass and momentum are conserved. A widely used formulation for f_α^{eq} is

$$f_\alpha^{eq} = \rho\omega_\alpha\left[1+\frac{c_{i\alpha}u_i}{c_s^2}+\frac{1}{2c_s^4}(u_iu_j-c_s^2\delta_{ij})u_iu_j\right], \tag{2.65}$$

which is the same as Equation (2.42). ω_α are the weights to satisfy the exact Gauss-Hermite quadrature of the lattice, c_s is the lattice speed of sound and δ_{ij} is the Kronecker delta. Although the BGK approach has been applied to many flow problems, see Hänel (2004); Waldrow (2000); Chen and Doolen (1998); Peng (2014); Krause et al. (2013); Guo et al. (2000); Premnath et al. (2014) among others, it has been found to suffer from non-linear instabilities at high Reynolds numbers, which have its origins in unphysical velocity moments of f_α. Among of others, Lallemand and Luo (2000) and Lammers et al. (2006) showed, that the BGK model diverges for Mach numbers close to $Ma \approx 0.2$ for two- and three dimensional turbulent flows. In terms of a normalized wall distance in the simulation of a turbulent channel flow, the stability threshold on a equidistant grid, is described approximately by $y^+ = \frac{u_\tau H}{\nu} \leq 2.5$. This stability threshold is only correct for simulations with a simple bounce-back rule for representing the solid walls.

2.4.2. The Multi Relaxation Time Scheme

To remedy the shortcomings of the BGK scheme, the Multi-Relaxation-Time (MRT) scheme was developed by d'Humiéres et al. (2002), analyzed and optimized by Lallemand and Luo (2000) and applied in Yu et al. (2006); Yu and Girimaji (2005); Premnath et al. (2009); Geller et al. (2013); Du et al. (2006) amongst others. The main idea is to transform the collision step into momentum space and to relax each moment separately in order to reduce the non-linear instabilities arising from the temporal growth of unphysical moments.

In order to describe the motivation of the MRT model in more detail, we rewrite the discrete BGK Boltzmann Equation (2.64) in a scattering matrix form by using a relaxation time matrix $\boldsymbol{\Lambda} = diag(\lambda_0, \lambda_1, ..., \lambda_{q-1})$, leading to

$$f_\alpha(x_i, x_i + \boldsymbol{c}_\alpha \Delta t, t + \Delta t) = f_\alpha(x_i, \boldsymbol{c}_\alpha, t) - \boldsymbol{\Lambda} \left(f_\alpha(x_i, \boldsymbol{c}_\alpha, t) - f_\alpha^{eq}(x_i, \boldsymbol{c}_\alpha, t) \right). \tag{2.66}$$

In Equation (2.66), each velocity link can be relaxed separately by different diagonal elements of $\boldsymbol{\Lambda}$. For $\lambda_0 = \lambda_1 = ... = \lambda_{q-1} = \frac{1}{\tau}$ the original BGK model is obtained.

So far, the collide and stream algorithm is performed in velocity space $\mathbb{V}$. The unphysical velocity moments lead to non-linear instabilities which can cause a blow-up of the simulation, thus, the collision steps are defined in momentum space $\mathbb{M}$ in the MRT framework by relaxing each moment separately, to avoid the unphysical velocity moments from growing transiently. These moments are defined as polynomial expansions of f_α based on the discrete velocity $\boldsymbol{c}_\alpha$, see Guo and Shu (2013), as

$$m_\alpha = \boldsymbol{M} f_\alpha \ . \tag{2.67}$$

The transformation matrix $\boldsymbol{M}$ is given in Appendix D. $\boldsymbol{M}$ is constructed based on the *Gram-Schmidt* orthogonalization, see Bouzidi et al. (2001), where the polynomials $c_{\alpha x}^m c_{\alpha y}^n c_{\alpha z}^l$ with $(m,\ n,\ l) \geq 0$ are applied based on the pairwise orthogonal basis vectors $\boldsymbol{e}_i$. The basis vector $\boldsymbol{e}_i$ is restricted by the discrete velocity model applied and, thus, the moments obtained by Equation (2.67) can be interpreted physically. For the $D3Q19$ model, we can define the 19 discrete moments as

$$\begin{aligned} m_\alpha = (m_0, ..., m_{q-1}) = \\ (\rho, e, \lambda, j_x, q_x, j_y, q_y, j_z, q_z, S_{xx}, S_{zz}, S_{xy}, S_{xz}, S_{yz}, Q_1, Q_2, g_x, g_y, g_z) \end{aligned} \tag{2.68}$$

where e is the energy, λ is the energy flux squared, j_i the momentum, q_i the heat flux and S_{ij} the viscous momentum flux. Q_1 and Q_2, as well as, g_i are not related to an interpretable flow-physical moment in particular.

As already mentioned before, the corresponding algorithm of the MRT model is based on a collision step in momentum space $\mathbb{M}$, while advection or streaming is performed in velocity space $\mathbb{V}$. The underlying algorithm can be summarized as

$$f_\alpha(x_i, x_i + \boldsymbol{c}_\alpha \Delta t, t + \Delta t) = f_\alpha(x_i, \boldsymbol{c}_\alpha, t) - \boldsymbol{M}^{-1} \boldsymbol{\Lambda} (m_\alpha(x_i, \boldsymbol{c}_\alpha, t) - m_\alpha^{eq}(x_i, \boldsymbol{c}_\alpha, t)). \tag{2.69}$$

The equilibrium functions of the MRT model are given in Appendix D, see Equations (D.3a)-(D.3s). They are designed to increase the stability and reconstruct the NSE at the same time. Similar to the Chapman-Enskog expansion for the BGK model, this multi-scale separation can be performed for the MRT collision model as well. Based on the work of Yu et al. (2006); Yu and Girimaji (2005); Lallemand and Luo (2000), we define the relaxation time matrix as

$$\begin{aligned} \boldsymbol{\Lambda} = diag(s_0, s_1, ..., s_{q-1}) = \\ (0, \lambda_e, \lambda_\epsilon, 0, \lambda_{q_x}, 0, \lambda_{q_y}, 0, \lambda_{q_z}, \lambda_\nu, \lambda_\nu, \lambda_\nu, \lambda_\nu, \lambda_\nu, \lambda_{Q_1}, \lambda_{Q_2}, \lambda_{g_x}, \lambda_{g_y}, \lambda_{g_z}) \end{aligned} \tag{2.70}$$

The values given in Equation (2.70) are the result of a Neumann stability analysis, see Lallemand and Luo (2000) or Lammers (2004), emerging from the linearized LBM. As a result one receives the eigenvalues λ_α which lead to an increased stability for the MRT based LBM. The optimized parameters are shown in Appendix D, see Equation (D.2). The relaxation parameters λ_ν are related to the viscosity as $\nu = c_s^2\left(\frac{1}{\lambda_\nu} - \frac{1}{2}\right)\Delta_t$, which corresponds to the lattice BGK model. Compared to the lattice BGK scheme, the algorithm given in Equation (2.69) needs approximately 15% more computational time.

Yet, due to the inconsistent derivation of boundary conditions for stresses on domain boundaries, where velocities or the pressure are prescribed, instabilities arise in the MRT model for Reynolds numbers larger than approximately $\mathcal{O}(10^4)$ in three dimensional turbulent flows, see Freitas et al. (2011). In order to suppress these exponentially growing disturbances, Latt (2007) proposed a regularization of the classical BGK algorithm.

2.4.3. THE REGULARIZED BGK APPROACH

Apart from the stabilisation technique introduced in Section 2.4.2, another class of BGK models exist, which was introduced by Latt and Chopard in Latt (2007); Latt and Chopard (2006); Latt et al. (2008) along with Zhang et al. (2006). In order to increase the stability of the lattice BGK approach, a regularisation is performed each time step with an approximation of the first order non-equilibrium part of the velocity distribution function

$$f(x_i, \boldsymbol{\xi}, t) = f^{eq}(x_i, \boldsymbol{\xi}, t) + f^{neq}(x_i, \boldsymbol{\xi}, t) \Rightarrow f(x_i, \boldsymbol{\xi}, t) = f^{eq}(x_i, \boldsymbol{\xi}, t) + f^{(1)}(x_i, \boldsymbol{\xi}, t). \quad (2.71)$$

In Equation (2.71), the first order non-equilibrium part $f^{(1)}(x_i, \boldsymbol{\xi}, t)$ can be written as

$$f_\alpha^{(1)}(x_i, \boldsymbol{c}_\alpha, t) = -\frac{\tau}{c_s^2}\omega_\alpha \boldsymbol{Q}_\alpha \frac{\partial \rho u_j}{\partial x_i}\ , \quad (2.72)$$

which is approximated by the corresponding $f_\alpha^{neq}(x_i, \boldsymbol{c}_\alpha, t)$ leading to

$$f_\alpha^{neq}(x_i, \boldsymbol{c}_\alpha, t) = f_\alpha(x_i, \boldsymbol{c}_\alpha, t) - f_\alpha^{eq}(x_i, \boldsymbol{c}_\alpha, t) \approx f_\alpha^{(1)}(x_i, \boldsymbol{c}_\alpha, t). \quad (2.73)$$

Similar to Equation (2.73), we can write the second-order moment as

$$\Pi_{ij}^{neq} \approx \sum_\alpha f^{(1)}(x_i, \boldsymbol{\xi}, t)\boldsymbol{c}_\alpha \boldsymbol{c}_\alpha = -\tau c_s^2 \left(\frac{\partial \rho u_j}{\partial x_i} + \frac{\partial \rho u_i}{\partial x_j}\right) \quad (2.74)$$

Combining Equation (2.73) and (2.74) leads to the first order Chapman-Enskog expanded approximation of $f^{(1)}(x_i, \boldsymbol{\xi}, t)$

$$f_\alpha^{(1)}(x_i, \boldsymbol{c}_\alpha, t) = -\frac{\tau}{2c_s^4}\omega_\alpha \boldsymbol{Q}_\alpha \Pi_{ij}^{neq} \quad (2.75)$$

The overall procedure in terms of regularisation of the common lattice BGK algorithm reads

$$f_\alpha(x_i, x_i + \boldsymbol{c}_\alpha \Delta t, t + \Delta t) = f_\alpha(x_i, \boldsymbol{c}_\alpha, t) + (1 - \omega) f_\alpha^{(1)}(x_i, \boldsymbol{c}_\alpha, t), \tag{2.76}$$

where $\omega = \frac{1}{\tau}$ is the relaxation frequency. The algorithm is summarized as

- Compute macroscopic moments with Equation (2.44c)
- Compute the equilibrium distribution function $f_\alpha^{eq}(x_i, \boldsymbol{c}_\alpha, t)$ with Equation (2.46)
- Compute $f^{neq}(x_i, \boldsymbol{\xi}, t)$ and Π_{ij}^{neq} according to Equation (2.71) and (2.74)
- Regularize the collision step with Equation (2.76)

This regularization technique removes all moments of order $n > 2$ in terms of the Hermite polynomial representation of the velocity distribution function. Thus, Equation (2.72) can be rewritten as

$$f_\alpha^{(1)}(x_i, \boldsymbol{c}_\alpha, t) = -\frac{1}{2c_s^4} \omega_\alpha \Upsilon_\alpha^{(2)} : \boldsymbol{a}_1^{(2)} \tag{2.77}$$

Following Latt (2007) and Malaspinas (2015) these higher-order moments are negligible at the hydrodynamic limit, i.e., for the weakly compressible NSE. Recent advances have been made by Malaspinas (2015) leading to a recursive formulation of the velocity moments, which lead to an improved stability of the compressible LBM formulation.

The regularization of the collision step needs to be applied to the bulk flow as well as at the boundaries. The main issue with respect to boundary conditions in the RLB framework is the proper reconstruction of the unknown distribution functions propagating opposed the domain boundaries. For the regularization the discrete velocity information, i.e., an approximation of the non-equilibrium part $f_\alpha^{(1)}$ in Equation (2.73), is required. Different approaches to design $f_\alpha^{(1)}$ at the domain boundaries are proposed and analyzed in Latt and Chopard (2006); Latt et al. (2008). In the present study a linear finite differencing scheme for the approximation of the strain-rate is considered for all wall bounded flows.

CHAPTER 3

Accomplishments

This chapter summarizes the main contributions of this thesis including a short literature overview of the current state-of-the-art in research. Support is given by the author's publications that can be found in Appendix B.

3.1. DNS Analysis of Turbulent Flow Benchmarks with the Lattice-Boltzmann Method

The application of the LBM for turbulent flows is still part of intensive research, since the original formulation of the underlying BGK Boltzmann equations allow only for simulations at rather low Reynolds numbers. The appearance of spurious unphysical velocity oscillations is inherently observable, see Succi (2001), and they propagate and grow exponentially in the flow field. More advanced collision models, like the multi-relaxation time scheme of d'Humiéres et al. (2002) or the cumulent LBM from Geier et al. (2015) are coping with these stability issues with huge success.

For high Reynolds number flow simulations in the framework of classical Boltzmann schemes, Smagorinsky like subgrid-scale models, see e.g. Yu et al. (2006); Yu and Girimaji (2005); Premnath et al. (2009) were extrapolated from the continuous Navier-Stokes framework into the kinetic theory without investigating the numerical interaction between the turbulence model and the collision term closure of the discrete Boltzmann equation. Without assessing the amount of numerical dissipation on the range of wavenumbers obtained by the pure collision models, simple adaption of standard LES models can lead to a wrongly predicted energy transfer and dissipation and, thus, the incorrect prediction of turbulent flow structures.

In order to allow for high accuracy turbulence modeling in the LBM-LES framework, a detailed analysis of the turbulent flow structures predicted by pure Boltzmann schemes is necessary. These insights can help to advance classical subgrid-scale closures in the LBM framework to obtain more physical motivated energy transfer, dependent on the applied collision model.

P. NATHEN, D. GAUDLITZ, M. J. KRAUSE AND N. A. ADAMS (2018)

On the Stability and Accuracy of the BGK, MRT and RLB Boltzmann Schemes for the Simulation of Turbulent Flows

Journal of Communications in Computational Physics, **23(3)**, 846-876

The first paper of this work (Nathen et al. (2018a)) attached in Appendix B.1 investigates the interaction of different Lattice-Boltzmann schemes with turbulent flows. The Bhatnagar-Gross-Krook (BGK) or single-relaxation time (SRT) the multi-relaxation time (MRT) and the regularized lattice Boltzmann (RLB) model were part of this investigation. These schemes are applied to turbulent flow benchmarks, namely the Taylor-Green vortex, representing transitional and decaying isotropic turbulence and the turbulent channel flow, representing wall-bounded turbulent flows. Different Reynolds number and resolutions are applied in order to investigate numerical effects coming from under-resolved and well resolved flow setups.

For the Taylor-Green vortex, the Reynolds number is varied from $Re = 800$ to $Re = 3000$, while the resolution is set to $N = 64,\ 128,\ 256,\ 512$. Integral turbulent scales were investigated in real and spectral space.

The half-width of the turbulent channel flow is resolved by $N = 31,\ 91,\ 151$ cells, while the friction Reynolds number is varied from $Re_\tau = 180$ to $Re_\tau = 590$. To the authors knowledge, for the first time an analysis of wall-bounded flows with Reynolds numbers up to $Re_\tau = 590$ on an equidistant grid are performed employing LBM. In depth analysis is conducted for the average velocity profiles, Reynolds stresses and the wall-normal turbulent energy spectra.

The results obtained from direct computations of the Taylor-Green vortex as well as for the turbulent channel flow showed similar results with respect to non-intuitive mesh convergence behavior, which is described for the first time in such detail. The BGK showed reliable mesh convergence behavior, while the MRT scheme predicted the flow fields only well for under-resolved flow setups. Increasing the resolution at fixed Reynolds numbers lead to diverging simulations for the cases investigated here. The conclusions drawn from this investigation deliver useful insights for advanced turbulence modeling in the LBM framework. By knowing how much energy is dissipated and spurious energy is created on different wavenumber ranges, future turbulence models can be calibrated with more diligence for different collision schemes.

My contribution to this work was the testing of the implementation of all necessary features in order to conduct the simulations in the open-source LBM code *OpenLB*. I tested and validated the boundary condition algorithms, performed the numerical simulations including grid generation and mesh-convergence studies, conducted, tested and implemented major parts of the post-processing and wrote all parts of the manuscript for the publication.

3.2. Selective Viscosity Filters for LES based Lattice-Boltzmann Simulations

Turbulence models for LBM based LES, commonly used in the LBM community are simple extrapolations of common NSE based SGS models. The turbulent viscosity approach known from Smagorinsky (1963) is related to a turbulent relaxation rate $\tau_{eff} = \tau_{mol} + \tau_{num}$. Numerical simulations of a standard like Smagorinsky approach in the LBM framework were shown in Yu et al. (2005, 2006); Weickert et al. (2010). These models do not necessarily satisfy the hydrodynamic limit in terms of the filtered NSE equation, see Malaspinas and Sagaut (2012, 2011); Sagaut (2010). Additionally, from Nathen et al. (2018a) it can be concluded that different collision models predict turbulent flow structures differently with the same turbulence model.

Based on these findings, more advanced turbulence models, namely the Approximate Deconvolution Method (ADM), see Stolz and Adams (1999); Stolz et al. (2001); Adams and Stolz (2002), were adapted to the LBM framework by Sagaut (2010) and Malaspinas and Sagaut (2011). This approach which is also consistent with the incompressible limit of the filtered NSE, aims to reconstruct at least parts of the sub-filter energy by an inverse filter operation. The original implementation of the ADM in the LBM framework by Malaspinas and Sagaut (2011) is based on an explicit filter operation employing viscosity filters with a constant filter strength. Fauconnier et al. (2013) already demonstrated, that a straightforward application of constant filter strengths for any given filter stencil for viscosity filters requires fine adjustment to the underlying test case, to aim for stability and accuracy at the same time.

We developed a self-adapting filter, which decreases the need for filter strength adjustment and delivers conditional stability with the required amount of numerical dissipation in order to be consistent with turbulent theory. Similar ideas were introduced by Lèveque et al. (2007) and Marié and Gloerfelt (2017).

P. Nathen, M. Haussmann, M. J. Krause and N. A. Adams (2018)
Adaptive Filtering for the Simulation of Turbulent Flows with Lattice Boltzmann Methods
Computers & Fluids, ??(?)**ACCEPTED, IN PRESS**, XXX-XXX

In the second main contribution of this work (Nathen et al. (2018b)) attached in B.2, a selective filter is introduced. The dynamic filtering procedure exploits resolved scales in order to adapt the filter strength according to the flow field. Adaptive filter strengths are calculated by a phase averaged strain-rate, which is related to a resolved dissipation time scale. By this procedure, filtering will be only applied in regions where the flow is under-resolved. Filtering is canceled out in flow regions, where the turbulent flow structures are resolved properly.

The Taylor-Green vortex and the turbulent channel flow at very low resolutions and very high Reynolds numbers serve as turbulent benchmarks. For the Taylor-Green vortex, the Reynolds number is set to $Re = 800$, $Re = 1600$ and $Re = 3000$, while the length of th 2π

periodic box is resolved equidistantly by $N = 32,\ 64,\ 128$ and 256 cells. Integral length scales are calculated dynamically, to evaluate new time phases, over which the strain-rate is averaged in order to update the filter strength accordingly.

Finally, the adaptive filter approach is applied to the turbulent channel flow at at varying Reynolds numbers and resolutions: $Re_\tau = 180$, $Re_\tau = 395$ and $Re_\tau = 590$ are simulated with $N = 31,\ 71,\ 91$ cells per channel half-width. Since the turbulent channel flow turbulence statistics are homogeneous in stream-wise and span-wise directions after it reaches it's fully decorrelated state from initialization, no need for adaptive phases is given and the averaging procedure simplifies to a standard procedure.

With respect to the decaying isotropic turbulence test case, the adaptive filtering procedure showed superior agreement with reference DNS data compared to the original ADM implementation. Beyond that, more stable flow setups are established ($Re = 3000$, $Re = 1600$ and $N = 32$), which would not be possible with the standard BGK scheme. For the turbulent channel flow, it is shown that the Reynolds stresses as well as the mean flow field are predicted accurately and only for very high Reynolds numbers ($Re_\tau = 590$) and very low resolutions ($N = 31$) a significant discrepancy can be found. It is shown, that a constant filter strength needs iterative calibration work in order to achieve the same quality of results as an adaptive filter.

My contribution to this work was the development and the implementation of the adaptive filter method in the open-source LBM code *OpenLB*. I tested and validated the algorithms, performed the numerical simulations including grid generation, refinement studies, conducted major parts of the post-processing and wrote all parts of the manuscript for the publication.

3.3. Arbitrary shaped boundary treatment for turbulent Flow Simulation with the Lattice-Boltzmann Method

The simulation of turbulent flows around complex shaped geometries is of essential interest for industrial flow simulation. LBM exposed itself as an reliable framework for efficient flow simulation for low Reynolds number flows around simple shaped geometries. The industrial application of LBM requires intense work on how the predictability changes, when the complexity is increased by means of high Reynolds numbers and complex shaped geometries.

Since the original discrete lattice approach introduced in Section 2.2.3, only allows for staircase approximations of a given geometry and, thus, tremendous amounts of cells are required to represent complex shaped geometries properly, advanced techniques were introduced by Bouzidi et al. (2002) and further analyzed by Lallemand and Luo (2003). The underlying idea for methods like the Bouzidi scheme is an interpolation technique, which takes the geometries shape into account in order to calculate the unknown velocity distribution functions propagating into the flow field. Interpolation techniques employing this method are quite robust and computationally inexpensive. For completion, it shall be noted that methods similar to the immersed boundary methods for the Navier-Stokes equations (Peskin (1972); Mittal and Iaccarino (2005); Clarke et al. (1986); Udaykumar et al. (2001)) are existing for the LBM, see Feng and Michaelidis (2004, 2005); Inamoru (2012); Shu and Wu (2009) among others.

The combination of complex boundary treatment and the prediction of turbulent flow structures is still a major subject of research in the LBM community.

P. Nathen, D. Gaudlitz, J. Kratzke and M. J. Krause (2013).
An extension of the Lattice-Boltzmann Method for simulating turbulent flows around rotating geometries of arbitrary shape.
21^{st} *AIAA Computational Fluid Dynamics Conference*, **June 24 - 27, 2013, San Diego, CA, USA.**

The first contribution of this work, see Nathen et al. (2013), deals with the simulation of turbulent flow structures around static and moving bodies. A multi-relaxation time (MRT) scheme is employed with Bouzidi's interpolation technique in order to represent solid walls of arbitrary geometries. For the additional high Reynolds number benchmarks a Smagorinsky LES model is implemented. The implementation of the model is consistent with the incompressible limit of the filtered Navier-Stokes equations. This work aims to demonstrate capabilities of the LBM for simulation of turbulent flows around complex shaped geometries with and without movement.

For two dimensional flows at low Reynolds numbers around static and solid bodies, the test case of Breuer et al. (2000) serves as a reference. The reference length D of a square cylinder is resolved by $N = 40$ cells, in a $L_x = 50D$ long and $L_y = 8D$ high domain.

An equidistant grid is employed and the Reynolds number based on the reference length D is varied from $Re = 50...300$. At the inlet a laminar *Poiseuille* profile is imposed, at the outlet a pressure outlet is given and the upper and lower walls were represented by a bounce-back scheme. Very good agreement with reference drag values was achieved. Additional successful validation for static bodies was done for an increased Reynolds number at $Re = 21400$. Increasing the complexity by applying the method to two-dimensional rotating cylinders, the trends were in accordance with the reference data of Kang et al. (1999); Mittal and Kumar (2003); Nair et al. (1998) as well.

Employing LBM with a MRT scheme and Bouzidi wall treatment to three-dimensional flows around rotating cylinders, only for relatively small Reynolds numbers ($Re = 5000$) and fairly resolved simulation setups, a reliable flow field was predicted. Increasing the resolution on an equidistant grid, the MRT setup lead to divergence. The conference publication attached in C.1 was the initial trigger for the first main publication Nathen et al. (2018a).

My contribution was the implementation, validation and testing of the Smagorinsky model, the combined implementation of MRT and Bouzidi scheme and the conduction of all validation simulations. All parts of the manuscript for publication were written by me.

3.4. Towards advanced LES filtering for Turbulent Flow Simulation in the Lattice-Boltzmann Framework

The initial motivation, framework and literature review is similar to the one presented in Section 3.2.

P. Nathen, D. Gaudlitz, and N. A. Adams (2015).
Towards wall-adaption of turbulence models within the Lattice-Boltzmann framework.
The 9^{th} Symposium on Turbulence and Shear Flow Phenomena (TSFP-9), **June 30 - July 3, 2015, Melbourne, Melbourne, Australia.**

The second conference paper, see Nathen et al. (2015) attached in C.2, is the initial work on the adaptive filter presented in Nathen et al. (2018b). The constant filter strength was replaced by an adaptive one, which triggers filtering only in regions, where the flow is under-resolved while suppressing explicit filtering in well resolved flow regions. Compared to the calculation of the filter strength $\sigma(\boldsymbol{x}, t)$ in Nathen et al. (2018b), a simple time averaging procedure for the strain rate $S_{ij}(\boldsymbol{x})$ is applied. The time scale for normalization is related to a turbulence time scale.

The Taylor-Green vortex and the turbulent channel flow at low and high resolutions and high Reynolds numbers serve as turbulent benchmarks. For the Taylor-Green vortex, the Reynolds number is set to $Re = 3000$, while the length of th 2π periodic box is resolved equidistantly by $N = 64$ and $N = 256$ cells. Averaging of the local strain-rate for the relaxation of the filter strength was started immediately.

The initial adaptive filter approach is also applied to the turbulent channel flow at varying Reynolds numbers and grid resolutions: $Re_\tau = 180$ and $Re_\tau = 395$ are simulated with $N = 31$ and $N = 71$ cells per channel half-width. Beyond that, the original ADM-LBM approach is employed to the author's knowledge for the first time with constant $\sigma = 0.005$ and $\sigma = 0.001$ to wall-bounded turbulence.

Compared to original ADM implementation, the adaptive filter approach lead to good prediction of the reference data and improved stability properties. Due to the instant starting and simple time averaging procedure the prediction of the dissipation rate is not as good as shown in Nathen et al. (2018b), yet the results already showed the superior properties of adaptive filtering.

My contribution to this work was the development and the implementation of the original ADM and initial adaptive filter method in the open-source LBM code *OpenLB*. I tested and validated the algorithms, performed the numerical simulations including grid generation, refinement studies, conducted all parts of the post-processing and wrote all parts of the manuscript for the publication.

CHAPTER 4

Conclusion

In this work a new methodology was presented for the simulation of turbulent flows with the Lattice Boltzmann Method (LBM). Turbulent flow simulations with the LBM is commonly done without the in-depth analysis of the numerical dissipation coming from the underlying collision modeling and the turbulence model itself. Since the collision operation inhabits both, the non-linear as well as the diffusive effects of fluid flows, the analysis of the individual contribution of this operation to the development of turbulent flow structures is of great interest. This work was two-folded and started with the DNS analysis of turbulent flow benchmarks within the LBM framework. First, the LBM without any turbulence models was analyzed for the simulation of turbulent flows and it was found, that the convergence behavior depends heavily on the applied collision operator. Based on these findings, a new explicit filter model was derived, which is not considered as an eddy viscosity model. This model lead to superior stability compared to the original formulation of the ADM-LBM model and computational results showed great agreement with the reference data.

For the first part, the Single- and Multi-Relaxation time (BGK and MRT) model as well as the Regularized Lattice Boltzmann (RLB) scheme, were part of the discussion. All collision models were applied for turbulent simulation benchmarks, namely Homogeneous Isotropic Turbulence (HIT) and the Turbulent Channel Flow (TCF). All benchmarks were investigated at different Reynolds numbers and resolutions. The flow field of HIT was investigated in real and spectral space in terms of the integral dissipation rate, the energy and dissipation spectra. For the TCF the mean velocity field as well as the Reynolds stresses were compared to reference DNS data. For both benchmarks, correlating results were found, which showed that the pure BGK scheme is the least dissipative one. The BGK scheme suffers from non-linear numerical instabilities, which lead to diverging simulations if the Reynolds number is increased for underresolved setups. Convergence was shown for increasing resolutions at fixed Reynolds numbers and thus mesh convergence was achieved. The RLB scheme exhibits excessive numerical dissipation but remained in all numerical setups stable, even if the numerical setup is strongly underresolved. For the RLB scheme mesh convergence was also shown, although the computational effort has to be increased in terms of the resolution compared to the BGK scheme for the same quality of results. The results obtained with the MRT scheme revealed different findings. For underresolved numerical setups, the model showed good agreement with the reference DNS data. However increasing the resolution showed an amplification of high-order moments, which lead to diverging simulations. In our test cases, these moments were amplified in the intermediate wavenumber range, leading to unphysical growing amplitudes of the macroscopic flow moments for all wavenumber ranges. For DNS like setups at high Reynolds numbers, no mesh convergence was achieved at the incompressible limit of the Navier-Stokes equations, neither for HIT nor for turbulent channel flows. Thus, the BGK was the model of choice for all analysis of turbulent flows.

The second part of this work was devoted to the development and validation of a novel explicit subgrid-scale model for LBM based LES, which is consistent with the filtered Navier-Stokes equations at the hydrodynamic limit. This model is based on the Approximate Deconvolution Method (ADM) and in contrast to standard approaches, using convolution filters with a *van Cittert* iteration, a viscosity filter is applied. The novel approach exploits resolved flow scales in order to adapt the filter strength locally. As a trigger mechanism the phase averaged strain-rate is employed in order to detect wether the flow field is well-resolved locally or not. In regions where the turbulent flow scales are under-resolved, numerical dissipation is added. When the grid size is fine enough to represent the smallest turbulent flow scales, the filtering effect is negligible. Although, this model belongs to the category of explicit LES models, the adaptive ADM approach differs fundamentally from explicit eddy viscosity closure models. It was shown that for the Taylor-Green vortex and turbulent channel flow benchmarks, this implementation leads to good results for marginally resolved flow setups and improved stability characteristics of the standard BGK scheme are found. The originally proposed ADM showed diverging simulations for underresolved setups and suffered from numerical inaccuracy for wall bounded turbulent flows. Furthermore, it was confirmed that for high order explicit filter stencils the filter strength has a minor influence on the results or stability issues. Only for low order filter stencils the results are dominated by the filter strength. For an efficient parallel implementation of the ADM-BGK approach, the filter stencil should rather be of low order $N < 4$ and the filter strength should to be adapted as proposed accordingly to reduce the computational cost.

For future work on turbulent flow simulation with the LBM, additional work has to be done on the in-depth analysis of DNS simulations with standard LBM schemes on more complex turbulent benchmark test cases, in order to improve advanced subgrid-scale models like the adaptive ADM. This proposed approach is a promising alternative to commonly used LES models for the LBM framework.

APPENDIX A

List of publications

A.1. PEER-REVIEWED JOURNAL PUBLICATIONS

- **P. Nathen**, D. Gaudlitz, M. J. Krause and N. A. Adams (2018). On the Stability and Accuracy of the BGK, MRT and RLB Boltzmann Schemes for the Simulation of Turbulent Flows. *Journal of Communications in Computational Physics*, **23(3)**, 846-876.

- **P. Nathen**, M. Haussmann, M. J. Krause and N. A. Adams (2018). Adaptive Filtering for the Simulation of Turbulent Flows with Lattice Boltzmann Methods. *Computers & Fluids*, **ACCEPTED IN PRESS, XX(X)**, AAA-BBB.

A.2. CONFERENCES

- **P. Nathen**, D. Gaudlitz, J. Kratzke and M. J. Krause (2013). An extension of the Lattice-Boltzmann Method for simulating turbulent flows around rotating geometries of arbitrary shape. 21st *AIAA Computational Fluid Dynamics Conference*, June 24 - 27, 2013, San Diego, CA, USA.

- **P. Nathen**, D. Gaudlitz, M. J. Krause and N. A. Adams (2013). Stochastic extension of the Smagorinsky LES model for the simulation of turbulent Flows. 10th *International Conference for Mesoscopic Methods in Engineering and Science*, July 22 - 26, 2013, Oxford, UK.

- **P. Nathen**, D. Gaudlitz and N. A. Adams (2015). Towards wall-adaption of turbulence models within the Lattice-Boltzmann framework. The 9th *Symposium on*

Turbulence and Shear Flow Phenomena (TSFP-9), June 30 - July 3, 2015, Melbourne, Australia.

- **P. Nathen**, D. Gaudlitz, M. J. Krause and N. A. Adams (2017). Adaptive Filtering for the Simulation of Turbulent Flows with the Lattice Boltzmann Method. 26th *International Conference on Discrete Simulation of Fluid Dynamics (DSFD 2017)*, July 10 - 14, 2017, Erlangen, Germany.

APPENDIX B

Selected publications

Here, the main publications are attached.

B.1. Direct Simulation of Turbulent Flows with the Lattice-Boltzmann Method

Commun. Comput. Phys.
doi: 10.4208/cicp.OA-2016-0229

Vol. **23**, No. 3, pp. 846-876
March 2018

On the Stability and Accuracy of the BGK, MRT and RLB Boltzmann Schemes for the Simulation of Turbulent Flows

Patrick Nathen[1,*], Daniel Gaudlitz[2], Mathias J. Krause[3] and Nikolaus A. Adams[1]

[1] *Insitute of Aerodynamics and Fluid Mechanics, Technische Universität München, Boltzmannstrasse 15, 85748 Garching bei München, Germany.*
[2] *Institute of Automotive Engineering, University of Applied Sciences Zwickau, Scheffelstraße 39, 08066 Zwickau, Germany.*
[3] *Institute for Mechanical Process Engineering and Mechanics, Institute for Applied and Numerical Mathematics, Karlsruhe Institute of Technology, Strasse am Forum 8, 76131 Karlsruhe, Germany.*

Received 1 December 2016; Accepted (in revised version) 22 August 2017

Abstract. This paper presents an analysis of the stability and accuracy of different Lattice Boltzmann schemes when employed for direct numerical simulations of turbulent flows. The Single-Relaxation-Time scheme of Bhatnagar, Gross and Krook (BGK), the Multi-Relaxation-Time scheme (MRT) and the Regularized Lattice Boltzmann scheme (RLB) are considered. The stability and accuracy properties of these schemes are investigated by computing three-dimensional Taylor-Green vortices representing homogeneous isotropic turbulent flows. Varying Reynolds numbers and grid resolutions were considered. As expected, the BGK scheme requires sufficiently high grid resolutions for stable and accurate simulations. Surprisingly, the MRT scheme when used without any turbulence model fails to obtain mesh convergence for the type of flow considered here. The RLB scheme allows for stable simulations but exhibits a strong dissipative behavior. A similar behavior was found when employing the mentioned LBM schemes for numerical simulations of turbulent channel flows at varying Reynolds numbers and resolutions. The obtained insights on accuracy and stability of the considered Lattice Boltzmann methods can become useful especially for the design of effective turbulence models to be used for high Reynolds number flows.

AMS subject classifications: 35Q20

Key words: Lattice Boltzmann, homogeneous isotropic turbulence, wall bounded turbulent flows.

---

*Corresponding author. *Email addresses:* `patrick.nathen@aer.mw.tum.de` (P. Nathen), `Daniel.Gaudlitz@aer.mw.tum.de` (D. Gaudlitz), `mathias.krause@kit.edu` (M. J. Krause), `nikolaus.adams@tum.de` (N. A. Adams)

1 Introduction

In the last three decades, the Lattice Boltzmann Method (LBM) became a promising alternative to conventional methods, like solving the Navier-Stokes equations with Finite Volumes or Finite Elements. Flows through porous media, multi-phase and multi-component flows with and without heat transfer as well as flows around complex geometries have been investigated by several authors, see, e.g. [1,7]. With LBM the computational domain is discretized by an equidistant mesh, on which a discrete set of velocity distribution functions is solved numerically. This set of velocity distribution functions corresponds to discrete lattice velocities, which are used to recover the macroscopic moments in terms of a Hermite Polynomial expansion. Although the LBM has been applied to a wide range of fluid-dynamics applications, turbulence modeling in the LBM framework still requires considerable research and has not reached the level of maturity as seen for Navier-Stokes-based methods, see references [37, 38] and [39]. Important recent advances have been made by Sagaut et al., see Sagaut [39] and Malaspinas and Sagaut [31, 32]. The approach proposed by Malaspinas and Sagaut [31] is based on the Approximate Deconvolution Method (ADM) of Stolz and Adams [40]. The discrete Boltzmann equations are filtered and subsequently deconvoluted with a regularized inverse filter operation in order to reconstruct the proper macroscopic equations for LES within the kinetic theory. The ADM as implemented in [31] is based on the BGK collision approach, yet it can be extended for any other standard collision operator like the MRT and the RLB approach. Due to the substantial differences of the different collision models, see also Section 2, it is crucial to understand their properties in terms of stability and accuracy, when used for the simulation of turbulent flows. Moreover, these properties have to be taken into account when adapting turbulence models to LBM schemes.

To the author's knowledge, a comparison of the stability and accuracy of different discrete LBM schemes without turbulence models when applied to three-dimensional turbulent flows of varying Reynolds number and employing different mesh resolutions has not been presented so far. For Navier-Stokes equation based methods it is common practice to investigate the properties of the discretization scheme in terms of spatial and temporal properties. The Lattice Boltzmann algorithm corresponds to a finite difference scheme with spatial accuracy $\mathcal{O}(\Delta x^2)$ and a temporal accuracy $\mathcal{O}(\Delta t)$. This work aims to investigate the stability and accuracy of different discrete collision schemes for the LBM by carrying out resolved and under-resolved Direct Numerical Simulations (DNS) of Homogeneous Isotropic Turbulence at varying Reynolds numbers. Since no turbulence models will be employed, the observed dissipation will be only due to viscous effects and numerical dissipation of the selected collision scheme. For selected LBM schemes we will provide insights on the accuracy and stability, which can be useful for the further development of turbulence models in the LES-LBM framework. The effectiveness of turbulence models strongly depends on the properties of the numerical scheme employed to solve the basic flow equations. For the type of flow considered in this work some of the recently presented LBM schemes can provide stable simulations of appropriate accuracy.

The Karlin-Bösch-Chikatamarla (KBC) model, see Karlin et al. [21], uses an entropic formulation, which increases stability significantly. This model was developed further by Dorschner et al. [9, 10]. Geier [14] and Geier et al. [13] introduced another advanced LB model, which showed excellent stability for the simulation of turbulent flows. However, in this work we investigate the stability and accuracy of three widely used Lattice Boltzmann collision operators: the Bhatnagar, Gross and Krook (BGK), the Multi-Relaxation-Time (MRT) and the Regularized Lattice Boltzmann scheme (RLB), when computing the Taylor-Green vortex which represents a typical homogeneous isotropic turbulent flow. For assessing details on numerical stability and accuracy for wall-bounded turbulent flows, we employ these three models also for the turbulent channel flow as a benchmark test case.

The paper is structured as follows: In Section 2 the LBM is introduced briefly, and differences between the Single-Relaxation-Time scheme of Bhatnagar, Gross and Krook (BGK), the Multi-Relaxation-Time (MRT) and the regularized Lattice Boltzmann scheme (RLB) are explained. Simulations of HIT without turbulence models at different Reynolds numbers, mesh resolutions and with different discrete lattice schemes are compared in Section 3. The results of the three LBM schemes to the turbulent channel flow at $Re_\tau=180$, $Re_\tau=395$ and $Re_\tau=590$ for varying resolutions are outlined in Section 4. Based on spectral analyses of the flow field the lattice schemes are analyzed systematically. The interaction between the discrete schemes and mesh resolutions are investigated and the limitations of individual discrete schemes for the simulation of turbulent flows will be discussed. Finally, conclusions are drawn in Section 5.

2 The Lattice Boltzmann Methods

With LBM, a set of kinetic equations in terms of discrete velocity distribution functions $f_\alpha(t,\boldsymbol{x})$ are solved numerically at time t and position $\boldsymbol{x}$. The discrete Boltzmann equations can be written as

$$f_\alpha(t+\Delta t,\boldsymbol{x}+\boldsymbol{c}_\alpha\Delta t)=f_\alpha(t,\boldsymbol{x})+\Omega_\alpha, \tag{2.1}$$

where Ω_α is the collision operator, which represents non-linear and viscous effects and $\boldsymbol{c}_\alpha$ with $\alpha=0,1,\cdots,q-1$ is a set of discrete lattice velocities. Depending on the particular scheme (BGK, MRT or RLB), the collision term is modeled in different ways, see [1,3,7,8,28,29]. Macroscopic moments are reconstructed with a Gauss-Hermite quadrature based on the Hermite Polynomial expansion of f_α on a discrete lattice. The first two moments of the velocity distribution functions are the conserved moments, namely the density ρ and the momentum $\rho\boldsymbol{u}$, which read

$$\rho=\sum_\alpha f_\alpha, \tag{2.2a}$$

$$\rho\boldsymbol{u}=\sum_\alpha \boldsymbol{c}_\alpha f_\alpha, \tag{2.2b}$$

while the momentum flux is the second-order off-equilibrium moment of the velocity distribution functions

$$\boldsymbol{\Pi} = \sum_\alpha f_\alpha^{neq} \boldsymbol{c}_\alpha \boldsymbol{c}_\alpha. \tag{2.3}$$

In order to reconstruct the macroscopic equations of fluid motion, a Chapman Enskog expansion is used, see references [2,27] among others. In Eq. (2.3) $f_\alpha^{neq} = f_\alpha - f_\alpha^{eq}$ is the non-equilibrium part of the velocity distribution function. The velocity distribution functions are expanded with a simple multi-scale expansion factor, which is directly related to the Knudsen number ϵ. For the discrete distribution functions this procedure can be written as

$$f_\alpha = f_\alpha^{(0)} + \epsilon f_\alpha^{(1)} + \epsilon^2 f_\alpha^{(2)} + \cdots \tag{2.4}$$

and is subsequently inserted into the discrete Lattice Boltzmann equation, which is Taylor-expanded in space and time up to second order. The macroscopic equations are obtained by taking the zeroth- and first-order velocity moments and a subsequent integration over the velocity space.

To close the evolution equation of the particle distribution function (2.1), the collision term needs to be modeled. One well-known approach is the linearization around small perturbations of the thermodynamic equilibrium f_α^{eq}. This approach is called the Bhatnagar-Gross-Krook (BGK) ansatz, see [15, 16, 18, 41], which represents the collision term as a linear relaxation towards Maxwellian equilibrium

$$\Omega_\alpha := -\frac{1}{\tau}\left(f_\alpha(t,\boldsymbol{x}) - f_\alpha^{eq}(t,\boldsymbol{x})\right). \tag{2.5}$$

The relaxation time τ is related to the viscosity and f_α^{eq} is a low Mach number truncated Maxwell-Boltzmann distribution, which is adjusted in such a way, that Eq. (2.3) is satisfied and mass and momentum are conserved. A widely used formulation for f_α^{eq} is given by

$$f_\alpha^{eq} = \rho\omega_\alpha \left[1 + \frac{\boldsymbol{c}_\alpha \boldsymbol{u}}{c_s^2} + \frac{1}{2c_s^4}(\boldsymbol{u}\boldsymbol{u} - c_s^2\delta)\boldsymbol{u}\boldsymbol{u}\right]. \tag{2.6}$$

The constant weights ω_α are obtained by a Gauss-Hermite quadrature on the lattice, c_s is the lattice speed of sound and δ is the Kronecker delta. Although, the BGK approach has been applied successfully to a wide range of fluid mechanics, see [17, 43], it suffers from instabilities at high Reynolds numbers, which originate from the evolution of moments of f_α, which can not be attributed directly to physical quantities in fluid mechanics. To remedy this shortcoming, a Multi-Relaxation-Time (MRT) scheme was developed by D'Humiéres et al. [8]. The main idea is to transform the collision step into the momentum space and to relax each moment separately in order to reduce instabilities arising from the temporal growth of such unphysical moments. Thus, the single relaxation time τ from the BGK model is replaced by a relaxation time matrix $\boldsymbol{S}$, which relaxes each moment $m_\alpha := \boldsymbol{M} f_\alpha$ independently. The matrix $\boldsymbol{M}$ is a linear transformation matrix and the corresponding algorithm for the MRT scheme reads

$$f_\alpha(t+\Delta t,\boldsymbol{x}+\boldsymbol{c}_\alpha\Delta t)=f_\alpha(t,\boldsymbol{x})-\boldsymbol{M}^{-1}\boldsymbol{S}(m_\alpha(t,\boldsymbol{x})-m_\alpha^{eq}(t,\boldsymbol{x})). \tag{2.7}$$

Our implementation is based on the original formulation of D'Humiéres et al. [8], where the moments are defined as

$$m_\alpha=(\rho,e,\epsilon,j_x,q_x,j_y,q_y,j_z,q_z,3p_{xx},3\pi_{xx},p_{ww},\pi_{ww},p_{xy},p_{yz},p_{xz},m_x,m_y,m_z) \tag{2.8}$$

and the diagonal relaxation time matrix is given by

$$\boldsymbol{S}=diag(0,s_1,s_2,0,s_4,0,s_4,0,s_4,s_9,s_{10},s_9,s_{10},s_{13},s_{13},s_{13},s_{16},s_{16},s_{16}), \tag{2.9}$$

where $s_1=1.19$, $s_2=s_{10}=1.4$, $s_4=1.2$, and $s_{16}=1.98$. The coefficients s_9 and s_{13} are related to the viscosity ν as

$$\nu=\frac{1}{3}\left(\frac{1}{s_9}-\frac{1}{2}\right)=\frac{1}{3}\left(\frac{1}{s_{13}}-\frac{1}{2}\right). \tag{2.10}$$

The MRT model has been found to increase the stability of the LBM method substantially. Yet, Freitas et al. [11] have shown that inconsistent formulation of boundary conditions for stresses on domain boundaries, where velocities are prescribed, can also cause instabilities of the MRT model for Reynolds numbers larger than $Re\approx 5000$ for three-dimensional flows. More recently, Geier et al. [13] showed stability and accuracy problems for the MRT model at high Reynolds number flows.

In another attempt to suppress instabilities, Latt [28] proposed a regularization of the aforementioned BGK algorithm, employing an approximation of the first-order multiscale expansion term

$$f_\alpha^{neq}=f_\alpha-f_\alpha^{eq}\approx f_\alpha^{(1)}=-\frac{\Delta t}{\omega c_s^2}\omega_\alpha\boldsymbol{Q}_\alpha:\nabla\rho\boldsymbol{u}. \tag{2.11}$$

Here, $\boldsymbol{Q}_\alpha$ is the first-order non equilibrium moment $\boldsymbol{Q}_\alpha=\sum\boldsymbol{c}_\alpha\boldsymbol{c}_\alpha f_\alpha^{neq}$. The non-equilibrium distribution function f_α^{neq} is used to approximate the first-order multiscale expansion term in Eq. (2.4). This term is included in the BGK model, such that the regularized BGK algorithm reads

$$f_\alpha(t+\Delta t,\boldsymbol{x}+\boldsymbol{c}_\alpha\Delta t)=f_\alpha(t,\boldsymbol{x})+(1-\omega)f_\alpha^{(1)}(t,\boldsymbol{x}). \tag{2.12}$$

This regularization operation is not only necessary within the flow field, but also at the boundaries. The main issue with respect to boundary conditions in the RLB scheme is the proper reconstruction of the unknown distribution functions propagating into the flow domain. Different approaches to model $f_\alpha^{(1)}$ at domain boundaries are proposed in [29, 30]. All simulations conducted in this work are performed with the open source LBM software *openLB*, see [20, 23, 24].

3 Homogeneous Isotropic Turbulence: The Taylor-Green Vortex

By computing the evolution of the well-known three-dimensional Taylor-Green vortex [4], properties of the Lattice Boltzmann collision schemes outlined in Section 2, are investigated. The velocity and density field of a three-dimensional cubic domain of length 2π has been initialized with

$$\begin{aligned} u^0 &= \frac{2}{\sqrt{3}}\sin\left(\frac{2}{3}\pi\right)\sin(x)\cos(y)\cos(z), \\ v^0 &= \frac{2}{\sqrt{3}}\sin\left(-\frac{2}{3}\pi\right)\cos(x)\sin(y)\cos(z), \\ w^0 &= 0, \\ \rho^0 &= 1. \end{aligned} \tag{3.1}$$

Periodic boundary conditions are applied in all spatial directions. Reynolds numbers of $Re = 800$, 1600, 3000 and resolutions of $N = 64$, 128, 256 and 512 mesh points for each spatial direction were considered. The results were compared to DNS results of Brachet [4]. For adapting the time step according to the resolution we applied diffusive scaling in order to reconstruct the incompressible limit of the Navier-Stokes equations, see [34] among others. The numerical setups in terms of the lattice velocity u_L as well as the Mach number $Ma = u_L/c_s$ are listed in Table 1.

Table 1: Numerical setup for the Taylor-Green-Vortex at different resolutions.

N	u_L	Ma	Δx	Δt
64	0.1	0.1730	0.0981	0.00981
128	0.05	0.0865	0.0490	0.00245
256	0.025	0.0432	0.0245	0.000612
512	0.0125	0.0216	0.0122	0.000152

In the following, stability properties of the LBM schemes and their accuracy regarding the prediction of the temporal evolution of the integral energy dissipation rate computed from the resolved flow scales are discussed. In Fig. 1 the integral energy dissipation rate $\epsilon = \frac{dE(t)}{dt}$ for $Re = 800$ is shown.

For the coarsest resolution of N=64 the MRT as well as the RLB scheme underestimate dissipation rates compared to the BGK scheme and the reference DNS data of Brachet [4]. When increasing the resolution to $N = 128$, the evolution of the dissipation rate is slightly better recovered by the MRT approach compared to the BGK scheme. Again dissipation rates are always predicted lower by the RLB model compared to results of the BGK or the MRT scheme. For a resolution of $N = 256$ only small differences between the three considered LBM schemes can be found, and at the highest resolution of N=512 at Re=800 they are in very good agreement with the reference DNS data. For $Re = 1600$, see Fig. 2,

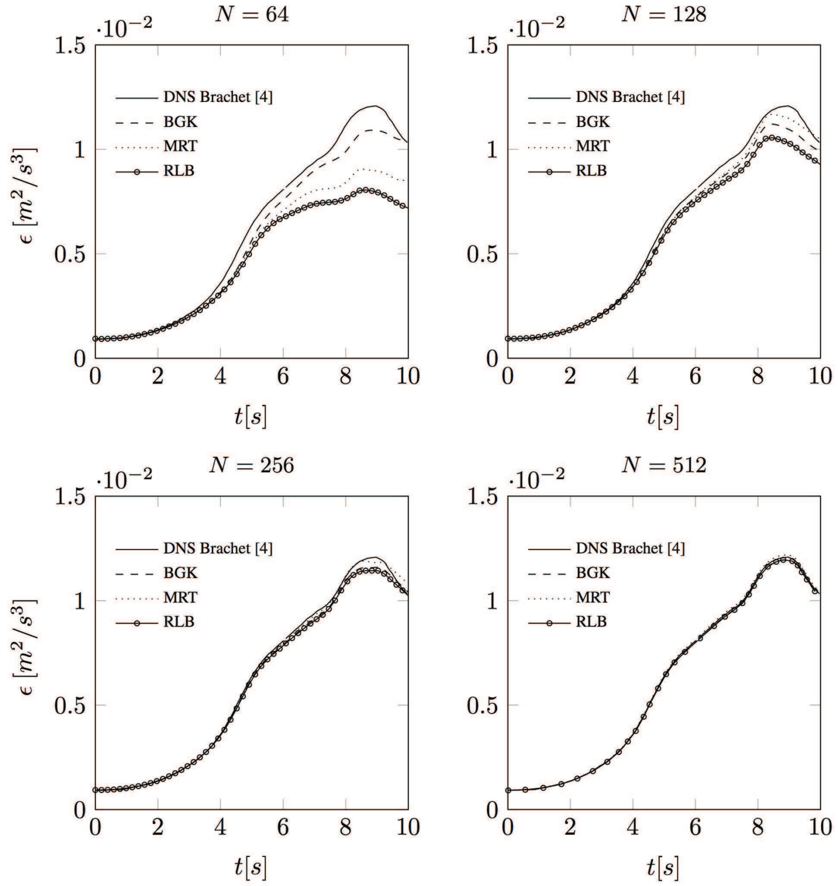

Figure 1: Temporal evolution of the dissipation rate of the Taylor-Green vortex predicted by the BGK, MRT and RLB scheme at $Re=800$ for the resolutions $N=64$, 128, 256 and 512 compared to DNS.

distinct differences between the schemes can be observed. When using the BGK scheme at the coarsest resolution of $N=64$ instabilities in the flow variables develop at $t\approx 5s$, which lead to diverging simulations. Employing methods for a pressure initialization according to [6] did not improve the stability of the BGK scheme. It can be concluded, that these instabilities of the BGK scheme result from a too coarse resolution of the developing flow scales, which is similar to the characteristics of linear finite-difference schemes. In [26] a similar behavior of the BGK scheme had been observed. At the coarsest resolution, the MRT and the RLB scheme allow for stable simulations, however dissipation rates are predicted significantly lower compared to DNS reference data.

At an increased resolution of $N=128$ the flow scales developing during the simulation are sufficiently resolved for BGK scheme to remain stable and predict dissipation rates

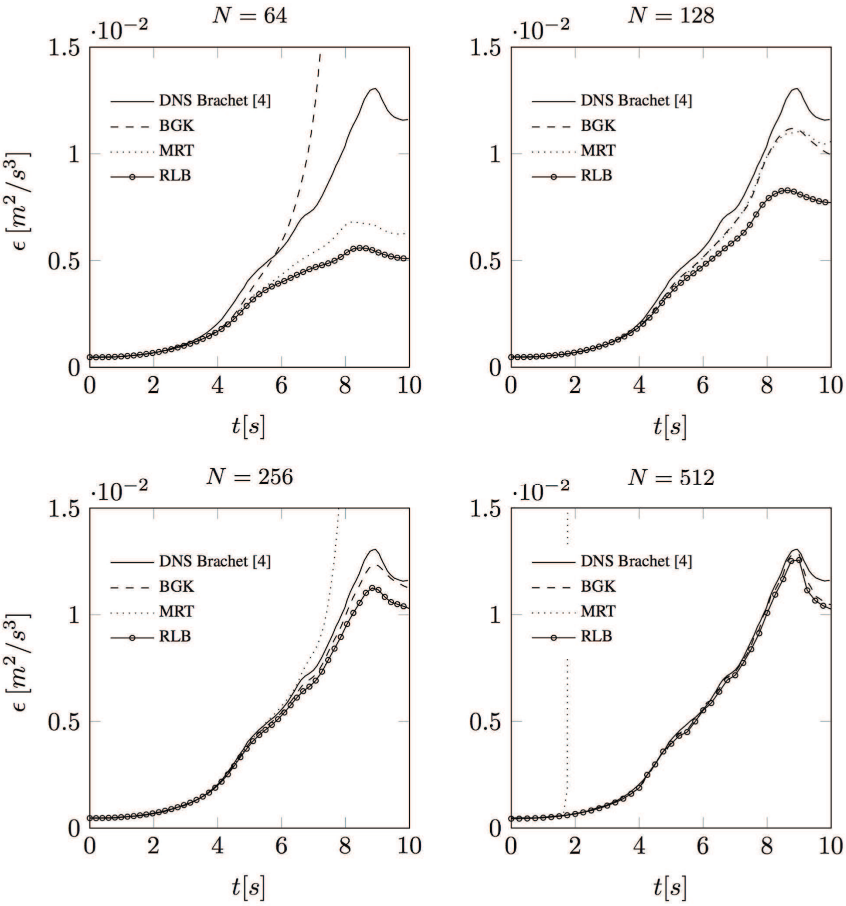

Figure 2: Temporal evolution of the dissipation rate of the Taylor-Green vortex predicted by the BGK, MRT and RLB scheme at $Re=1600$ for the resolutions $N=64$, 128, 256 and 512 compared to DNS.

with similar accuracy as with the MRT scheme. Again, the RLB scheme captures the peak dissipation rate at $t \approx 9s$ but predicts its magnitude by approximately 38% too low with respect to the DNS reference data, and by approximately 23% too low with respect to the BGK and MRT results. When increasing the resolution further to $N=256$ the accuracy of the BGK and of the RLB scheme improves, whereas the MRT scheme exhibits instabilities from $t \approx 7s$ onwards. In an attempt to stabilize the simulations a pressure initialization according to [6] was carried out, which however did not alter the observed behavior of the MRT scheme. At the highest resolution of $N=512$ the BGK and the RLB scheme showed good agreement with reference DNS data and only after the peak of the dissipation rate at $t \approx 9s$ notable differences become visible. At $N=512$ the MRT scheme

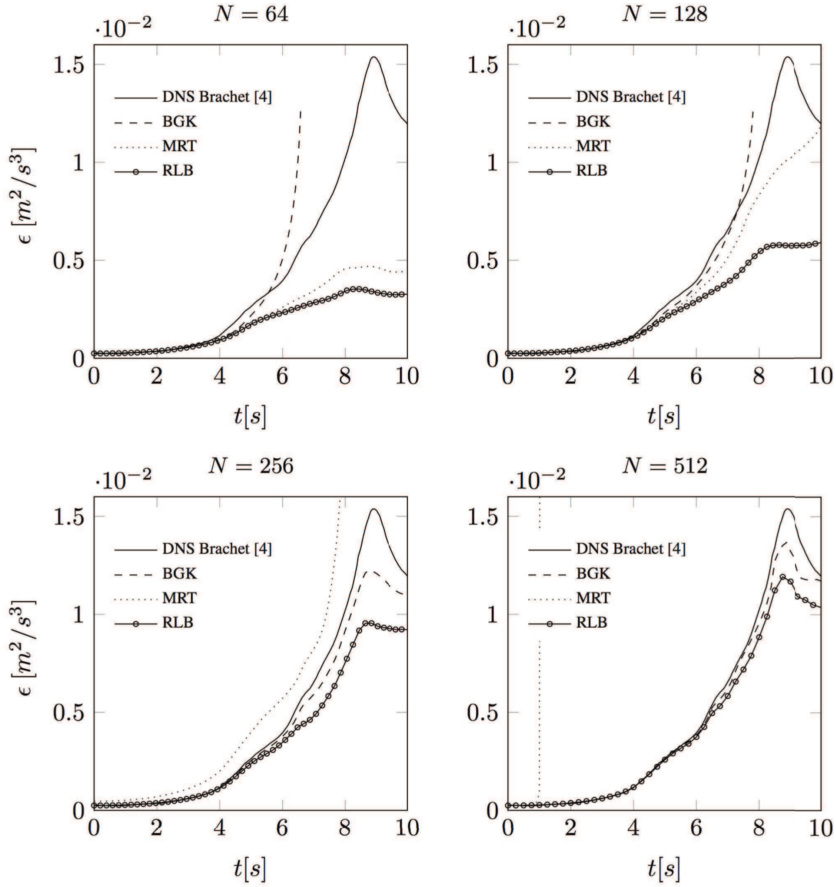

Figure 3: Temporal evolution of the dissipation rate of the Taylor-Green vortex predicted by the BGK, MRT and RLB scheme at $Re=3000$ for the resolutions $N=64$, 128, 256 and 512 compared to DNS.

exhibits instabilities at $t\approx 1.5s$, which is significantly earlier compared to the simulation at $N=256$, and the simulation diverges again.

The same tendencies found before for both lower Reynolds numbers, also prevail at Re=3000, see Fig. 3. The RLB scheme again is stable for all resolutions considered, yet dissipation rates are less accurate compared to successful simulations employing the BGK or the MRT scheme. The MRT scheme allows for stable simulations only when using a strongly under-resolved setup with $N=64$ mesh cells in each direction at this Reynolds number of Re=3000. For the resolutions $N=256$, 512 the MRT simulations diverged and by employing $N=128$ cells in each direction the solution converged towards an unphysical state for $t>10s$. Using the BGK scheme stable and reasonable accurate simulations where performed for mesh resolutions of $N=256$ and $N=512$.

The distinct differences between the schemes with respect to mesh resolution and Reynolds number found so far are summarized as follows:

- The BGK scheme allows for stable simulations in case flow scales are sufficiently resolved by the employed mesh. Yet, a criterion to quantify this Reynolds number dependent resolution requirement for turbulent flows has not been found so far. For increasing mesh resolution an increasing accuracy and hence mesh convergence can be obtained. If the turbulent flow scales are not sufficiently resolved, non-linear instabilities were found to develop, which is in agreement with previous observations, e.g., Luo and Lallemand [26].

- The MRT scheme shows good results regarding the integral energy dissipation rates for under-resolved DNS setups. For increasing resolutions, accuracy improved for the lowest Reynolds number of $Re=800$ considered here. However, for increased resolutions at higher Reynolds numbers of $Re=1600$, 3000 non-linear instabilities became apparent and simulations diverged. The latter finding seems to prevent the MRT scheme to obtain mesh convergence when used in a DNS setting.

- The RLB scheme has been found to perform stable simulations at all Reynolds numbers and resolutions considered here. Yet it suffers from the largest numerical dissipation compared to the other schemes.

For further analysis of the behavior of the LBM schemes, three-dimensional energy spectra $E(\xi,t)=\frac{1}{2}<\hat{u}(\xi,t)\hat{u^*}(\xi,t)>$ for all three Reynolds numbers, different spatial resolutions and at two instants in time, $t=6s$ and $t=8s$, are considered in the following. Here $\hat{u}(\xi,t)$ is the complex Fourier transform of the velocity field and $\hat{u^*}(\xi,t)$ is the complex conjugate respectively [40]. In Fig. 4, energy spectra at $Re=800$ for the resolutions $N=64$, 128, 256 are shown. When employing the BGK scheme at the coarsest resolution $N=64$ significantly large energy levels are present at the highest wave numbers for both instants in time $t=6s$ and $t=8s$. For this resolution, the spectra of the BGK scheme do not show the expected strong decrease of energy in the dissipative range at the highest wavenumbers, whereas the MRT as well as the RLB scheme exhibit this characteristic. Therefore, the more accurate prediction of the energy dissipation rate of the BGK scheme for $N=64$ compared to the MRT and RLB scheme, see Fig. 1, is due to this unphysical effect in the high wave number range. If the resolution is increased to $N=128$ and $N=256$, this accumulation of energy at high wave numbers when using the BGK scheme is reduced, see Fig. 4. For $N\geq 256$ all three LBM schemes show very similar energy spectra and a short inertial as well as a dissipative range can be observed.

In Fig. 5 energy spectra are shown for $Re=1600$. For the BGK scheme again increased energy levels at high wave numbers can be observed in case flow structures are not sufficiently resolved by the computational mesh. This behavior leads to a diverging simulation using a resolution of $N=64$ for $t>6s$, see Fig. 5. The spectrum shows a large accumulation of energy in the highest dissipative wave numbers, which changes the slope of $E(\xi)$ in this region being even larger than the well known slope of $-5/3$ for the inertial

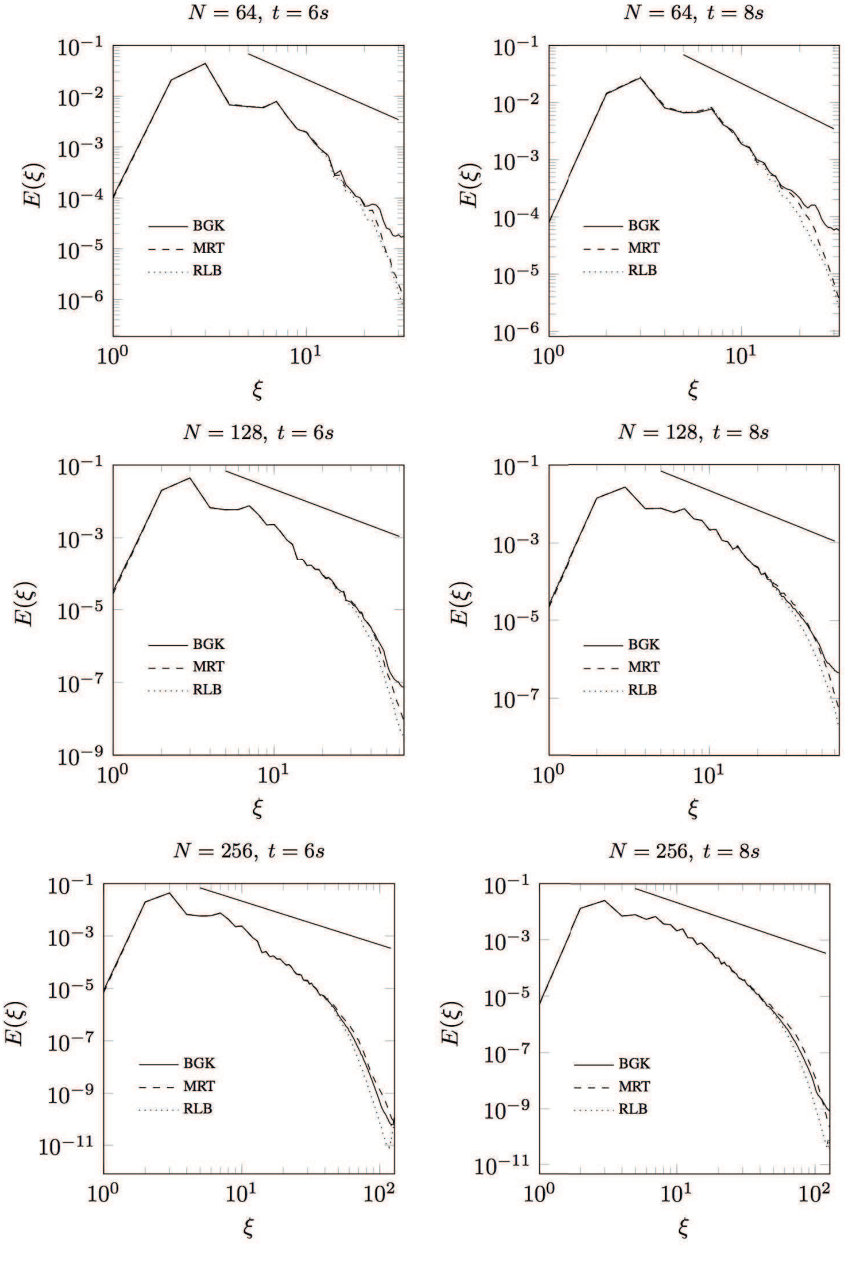

Figure 4: Energy spectra of the Taylor-Green vortex for different times and resolutions at Re=800 for the BGK, MRT and RLB scheme and a straight line of slope $-\frac{5}{3}$ being characteristic for the inertial range of homogeneous isotropic turbulence.

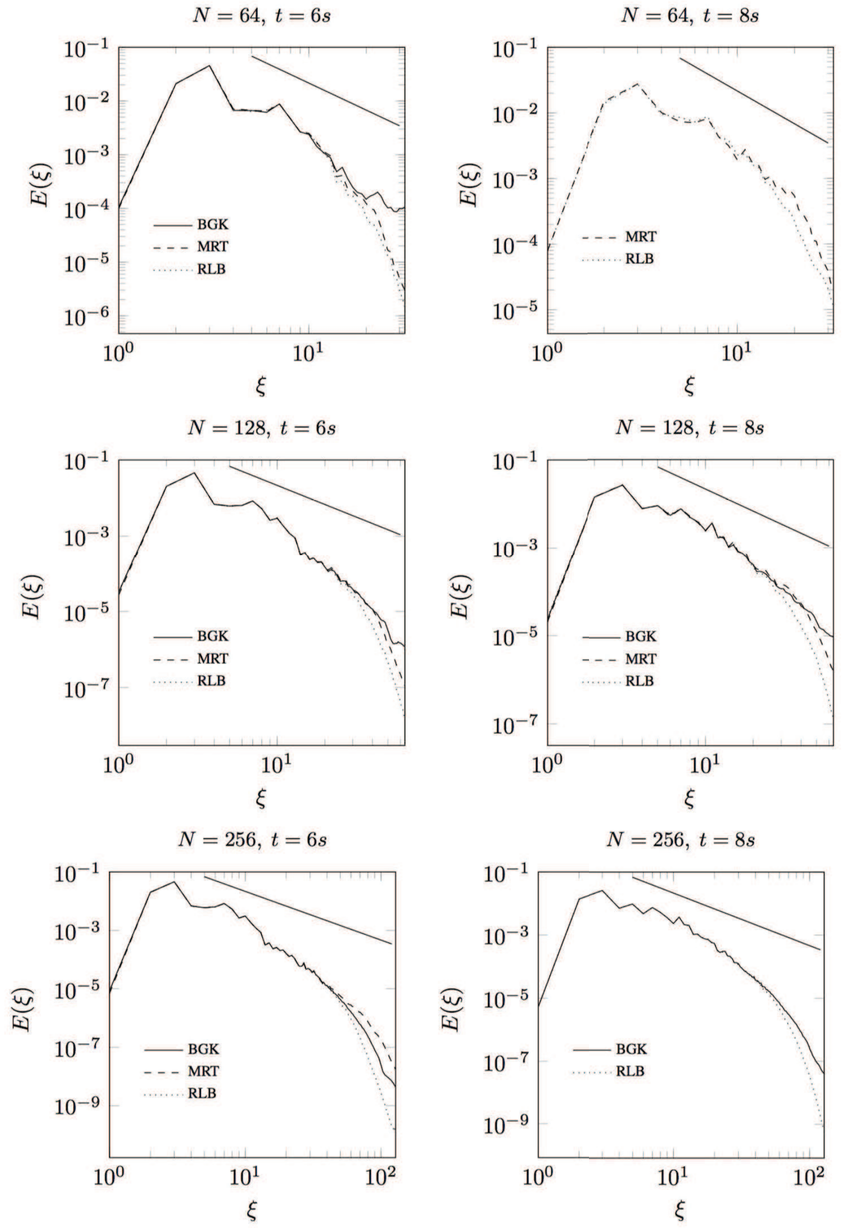

$N=64,\ t=6s$ $N=64,\ t=8s$ $N=128,\ t=6s$ $N=128,\ t=8s$ $N=256,\ t=6s$ $N=256,\ t=8s$

Figure 5: Energy spectra of the Taylor-Green vortex for different times and resolutions at $Re=1600$ for the BGK, MRT and RLB scheme and a straight line of slope $-\frac{5}{3}$ being characteristic for the inertial range of homogeneous isotropic turbulence.

range. At $t=8s$ the simulation of the Taylor-Green vortex at $Re=1600$ using the BGK scheme and $N=64$ already diverged, so no graph is shown in the corresponding figure. In case the resolution is increased to $N=128$ the BGK scheme still exhibits increased energy levels in the highest wave numbers, yet the simulations remain stable and integral dissipation rates of acceptable accuracy where obtained. For resolutions $N \geq 256$ spectra of the BGK scheme feature distinct inertial and dissipative wave number ranges. Using the MRT scheme for simulations at $Re=1600$ reasonable results were obtained for low resolutions. However for $N \geq 256$ the simulations diverged. The reason for this behavior can bee seen in Fig. 5 at $N=256$, $t=6s-8s$: The MRT scheme exhibits unphysical large energy levels in the highest wave number region, which subsequently lead to the development of instabilities and a break-down of the method well before $t=8s$. This finding is similar to that for the BGK scheme in under-resolved setups, whereas for the MRT scheme this accumulation of energy occurs for well-resolved setups. For the RLB scheme an inertial as well as a dissipative region can be observed in all spectra considered. However, the onset of the dissipative range, i.e. the strong decrease of kinetic energy, takes place always at significantly lower wave numbers compared to the BGK and the MRT scheme. This pronounced reduction of energy in the high wave number range allows for stable simulations, but it is also the reason for the strong numerical dissipation which impairs the accuracy of integral dissipation rates as seen in Figs. 1-3. The obtained energy spectra for the highest Reynolds number of $Re=3000$, see Fig. 6, confirm the previously found behavior of the considered LBM schemes. The RLB scheme allows for stable simulations at all resolutions considered, but exhibits high numerical viscosity and consequently low mesh convergence rates. The BGK scheme requires resolutions of $N \geq 256$ for converging simulations of the Taylor-Green vortex at $Re=3000$. At $N=256$ unphysical energy levels at high wave numbers develop at later times $t \geq 8s$, however these effects can still be tolerated by the scheme and do not lead to instabilities yet. For the MRT scheme the opposite behavior is found again: Only for the very coarse resolution of $N=64$ of Taylor-Green vortex at $Re=3000$ stable computations are obtained. Of course, the accuracy with respect to dissipation rates is rather low as expected. For increased resolutions of $N=128$ and $N=256$ the simulations became unstable after $t=8s$ and $t=2s$, respectively.

For further investigation of the observed instabilities of the BGK as well as the MRT scheme at $Re=3000$ and a spatial resolution of $N=256$ the temporal evolution of single modes of the dissipation spectra $\epsilon(\xi,t)=\frac{dE(\xi,t)}{dt}$ are considered, see Fig. 7. The reference data of Brachet [4] on the temporal evolution of the integral dissipation rate at this Reynolds number shows two characteristic changes before reaching its peak value at $t \approx 9s$, see Fig. 3: At $t \approx 4s$ the growth rate of the dissipation rate increases and at $t \approx 6s$ again a further increase of the slope of the dissipation-rate curve can be observed. When considering the modes of the dissipation rate, Fig. 7, for both the BGK and the MRT scheme the lower modes $\xi=1,\cdots,9$ are smoothly increasing starting at $t=0s$ until $t \approx 6s$, hereafter only slight changes are notable. However the dissipation rate magnitudes of higher modes $\xi=83,\cdots,127$ initially remain very low. At $t \approx 2s$ a strong growth of the higher dissipation modes can be observed featuring a steep slope, which starts to flatten

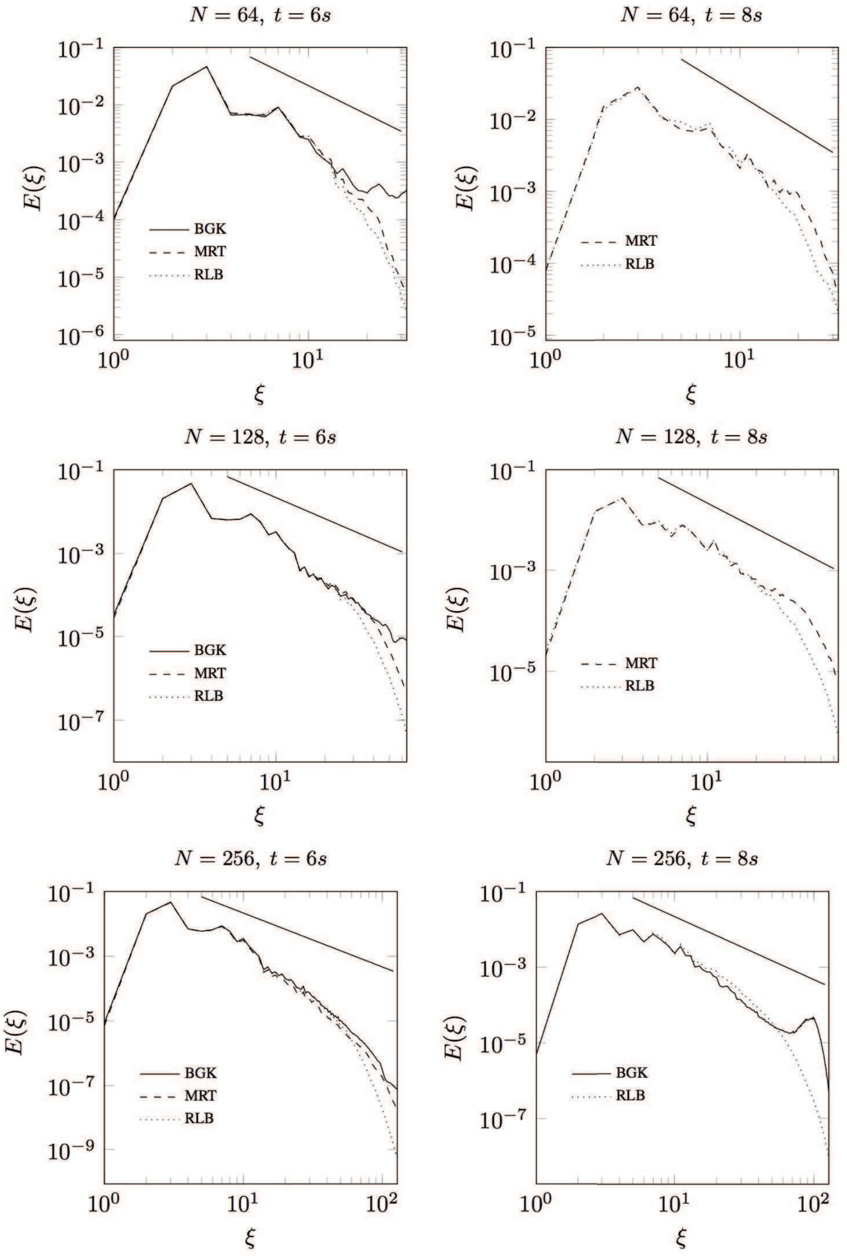

Figure 6: Energy spectra of the Taylor-Green vortex for different times and resolutions at Re=3000 for the BGK, MRT and RLB scheme and a straight line of slope $-\frac{5}{3}$ being characteristic for the inertial range of homogeneous isotropic turbulence.

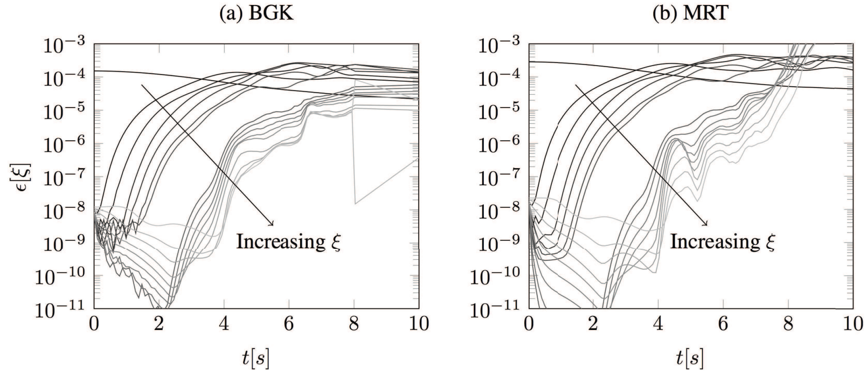

Figure 7: Temporal development of dissipation modes of the Taylor-Green vortex for the BGK and MRT scheme at $Re=3000$ and $N=256$.

only after $t\approx 4s$. At this instant in time, also the resulting first increase of the integral dissipation rate in Fig. 3 can be identified. For the BGK scheme this growth of the higher modes is accomplished rather smoothly without notable oscillations in the growth rates. For the MRT scheme however, following the initial strong growth of the higher modes a significant change of the growth rate can be observed for $t\geq 4.5s$, where even negative slopes can be found. This leads to oscillations in the magnitude of the higher modes, which subsequently are reduced in amplitude, but are still visible at later times, e.g. $t\approx 6s$. At $t\approx 7s$ a further increase especially of the highest dissipation modes can be observed for the BGK scheme, Fig. $7(a)$. This corresponds to second steepening of the slope of the integral dissipation rate as seen in Fig. 3. Thereafter the magnitude of the highest dissipation modes for the BGK scheme change only slightly with two exceptions: For $\xi=120$ a large increase by approximately one order of magnitude can be observed and for the mode $\xi=127$ an even larger decrease by three orders of magnitude can be identified at $t\approx 8s$. This is attributed to an instability of the BGK scheme in case flow structures are not sufficiently resolved by the underlying mesh. The result of this instability can also be seen in the energy spectrum for $Re=3000$, $N=256$, see Fig. 6, where for the instant in time $t=8s$ unphysical large energy levels at high wave numbers are present. Despite these instabilities, the BGK scheme allowed for converging simulation using this setup. This was not the case for the MRT scheme. In Fig. $7(b)$ a sudden increase of the three dissipation modes $\xi=113$, 120 and 127 by approximately four orders of magnitude indicate a large unphysical energy increase of these modes. Also the modes $\xi=90$, 97 and 104 are found to grow continuously, which is unphysical and lead to an unstable simulation.

4 Wall Bounded Turbulence: The Turbulent Channel Flow

In this section the BGK, MRT and RLB schemes are tested for the turbulent channel flow at three different Reynolds friction numbers ($Re_\tau=180$, $Re_\tau=395$ and $Re_\tau=590$) for varying resolutions. Results shall outline if the conclusions drawn for the homogenous isotropic turbulence test case, can be transferred to wall-bounded turbulence. In this section, we do not provide detailed mesh-convergence studies, but rather show results obtained by varying the resolution at fixed Reynolds numbers as done in the previous section.

Our numerical test case is based on the work of Bespalko [2] who performed a detailed grid convergence study for the turbulent channel flow by applying the BGK scheme. The domain has the extensions of $L_x=12H$, $L_z=4H$ and $L_y=2H$ in streamwise, lateral and wall-normal direction, respectively, with H being the channel half width. In streamwise and lateral direction, periodic boundary conditions were applied. In order to represent the upper and lower channel wall, an extended finite difference boundary condition, outlined by Latt et al. [30], is employed. Due to the abundance of populations propagating from the wall into the bulk flow, all populations in the wall cells are reconstructed to conserve density ρ and momentum $\rho\boldsymbol{u}$ and to calculate the stress tensor σ_{ij}. The stress tensor is obtained by relating it to the strain rate tensor, which is constructed by finite differences of the velocity in the neighboring cells. Latt et al. [30] showed that this boundary condition yields numerical stability and accuracy of second order, which makes it suitable for the simulation of flows at high Reynolds numbers. In contrast to other boundary conditions, representing solid no-slip walls, the wall nodes are fixed on the wall leading to a constant cell size and wall distance $\Delta x=\Delta y=\Delta z$.

Resolution is varied in a similar way as for the Taylor-Green vortex, leading to resolved and under-resolved test cases. Adjusting the friction Reynolds number is achieved by applying diffusive scaling. The viscosity is changed according to the Reynolds number and the lattice velocity according to the resolution. To estimate the viscosity we use the Dean correlation, see [33]

$$Re_B=\left(\frac{8}{0.073}\right)^{4/7} Re_\tau^{8/7}, \tag{4.1}$$

which connects the bulk Reynolds number Re_B to the friction Reynolds number Re_τ. With $Re_B=\frac{u_B L_z}{\nu}$, we can rewrite Eq. (4.1) as

$$\nu=\frac{u_B L_z}{\left(\frac{8}{0.073}\right)^{4/7} Re_\tau^{8/7}}. \tag{4.2}$$

Based on the work of Bespalko [2], we set $u_B=0.111\frac{m}{s}$. To account for the limited validity of the Dean correlation at low Reynolds numbers, the viscosity for $Re_\tau=180$ is obtained by a virtual log law which spans from the wall to the channel half height as described in [2]

$$\nu=\frac{u_B L_z}{2Re_\tau\left(\frac{1}{\kappa}ln(Re_\tau)+A\right)}. \tag{4.3}$$

A full list of conducted simulations with the final physical state, lattice velocities u_L, resolution N and Mach number is given in Table 2.

Table 2: Performed simulations for the Turbulent Channel Flow.

Model	N	Δy^+	$Re_{\tau,target}$	$Re_{\tau,real}$	u_L	Ma
BGK	31	≈ 5.8	180	–	0.111	0.1902
BGK	91	2.065	180	188.81	0.0378	0.0654
MRT	31	≈ 5.8	180	–	0.111	0.1902
MRT	91	1.87	180	177.32	0.0378	0.0654
RLB	31	≈ 5.8	180	–	0.111	0.1902
RLB	91	–	180	55.97	0.0378	0.0654
BGK	91	4.031	395	389.97	0.0378	0.0654
BGK	151	2.615	395	394.865	0.0227	0.0394
MRT	91	3.705	395	363.02	0.0378	0.0654
MRT	151	2.383	395	359.75	0.0227	0.0394
BGK	91	≈ 6.48	590	–	0.0378	0.0654
BGK	151	3.981	590	589.91	0.0227	0.0394
MRT	91	≈ 6.48	590	–	0.0378	0.0654
MRT	151	≈ 3.907	590	–	0.0227	0.0394

Since the variation of the resolution leads to different wall distances in terms of the non-dimensional $y^+ = \frac{u_\tau \Delta z}{\nu}$ value, the evaluation of the skin friction velocity u_τ is different. For properly resolved setups, i.e. $\Delta y^+ < 5$, u_τ can be calculated as $u_\tau = \sqrt{\frac{\tau_w}{\rho}}$ with τ_w being the wall shear stress. Configurations with $\Delta y^+ > 5$ we use Eq. (4.1) for calculating u_τ. The different resolutions with the corresponding target and calculated Re_τ are listed in Table 2 as well. Note that proper Δy^+ values for the MRT model at $Re_\tau = 590$ are not given since the simulations reproduced an unphysical state. This will be discussed later in this section. The RLB model did not achieve a turbulent state at $Re_\tau = 180$ with $N=31$ and $N=91$, leading to friction Reynolds numbers which indicate laminar flow, see also [42].

The target mass flow is imposed by applying adaptive forcing according to the work of Cabrit [5]. The volume force is computed as

$$g = \frac{u_\tau^2}{N} + (u_B - \langle u_x \rangle)\frac{u_B}{N}, \tag{4.4}$$

where u_B is the bulk velocity, $\langle u_x \rangle$ the instantaneous space average of the streamwise velocity component and g the resulting volume force. The force is included into the LBM schemes by employing the approach of He et al. [19] for the BGK and RLB scheme. For the MRT scheme we make use of the forcing approach of Ladd and Verberg [25].

A proper initialization of the velocity field and triggering of turbulence is needed in order to reach the desired turbulent state. We employ a 1/7 power law i.e. $u(z) = u_{char}(z/H)^{\frac{1}{7}}$, which is superimposed with statistically random perturbations u', v' and

w' drawn from a normal distribution $\frac{1}{\sigma\sqrt{2\pi}}e^{-\frac{r-\mu}{2\sigma^2}}$. Hereby r is a random number between -1 and 1, $\mu=0$ is the mean and σ the standard deviation, which was set to 5%.

Statistics are obtained for all schemes in the same way to have a consistent comparison of the applied models. Averaging is performed spatially over horizontal planes in the homogeneous directions and temporally after the flow was uncorrelated. Based on the work of Moser [35] the flow is weakly correlated (≈ 0.08) at a streamwise distance of $2m$. This leads to a sampling time of $\Delta t=18.01s$ with $u_B=0.111\frac{m}{s}$. After a physical simulation time of $t=163.12s$, we continue averaging over a time period of $\Delta t=8596s$, i.e. 79.5 flow through times for $Re_\tau=180$. For increasing Re_τ, the correlation decreases, yet we kept the sampling time constant and increased the flow through times according to the increase of the turbulent time scale. By assuming the ratio of the large- and small-time turbulence scale behaves as $\frac{t_L}{t_\eta}=\sqrt{Re_\tau}$, see [36], the flow through times increased to 117.7 and 143.9 for $Re_\tau=395$ and $Re_\tau=590$ respectively.

4.1 Convergence analysis of the turbulent channel flow

Before mean statistics are shown, a visualization of the unsteady flow field is given and the statistical convergence of the simulations is demonstrated. For increasing Reynolds number the BGK approach consistently predicts an increasing number of small scale flow structures, see Fig. 8. When the MRT scheme is employed, only for the lowest Reynolds number $Re_\tau=180$ a reasonable flow field can be obtained, see Fig. 9. For $Re_\tau=395$ and $Re_\tau=590$, strong unphysical oscillations develop. The presence of side walls and the viscous damping in these regions presumably prevents instability of the simulations, yet the results are not physically meaningful.

The RLB scheme is not shown in this context, since we found it to re-laminarize for $N=31$ and $N=91$ at $Re_\tau=180$. Strong numerical dissipation, which already lead to under predicted dissipation rates in the previous section, apparently damps the initial disturbances, which in turn should trigger the flow to a turbulent state. Increasing the resolution from $N=31$ to $N=91$ amplifies this effect, since the imposed fluctuations are now distributed across a larger range of wavenumbers. Consequently, for an equal amount of kinetic energy that is associated to the fluctuations, the relative kinetic energy per wavenumber is decreased. Since we did not employ better initialization techniques or restarted a RLB simulation from a converged BGK solution we omit further investigations of the RLB model for $Re_\tau=395$ and $Re_\tau=590$. The convergence of the Reynolds friction number $Re_\tau=180$ during the initial transition phase is depicted in Fig. 10 for $N=91$.

In Fig. 11 we demonstrate the symmetry for the streamwise Reynolds stresses $\overline{u'u'}$ at $Re_\tau=180$. For both, MRT as well as the BGK scheme, the differences in the peak value is below 3%. Although one could argue that this value leads to poorly-converged statistics, the symmetry across the channel height is satisfied to be more than 99.5% for both schemes. Consequently we can assume that, (i) the flow statistics are practically converged and (ii) since for all simulations outlined, the overall discrepancies in terms

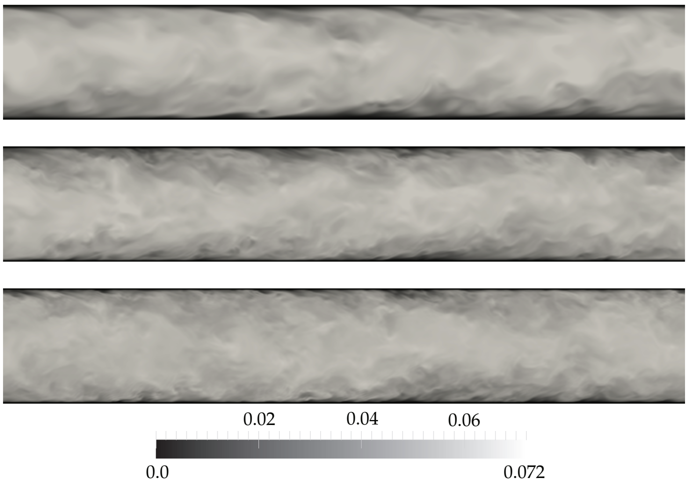

Figure 8: Instantaneous velocity magnitude in m/s on a xz-plane located at $y=0.5L_y$ predicted by the BGK collision model. $Re_\tau=180$, 395 and 590 from top to bottom.

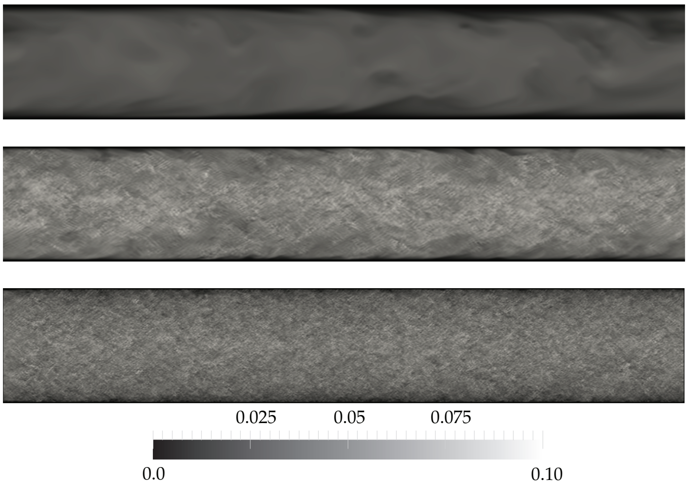

Figure 9: Instantaneous velocity magnitude in m/s on a xz-plane located at $y=0.5L_y$ predicted by the MRT collision model. $Re_\tau=180$, 395 and 590 from top to bottom.

of the peak value prediction between the different numerical schemes is higher than the error in the statistics, the interpretation of the results is not affected by the averaging procedure.

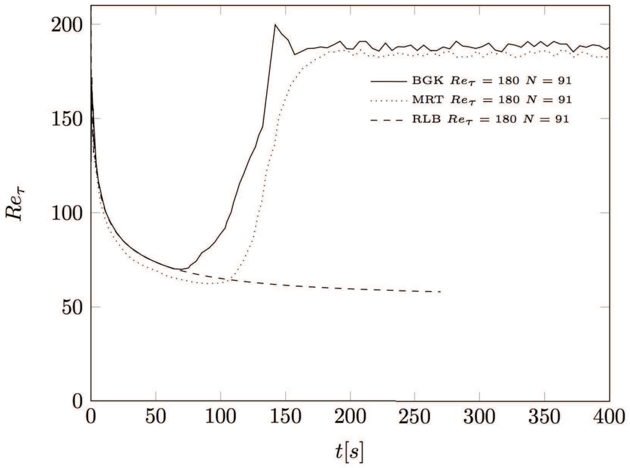

Figure 10: Convergence of Re_τ as a function of time for $Re_\tau = 180$ and $N = 91$.

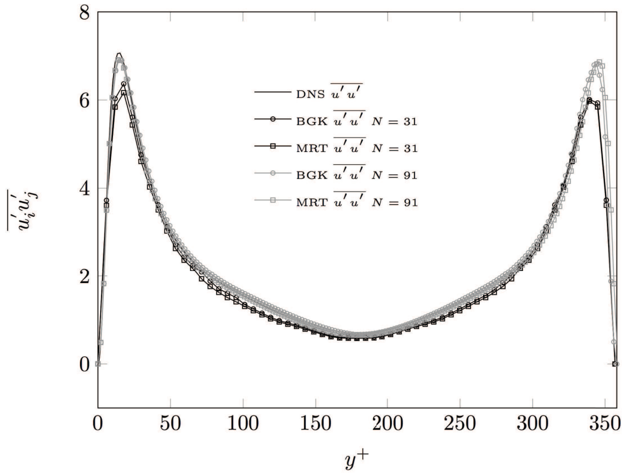

Figure 11: Symmetry proof for the streamwise Reynolds stress at $Re_\tau = 180$ for $N = 31$ and $N = 91$ compared to the DNS results of Kim et al. [22]. For the reference DNS only data for the channel half is provided.

4.2 Mean velocity statistics

In Fig. 12 the mean velocity profiles for $Re_\tau = 180$ from DNS of Kim et al. [22] are shown along with the under-resolved simulations using the BGK, MRT and RLB schemes. For $y^+ <= 10$ the reference DNS and the under-resolved simulations of the BGK and MRT scheme are in fair agreement. In the logarithmic region an increased normalized velocity

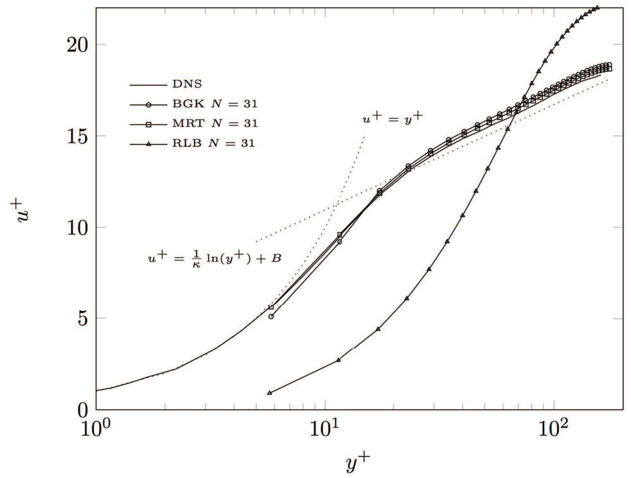

Figure 12: Mean velocity profiles of turbulent channel flow at $Re_\tau = 180$ and $N = 31$ compared to the DNS of Kim et al. [22].

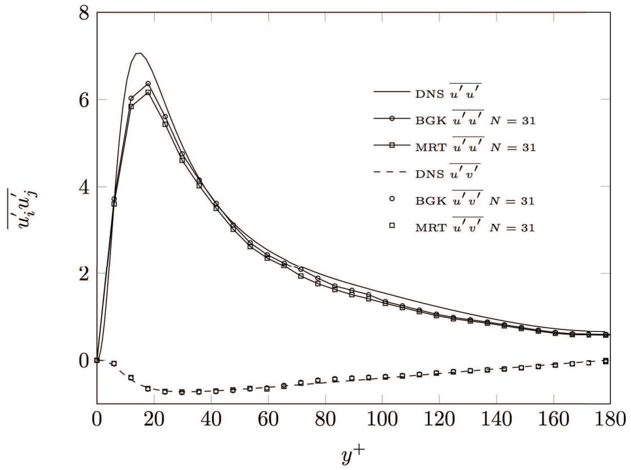

Figure 13: Mean Reynolds stresses of turbulent channel flow at $Re_\tau = 180$ and $N = 31$ compared to the DNS of Kim et al. [22].

$u^+ = \frac{\overline{u}}{u_\tau}$ by ≈5% for the BGK simulation and by approximately 3% for the MRT simulation can be found. The average velocity profile of the RLB scheme corresponds to a laminar flow profile. The employed resolution is, compared to the Reynolds number applied, at an intermediate level in the bulk ($\Delta y^+ \approx 5.8$). In Fig. 13 the corresponding Reynolds stresses $\overline{u'u'}$ and $\overline{u'v'}$ for this setup are shown.

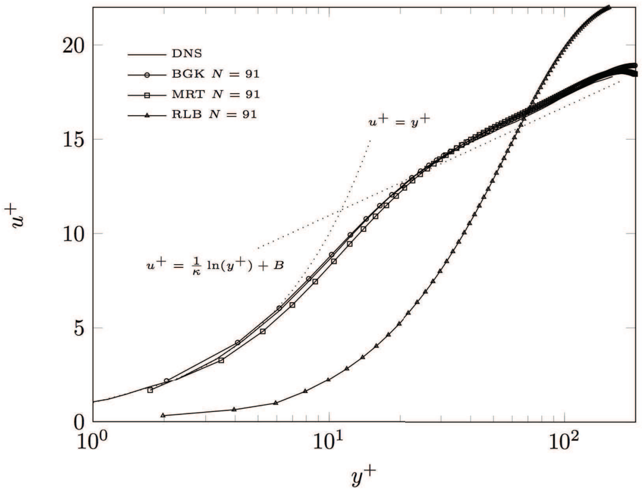

Figure 14: Mean velocity profiles of turbulent channel flow at $Re_\tau = 180$ and $N = 91$ compared to the DNS of Kim et al. [22].

The $\overline{u'u'}$ stresses are underestimated by both schemes, which is caused by the low resolution applied. The BGK model has a slightly better agreement with the reference data compared to the MRT model over the whole channel height. Although both LBM models predict reduced magnitudes for $\overline{u'u'}$ compared to the reference data, the wall normal location of the peak value of this stress component was found correctly. The mean $\overline{u'v'}$ stresses are predicted with good accuracy by the BGK and MRT scheme when compared to the reference DNS.

For a resolved simulation at $Re_\tau = 180$ the resolution was increased to $N = 91$, which corresponds to the setup of Bespalko [2] and gives a resolution of $\Delta y^+ \approx 2$ within the bulk and wall region. The simulations with the MRT and the BGK model run stable. For the mean velocity profiles very good agreement of the BGK and MRT results with reference DNS can be found. While the MRT model slightly underpredicts the velocities close to the wall, an over estimation of the mean velocities is found in the bulk flow. On the other hand the BGK scheme overpredicts the velocity field slightly in the wall-nearest region whilst excellent agreement was found in the bulk region when compared to the DNS data, see Fig. 14.

Fig. 15 shows that the $\overline{u'u'}$ and $\overline{u'v'}$ stresses predicted by the BGK scheme are in good agreement with the reference DNS data. Differences in the amplitude of the stresses in the bulk region can be related to the higher predicted $Re_{\tau,real}$, see Table 2. For the MRT scheme, the peak value and the magnitude of the $\overline{u'u'}$ stress are in very good agreement with the reference data. For the $\overline{u'v'}$ stress minor deviations from the reference DNS are visible for both the MRT and BGK scheme. Since this resolution is nearly the same as

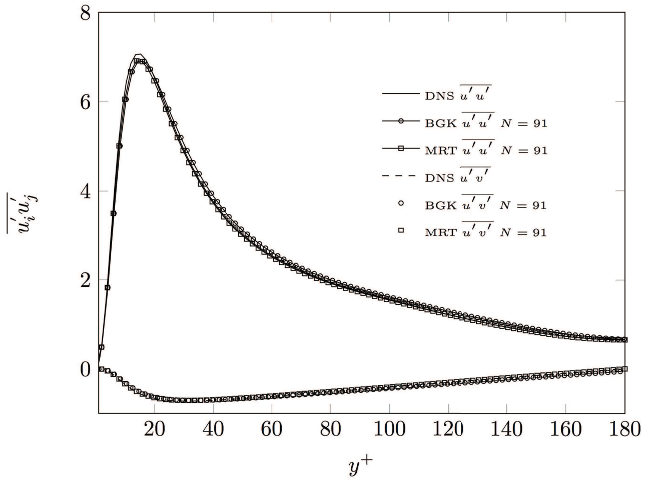

Figure 15: Mean Reynolds stresses for turbulent channel flow at $Re_\tau = 180$ and $N = 91$ compared to the DNS of Kim et al. [22].

in the numerical setup applied by Wang et al. [44], who found excellent agreement for the Reynolds stresses by applying the MRT scheme at $Re_\tau = 180$, we assume that for this low Reynolds number both the different forcing approach as well as the straight velocity boundary condition have a negative influence on the accurate prediction of the stresses in vicinity of the wall in our case.

By increasing the friction Reynolds number up to $Re_\tau = 395$ with $N = 91$, again the BGK model shows good agreement with the reference data of Moser et al. [35] for both the velocity field and the Reynolds stresses, see Figs. 16 and 17. Discrepancy of the peaks predicted by the BGK scheme are $\approx$7.9% and $\approx$11.2% for the $\overline{u'u'}$ and $\overline{u'v'}$ stresses respectively. The MRT model underpredicts the mean flow field in vicinity of the wall $y^+ < 40$, while the bulk region was overpredicted. Regarding the Reynolds stresses, see Fig. 17, one can see that the $\overline{u'u'}$ as well as the $\overline{u'v'}$ stresses are grossly and irregularly overpredicted by the MRT scheme for the same amount of physical time averages. For $Re_\tau = 395$ and $N = 91$ the MRT model converged to a state exhibiting unphysical oscillations. A similar behavior was found when increasing the resolution to $N = 151$, see Figs. 18 and 19. The difference of the $\overline{u'u'}$ and $\overline{u'v'}$ stresses predicted by the BGK scheme are only $\approx$6.8% and $\approx$9.1% respectively compared to the reference DNS data. For the MRT scheme, the mean velocity profile is under predicted in the wall-nearest region, while the mean velocity exceeds the DNS data in the bulk region by $\approx$6%. The stresses are similar as for $N = 91$, yet even for the same physical time of averaging, more fluctuations are observed.

In Fig. 20 the velocity field predicted by the BGK scheme for $Re_\tau = 590$ and $N = 91$ is illustrated. Although the resolution is quite coarse at this Reynolds number ($y^+ \approx 6.48$), the simulation covers the fully turbulent state, see also Fig. 8. The agreement of the

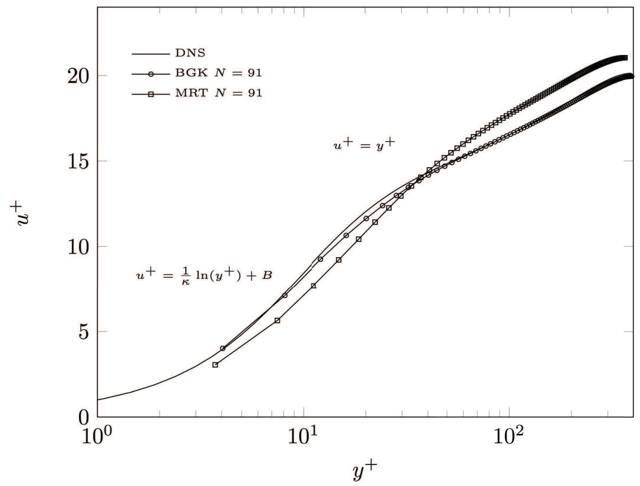

Figure 16: Mean velocity profiles of turbulent channel flow at $Re_\tau = 395$ and $N = 91$ compared to the DNS of Moser et al. [35].

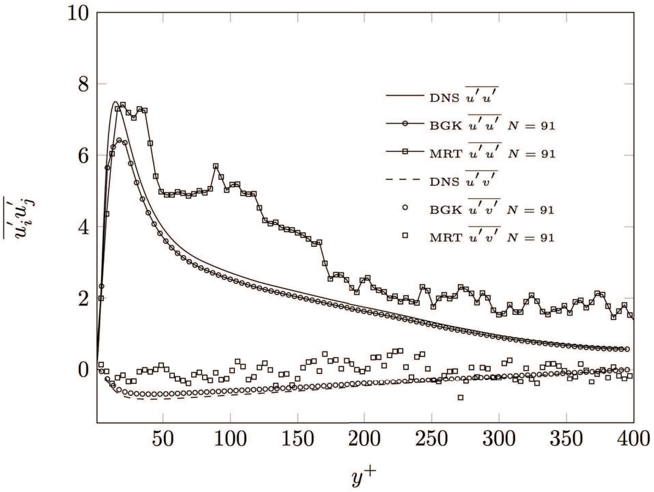

Figure 17: Mean Reynolds stresses of turbulent channel flow at $Re_\tau = 395$ and $N = 91$ compared to the DNS of Moser et al. [35].

mean velocity field with the reference DNS data is found to be excellent, see Fig. 20, while the stresses are under-predicted by almost 20% over the whole channel height, see Fig. 21. Beyond that, the location of the stress maximum is shifted for the $\overline{u'u'}$ and $\overline{u'v'}$ stresses, which is most probably caused by the very low resolution of $\Delta y^+ \approx 6.48$. The

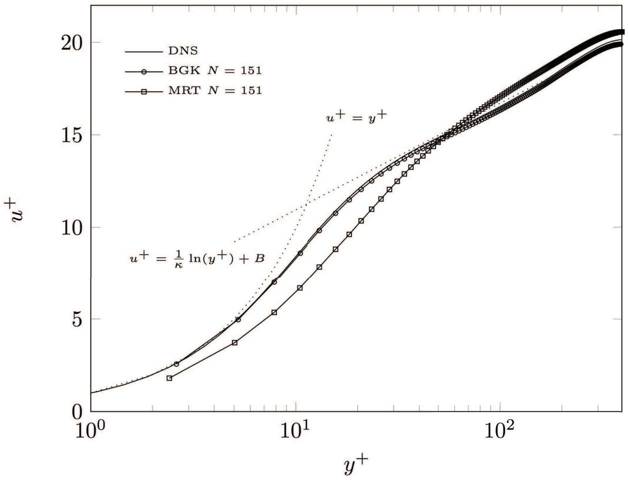

Figure 18: Mean velocity profiles of turbulent channel flow at $Re_\tau = 395$ and $N = 151$ compared to the DNS of Moser et al. [35].

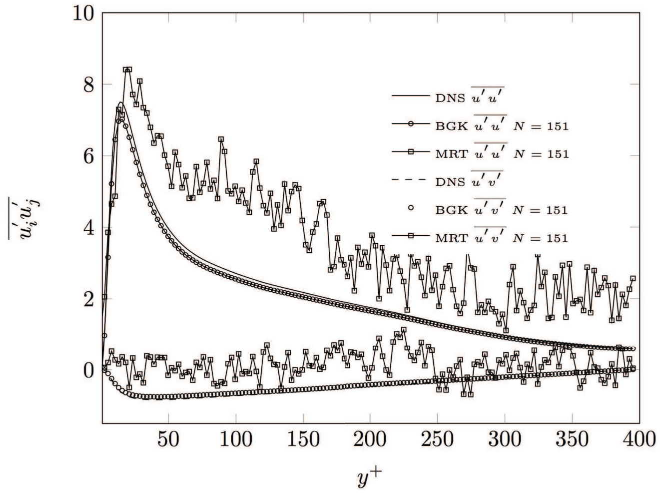

Figure 19: Mean Reynolds stresses of turbulent channel flow at $Re_\tau = 395$ and $N = 151$ compared to the DNS of Moser et al. [35].

MRT model assumed an unphysical state for the resolution $N = 91$, which is evident from unphysical spurious oscillations, that propagate throughout the whole channel, see also Figs. 9 and 21. For this setup, even the general quality of the evolution of the stresses is not in accordance with the DNS data. The quality of the results does not change by

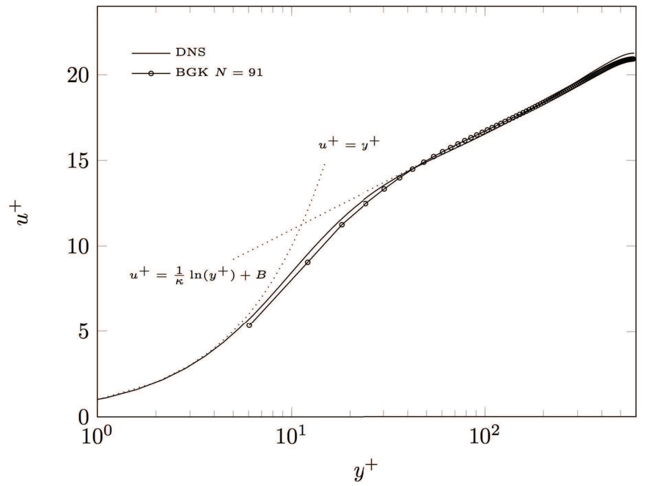

Figure 20: Mean velocity profiles of turbulent channel flow at $Re_\tau = 590$ and $N = 91$ compared to the DNS of Moser et al. [35].

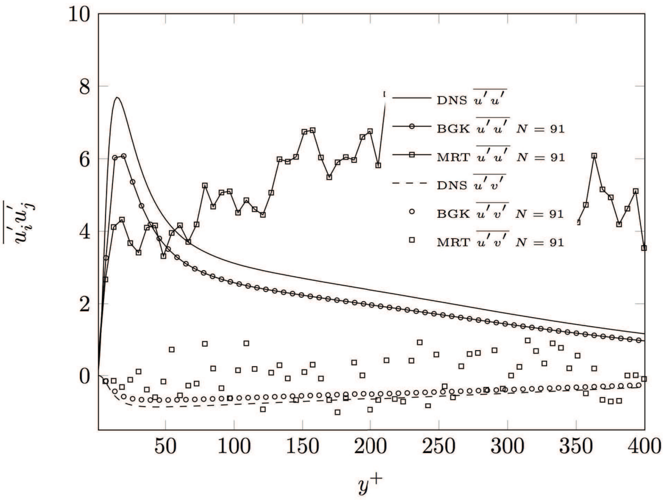

Figure 21: Mean Reynolds stresses of turbulent channel flow at $Re_\tau = 590$ and $N = 91$ compared to the DNS of Moser et al. [35].

increasing the resolution to $N = 151$, see Figs. 22 and 23, except that the uncertainty of the stresses predicted by the BGK scheme decreased to $\approx 10\%$.

Recently, Gehrke et al. [12] presented similar results when computing the turbulent channel flow. Although the boundary conditions were not identical, the MRT model

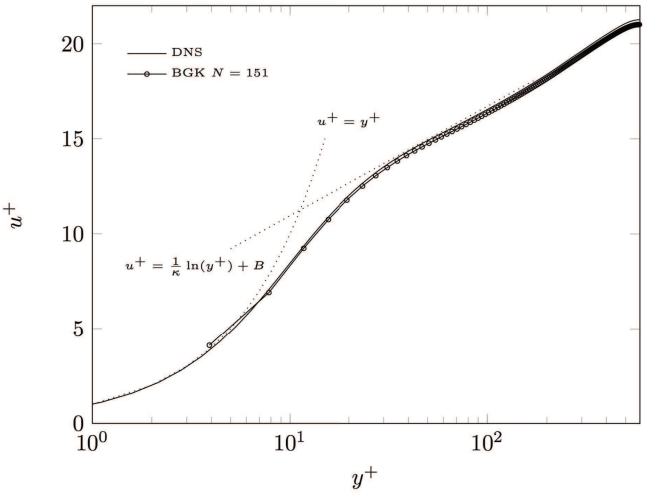

Figure 22: Mean velocity profiles of turbulent channel flow at $Re_\tau = 590$ and $N = 151$ compared to the DNS of Moser et al. [35].

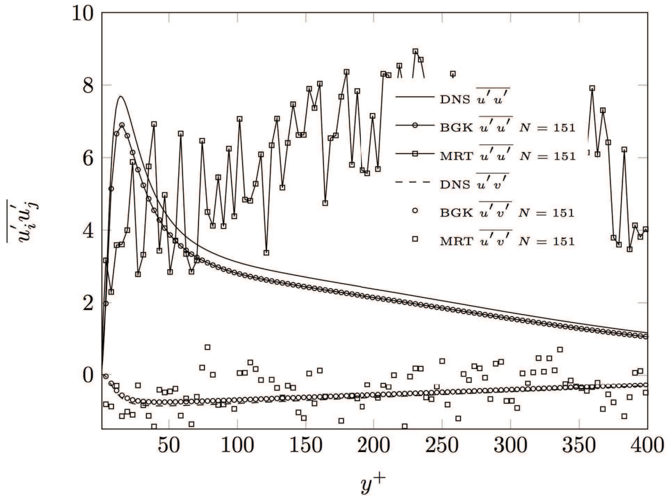

Figure 23: Mean Reynolds stresses of turbulent channel flow at $Re_\tau = 590$ and $N = 151$ compared to the DNS of Moser et al. [35].

produced similar spurious noise in their simulations and the BGK model was able to reproduce the reference data with increased accuracy. The independency of the boundary conditions indicate, that the problems of the MRT model are intrinsic when calculating turbulent flows directly on different mesh levels.

4.3 Spectral analysis

We analyze the wall-normal energy distribution in spectral space. Fig. 24 shows the normalized energy for the BGK and MRT scheme at all investigated Reynolds numbers and $N=91$. Similarly to the energy spectra depicted in Section 3, the MRT model shows an unphysical increase of energy in the high-frequency range for $Re_\tau=395$ and $Re_\tau=590$. Since the energy is normalized, it is visible, that a high amount of energy is shifted from the low wavenumber range towards the high wavenumber range for $Re_\tau=395$, which is even more apparent for $Re_\tau=590$. These high wavenumber fluctuations of the velocity represent the unphysical flow state shown in Fig. 9.

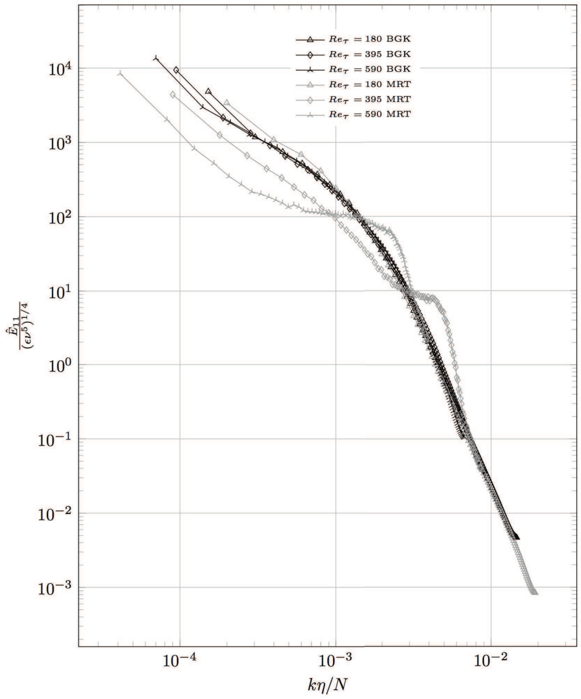

Figure 24: Wall normal spectra of the normalized energy of the BGK and MRT scheme for all investigated Reynolds numbers and $N=91$.

5 Conclusions

In this paper, the accuracy and stability of three popular lattice schemes, the BGK, MRT and RLB approach, when employed for simulations of turbulent flows were investigated. Homogeneous isotropic turbulence was considered by computing the Taylor-Green vortex. Different resolutions and Reynolds numbers were considered. As it was found earlier by several authors, the BGK scheme [7] suffers from numerical instabilities for increasing Reynolds numbers at fixed resolutions. The reasons are unphysical moments, which are amplified exponentially in time for under-resolved setups. Nevertheless, when increasing the resolution, mesh convergence and accurate results were obtained. Due to the low dissipation found for the BGK model at medium and well resolved setups, the adaption of advanced turbulence models, such as ADM, seems to be promising for this type of collision operator. To circumvent the instabilities of the BGK scheme at low resolutions, the MRT scheme [8] was derived. In our investigation this expected feature of the MRT scheme was confirmed, but only in under-resolved test cases. Increasing the resolution towards DNS lead to unstable simulations, and no mesh convergence could be achieved with the MRT-LBM for of homogeneous turbulence considered in this work. The RLB scheme allowed for stable simulations at all resolutions and Reynolds numbers considered for the Taylor-Green vortex and mesh convergence was achieved. The RLB suffers from large numerical dissipation, which grossly decreases accuracy.

By computing turbulent channel flows at $Re_\tau = 180$, $Re_\tau = 395$ and $Re_\tau = 590$ for varying resolutions, some features found for the Taylor-Green vortex could be confirmed. For the rather low Reynolds number of $Re_\tau = 180$, very good agreement was found for both the BGK and MRT scheme, while the MRT scheme showed even better agreement with the reference data. By increasing the Reynolds number to $Re_\tau = 395$ and $Re_\tau = 590$, no mesh convergence for the MRT model was found. While the BGK model lead to reasonable and good results, the MRT model showed the appearance of spurious velocity oscillations in the bulk. For an increasing Reynolds number these oscillations were also found in the vicinity of the wall. Although the MRT model did not became unstable, the simulations reproduced an unphysical state. The RLB model was only applied for the lowest Reynolds number at $Re_\tau = 180$ and it was found, that the flow field resulted in a laminar state, which was confirmed by the velocity profile and the temporal evolution of the Re_τ. Additional work has to be performed on the validation of the forcing approach to reach the target turbulence state. Since the mean velocity profile is maybe affected by the development of spurious oscillations, mode coupling between such spurious fluctuations and forcing oscillations may occur. Different initialization techniques and Reynolds numbers should be applied by computing the turbulent channel flow with the RLB scheme to test the general application of this model for wall-bounded turbulent flows.

For the MRT model it is believed, that the high order moments are responsible for the absence of mesh convergence at high Reynolds numbers employing a resolved numerical setup with diffusive scaling, see Sections 3 and 4. It was shown, that the MRT model produces an unphysical amount of energy in the high frequency space. Due to the developing strong oscillations, the classical energy transfer of a turbulent flow is disturbed. The results obtained in this work can be useful for further development of turbulence models and underline the suitability of the BGK scheme as an efficient and accurate DNS tool for turbulent fluid flows.

References

[1] C. K. Aidun and J. R. Clausen. Lattice-boltzmann method for complex flows. *Annual Review of Fluid Mechanics*, 42:439–472, 2010.

[2] D. J. Bespalko. *Validation of the Lattice Boltzmann Method for Direct Numerical Simulation of Wall-Bounded Turbulent Flows*. dissertation, Queen's University, 2011.

[3] P. L. Bhatnagar, E. P. Gross, and M. Krook. A model for collision processes in gases. i. small amplitude processes in charged and neutral one-component systems. *Phys. Rev.*, 94:511–525, 1954.

[4] M. E. Brachet. Direct simulation of the three-dimensional turbulence in th taylor-green vortex. *Fluid Dynamics Research*, 8:1–8, 1991.

[5] O. Cabrit. Direct simulations for wall modeling of multicomponent reacting compressible turbulent flows. *Phys. Fluids*, 21:055108, 2009.

[6] A. Caiazzo. Analysis of lattice boltzmann initialization routines. *J. Stat. Ph.*, 121:37–48, 2005.

[7] S. Chen and G. D. Doolen. Lattice boltzmann method for fluid flows. *Annu. Rev. Fluid Mech.*, 30:329–364, 1998.

[8] D. D'Humiéres, I. Ginzburg, M. Krafczyk, P. Lallemand, and L.-S. Luo. Multiple-relaxation-time lattice boltzmann models in three dimensions. *Phil. Trans. R. Soc. Lond. A*, 361:437–451, 2002.

[9] B. Dorschner, F. Bösch, S. S. Chikatamarla, K Boulouchos, and I. V. Karlin. Entropic multi-relaxation time lattice boltzmann model for complex flows. *J. Fluid Mech.*, 801:623–651, 2016.

[10] B. Dorschner, N. Frapolli, S. S. Chikatamarla, and I. V. Karlin. Grid refinement for entropic lattice boltzmann models. *Phys. Rev. E*, 94:053311, 2016.

[11] R. K. Freitas, A. Henze, M. Meinke, and W. Schröder. Anaysis of lattice-boltzmann methods for internal flows. *Comp. Fl.*, 47:115–121, 2011.

[12] M. Gehrke, C.F. Janßen, and T Rung. Scrutinizing lattice boltzmann methods for direct numerical simulations of turbulent channel flows. *Computers & Fluids*, 156:247–263, 2017.

[13] M. Geier, M. Schoenherr, A. Pasquali, and M. Krafczyk. The cumulant lattice Boltzmann equation in three dimensions: theory and validation. *Computers and Mathematics with Applications*, 70:507, 2015.

[14] M. C. Geier. *Ab initio derivation of the cascaded lattice Boltzmann automaton*. dissertation, Universität Freiburg, 2006.

[15] Z. Guo, S. Baochang, and W. Nengchao. Lattice bgk model for incompressible navier stokes equation. *J. Comp. Ph.*, 165:288–306, 2000.

[16] Z. Guo and S. Shu. *Lattice Boltzmann Method and its Applications in Engineering*. World Scientific, 2013.

[17] D. Hänel. *Molekulare Gasdynamik*. Springer-Verlag, 2004.

[18] X. He and L.-S. Luo. Lattice boltzmann model for the incompressible navier stokes equation. *J. Stat. Phys.*, 88:927–944, 1997.

[19] X. He and G. D. Shan, X.and Doolen. Discrete boltzmann equation model for nonideal gases. *Phys. Rev. E*, 57:R13–R16, 1998.

[20] T. Henn, G. Thäter, W. Dörfler, H. Nirschl, and M.J. Krause. Parallel dilute particulate flow simulations in the human nasal cavity. *Computers & Fluids*, 124:197–207, 2016.

[21] I. V. Karlin, F. Bösch, and S. S. Chikatamarla. Gibbs' principle for the lattice-kinetic theory of fluid dynamics. *Phys. Rev. E*, 90:031302, 2014.

[22] J. Kim, P. Moin, and R. Moser. Turbulence statistics in fully-developed channel flow at low reynolds-number. *J. Fluid Mech.*, 177:133–166, 1987.

[23] M.J. Krause, T. Gengenbach, and V. Heuveline. *Hybrid Parallel Simulations of Fluid Flows in Complex Geometries: Application to the Human Lungs*, volume 6586. Springer Berlin / Heidelberg, 2011.

[24] M.J. Krause and V. Heuveline. Parallel Fluid Flow Control and Optimisation with Lattice Boltzmann Methods and Automatic Differentiation. *Computers and Fluids*, 80(0):28–36, 2013.

[25] A. J. C. Ladd and R. Verberg. Lattice-boltzmann simulations of particle-fluid suspensions. *J. Stat. Phys.*, 104:1191–1251, 2001.

[26] P. Lallemand and L. S. Luo. Theory of the lattice boltzmann method: Dispersion, dissipation, isotropy, galilean invariance, and stability. *Phys. Rev. E*, 61:6546, 2000.

[27] P. Lammers, K. N. Bernonov, R. Volkert, G. Brenner, and F. Durst. Lattice bgk direct numerical simulation of fully developed turbulence in incompressible plane channel flow. *Comp. Fl.*, 35:1137–1153, 2006.

[28] J. Latt. *Hydrodynamic Limit of Lattice Boltzmann Equations*. dissertation, Université de Genève, 2007.

[29] J. Latt and B. Chopard. Lattice boltzmann method with regularized non-equilirbium distribution functions. *Mathematics and Computer in Simulation*, 72:165–168, 2006.

[30] J Latt, B. Chopard, O. Malaspinas, M. Deville, and A. Michler. Straight velocity boundaries in the lattice boltzmann method. *Phys. Rev. E*, 77:056703, 2008.

[31] O. Malaspinas and P. Sagaut. Advanced large-eddy simulation for lattice boltzmann methods: The approximate deconvolution model. *Phys. Fluids*, 23:105103, 2011.

[32] O. Malaspinas and P. Sagaut. Consistent subgrid scal modelling for lattice boltzmann methods. *J. Fluid Mech.*, 700:514–542, 2012.

[33] O. Malaspinas and P. Sagaut. Wall model for large-eddy simulation based on the lattice boltzmann methodl. *J. Comp. Phys.*, 275:25–40, 2014.

[34] M. J. Mathias. *Fluid Flow Simulation and Optimisation with Lattice Boltzmann Methods on High Performance Computers*. dissertation, Universität Karlsruhe, 2010.

[35] R. D. Moser, J. Kim, and N. N. Mansour. Direct numerical simulation of turbulent channel flow up to $re_\tau = 590$. *Phys. Fl.*, 11:943–945, 1999.

[36] S. B. Pope. *Turbulent Flows*. Cambridge University Press, 2013.

[37] D. Ricot, V. Maillar, and C. Bailly. Numerical simulation of unsteady cavity flow using lattice boltzmann method. In *8th AIAA/CEAS Aeroacoustics Conference & Exhibit*, 2002.

[38] D. Ricot, S. Marie, P. Sagaut, and C. Bailly. Lattice boltzmann method with selective viscosity filter. *J. Comp. Phys*, 228:4478–4490, 2009.

[39] P. Sagaut. Toward advanced subgrid models for lattice boltzmann based large-eddy simulation: Theoretical formulations. *Computers and Mathematics with Applications*, 59:2194–2199, 2010.

[40] S. Stolz and N. A. Adams. An approximate deconvolution procedure for large-eddy simulation. *Phys. Fluids*, 11:1699, 1999.

[41] M. C. Sukop and D. T. Thorne. *Lattice Boltzmann Modeling*. Springer-Verlag, 2006.

[42] Takahiro Tsukahara, Yohji Seki, Hiroshi Kawamura, and Daisuke Tochio. Dns of turbulent channel flow at very low reynolds numbers. In *TSFP DIGITAL LIBRARY ONLINE*. Begel House Inc., 2005.

[43] D. A. Waldrow. *Lattice-Gas Cellular Automata and Lattice Boltzmann Models: An Introduction*. Springer-Verlag, 2000.

[44] L. P. Wang, C. Peng, Z. Guo, and Z. Yu. Lattice boltzmann simulation of particle-laden turbulent channel flow. *Comp. Fl.*, 124:226–236, 2016.

B.2. ADAPTIVE FILTERING FOR THE SIMULATION OF TURBULENT FLOWS WITH THE LATTICE BOLTZMANN METHOD

Computers and Fluids 000 (2018) 1–14

Contents lists available at ScienceDirect

Computers and Fluids

journal homepage: www.elsevier.com/locate/compfluid

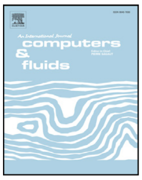

Adaptive filtering for the simulation of turbulent flows with lattice Boltzmann methods

P. Nathen[a,*], M. Haussmann[b], M.J. Krause[b], N.A. Adams[a]

[a] *Insitute of Aerodynamics and Fluid Mechanics, Technische Universität München,Boltzmannstrasse 15, Garching bei München 85748, Germany*
[b] *Lattice Boltzmann Research Group, Institute for Mechanical Process Engineering and Mechanics, Institute for Applied and Numerical Mathematics, Karlsruhe Institute of Technology, Strasse am Forum 8, Karlsruhe, 76131, Germany*

ARTICLE INFO

Article history:
Received 31 October 2017
Revised 6 March 2018
Accepted 13 March 2018
Available online xxx

Keywords:
Lattice Boltzmann
Turbulence
Turbulence modeling
Homogeneous Isotropic Turbulence
Turbulent channel flow

ABSTRACT

This paper presents an extension of a Large Eddy Simulation based approach in the framework of Lattice Boltzmann Methods. An extended filter technique is introduced based on selective viscosity filters. In contrast to previous approaches we omit adjusting parameters, a technique frequently used in literature to achieve good fit with turbulence benchmarks. Such parameters have to be adapted manually for different Reynolds numbers and grid resolutions. The new filter approach is based on a time dependent coupling between resolved scales and a phase averaged strain-rate. We demonstrate that our method is able to recover turbulent statistics of the Taylor–Green vortex benchmark, representing Homogeneous Isotropic Turbulence for varying mesh resolutions and Reynolds numbers. Beyond that, we show the applicability to wall-bounded turbulence represented by the turbulent channel flow at friction Reynolds numbers $Re_\tau = 180$, $Re_\tau = 395$ and $Re_\tau = 590$. A spectral viscosity analysis is performed in order to demonstrate the methods ability to adapt the numerical dissipation according to the mesh resolution.

1. Introduction

In the last three decades, Lattice Boltzmann Methods (LBM) have become a promising alternative for the simulation of fluid flows [1–3]. The kinetic nature of LBM allows their application even for complex flow physics like fluid-structure interaction or multi-phase and -component flows, see [4–7].

Although LBM have been applied to a wide range of fluid dynamic applications, turbulence modeling in the LBM framework still requires considerable work and has not reached a level of maturity as seen for Navier–Stokes based methods, see [8–10]. The concept of turbulence modeling in the LBM framework is primarily based on simple extrapolations of Large Eddy Simulation (LES) models as used for simulations based on the filtered Navier–Stokes equations. These models make use of an effective relaxation rate which corresponds to an effective viscosity concept in moment space. Corresponding models were presented and applied to different benchmarks in [11–15] among others. Important recent advances have been made by Sagaut et al., see [10,16,17]. They showed that the concept of an effective relaxation rate adopted from the Navier–Stokes based LES does not necessarily lead to the correct macroscopic equations. Consequently, the underlying equations for LES in the framework of LBM do not resemble the filtered macroscopic equations. A recently presented approach proposed by Sagaut [10] and Malaspinas and Sagaut [17] is based on the Approximate Deconvolution Method (ADM) of Stolz, see Stolz and Adams [18] and Stolz et al. [19]. ADM exploits a range of scales in order to partially mimic the Subgrid-Scale (SGS) energy transfer in the subfilter-range, see [20,21]. An implementation of the ADM algorithm in a DNS LBM code was demonstrated in [17], where the discrete Boltzmann equations are filtered with an explicit filter stencil and subsequently deconvolved with a regularized inverse filter operation in order to reconstruct the proper macroscopic equations for LES within the kinetic theory.

Tam et al. [22] proposed a selective viscosity filter stencil where the filter intensity is modified with an artificial viscosity. This class of filters was also the underlying ADM approach of Malaspinas and Sagaut [17], which was also successfully validated by Ricot et al. [8,9]. Fauconnier et al. [23] employed this class of filters for the simulation of Homogeneous Isotropic Turbulence (HIT) and they showed that the accuracy of the numerical results strongly depends on the artificial viscosity, which needs to be adapted according to the mesh resolution and the consideration of stability issues. Similar results were found in [17] by computing a turbulent shear layer. Only for very well resolved numerical test cases satisfying agreement with reference data was achieved while showing

---

[*] Corresponding author.
E-mail addresses: patrick.nathen@aer.mw.tum.de, patrick@lilium.com (P. Nathen), mathias.krause@kit.edu (M.J. Krause).

https://doi.org/10.1016/j.compfluid.2018.03.042
0045-7930/

a minor influence of the filters artificial viscosity. For rather under resolved setups the development of turbulent structures strongly depends on the filter stencil and the applied artificial viscosity. In conclusion, no general strategy can be found in the literature for employing selective viscosity filters of Tam et al. [22] for the simulation of turbulent flows within the ADM theory for LBM. Depending on the test case and under consideration of the resolution, the artificial viscosity as well as the filter stencil have to be tuned with care.

Our goal is to improve the prediction of turbulent flows in the LBM-LES framework by extending an existing ADM approach to self-adapting filter stencils. By doing so, we aim for less mesh-sensitivity for a given Reynolds number in order to derive a more general framework for the simulation of turbulent flows with LBM. A connection between spatial and temporal resolution and locally resolved scales is to be enabled which features the desired properties of the filter to be self-adaptive.

This paper is structured as follows: After a short introduction of the basic theory of LBM in Section 2.1, the main aspects for ADM in the LBM framework are given in Section 2.2. In Section 2.3, we propose a novel filtering approach which dynamically adapts to mesh size and Reynolds number of the flow. This replaces a fixed artificial viscosity and thus enables higher flexibility between filter stencil and applied mesh resolution. Validation of the approach is conducted for the Taylor–Green vortex (TGV) benchmark, representing HIT in Section 3.1. In order to assess numerical dissipation, we perform a spectral decomposition of the flow field in terms of the wavenumber dependent spectral dissipation and spectral viscosity, similar to [24–26]. To the authors knowledge, no prior analysis of the spectral distribution of the numerical viscosity has been performed in the LBM framework. In Section 2.4 this spectral space analysis for LBM will be shortly introduced and the numerical validation will be depicted in Section 3. Additional validation data is provided for wall-bounded turbulence in Section 3.3 by investigating the turbulent channel flow at $Re_\tau = 180$, $Re_\tau = 390$ and $Re_\tau = 590$.

2. Theoretical background

2.1. Lattice Boltzmann methods

With LBM the computational domain is discretized by an equidistant mesh on which a discrete set of velocity distribution functions f_α is solved numerically for any given instance of time t and spatial position $\boldsymbol{x}$. This set of velocity distribution functions corresponds to discrete lattice velocities $\boldsymbol{c}_\alpha$, which are used to recover the macroscopic moments in terms of a Hermite polynomial expansion. The discrete Boltzmann equations can be written as

$$f_\alpha(t+\Delta t, \boldsymbol{x}+\boldsymbol{c}_\alpha \Delta t) = f_\alpha(t,\boldsymbol{x}) + \Omega_\alpha(f_\alpha) \ , \qquad (1)$$

where $\Omega_\alpha(f_\alpha)$ is the non-linear discrete collision operator which also accounts for viscous effects, $\boldsymbol{c}_\alpha$ with $\alpha = 0, 1 \ldots, q-1$ is a set of discrete lattice velocities associated to q discrete lattice links and Δt is the discrete time step. Macroscopic moments are reconstructed with a Gauss–Hermite quadrature based on the Hermite polynomial expansion of f_α on a discrete lattice. The first two moments of the velocity distribution functions are the conserved moments, namely the density ρ and the momentum $\rho\boldsymbol{u}$, which read

$$\rho = \sum_\alpha f_\alpha \ , \qquad (2a)$$

$$\rho\boldsymbol{u} = \sum_\alpha \boldsymbol{c}_\alpha f_\alpha, \qquad (2b)$$

while the momentum flux is the second-order off-equilibrium moment of the velocity distribution functions

$$\boldsymbol{\Pi}^{neq} = \sum_\alpha f_\alpha^{neq} \boldsymbol{c}_\alpha \boldsymbol{c}_\alpha. \qquad (3)$$

To close Eq. (1), the collision term needs to be modeled. Depending on the particular closing approach, the collision term is modeled in different ways, see [1–3,27–29]. Linearization around small perturbations of the thermodynamic equilibrium f_α^{eq} leads to the Bhatnagar–Gross–Krook (BGK) closure, see [30–33]. The collision term is handled as a linear relaxation towards Maxwellian equilibrium

$$\Omega_\alpha(f_\alpha) = -\frac{1}{\tau}\left(f_\alpha(t,\boldsymbol{x}) - f_\alpha^{eq}(t,\boldsymbol{x})\right) \ . \qquad (4)$$

The relaxation time τ is related to the viscosity $\nu = c_s^2\left(\tau - \frac{1}{2}\right)\Delta t$ and f_α^{eq} is a low Mach number truncated Maxwell–Boltzmann distribution, which is adjusted in such a way that Eq. (3) is satisfied and both mass and momentum are conserved. A widely used formulation for f_α^{eq} is given by

$$f_\alpha^{eq} = \rho\omega_\alpha\left[1 + \frac{\boldsymbol{c}_\alpha \boldsymbol{u}}{c_s^2} + \frac{1}{2c_s^4}(\boldsymbol{uu} - c_s^2\boldsymbol{\delta})\boldsymbol{uu}\right]. \qquad (5)$$

The weights ω_α are obtained by a Gauss–Hermite quadrature with the discrete lattice links, $c_s = 1/\sqrt{3}$ is the lattice speed of sound which is valid for the $D3Q19$ lattice used in this work and $\boldsymbol{\delta}$ is the Kronecker delta. The BGK approach is a very well understood closure for the Lattice Boltzmann equation and is being frequently used in the literature, see Wolf-Galdrow [34] among others.

2.2. Approximate deconvolution method for LBM

The ADM was first introduced by Stolz and Adams [18] and Stolz et al. [19], and adapted for LBM by Sagaut [10] and Malaspinas and Sagaut [17]. Starting point is the discrete Boltzmann equation (1) with the single relaxation time approach given by Eq. (4). By applying a filter kernel $\mathcal{G}$ to Eq. (1) we can write the discrete filtered LBM equation as

$$\frac{D\bar{f}_\alpha}{Dt} - \Omega_\alpha(\bar{f}_\alpha) = \mathcal{G} * \Omega_\alpha(f_\alpha) = \overline{\Omega_\alpha(f_\alpha)} - \Omega_\alpha(\bar{f}_\alpha) = \mathcal{R}_\alpha \ , \qquad (6)$$

where $\bar{f}_\alpha = \mathcal{G} * f_\alpha$ is the filtered counterpart to the velocity distribution function and $\mathcal{R}_\alpha$ is the Subgrid-Scale (SGS) collision term, which has to be modeled. The term $\mathcal{R}_\alpha$ represents the difference between exact filtered collision and collision evaluated with the filtered veloctiy distribution functions $\bar{f}_\alpha$. In the ADM-LBM framework, the solution of the inverse filtered solution of $\bar{f}_\alpha$ is of interest which is achieved by an regularized inverse filter operation given by

$$\mathcal{Q} * (\mathcal{G} * f_\alpha) = \widehat{f}_\alpha \ , \qquad (7)$$

with the inverse filter properties

$$\mathcal{Q} * \mathcal{G} = \mathcal{I} + \mathcal{O}(h^l) \ . \qquad (8)$$

In Eq. (8) $\mathcal{I}$ is the identity and h corresponds to the grid resolution, see also Stolz and Adams [18] and Malaspinas and Sagaut [17]. The order of deconvolution is determined by $l > 0$. Following Mathew et al. [35], $\mathcal{R}_\alpha$ on the right hands side of Eq. (10) can be rewritten as

$$\mathcal{R}_\alpha = \mathcal{R}_{\alpha,1} + \mathcal{R}_{\alpha,2} = \overline{\Omega_\alpha(\widehat{f}_\alpha)} - \Omega_\alpha(\bar{f}_\alpha) + \overline{\Omega_\alpha(f_\alpha)} - \overline{\Omega_\alpha(\widehat{f}_\alpha)} \ . \qquad (9)$$

Term $\mathcal{R}_{\alpha,2} = \overline{\Omega_\alpha(f_\alpha)} - \overline{\Omega_\alpha(\widehat{f}_\alpha)}$ of Eq. (9) has to be modeled. The derivation of the SGS collision term will not be shown here since it was derived in detail in the work of Malaspinas and Sagaut

Please cite this article as: P. Nathen et al., Adaptive filtering for the simulation of turbulent flows with lattice Boltzmann methods, Computers and Fluids (2018), https://doi.org/10.1016/j.compfluid.2018.03.042

Table 1
Weighting coefficients for the selective viscosity filters up to order $M = 4$.

M	d_0	d_1	d_2	d_3	d_4
1	1/2	−1/4	–	–	–
2	6/16	−4/16	1/16	–	–
3	5/16	−15/64	3/32	−1/64	–
4	35/128	−7/32	7/64	−1/32	1/256

[17] and Sagaut [10]. The final result for the full ADM-LBM equation is given by

$$\mathcal{G} * \left(\frac{D\widehat{f}_\alpha}{Dt} + \frac{1}{\tau}\left(\widehat{f}_\alpha - f_\alpha^{eq}(\widehat{f})\right)\right) = \frac{1}{\tau}\mathcal{G} * \mathcal{R}_{\alpha,SGS} \ , \tag{10}$$

with

$$\begin{aligned}\mathcal{R}_{\alpha,SGS} = \Delta\widehat{f}_\alpha - \omega_\alpha \Bigg(& \Delta\widehat{\rho} + \frac{\boldsymbol{c}_\alpha \cdot \Delta\widehat{\boldsymbol{j}}}{c_s^2} \\ & + \frac{1}{2c_s^4}\mathcal{H}^{(2)} : \left(-\frac{\Delta\widehat{\rho}}{\widehat{\rho}^2}\widehat{\boldsymbol{j}\boldsymbol{j}} + \frac{1}{\widehat{\rho}}\left(\Delta\widehat{\boldsymbol{j}\boldsymbol{j}} + \widehat{\boldsymbol{j}}\Delta\widehat{\boldsymbol{j}}\right)\right)\Bigg),\end{aligned} \tag{11}$$

where $\Delta = (\mathcal{I} - \mathcal{Q} * \mathcal{G})$, $\mathcal{H}^{(2)}$ is the Hermite base of second order and $\boldsymbol{j} = \rho\boldsymbol{u}$ is the momentum.

Following Mathew et al. [35] and Malaspinas and Sagaut [17], we neglect the term $\mathcal{R}_{\alpha,2}$ as well, leading to the simplified version of the full ADM-LBM Eq. (10) as

$$\mathcal{G} * \left(\frac{D\widehat{f}_\alpha}{Dt} + \frac{1}{\tau}\left(\widehat{f}_\alpha - f_\alpha^{eq}(\widehat{f})\right)\right) = 0 \ . \tag{12}$$

The simplified ADM approach in Eq. (12) can be implemented in any DNS like LBM code.

2.3. The extension of viscosity filters for the ADM-LBM approach

The original implementation of the ADM-LBM in [17] is based on an explicit filtering step with viscosity filters. By employing the simplified Eq. (12) the algorithm for any ADM-LBM implementation reads:

1. Standard BGK collision of the populations $\widehat{f}_\alpha$.
2. Stream of the relaxed populations to the neighboring cells $\widehat{f}_\alpha(\boldsymbol{x} + \Delta t\boldsymbol{c}, t + \Delta t) = \widehat{f}_\alpha^p(\boldsymbol{x}, t)$.
3. Explicit filter operation.

The sup-script in $\widehat{f}_\alpha^p(\boldsymbol{x}, t)$ indicates the post-collision state of the velocity distribution function. The explicit viscosity filter was originally proposed by Tam et al. [22] and analyzed in detail for the LBM framework by Ricot et al. [8,9] and Malaspinas and Sagaut [16]. The explicit filter step reads

$$\mathcal{Q} * \mathcal{G} * \widehat{f}_\alpha(\boldsymbol{x}, t) = \widehat{f}_\alpha(\boldsymbol{x}, t) - \sigma \sum_{j=1}^{D} \sum_{m=-M}^{M} d_m \widehat{f}_\alpha(\boldsymbol{x} + m\boldsymbol{e}_j, t) \ . \tag{13}$$

Here, d_m are the filter weights, $\boldsymbol{e}$ the Cartesian basis vectors in D dimensions and M the filter stencil size. Our focus is on the artificial viscosity σ. In previous publications, see [8,9,17,23], the selection of σ is not straight forward. Depending on the grid resolution and the applied filter stencil, the results varied significantly. For sake of clarity, the weights d_m are shown in Table 1 for $M = 1..4$.

The underlying assumption for neglecting the right hands side of Eq. (10) and the derivation of Eq. (11) is

$$|\widehat{f}_\alpha - f_\alpha| \ll 1 \ , \tag{14}$$

which refers to a resolved simulation where the filter width has the size of the scales in the dissipation range. This filter width scale is of order $|\widehat{f}_\alpha - f_\alpha| = \mathcal{O}(h^l)f$, see also Eq. (8). Since l determines the order of reconstruction, the connection between grid resolution, order of reconstruction and the validity of $\mathcal{O}(h^l)f \ll 1$ is now visible. Since the ADM-BGK approach is a LES based model, the aim is to account for resolved large scales and model the unresolved scales. This leads to the assumption that the filter construction has to be performed carefully, in order to reduce eventually excessive amounts of numerical dissipation when the flow setup is under resolved and keeping the assumption of Eq. (14) valid.

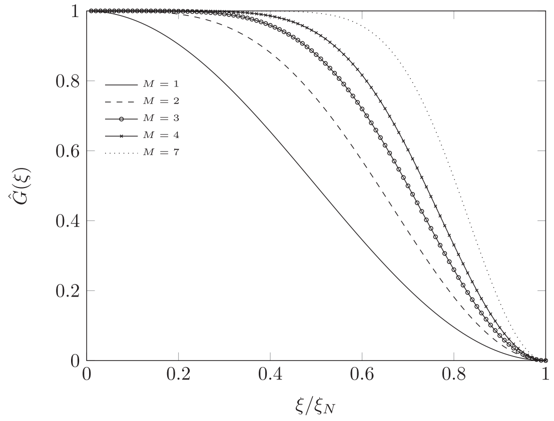

Fig. 1. Transfer functions of the filters used by Malaspinas and Sagaut [17] for ADM with $M = 1, 2, 3, 4$ and an additional high-order viscosity filter $M = 7$ from [22]. The wavenumber is normalized with the Nyquist wavenumber ξ_N.

In Fig. 1 the transfer functions for typical viscosity filters introduced by Tam et al. [22] are shown for orders up to $M = 7$. For low orders the transfer function strongly decreases for low ratios of ξ/ξ_N. It is thus questionable whether the assumption given by Eq. (14) is still valid for such filter stencils when applied to marginally resolved flow setups.

In order to decrease the sensitivity of the filters, we introduce a method which dynamically shifts a constant filter stencil towards wavenumber ratios ξ/ξ_N where the resolution is not high enough to accurately capture the correct energy transfer. Our starting point is the assumption of a variable artificial viscosity in space and time $\sigma(\boldsymbol{x}, t)$, which should be approaching zero in regions where the flow structures are resolved, i.e. , $|\widehat{f}_\alpha - f_\alpha| \ll 1$ holds and dynamically adapted in regions where this assumption is not fulfilled sufficiently. In LBM a spatially fully resolved flow consequently leads to good temporal accuracy. Spatial and temporal resolution are connected to the Mach number. A well resolved flow in the context of diffusive scaling is characterized by a low Mach number, leading to the incompressible limit of LBM in terms of the incompressible Navier–Stokes equations. In this case, the temporal and spatial resolution are connected to each other by $\Delta t \propto \Delta x^2$, see [36] among others. A reasonable measure for this connection is the strain-rate tensor

$$S_{ij} = -\Pi_{ij}\frac{\omega}{2\rho c_s^2} \ . \tag{15}$$

Π_{ij} was already defined by Eq. (3), being the second order moment of non-equilibrium distributions, which represents the stress tensor. Our approach is to measure differences from a temporal developing strain-rate representing unsteady turbulent flow structures by a simple relaxation. Temporal developing turbulent structures (e.g. decaying turbulence) require a dynamic adaption of relaxation. Using the local resolved strain-rate and relax it towards a phase averaged strain-rate is a reasonable approach. The filter

Please cite this article as: P. Nathen et al., Adaptive filtering for the simulation of turbulent flows with lattice Boltzmann methods, Computers and Fluids (2018), https://doi.org/10.1016/j.compfluid.2018.03.042

strength is computed as

$$\sigma(\boldsymbol{x},t) = (|S_{ij}(\boldsymbol{x},t) - \langle S_{ij}(\boldsymbol{x},\tilde{t})\rangle|)\left(\frac{2\Delta t^2}{|\Pi_{ij}|\left(\frac{1}{\rho c_s^2}\right)}\right)^{1/2} \tag{16}$$

where $\langle S_{ij}(\boldsymbol{x},\tilde{t})\rangle$ is the phase averaged resolved strain-rate and Δt the physical time step. The second term of Eq. (16) represents a normalization with a dissipation time scale. Different normalization techniques with different time scales were applied. Yet all of them showed equivalent results without significant difference. Our choice is based on the robustness and the local estimation without using finite differences. A similar idea was already demonstrated to be sufficiently accurate in terms of the shear-improved Smagorinsky for fully developed turbulent channel flows by Leveque et al. [37]. The classical Smagorinsky eddy-viscosity approach is decomposed into two parts. One part accounts for the non-linear energy cascade of HIT and the other part is responsible for mean shear flows associated with anisotropy. The resolved strain-rate is relaxed towards an average strain-rate and, thus, the fluctuating part of the strain-rate is significant at scales of filter size Δ_x. In flow regions, where the fluctuating part of the strain-rate is larger than the average strain-rate, the turbulent flow can be considered homogeneous and the energy transfer from large to smalls scales is adapted accordingly. Similar to our approach, Eq. (16) leads to an equivalent SGS energy budget in terms of a turbulent kinetic energy drain from resolved-scales to SGS as

$$\epsilon \propto (|S|_{ij}^3(\boldsymbol{x},t) - |S|_{ij}(\boldsymbol{x},t)\langle|S|_{ij}^2(\boldsymbol{x},\tilde{t})\rangle)\Delta_x^2, \tag{17}$$

see also Leveque et al. [37].

2.4. Spectral viscosity analysis

This section shortly describes the underlying theory of the spectral analysis used in Section 3.2. In order to evaluate and quantify the numerical viscosity which is associated to the adapted filter strength, we analyze the macroscopic equation in spectral space.

In a 2π-periodic box, which is discretized by N equally spread cells we define the Fourier transformed velocity field as

$$\tilde{\boldsymbol{u}}(\boldsymbol{\xi},t) = \begin{cases} \tilde{\boldsymbol{u}}(\boldsymbol{\xi},t), & \xi < N/2-1 \\ 0, & \text{otherwise} \end{cases} \tag{18}$$

with $\boldsymbol{\xi} = \{\xi_x, \xi_y, \xi_z\}$ being the wavenumber vector and $\xi = |\boldsymbol{\xi}| < N/2-1$ is the cut-off wavenumber. By defining the complex conjugate of the spectral velocity as $\tilde{\boldsymbol{u}}^*$, we can define the three-dimensional kinetic energy spectra with the deconvolved spectral velocity $\widehat{\tilde{\boldsymbol{u}}}$ as

$$\widehat{e}(\boldsymbol{\xi},t) = \frac{1}{2}\widehat{\tilde{\boldsymbol{u}}}\widehat{\tilde{\boldsymbol{u}}}^*. \tag{19}$$

Accordingly one can derive the spectral viscous dissipation, see [38], as

$$\widehat{\epsilon}(\boldsymbol{\xi},t) = 2\nu\boldsymbol{\xi}^2\widehat{e}(\boldsymbol{\xi},t). \tag{20}$$

Transformation of the Navier–Stokes equations into spectral space and subsequent multiplication with the complex transformation leads to the spectral energy transport equation

$$\frac{\partial\widehat{e}(\boldsymbol{\xi},t)}{\partial t} = \widehat{T}(\boldsymbol{\xi},t) - \widehat{\epsilon}(\boldsymbol{\xi},t), \tag{21}$$

with $\widehat{T}(\boldsymbol{\xi},t)$ being the non-linear transfer term defined by

$$\widehat{T}(\boldsymbol{\xi},t) = \widehat{\tilde{\boldsymbol{u}}}^*(\boldsymbol{\xi},t)\cdot\boldsymbol{P}(\boldsymbol{\xi},t) : \sum_{\xi'}\widehat{\tilde{\boldsymbol{u}}}(\boldsymbol{\xi}',t)\widehat{\tilde{\boldsymbol{u}}}(\boldsymbol{\xi}-\boldsymbol{\xi}',t) \tag{22}$$

and the 3*rd*-rank tensor $\boldsymbol{P}(\boldsymbol{\xi}, t)$ is given as

$$\boldsymbol{P}(\boldsymbol{\xi},t) = \boldsymbol{\xi}\boldsymbol{\delta} - \boldsymbol{\xi}\boldsymbol{\xi}\boldsymbol{\xi}|\boldsymbol{\xi}|^{-2}. \tag{23}$$

We now follow the approach of Domaradzki et al. [26], Schranner et al. [24] and Hickel et al. [25], who described the assessment of the numerical dissipation associated to a spectral numerical viscosity. For an arbitrary discretization scheme of the Navier–Stokes equations, for instance the LBM scheme, Eqs. (19)–(21) can be evaluated exactly. The computation of the energy decay in Eq. (21) is associated to the numerical discretization error. Thus, calculation of the macroscopic moments by LBM, mapping them in spectral space and calculating the energy decay leads to an accurate prediction of the numerical dissipation. Following [26], the derivative on the l.h.s. of Eq. (21) can be approximated by

$$\frac{\partial\widehat{e}(\boldsymbol{\xi},t)}{\partial t} \approx \frac{\widehat{e}(\boldsymbol{\xi},t) - \widehat{e}(\boldsymbol{\xi},t-\Delta t)}{\Delta t}, \tag{24}$$

leading to numerical dissipation spectra with Eq. (21)

$$\begin{aligned} -2\nu_{num}\boldsymbol{\xi}^2\widehat{e}(\boldsymbol{\xi},t) &= -\widehat{\epsilon}_{num}(\boldsymbol{\xi},t) \\ &= \frac{\widehat{e}(\boldsymbol{\xi},t) - \widehat{e}(\boldsymbol{\xi},t-\Delta t)}{\Delta t} - \widehat{T}(\boldsymbol{\xi},t) \\ &\quad + 2\nu\boldsymbol{\xi}^2\widehat{e}(\boldsymbol{\xi},t), \end{aligned} \tag{25}$$

where ν_{num} is the numerical viscosity. Assuming that the numerical dissipation inherent to the BGK Boltzmann scheme is very low, see also [1–3], the obtained numerical viscosity will originate from the adaptive ADM step only. The numerical implementation is based on the algorithm proposed in [25]. Since the calculation of the energy decay in Eq. (24) is a first-order finite difference approximation at time $t_{n-1/2}$ the energy spectra and transfer spectra are approximated accordingly as

$$\widehat{e}(\boldsymbol{\xi},t_{n-1/2}) \approx \frac{\widehat{e}(\boldsymbol{\xi},t) + \widehat{e}(\boldsymbol{\xi},t-\Delta t)}{2}, \tag{26}$$

and

$$\widehat{T}(\boldsymbol{\xi},t_{n-1/2}) \approx \frac{\widehat{T}(\boldsymbol{\xi},t) + \widehat{T}(\boldsymbol{\xi},t-\Delta t)}{2}. \tag{27}$$

Inserting the interpolated values at times $t_{n-1/2}$ into Eq. (25) we finally obtain

$$\nu_{num}(\boldsymbol{\xi},t) = \frac{1}{2\boldsymbol{\xi}^2\widehat{e}(\boldsymbol{\xi},t_{t_{n-1/2}})}\left(\widehat{T}(\boldsymbol{\xi},t_{t_{n-1/2}}) - \frac{\partial\widehat{e}(\boldsymbol{\xi},t)}{\partial t}\bigg|_{t_{n-1/2}}\right) - \nu \tag{28}$$

Eq. (28) will be evaluated for HIT in Section 3.1.

3. Numerical validation

3.1. Taylor–Green vortex

The extended filter approach is tested for HIT represented by the three-dimensional Taylor–Green vortex benchmark according to [39]. The Reynolds number is set to $Re = 800$, $Re = 1600$ and $Re = 3000$ at varying resolutions. The 2π-periodic box is discretized equidistantly by $N = 32$, $N = 64$, $N = 128$ and $N = 256$ in each direction to account for under- and well-resolved flow setups. A second- ($M = 2$) and third-order ($M = 3$) stencil is used for Eq. (13) in this investigation. In this section, the integral dissipation rate $\epsilon = \nu\overline{\frac{\partial u_i'}{\partial x_k}\frac{\partial u_i'}{\partial x_k}}$ is assessed by means of the effective, the molecular and the numerical dissipation. Diffusive scaling is employed, leading to the flow setups depicted in Table 2.

Phase averaging of $\langle S_{ij}(\boldsymbol{x},\tilde{t})\rangle$ is done in such way that it automatically adapts to the investigated turbulent flow structures. By doing so we achieve the correct energy drain from the inertial range to the SGS range by means of $\sigma(\boldsymbol{x}, t)$. For decaying turbulence, the turbulent flow structures differ over time and space. A proper approach is to adapt the averaging phase to the eddy-turnover time. This time scale describes the dynamic behavior of

Please cite this article as: P. Nathen et al., Adaptive filtering for the simulation of turbulent flows with lattice Boltzmann methods, Computers and Fluids (2018), https://doi.org/10.1016/j.compfluid.2018.03.042

Table 2
Numerical setup for the Taylor–Green vortex at different resolutions *N*.

N	u_L	Ma	Δx	Δt
32	0.2	0.346	0.196	0.03926
64	0.1	0.1730	0.0981	0.00981
128	0.05	0.0865	0.0490	0.00245
256	0.025	0.0432	0.0245	0.000612

turbulent scales in time and depends on the characteristic turbulence length scale l and the dissipation rate ϵ. From dimensional analysis it can be derived that

$$\tilde{t}_{eddy} \propto \left(\frac{l^2}{\epsilon}\right)^{\frac{1}{3}}, \tag{29}$$

where ϵ is the turbulent kinetic energy dissipation expressed in spectral space by Eq. (20), which is evaluated in real space by

$$\epsilon(t) = \frac{2\nu}{V}\int_V \left(\frac{\partial u_i'}{\partial x_j}\frac{\partial u_i'}{\partial x_j}\right) dV, \tag{30}$$

using 8th order finite differences, see [38]. Here, u_i' is the ith component of the velocity fluctuation. The period over which the strain-rate in Eq. (16) is averaged, is evaluated as

$$\Delta\tilde{t}_{eddy}(t^n) \propto \left(\frac{l^2(t^n)}{\epsilon(t^n)}\right)^{\frac{1}{3}}, \tag{31}$$

where t^n is the discrete time step. After time $t^n + \Delta\tilde{t}_{eddy}(t^n)$ the period is evaluated new and the initial value for averaging is approximated as $\frac{\epsilon(t^n)+\epsilon(t^n-\Delta\tilde{t}_{eddy}(t^n))}{2}$. This is valid for low time steps and later time instances, since the dissipation is increasing and $\Delta\tilde{t}_{eddy}$ is decreasing. The length scale l at an instance of time t^n is calculated as

$$l(t^n) = \frac{\sum_0^{N/2-1}\boldsymbol{\xi}^{-1}\hat{e}(\boldsymbol{\xi},t^n)d\boldsymbol{\xi}}{\sum_0^{N/2-1}\hat{e}(\boldsymbol{\xi},t^n)d\boldsymbol{\xi}}, \tag{32}$$

see also [38,40–42].

For $Re = 800$ and $N > 32$ the results are only in fair agreement with the reference data of Brachtet et al. [39], see Fig. 2. For $N = 64$ the transition to turbulence was predicted too early by both the 2nd and 3rd order filter stencil. The development of the molecular dissipation rate is predicted too flat for both cases, which is probably caused by the low resolution applied. The numerical dissipation increases during the initial transition phase at $t \approx 4$ s and remains on a nearly constant plateau until it increases again at $t \approx 8$ s, where also the maximum effective dissipation rate is achieved. The numerical dissipation shows a peak of maximum dissipation rate which corresponds to the reference DNS data. For increasing resolution $N = 128$ and 256 the run of the molecular dissipation rate is in acceptable agreement with the reference data. For $N = 128$ the total amount of dissipation is a bit smaller compared with $N = 256$, leading with the under-predicted molecular dissipation to a slight discrepancy between reference data and numerical results. Again, the overall agreement with the second order stencil is less accurate compared to the third order stencil. For $N = 256$ the results of the effective dissipation rate are in very good agreement with DNS data for both stencil sizes. The influence of the filter seems to be negligible, which corresponds to a well resolved setup.

Similar results are found for $Re = 1600$, see Fig. 3. For $N = 32$ the under resolved simulation leads to an unphysical amount of numerical dissipation, probably caused by the high Mach number, see Table 2. High Mach numbers correlate to a high non-equilibrium part of the velocity distribution function, which vice versa leads to high predicted strain-rates, see Eq. (15), and finally to high dissipation rates. Comparing the results for $Re = 1600$ to those of $Re = 800$ one can see, that for $N = 64$ the early state transition is predicted too early again. The discrepancy between the second and third order stencil indicates a first dependency between applied resolution and Reynolds number in order to achieve reliable results. For $Re = 800$ and $N = 64$ this discrepancy in the dissipation rate was smaller, while for $Re = 1600$ and $N = 128$ the differences are of comparable magnitude. Only for $Re = 1600$ and $N = 256$ a good accordance between second and third order stencil can be found. This indicates, that the lower the resolution is the higher the discrepancy between the 2nd and 3rd stencils are. The third order stencil shows a general better agreement with the reference data for all resolutions applied.

The discrepancy found between the two different stencils is also evident for $Re = 3000$, see Fig. 4. Although all simulations converged and remained stable, the correct initial transitional phase is only captured by the simulations with $N = 128$ and $N = 256$, yet only the simulation with $N = 256$ predict the correct temporal evolution of the maximum of the dissipation rate. For $Re = 3000$ all simulations show a non-negligible difference between the stencils, which varies from $\approx 52\%$ to $\approx 23\%$ for the peak value of the dissipation rate for $N = 64$ to $N = 256$ respectively. Throughout, it is visible that for increasing Reynolds numbers at same resolution the numerical dissipation increases, yet the different filter stencils lead to varying ranges. With respect to the results obtained for the lower Reynolds numbers, the adaption of the filter strength for the simulation of turbulent flows can lead to a very good agreement with the reference data. This holds for both filter stencils as long as a certain ratio of $\frac{\Delta x}{\eta}$ is not exceeded, where η describes the Kolmogorov length scale which successively decreases with increasing Reynolds number.

In Fig. 5, the temporal evolution of the volume averaged filter strength $\sigma^V(t)$ is depicted for all simulations of HIT. Clearly visible, $\sigma^V(t)$ is varying for different resolutions at fixed Reynolds numbers over two orders of magnitude. For constant resolutions and Reynolds numbers the values for σ^V still vary e.g. for $Re = 1600$ and $N = 64$ from $\sigma^V_{min}(t) = 0.000945367$ to $\sigma^V_{max}(t) = 0.0132248$ for the third order stencil. While for $N = 32$, the averaged $\sigma^V(t)$ is of order of magnitude of 10^{-1}, we find $\sigma^V(t)$ decreasing on average to 10^{-4} for $N = 256$. The strongly varying range for the artificial viscosity $\sigma^V(t)$ underlines the findings of Fauconnier et al. [23], who demonstrated that the filter strength has to be adapted carefully depending on resolution and Reynolds number applied for HIT. Similar results were found by Malaspinas and Sagaut [17] for the computation of a turbulent shear layer. In their work, a careful adaption of a constant σ leads to more reasonable results for same filter stencil orders. Setting the artificial viscosity too high yields to spatially wrong predicted shear-layer thicknesses. Beyond that, the differences between the magnitude of the filter strengths for the third and second order stencils decreases by increasing the resolution, as one can see in more detail on the right side of Fig. 5. Conversely, for high Reynolds numbers and marginally resolved setups like $Re = 1600$ with $N = 128$ and $Re = 3000$ with $N = 256$, the differences between different filter stencils is originating from the filter itself. It is assumed that filter independency for a given Reynolds number can be reached only by keeping the resolution over a certain threshold in order to obtain reliable results.

In order to illustrate the difference to a constant filter strength, Fig. 6 shows the temporal development of the molecular, effective and numerical dissipation rates obtained for the Taylor–Green vortex at $Re = 3000$ and constant σ values ranging from $\sigma = 0.001$ to $\sigma = 0.005$. The resolution is varied from $N = 128$ to $N = 256$ and diffusive scaling is made according to Table 2. For $N = 128$ during the initial phase up to $t \approx 6$ s the flow field remains stable and

Please cite this article as: P. Nathen et al., Adaptive filtering for the simulation of turbulent flows with lattice Boltzmann methods, Computers and Fluids (2018), https://doi.org/10.1016/j.compfluid.2018.03.042

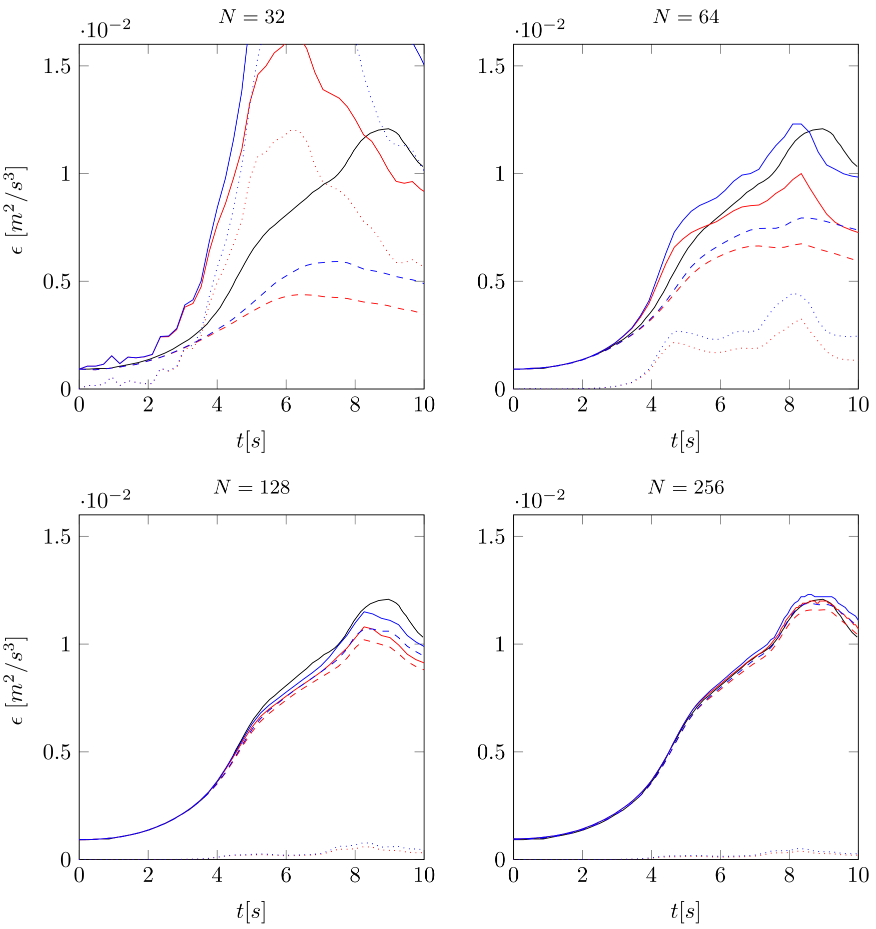

Fig. 2. Temporal evolution of the dissipation rate of the Taylor–Green vortex at $Re = 800$ predicted by the selective ADM-BGK scheme at varying resolutions. Red: $\mathcal{O}(2)$ —. Blue: $\mathcal{O}(3)$ —. The solid line corresponds to the effective dissipation rate, the dashed one to the molecular part and the dotted one to the numerical dissipation respectively. The solid black line represents the reference DNS data of Brachet et al. [39]. (For interpretation of the references to colour in this figure legend, the reader is referred to the web version of this article.)

the dissipation rate follows the DNS reference in good quality. After $t \approx 6$s and for $\sigma = 0.001$ the dissipation rate increases exponentially caused by unstable simulation setup. Increasing the filter strength to $\sigma = 0.005$ leads to a stable flow field until $t \approx 9.2$ s until the flow field diverged again. Comparing these results with the dissipation rates obtained by adaptive filtering and $N = 128$, see Fig. 4, it is visible see that the numerical dissipation predicted by the novel ADM approach is higher which leads to better stability properties. Increasing the resolution to $N = 256$, all setups remained stable and show qualitatively good agreement with the reference DNS. The maximum value of the molecular dissipation rate peak is predicted very good in time, yet only for $\sigma = 0.005$ and a filter stencil of order $\mathcal{O}(2)$, a higher discrepancy from the reference solution is found. In general it is visible that the results differ over a broad range for $N = 128$, which underlines the non straight-forwards application of a constant σ for viscosity filter based ADM approaches in the BGK-LBM framework. This discrepancy is smaller by increasing the resolution, which was found in a similar way for the adaptive ADM approach. Additionally, the temporal position as well as the maximum value of the effective dissipation is predicted in better accordance with the reference solution compared to the solutions with constant filter values. The findings for constant filter strengths are in accordance with the results of the adaptive ADM approach as long as the resolution and σ values are high enough to suppress divergence of the flow field. For higher values of σ the increased numerical dissipation leads to lower predicted molecular dissipation rates and the higher filter stencil leads to better agreement with the reference data. The adaptive ADM approach showed stable results for $Re = 3000$ and $N = 128$, leading to a good representation of the reference DNS results, see Fig. 4. Beyond that, the adaptive approach allowed for a stable simulation without adapting σ iteratively in order to keep the simulation stable. For $N = 256$ it is visible, that the molecular part of the dissipation rate is slightly better predicted by the adaptive ADM approach, see also Fig. 4, which is most probably caused by the lower input of dissipation during the initial transition phase up to $t = 4$s. This leads to a higher resolved energy budget in later stages of the flow and, thus, to a better predicted flow field compared to the reference DNS of Brachet et al. [39].

3.2. Analysis of the spectral viscosity for the LBM

In order to investigate the dissipative properties of the scheme proposed in Section 2.3 in more detail, we use the spectral analysis introduced in Section 2.4. The underlying algorithm allows for a detailed analysis of numerical viscosities in spectral space. This methodology is applied in Domaradzki et al. [26], Schranner et al.

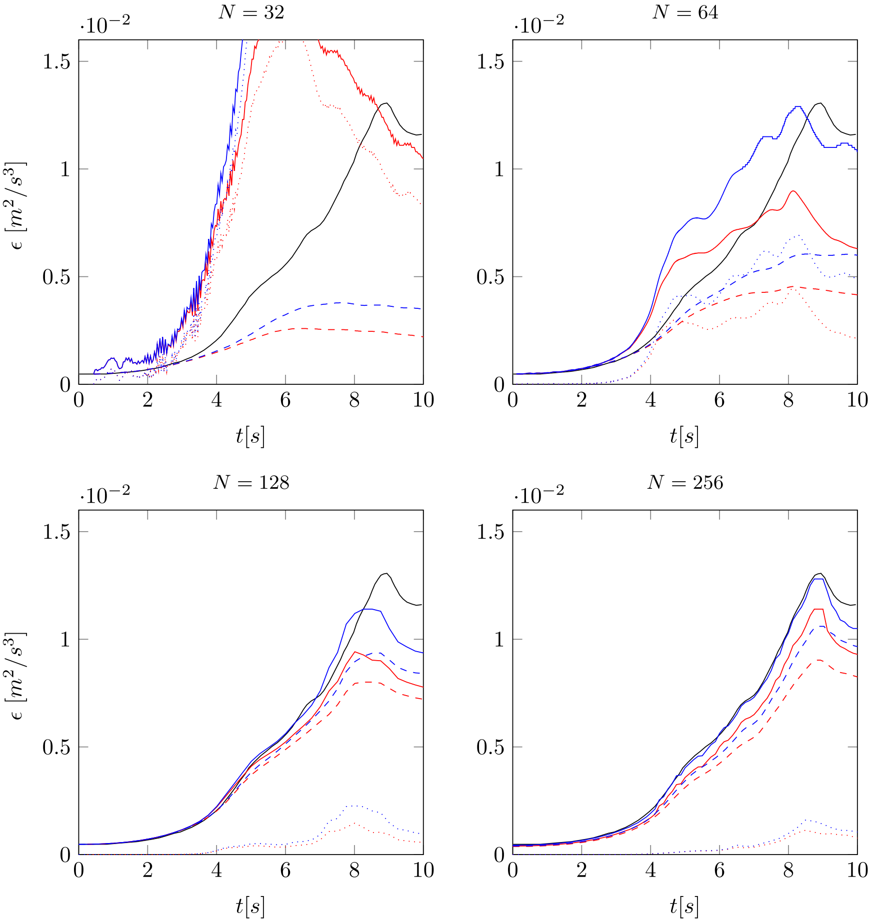

Fig. 3. Temporal evolution of the dissipation rate of the Taylor–Green vortex at $Re = 1600$ predicted by the selective ADM-BGK scheme at varying resolutions. Red: $\mathcal{O}(2)$ —. Blue: $\mathcal{O}(3)$ —. The solid line corresponds to the effective dissipation rate, the dashed one to the molecular part and the dotted one to the numerical dissipation respectively. (For interpretation of the references to colour in this figure legend, the reader is referred to the web version of this article.)

[24] and Hickel et al. [25] to investigate the numerical viscosity of different finite volume schemes. Since our approach is based on an explicit filtering step and dependent on the actual Reynolds number and resolution applied, we assume varying results for different test cases. Thus, the comparability of the results is limited to those obtained by the BGK based ADM model. Since the BGK based LBM model can be interpreted as a finite difference scheme with second order spatial accuracy, we compare our results to those of pure finite difference schemes, see [25]. As a reference for HIT we take the Eddy-Damped Quasi Normal Markovian (EDQNM) analysis [42] into account, which describes the evolution of SGS viscosity for turbulence with a Kolmogorov range $\widehat{e}(\xi) = C_k \widehat{\epsilon}^{3/2} \xi^{-5/3}$. Results from Chollet [43] to Chollet and Lesieur [44] show that the expression

$$\nu^+_{Chollet}(\xi/\xi_c) = 0.441 C_k^{-3/2}(1 + 34.467 e^{-3.03\xi_c/\xi}) \tag{33}$$

is a proper fit to the exact solution. Since the artificial diffusivity is adapted dynamically, the numerical dissipation and the numerical viscosity of the scheme are time dependent. The results presented below show time averaged results after the start of the initial transition phase ($t > 4$s) until $t = 10$ s by evaluating Eq. (28) every $\Delta t = 0.025$ s. All simulations have been repeated ten times in order to cope with a statistically correlated Taylor–Green vortex. For the analysis presented here, we only considered the lowest and highest Reynolds number, i.e. $Re = 800$ and $Re = 3000$, respectively.

Fig. 7 shows the numerical results obtained from the spectral analysis of the numerical viscosity. The numerical viscosity is normalized equivalent to [25] as $\nu^+_{num} = \nu_{num}\sqrt{\frac{\xi_c}{\widehat{e}_c}}$ with ξ_c being the cut-off wavenumber and $\widehat{e}_c$ the energy of the cut-off wavenumber. The results are consistent with the findings for the dissipation rate in Section 3.1, see Figs. 2 and 4. For $Re = 800$ and $N > 64$ the obtained dissipation rates are in good agreement with the reference DNS for both filter stencils, see Fig. 2. In a similar way the numerical viscosity is only slightly varying for the second and third order stencil. By increasing the Reynolds number to $Re = 3000$ for a fixed resolution, the discrepancy between the different filter stencils is visible for the numerical viscosity. The third order stencil exhibits a higher numerical viscosity between $0.4 < \xi/\xi_c < 1$, leading to a higher numerical dissipation, see also Section 3.1. For $N = 256$ this discrepancy is decreased and numerical dissipation is created for $\xi/\xi_c > 0.6$.

3.3. Turbulent channel flow

In this section the BGK based ADM approach with selective viscosity estimation is employed for the simulation of the turbulent channel flow at three different friction Reynolds numbers

Please cite this article as: P. Nathen et al., Adaptive filtering for the simulation of turbulent flows with lattice Boltzmann methods, Computers and Fluids (2018), https://doi.org/10.1016/j.compfluid.2018.03.042

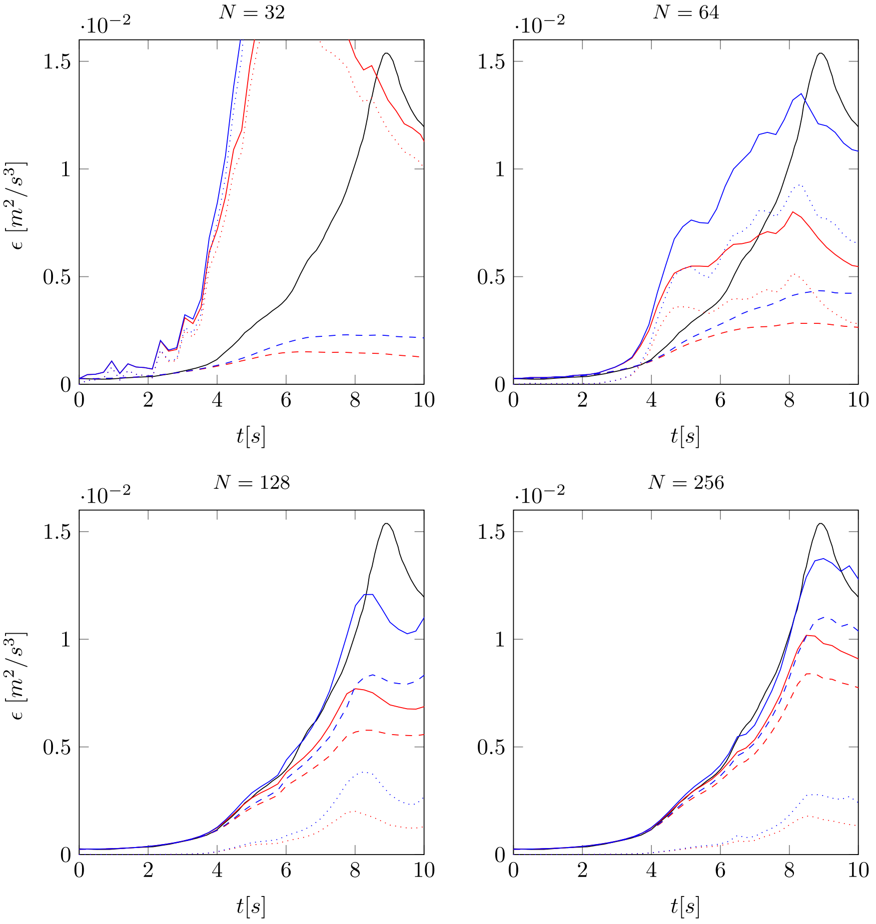

Fig. 4. Temporal evolution of the dissipation rate of the Taylor–Green vortex at $Re = 3000$ predicted by the selective ADM-BGK scheme at varying resolutions. Red: $\mathcal{O}(2)$ — Blue: $\mathcal{O}(3)$ —. The solid line corresponds to the effective dissipation rate, the dashed one to the molecular part and the dotted one to the numerical dissipation respectively. (For interpretation of the references to colour in this figure legend, the reader is referred to the web version of this article.)

($Re_\tau = 180$, $Re_\tau = 395$ and $Re_\tau = 590$) and varying resolutions. Results shall outline if similar findings as for the HIT test case are observed for wall-bounded turbulence. The results in this section aim not to demonstrate a detailed mesh convergence analysis for the model, but rather aim at elucidating the applicability of the model in vicinity of a wall. Based on the findings in the previous section we only consider the third order stencil, since the compromise between adaption of σ and numerical dissipation are assumed to be less sensitive compared to the second order stencil.

Our numerical test case is based on the work of Malaspinas and Sagaut [45], Lammers et al. [46] and Premnatha et al. [47] who obtained detailed statistics for the turbulent channel flow by applying the BGK and Mulit-Relaxation-Time (MRT) scheme with and without Smagorinsky SGS turbulence model. The domain has the extensions of $L_x = 2\pi H$, $L_z = 2\pi H$ and $L_y = 2H$ in streamwise, lateral and wall-normal direction respectively, with H being the channel half width. In streamwise and lateral direction periodic boundary conditions were applied. In order to represent the upper and lower channel wall, a full-way bounce back scheme representing solid no-slip walls is applied for $Re_\tau = 395$ and $Re_\tau = 590$. Thus, the wall nodes are fixed on the wall leading to a constant cell size and wall distance $\Delta x = \Delta y = \Delta z$. For $Re_\tau = 180$ we employ a half-way bounce back scheme in order to evaluate the accuracy of a well resolved boundary layer and to investigate the sensitivity of a symmetric stencil in vicinity of the wall. Applying a full-way bounce back to $Re_\tau = 180$ leads to undistinguishable results which is caused by the small values of $\sigma(\boldsymbol{x}, t)$, see also later discussion in this section.

Resolution is varied in a similar way as for the Taylor–Green vortex, leading to resolved and under resolved test cases. Adjusting the friction Reynolds number is achieved by applying diffusive scaling. The viscosity is changed according to the Reynolds number and the lattice velocity according to the resolution. To estimate the viscosity we use the Dean correlation, see [45]

$$Re_B = \left(\frac{8}{0.073}\right)^{4/7} Re_\tau^{8/7}\ , \tag{34}$$

which connects the bulk Reynolds number Re_B to the friction Reynolds number Re_τ. With $Re_B = \frac{u_B L_z}{\nu}$, we can rewrite Eq. (34) as

$$\nu = \frac{u_B L_z}{\left(\frac{8}{0.073}\right)^{4/7} Re_\tau^{8/7}}\ . \tag{35}$$

Based on the work of Bespalko [48] we set $u_B = 0.111\,\frac{m}{s}$. To account for the limited validity of the Dean correlation at low Reynolds numbers, the viscosity for $Re_\tau = 180$ is obtained by a virtual log law which spans from the wall to the channel half height as de-

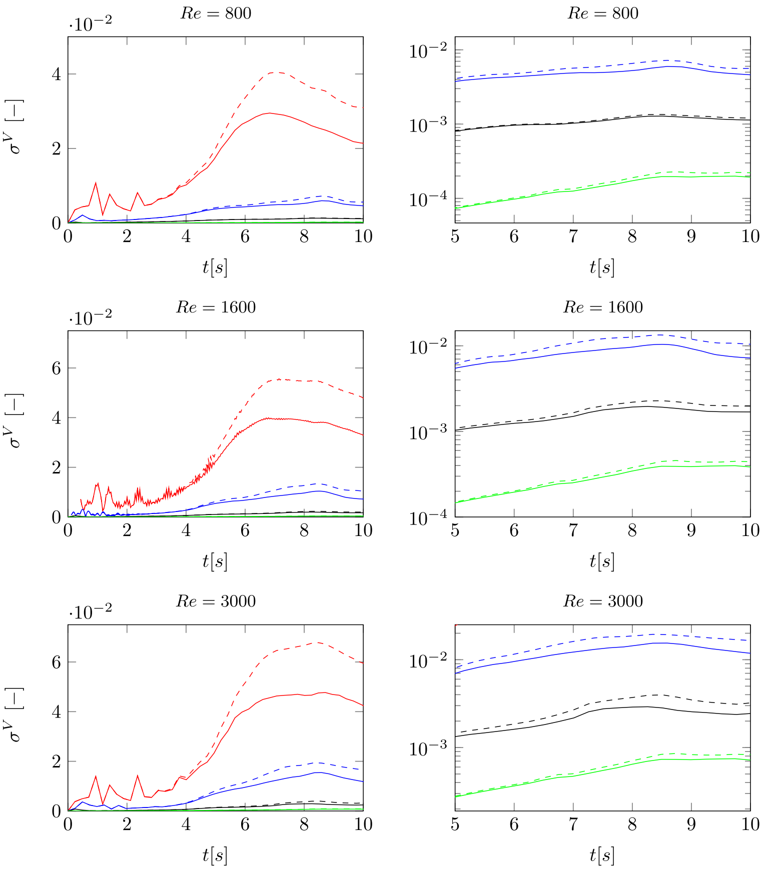

Fig. 5. Temporal evolution of the adaptive filter strength $\sigma(t)$ for $Re = 800$, $Re = 1600$ and $Re = 3000$ at different resolutions for the Taylor–Green vortex. The solid line corresponds to the second order stencil while the dashed line represents the third order stencil. $N = 32^3$ 🟥; $N = 64^3$ 🟦; $N = 128^3$ ⬛; $N = 256^3$ 🟩. Left: General overview; Right: Zoom in.

Table 3
Performed simulations for the turbulent channel flow.

N	Δy^+	$Re_{\tau,\ target}$	u_L	Ma
31	≈2.9	180	0.111	0.1902
71	≈1.26	180	0.0484	0.0830
91	≈0.98	180	0.0378	0.0654
31	≈12.74	395	0.111	0.1902
71	≈5.56	395	0.0484	0.0830
91	≈4.34	395	0.0378	0.0654
31	≈19.03	590	0.111	0.1902
71	≈8.30	590	0.0484	0.0830
91	≈6.48	590	0.0378	0.0654

scribed in [48]

$$\nu = \frac{u_B L_z}{2Re_\tau\left(\frac{1}{\kappa}ln(Re_\tau)+A\right)}\ . \tag{36}$$

A full list of conducted simulations with the final physical state, lattice velocities u_L, resolution N and Mach number is given in Table 3.

Δy^+ is used to measure the non-dimensional distance between two adjacent cells in the bulk flow.

The target mass flow is imposed by applying adaptive forcing according to the work of Cabrit [49]. The volume force is computed as

$$f = \frac{u_\tau^2}{N} + (u_B - \langle u_x\rangle)\frac{u_B}{L_z/2}, \tag{37}$$

where u_B is the bulk velocity, $< u_x >$ the instantaneous space average of the streamwise velocity component and f the resulting volume force. The force is included into the LBM schemes by employing the approach of He et al. [50] for the BGK.

A proper initialization of the velocity field and triggering of turbulence is needed in order to reach the desired turbulent state. Employing a 1/7 power law, i.e. $u(z) = u_{char}(z/H)^{\frac{1}{7}}$, with superimposed statistically random velocity fluctuations drawn from a normal distribution $\frac{1}{\psi\sqrt{2\pi}}e^{-\frac{r-\mu}{2\sigma^2}}$ lead to very long transition times. Setting the standard deviation ψ to an initial value of 5% lead only for $Re_\tau = 395$ and $Re_\tau = 590$ to a proper transition of the initial flow state. Thus, for $Re_\tau = 180$ we applied the forcing approach of Wang et al. [51], who used a phase shifted divergence-free forcing field during the initial period of time.

For all Reynolds numbers statistics are obtained in the same way to guarantee a consistent comparison. Averaging is performed spatially over horizontal planes in the homogeneous directions and temporally after the flow is uncorrelated. Following Moser et al. [52], the flow is weakly correlated (≈ 0.08) at a streamwise distance of 2 m. This leads to a sampling time of $\Delta t = 18.01$ s with $u_B = 0.111\,\frac{m}{s}$. For $Re_\tau = 180$ we start averaging after $t > 150$ s a time period of $\Delta T = 5205$ s, i.e. 92 flow through times in total. The

Please cite this article as: P. Nathen et al., Adaptive filtering for the simulation of turbulent flows with lattice Boltzmann methods, Computers and Fluids (2018), https://doi.org/10.1016/j.compfluid.2018.03.042

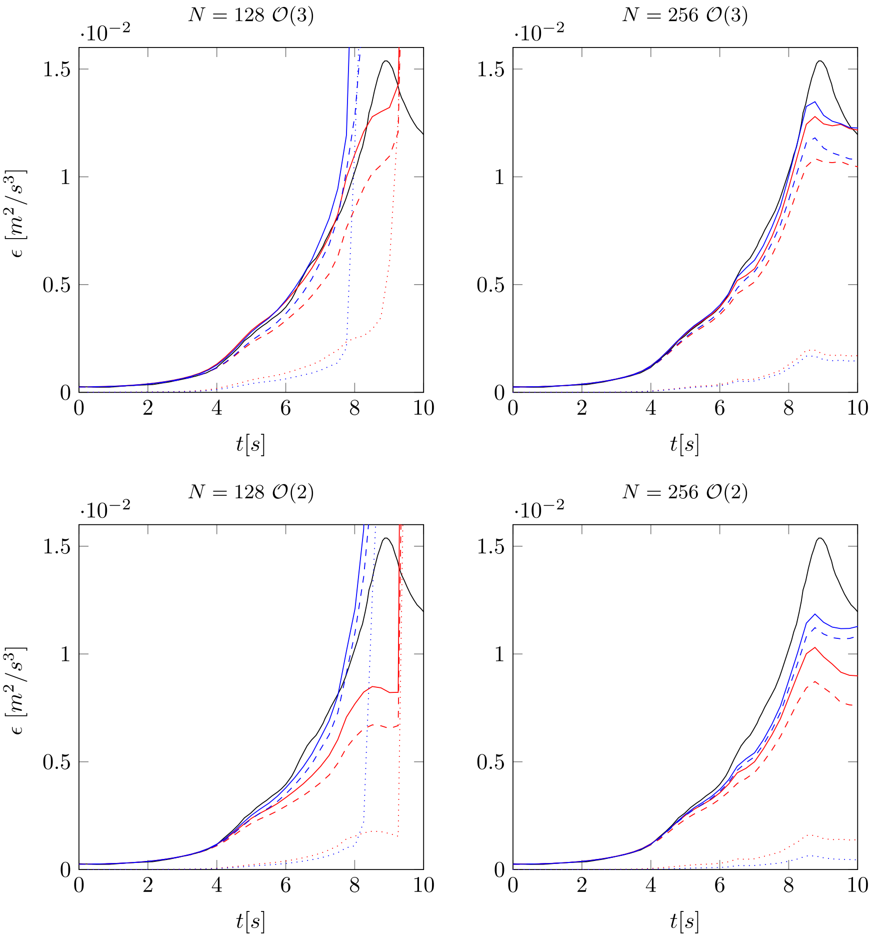
$N = 128\ \mathcal{O}(3)$ $N = 256\ \mathcal{O}(3)$ $N = 128\ \mathcal{O}(2)$ $N = 256\ \mathcal{O}(2)$

Fig. 6. Temporal evolution of the dissipation rates of the Taylor–Green vortex at $Re = 3000$ predicted by the ADM-BGK scheme. $\sigma = 0.001$ is represented by the blue lines —; $\sigma = 0.005$ is represented by the red lines— compared to DNS —. The solid line corresponds to the effective dissipation rate, the dashed one to the molecular part and the dotted one to the numerical dissipation respectively. (For interpretation of the references to colour in this figure legend, the reader is referred to the web version of this article.)

flow-through time is the time a particle needs to pass the geometry in mean-flow direction. In order to obtain converged statistics for the higher Reynolds numbers, the averaging times are adjusted accordingly. A reasonable assumption for higher Re_τ is a decreased correlation, nevertheless we keep the sampling time constant and increase the flow through times according to the increase of the turbulent time scale. The ratio between the large- and small-time turbulence scale can be written as $\frac{t_L}{t_\eta} = \sqrt{\frac{u_\tau H}{\nu}}$, see Pope [38]. Thus, the flow through times increase to 136 and 166 for $Re_\tau = 395$ and $Re_\tau = 590$ respectively.

For the turbulent channel flow the adaption of the artificial viscosity σ is done without phase averaging, since in quasi steady flows phase averaging reduces to local time averaging as soon as a quasi steady flow state is achieved. Since the turbulent channel flow refers to ergodic systems, spatial and local temporal averaging lead to the same statistics in homogeneous directions. Additionally, any temporal growth of unphysical moments is assumed to be suppressed, since non-physical strain are only appear locally and propagate in all spatial directions.

In order to adapt the filter strength for the turbulent channel flow accordingly, the averaging procedure starts after the flow field converged to a quasi steady state. Since we have varying resolutions, we track converged flow fields for all simulations in the same way. An autocorrelation function defined by

$$\zeta = \frac{\langle u_x(\boldsymbol{x}, t) u_x(\boldsymbol{x}, t+\tau)\rangle}{\langle u_x(\boldsymbol{x}, t) u_x(\boldsymbol{x}, t)\rangle} \tag{38}$$

is used in order to investigate the convergence of the flow.

Fig. 8depicts the mean velocity field for $Re_\tau = 180$ for resolutions $N = 31$, $N = 71$ and $N = 91$. The velocity field is normalized as $u^+ = \frac{u_{mean}}{u_\tau}$, with $u_\tau = \sqrt{\frac{\tau_W}{\rho}}$ and τ_W being the wall-shear stress. The wall normal distance is defined by $y^+ = \frac{u_\tau y}{\nu}$. Although the general quality of the results is in fair agreement with the reference DNS of Kim et al. [53], for all resolutions an over-estimation of the velocity field of approx. 3.6% was found, although for $N = 71$ and $N = 91$ the first cells are placed in the viscous sub-layer, see also Table 3. In order to verify how well the flow is resolved, energy spectra in wall normal direction are shown in Fig. 9. For higher wavenumbers and $N = 31$ the flow appears to be slightly under-resolved, which is presumably caused by the lower resolution. For $N = 71$ and $N = 91$ the spectra show marginal differences and, thus, the flow field can be assumed to be equivalently well resolved. Since the macroscopic velocity field is slightly over-predicted by approx. 3.6% , the applied forcing approach may have an influence on the results. Malaspinas and Sagaut [45] applied the

Please cite this article as: P. Nathen et al., Adaptive filtering for the simulation of turbulent flows with lattice Boltzmann methods, Computers and Fluids (2018), https://doi.org/10.1016/j.compfluid.2018.03.042

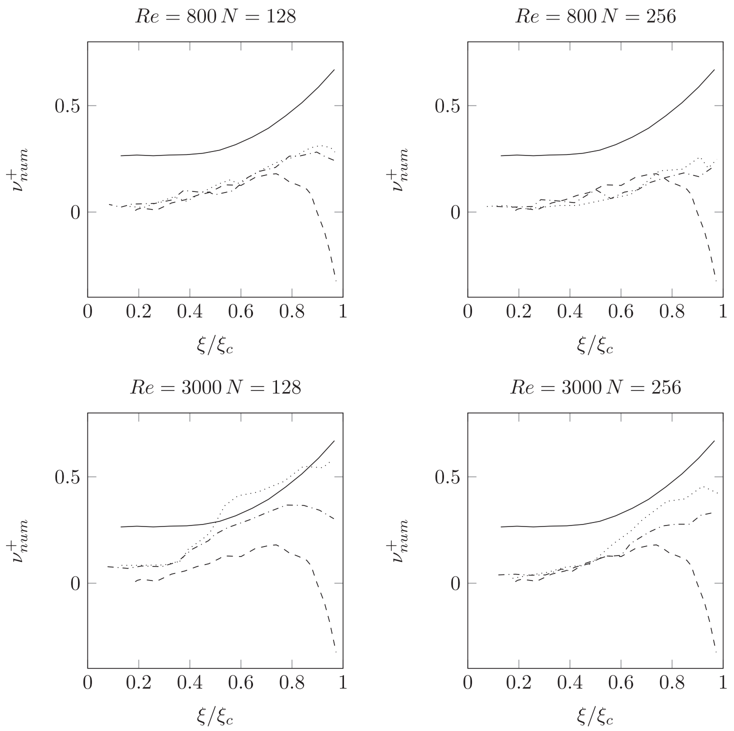

Fig. 7. Spectral distribution of the numerical viscosity for the Taylor–Green vortex for varying Reynolds numbers and resolutions. EDQNM theory ━━; 2nd order fintite differences ━━; 2nd order ADM stencil ......; 3rd order ADM stencil –·–·–

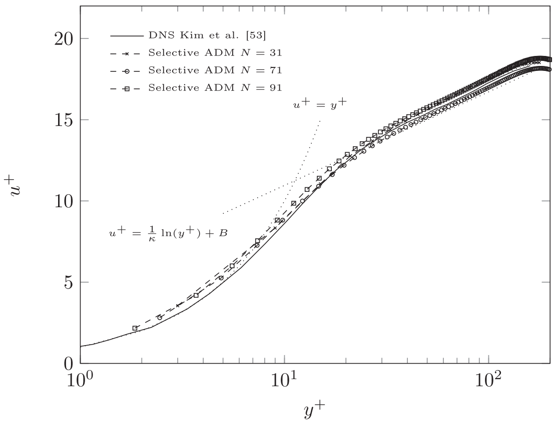

Fig. 8. Mean velocity profiles of turbulent channel flow at $Re_\tau = 180$ predicted by the selective filtered ADM-LES model.

forcing approach of Cabrit [49] only for very high Reynolds numbers $Re_\tau > 590$ and found great accordance of the bulk flow features with reference data. Future work may have to be done in order to evaluate the applicability of our forcing approach to lower Reynolds numbers.

The Reynolds stresses $\overline{u'u'}$ and $\overline{u'v'}$ are shown in Fig. 10. While the local position of the mean $\overline{u'u'}$ stresses is predicted accurately by all three resolutions, for $N = 91$ a slight over-prediction of the peak value is found. This discrepancy is found to be apparent over the whole channel width. For $N = 31$ and $N = 71$ the overall agreement with the reference DNS data is acceptable, although an under-prediction of the peak stress value is found. For the $\overline{u'v'}$ stresses all three resolutions show fair agreement with the reference data of Kim et al. [53]

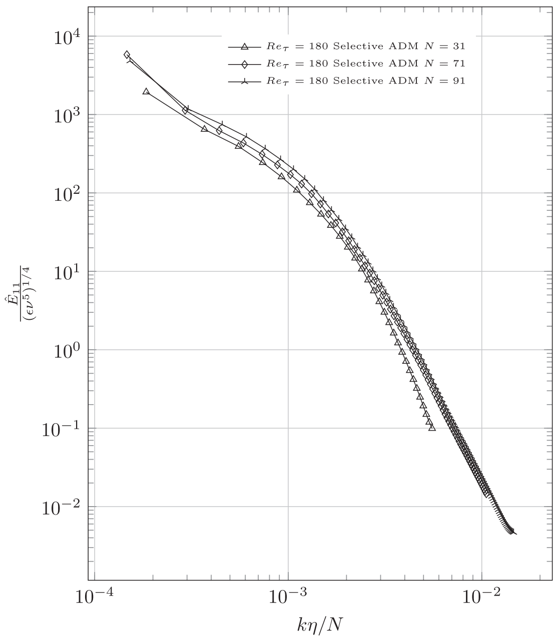

Fig. 9. Normalized wall-normal energy spectra of the velocity field for $Re_\tau = 180$ and varying resolutions.

Please cite this article as: P. Nathen et al., Adaptive filtering for the simulation of turbulent flows with lattice Boltzmann methods, Computers and Fluids (2018), https://doi.org/10.1016/j.compfluid.2018.03.042

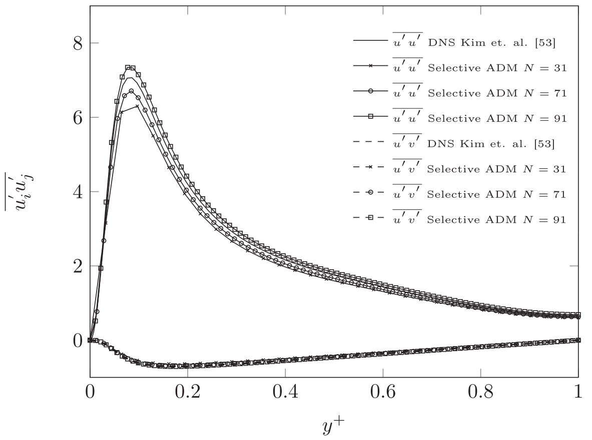

Fig. 10. Mean Reynolds stress profiles of turbulent channel flow at $Re_\tau = 180$ predicted by the selective filtered ADM-LES model.

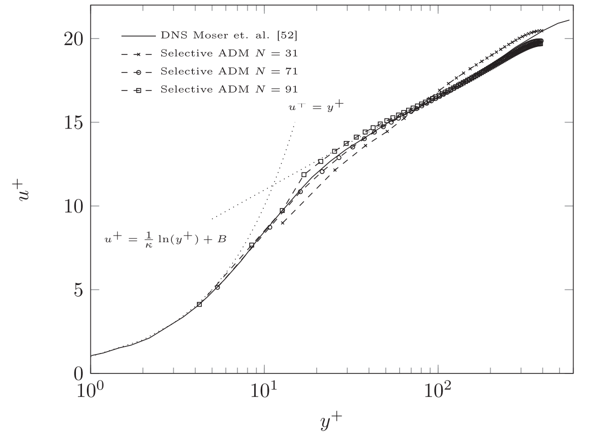

Fig. 11. Mean velocity profiles of turbulent channel flow at $Re_\tau = 395$ predicted by the selective filtered ADM-LES model.

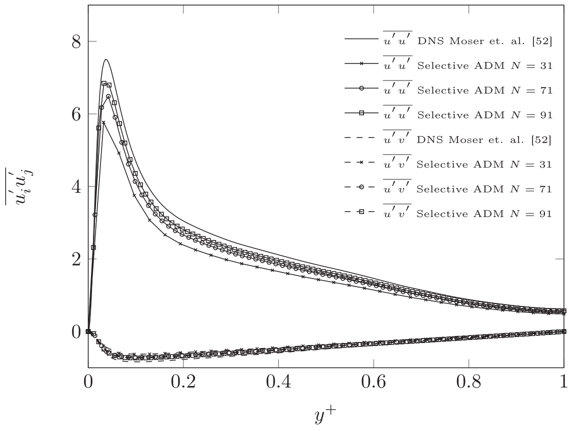

Fig. 12. Mean Reynolds stress profiles of turbulent channel flow at $Re_\tau = 395$ predicted by the selective filtered ADM-LES model.

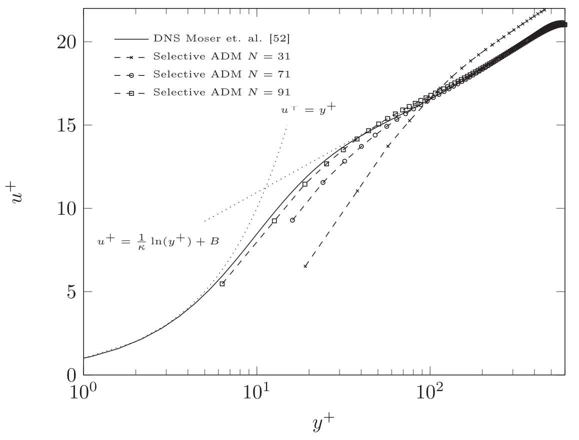

Fig. 13. Mean velocity profiles of turbulent channel flow at $Re_\tau = 590$ predicted by the selective filtered ADM-LES model.

In Fig. 11, the mean veloctiy fields for $Re_\tau = 395$ are shown. While for $N = 71$ and $N = 91$ the overall agreement with the reference data of Moser et al. [52] is found to be very good, for $N = 31$ an under estimation of the flow field is found for $y^+ < 80$ while for higher y^+ values the velocity is over-predicted. This could indicate higher Reynolds numbers, than those which are targeted. For $N = 91$ the velocity field was predicted accurately in vicinity of the wall, while for $10 < y^+ < 40$ a small overshot is visible compared to the excellent agreement with $N = 71$.

The results obtained for the Reynolds stresses shown in Fig. 12 outline inaccurate results of $\overline{u'u'}$ and $\overline{u'v'}$ for $N = 31$ compared to the reference data of Moser et al. [52]. The location of the maximum value of the stream- and cross-wise stresses are in fair agreement with the reference data, while the amplitude is not captured correctly. Apparently the low resolution and the high Reynolds number lead to a similar effect as for the Taylor–Green vortex test case discussed in Section 3.1. The high discrepancy between resolution and Reynolds number leads to strong non-linear amplifications of the non-equilibirum part of f_α which triggers high σ values, see Eqs. (15) and (16). The results is presumably higher predicted dissipation leading to under-predicted velocity fields in the wall-nearest cells. This would also underline the assumption of an under-predicted overall Reynolds number leading to a velocity field as depicted in Fig. 11. For the higher resolutions the maximum values obtained for the stresses are in fair agreement with the reference DNS data, yet an overall under-prediction of approximately 9.6% and 5.9% for $N = 71$ and $N = 91$ are visible.

Fig. 13 reveals the obtained velocity field for $Re_\tau = 590$ for all investigated resolutions. For $N = 31$ the simulation converged towards a flow field dominated by strong unphysical oscillations in the bulk region, characterized by an over-predicted velocity field in the bulk region while the near-wall flow field is under-predicted. For that reason, no reliable results are shown for the stresses in Fig. 14. For $N = 71$ a similar trend as for $Re_\tau = 395$ and $Re_\tau = 590$ with $N = 31$ is visible. The near-wall region shows an under-prediction of the velocity field while the bulk region is predicted in very good agreement with the reference data of Moser et al. [52]. In the same way as for $Re_\tau = 395$, the $\overline{u'u'}$ stresses are in fair agreement with respect to the location of the local maximum as well as with the shape along the channel height. Nevertheless, due to the low resolution applied, the average discrepancy compared to the reference data is almost 23% and the peak position for the $\overline{u'v'}$ stresses is predicted too close to the wall. Again, by increasing the resolution to $N = 91$ the overall agreement with the reference data is very good as already found for $Re_\tau = 180$ and $Re_\tau = 395$, yet the stresses are both marginally under-predicted.

In Fig. 15 the plane averaged values for $\sigma(\boldsymbol{x}, t)$ are illustrated. For $Re_\tau = 180$ the distribution of σ in vicinity of the wall is nearly zero, which underlines, the higher wall resolution for this Reynolds number. Increasing the Reynolds number, it is visible that only

Please cite this article as: P. Nathen et al., Adaptive filtering for the simulation of turbulent flows with lattice Boltzmann methods, Computers and Fluids (2018), https://doi.org/10.1016/j.compfluid.2018.03.042

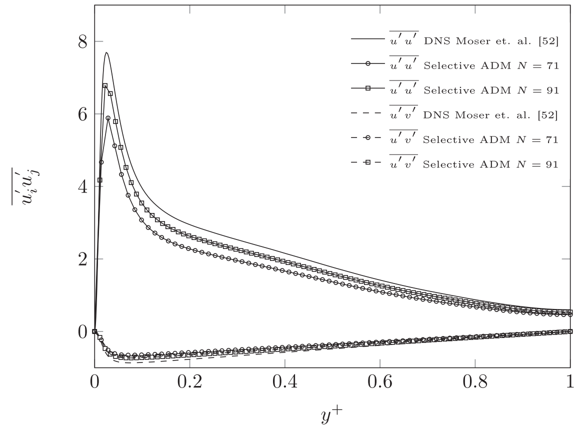

Fig. 14. Mean Reynolds stress profiles of turbulent channel flow at $Re_\tau = 590$ predicted by the selective filtered ADM-LES model.

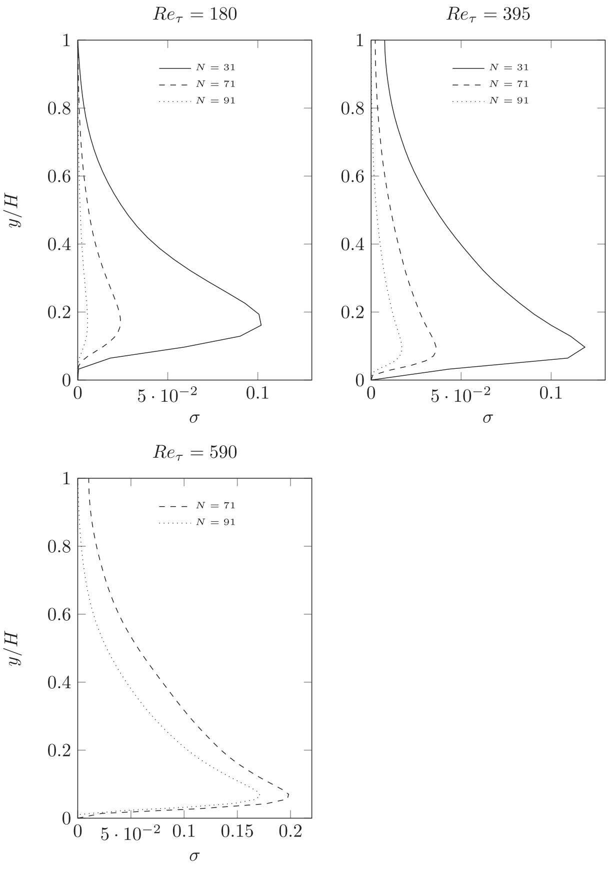

Fig. 15. Plane averaged values for the artificial viscosity $\sigma(\boldsymbol{x}, t)$ for varying Reynolds numbers and resolutions.

resolutions higher than $N = 31$ lead to artificial viscosity values around zero. For $N = 31$ and $Re_\tau = 395$ values for σ are not zero. This assumption leads to higher dissipation in this region which can also cause the under predicted velocity field, see also Fig. 11. Another reason for higher values of σ for rather small resolutions and high Reynolds numbers is the use of symmetric filter stencils in vicinity of the wall. It is assumed that unsymmetric filter stencils can lead to improved results when the first cell is in the buffer layer than in the wall nearest region for high Reynolds number flows. For $Re_\tau = 590$, the results are consistent with the previous findings. Interestingly, all results follow to a certain degree the general development of the production of the turbulent kinetic energy in the boundary layer, see also [38,52,53].

4. Conclusion

This paper introduced an extended filter approach for the ADM-BGK equations, which is based on a connection between temporal resolved scales and applied grid resolution. The quality of the results obtained by the classical ADM-BGK approach depends on a sensitive choice of a constant artificial viscosity σ. By adapting the artificial viscosity according to locally resolved flow scales with a phase averaged strain-rate relaxation, the sensitivity of our proposed model is strongly decreased, enabling a more general application of the ADM-BGK model independent of Reynolds and Mach number. The transfer function of a given viscosity filter can be partly adapted dynamically in regions where the resolution is not sufficiently high and, thus, a numerical model is necessary to account for a correct energy transfer.

We tested the selective ADM approach for HIT at varying Reynolds numbers, resolutions and filter stencil sizes. It was found to be stable and independent of applied Reynolds numbers, however the results were only in fair agreement with the reference DNS data for resolutions, where the large, energy containing scales are resolved properly and thus the self-adapting stencil lead to $|\widehat{f_\alpha} - f_\alpha| \ll 1$ being valid. With increasing Reynolds numbers at fixed resolutions, an increased discrepancy was found for a second and third order filter stencil. This discrepancy is assumed to be caused by the higher predicted $\sigma(\boldsymbol{x}, t)$ by the third order stencil. This higher predicted $\sigma(\boldsymbol{x}, t)$ is probably caused by the lower inherent filter dissipation, which similarly was found by Fauconnier et al. [23]. Additional work was carried out on the spectral analysis of the numerical viscosity in order to investigate dissipation in spectral space. The introduced procedure can only assess the total numerical dissipation coming from the filter stencil and the calculated $\sigma(\boldsymbol{x}, t)$ value. It was found that the model adapts dynamically to resolution and Reynolds number.

Finally, the new approach was tested for wall-bounded turbulence represented by the turbulent channel flows at $Re_\tau = 180$, $Re_\tau = 395$ and $Re_\tau = 590$ each case resolved by $N = 31$, $N = 71$ and $N = 91$ cells per channel half-width. The general agreement with reference DNS was very good and similar results as found for the Taylor–Green vortex test case were found. Increasing the Reynolds number for fixed resolutions lead to satisfying results as long as a certain threshold is not exceeded. This finding was observed slightly for $Re_\tau = 395$ and $Re_\tau = 590$ with $N = 31$ and $N = 71$ respectively. As expected, for $Re_\tau = 590$ and $N = 31$ strong unphysical oscillations were apparent in the flow field, caused by the low resolution applied.

The extended ADM-BGK version is a promising alternative for the simulation of turbulent flows in the framework of LES based LBM simulations. The adaptivity of the stencil lead to improved prediction of turbulent scales for marginally and well-resolved flow fields. A lower mesh-sensitivity was found for the investigated Reynolds numbers of freely decaying turbulence and wall-bounded turbulence. Future improvement has to be done, in order to quantify the dissipation coming from the pure filter stencil, in order to adapt the numerical dissipation more accurately.

References

[1] Bhatnagar PL, Gross EP, Krook M. A model for collision processes in gases. I. Small amplitude processes in charged and neutral one-component systems. Phys Rev 1954;94:511–25.

Please cite this article as: P. Nathen et al., Adaptive filtering for the simulation of turbulent flows with lattice Boltzmann methods, Computers and Fluids (2018), https://doi.org/10.1016/j.compfluid.2018.03.042

[2] Chen S, Doolen GD. Lattice Boltzmann method for fluid flows. Annu Rev Fluid Mech 1998;30:329–64.
[3] Aidun CK, Clausen JR. Lattice-Boltzmann method for complex flows. Annu Rev Fluid Mech 2010;42:439–72.
[4] Krause MJ, Thäter G, Heuveline V. Adjoint-based fluid flow control and optimisation with lattice Boltzmann methods. Comput Math Appl 2013;65:945–60.
[5] Henn T, Thäther G, Dörfler, Nirschl H, Krause MJ. Parallel dilute particulate flow simulations in the human nasal cavity. Comput Fluids 2016;124:197–207.
[6] Trunk R, Henn T, Dörfler, Nirschl H, Krause MJ. Inertial dilute particulate fluid flow simulations with an Euler-Euler lattice Boltzmann method. J Comput Sci 2016;17:438–45.
[7] Mink A, Thäther G, Nirschl H, Krause MJ. A 3d lattice Boltzmann method for light simulation in participating media. J Comput Sci 2016;17:431–7.
[8] Ricot D, Marie S, Sagaut P, Bailly C. Lattice Boltzmann method with selective viscosity filter. J Comput Phys 2009;228:4478–90.
[9] Ricot D, Maillar V, Bailly C. Numerical simulation of unsteady cavity flow using lattice Boltzmann method. In: 8th AIAA/CEAS Aeroacoustics Conference & Exhibit; 2002.
[10] Sagaut P. Toward advanced subgrid models for lattice Boltzmann based large-eddy simulation: theoretical formulations. Comput Math Appl 2010;59:2194–9.
[11] Hou S, Sterling J, Chen S, Doolen G. A lattice Boltzmann subgrid model for high Reynolds number flows. F Inst Commun 1996;6:151–66.
[12] Dong YH, Sagaut P. A study of time correlation in lattice Boltzmann-based large-eddy simulation of isotropic turbulence. Phys Fluids 2008;20:035105.
[13] Dong YH, Sagaut P, Marie S. Inertial consistent subgrid model for large-eddy simulation based on the lattice Boltzmann method. Phys Fluids 2008;20:035104.
[14] Filippova O, Succi S, Mazzoccoc F, Arrighettic C, Bellad G, Hänel D. Multiscale lattice Boltzmann schemes with turbulence modeling. J Comput Phys 2002;170:812–29.
[15] Yu H, Girimaji SS, Luo LS. DNS and LES of decaying isotropic turbulence with and without frame rotation using lattice Boltzmann method. J Comput Phys 2005;209:599–616.
[16] Malaspinas O, Sagaut P. Consistent subgrid scale modelling for lattice Boltzmann methods. J Fluid Mech 2012;700:514–42.
[17] Malaspinas O, Sagaut P. Advanced large-eddy simulation for lattice Boltzmann methods: the approximate deconvolution model. Phys Fluids 2011;23:105103.
[18] Stolz S, Adams NA. An approximate deconvolution procedure for large-eddy simulation. Phys Fluids 1999;11:1699.
[19] Stolz S, Adams NA, Kleiser L. An approximate deconvolution model for large-eddy simulation with application to incompressible wall-bounded flows. Phys Fluids 2001;13:997.
[20] Adams NA. A stochastic extension of the approximate deconvolution method. Phys Fluids 2011;23:055103.
[21] Layton WJ. Approximate deconvolution models of turbulence: analysis, phenomenology and numerical analysis. 1st. Springer-Verlag; 2010.
[22] Tam CKW, C WJ, Dong Z. A study of the short wave components in computational acoustics. J Comput Acous 1993;1:133–66.
[23] Fauconnier D, Bogey C, Dick E. On the performance of relaxation filtering for large-eddy simulation. J Turbul 2013;14:22–49.
[24] Schranner F, Domaradzki JA, Hickel S, Adams NA. Assessing the numerical dissipation rate and viscosity in numerical simulations of fluid flows. Comput Fluids 2015;114:84–97.
[25] Hickel S, Adams NA, Domaradzki JA. An adaptive local deconvolution method for implicit LES. J Comp Phys 2006;213:413–36.
[26] Domaradzki JA, Xiao Z, Smolarkiewicz PK. Effective eddy viscosities in implicit large eddy simulations of turbulent flows. Phys Fluids 2003;15:3890.
[27] D'Humiéres D, Ginzburg I, Krafczyk M, Lallemand P, Luo L-S. Multiple-relaxation-time lattice Boltzmann models in three dimensions. Phil Trans R Soc Lond A 2002;361:437–51.
[28] Latt J. Hydrodynamiclimit of lattice Boltzmann equations. Université de Genève; 2007. Dissertation.
[29] Latt J, Chopard B. Lattice Boltzmann method with regularized non-equilirbium distribution functions. Math Comput Simul 2006;72:165–8.
[30] He X, Luo L-S. Lattice Boltzmann model for the incompressible Navier Stokes equation. J Stat Phys 1997;88:927–44.
[31] Guo Z, Baochang S, Nengchao W. Lattice BGK model for incompressible Navier Stokes equation. J Comput Phys 2000;165:288–306.
[32] Guo Z, Shu S. Lattice Boltzmann method and its applications in engineering. World Scientific; 2013.
[33] Sukop MC, Thorne DT. Lattice Boltzmann modeling. Springer-Verlag; 2006.
[34] Waldrow DA. Lattice-gas cellular automata and lattice Boltzmann models: an introduction. Springer-Verlag; 2000.
[35] Mathew J, Lechner R, Foysi H, Sesterhenn J, Friedrich R. An explicit filtering method for large eddy simulation of compressible flows. Phys Fluids 2003;15:2279.
[36] Mathias MJ. Fluid flow simulation and optimisation with lattice Boltzmann methods on high performance computers. Universität Karlsruhe; 2010. Dissertation.
[37] Lèveque E, Toschi F, Shao L, Bertoglio JP. Shear-improved Smagorinsky model for large-eddy simulation of wall-bounded turbulent flows. J Fluid Mech 2007;570:491–502.
[38] Pope SB. Turbulent flows. Cambridge University Press; 2013.
[39] Brachet ME. Direct simulation of the three-dimensional turbulence in theTaylor-Green vortex. Fluid Dyn Res 1991;8:1–8.
[40] Batchelor GK. The theory of homegeneous turbulence. Cambdridge University Press; 1953.
[41] Özyilmaz N. Lattice Boltzmann computations of grid-generated turbulence. Universität Nürnberge Erlanagen; 2010. Dissertation.
[42] M L. Turbulence in fluids. 3rd. Kluwer Academic Publishers; 1997.
[43] Chollet JP. Two-point closures as a subgrid scale modeling for large eddy simulations. Turbulent shear flows IV. Durst F, Launder BE, editors. Springer; 1984.
[44] Chollet JP, Lesieur M. Parametrization of small scales of three-dimensional isotropic turbulence utilizing spectral closures. J Atmos Sci 1981;38:2747–57.
[45] Malaspinas O, Sagaut P. Wall model for large-eddy simulation based on the lattice Boltzmann method. J Comput Phys 2014;275:25–40.
[46] Lammers P, Bernonov KN, Volkert R, Brenner G, Durst F. Lattice BGK direct numerical simulation of fully developed turbulence in incompressible plane channel flow. Comput Fluids 2006;35:1137–53.
[47] Premnatha KN, Pattisona MJ, Banerjee S. Dynamic subgrid scale modeling of turbulent flows using lattice-Boltzmann method. Physica A 2009;388:2640–58.
[48] Bespalko DJ. Validation of the lattice Boltzmann method for direct numerical simulation of wall-bounded turbulent flows. Queen's University; 2011. Dissertation.
[49] Cabrit O. Direct simulations for wall modeling of multicomponent reacting compressible turbulent flows. Phys Fluids 2009;21:055108.
[50] He X, Shan X, Doolen GD. Discrete Boltzmann equation model for nonideal gases. Phys Rev E 1998;57:R13–16.
[51] Wang LP, Peng C, Guo Z, Yu Z. Lattice Boltzmann simulation of particle-laden turbulent channel flow. Comput Fluids 2016;124:226–36.
[52] Moser RD, Kim J, Mansour NN. Direct numerical simulation of turbulent channel flow up to $re_\tau = 590$. Phys Fluids 1999;11:943–5.
[53] Kim J, Moin P, Moser R. Turbulence statistics in fully-developed channel flow at low Reynolds-number. J Fluid Mech 1987;177:133–66.

Please cite this article as: P. Nathen et al., Adaptive filtering for the simulation of turbulent flows with lattice Boltzmann methods, Computers and Fluids (2018), https://doi.org/10.1016/j.compfluid.2018.03.042

APPENDIX C

Selected conference papers

Here, a selection of conference papers can be found.

C.1. ADVANCED LBM TREATMENT OF TURBULENT FLOWS FOR COMPLEX MOVING BOUNDARIES

Fluid Dynamics and Co-located Conferences
June 24-27, 2013, San Diego, CA
21st AIAA Computational Fluid Dynamics Conference

10.2514/6.2013-2573

An extension of the Lattice-Boltzmann Method for simulating turbulent flows around rotating geometries of arbitrary shape

P. Nathen, D. Gaudlitz
Institute of Aerodynamics and Fluid Mechanics TU München, Munich, Germany

J. Kratzke and M. J. Krause
Institute for Applied and Numerical Mathematics, Karlsruhe Institute of Technology, Karlsruhe, Germany

A Multi-Relaxation-Time Lattice-Boltzmann Method (MRT-LBM) is proposed for simulating unsteady three-dimensional turbulent flows. Turbulence modeling is performed with a state-of-the-art Large-Eddy-Simulation (LES) approach based on a explicit subgrid-scale model within the LBM framework. Additionally, a computational technique for treating rotating geometries is presented, which is based on an interpolation technique for the boundary fluid-cell interface.

A two dimensional double shear layer and a three-dimensional Taylor-Green vortex will be testcases for the MRT scheme. Beyond this, the MRT scheme including the turbulence model will be validated with a two dimensional flow around a square cylinder at low and high Reynolds numbers. Results of the vorticity field and the global Strouhal number of the detaching flow will be shown for the square cylinder. The laminar flow around a rotating cylinder is simulated with an interpolation based technique and results of the drag and lift coefficient will be shown and compared to reference cases. Finally, the three-dimensional flow at high Reynolds numbers around a rotating cylinder will be presented, which includes both techniques for turbulence modeling and complex boundary treatment.

Nomenclature

c_s	Speed of sound
C_s	Smagorinsky constant
e	Discrete velocities
f	Distribution functions for the $D3Q19$ model
m	Transformed momentum vector
M	Transformation matrix
n	Number of cells
N	Resolution of the reference length
S	Relaxation time matrix
α	Degrees of freedom
Δ	Physical discretization parameter
ϵ	Dissipation rate
ν	Kinematic viscosity
Π	Shear rate norm
ρ	Density
τ	Relaxation time

Superscripts:

0	Initial value
b	Boundary velocity
c	Post-collision pre-propagation state
eq	Equilibrium

Subscripts:

0	Reference value
i	Extensions in x-/ y-/ z-direction
eff	Effective value
L	Left direction
mol	Molecular value
sgs	Subgrid-scale value
t	Temporal discretization
$turb$	Turbulent value
x	Spatial discretization
α	Degrees of freedom

I. Introduction

Complex turbulent flows as they occur around rotating wheels at high Reynolds numbers, are challenging in two different ways. On one hand, tremendous experimental efforts are necessary to capture the unsteady pressure and velocity fields. On the other hand, a fully resolved CFD simulation is feasible only if appropriate numerical models for turbulence as well as for rotating geometries are employed. Increasing computational ressources allow for increasingly detailed simulations *e.g.* the detailed simulation of rotating geometries. The majority of the established CFD tools are based on the Navier-Stokes Equations (NSE). However, in the past decades alternative CFD tools were developed, which are based on Lagrangian particle formulations. A very promising method of these formulations is the Lattice-Boltzmann Method (LBM), an ensemble-averaged version of the Lattice-Gas Cellular Automata (LGCA).

In recent years the LBM proved to be an efficient method for simulating external and internal aerodynamics, see [1] and [2]. Its linear algorithm and straightforward implementation enabled its use for a multitude of problems in fluid dynamics. The method originates from the continuous Boltzmann Equation (BE) and is based on its explicit discretization in time and velocity space, which leads to the Lattice-Boltzman Equation (LBE). The LBE is strictly non-linear due to the collision term. The simplest version of the LBM is based on a single-relaxation-time (SRT) collision operation proposed by Bhatnagar, Gross and Krook (BGK) [3]. Due to its simplicity, the approximation of the collision operation with a SRT approach causes instabilities at high Reynolds-number flows. The reason for this behavior is the fixed ratio of shear and bulk viscosity and the inherent oscillations of the non-conserved flow variables [4]. Hence, a Multi-Relaxation-Time (MRT) scheme was originally proposed by D'Humières *et al.* [4] and later investigated by Dellar, Du and Chen [5]- [6]. Using the MRT approach, the authors showed increased stability for a lid-driven cavity flow and for a double shear layer testcase at high Reynolds numbers while maintaining the efficiency of the original method.

Almost all technical relevant flows exhibit turbulent flow structures. Additional modeling of these structures is necessary to consider their influence on the mean flow field. Adopted from the classical turbulence modeling for the NSE, a similar approach is employed in the LBM theory, which is based on eddy-viscosity schemes, see [7]- [10]. These eddy-viscosity models are based on an additional time scale, called turbulent collision time, which contributes to the effective collision time. The underlying equations for the eddy viscosity in LBM simulations are usually solved using a Finite Difference (FD) scheme which leads to higher computational efforts. A more intrinsic approach is based on a Subgrid-Scale (SGS) model which was successfully validated for many LES simulations with a conventional NSE approach. Without loss of efficiency a LBM-SGS model was proposed and tested by several authors [11]- [15].

In order to analyze problems of industrial relevance, turbulent flows in combination with curved, possibly rotating geometries have to be adequately represented by the LBM. Since the lattices are quadratic, the resolution of the investigated geometry has to be either very high, which would still lead to a staircase approximation, or the outline of the lattices has to be adjusted appropriatly. In literature the most common methods to represent complex geometries are based on body fitted grids [16]- [18], Immersed Boundary Methods (IBM) [19]- [23] or inter- extrapolation methods [24]- [29]. For treating rotating geometries we focus on an interpolation method proposed by Bouzidi *et al.* [30] which was reviewed and validated by Kao and Yang [31].

The paper is structured as follows: In section II an introduction to all three important building blocks for simulations of complex turbulent flows, namely: Multi-Relaxation-Time LBM, LES based SGS method for LBM and the interpolation technique for curved geometries, will be given. In section III validation testcases for the MRT scheme, as well as for the MRT scheme including turbulence modeling will be shown. In section IV the validation work as well as a test case for the combination of the techniques for further investigations of complex turbulent flows around moving geometries of arbitrary shapes will be presented. Finally, in section V the conclusions will be drawn.

II. Method

In this section details on techniques for the MRT theory, turbulence modeling and complex boundary treatment will be given. All three techniques were implemented separately in the framework of the open source LBM code *OpenLB*.

II.A. Multi-Relaxation-Time LBM

The following methods are shown for the *D3Q19* discrete LBM scheme. The governing equation for the LBM on a square lattice reads

$$f_\alpha\left(x_i + e_\alpha\delta_t, t+\delta_t\right) - f_\alpha\left(x_i, t\right) = -\frac{1}{\tau}\left(f_\alpha\left(x_i,t\right) - f_\alpha^{eq}\left(x_i,t\right)\right) \tag{1}$$

with the single relaxation time (SRT) τ determined by the BGK approach. The discrete velocities e_α in the *D3Q19* are given with

$$ce_\alpha = \begin{cases} (0,\ 0,\ 0) & ,\ for\ \alpha = 0 \\ (\pm1,\ 0,\ 0)c,\ (0,\ \pm1,\ 0)c,\ (0,\ 0,\ \pm1)c, & ,\ for\ \alpha = 1..6 \\ (\pm1,\ \pm1,\ 0)c,\ (\pm1,\ 0,\ \pm1)c,\ (0,\ \pm1,\ \pm1)c, & ,\ for\ \alpha = 7..18 \end{cases} \tag{2}$$

where $c = \delta_x/\delta_t$ is the discrete particle velocity. For simplification we shall use $\delta_x = \delta_t = 1$ from now. $f_\alpha^{eq}\left(x_i+, t\right)$ are the nine equilibrium distribution functions, which are based on a discrete expansion of a Maxwell distribution. They are defined as

$$f_\alpha^{eq}\left(x_i,t\right) = \begin{cases} \rho_0 - (1-\omega_0)\frac{p}{c_s^2} + \omega_0, & ,\ for\ \alpha = 0 \\ \omega_\alpha\rho\left[1 + e\frac{c_{\alpha i}u_i}{c^2} + \frac{9}{2}\frac{(c_{\alpha i}u_i)^2}{c^4} - \frac{3}{2}\frac{u_i u_i}{c^2}\right] & ,\ for\ \alpha = 1..18. \end{cases} \tag{3}$$

The weights are $\omega_0 = 1/3$, $\omega_{1-6} = 1/18$, $\omega_{7-18} = 1/36$ and $c_s = c/\sqrt{3}$ is the speed of sound. The macroscopic variables can be reconstructed by the appropriate moments of the distribution functions. Mass and momentum are conserved by

$$\rho_0 = \sum_{\alpha=0}^{18} f_\alpha^{eq}\left(x_i,t\right) = \sum_{\alpha=0}^{18} f_\alpha\left(x_i,t\right) \tag{4}$$

and

$$\rho_0 u_i = \sum_{\alpha=0}^{18} f_\alpha^{eq}\left(x_i,t\right) e_{i\alpha} = \sum_{\alpha=0}^{18} f_\alpha\left(x_i,t\right) e_{i\alpha}. \tag{5}$$

The algorithm consists of two elementary steps: a collision and an advection step which is shown for the MRT scheme in the following. The MRT-LBM is based on a linear transformation of the distribution functions

f_α from velocity space into momentum space $m_\alpha = M_{\alpha\beta} f_\beta$. With a SRT scheme at high Reynolds numbers (relaxation time approaching $\tau = \frac{1}{2}$) the non-conserved macroscopic variables, emerging from the remaining degrees of freedom, are not decaying but develop oscillations which lead to irreversible and exponentially growing instabilities. The main difference of the MRT- to the SRT-scheme is that the constant collision time is replaced by a collision time matrix. Regarding equation (1) the discrete LBE becomes

$$f_\alpha\left(x_i + e_\alpha \delta_t, t + \delta_t\right) - f_\alpha\left(x_i, t\right) = -S_{\alpha\beta}\left(f_\beta\left(x_i, t\right) - f_\beta^{eq}\left(x_i, t\right)\right) \tag{6}$$

The SRT scheme is directly reconstructed for a velocity space relaxation time matrix $S_{\alpha i} = \frac{1}{\tau} I_{\alpha i}$, where $I_{\alpha i}$ is the unity matrix. The two steps, collision and advection, are done in two different spaces. After transformation of f_α into momentum space the collision step is performed with subsequent advection in velocity space. The transformation, collision, re-transformation and advection can be summed up with

$$f_\alpha\left(x_i + e_\alpha \delta_t, t + \delta_t\right) - f_\alpha\left(x_i, t\right) = -M_{\alpha\gamma}^{-1} \widehat{S}_{\gamma\beta}\left(m_\beta\left(x_i, t\right) - m_\beta^{eq}\left(x_i, t\right)\right) \tag{7}$$

with $\widehat{S}_{\alpha\beta} \equiv diag\left(s_0, s_1, ...s_{Q-1}\right)$ being the collision matrix and

$$m_\alpha = \left(\rho, e, \epsilon, j_x, q_x, j_y, q_y, j_z, q_z, 3p_{xx}, p_{ww}, p_{xy}, p_{yz}, p_{zx}, m_{xyz}\right). \tag{8}$$

being the momentum vector. The equilibrium moments in equation (7) are given with

$$e^{eq} = -\rho + \frac{1}{\rho_0} j_i j_i, \tag{9}$$

$$\epsilon^{eq} = -\rho, \tag{10}$$

$$q_x^{eq} = -\frac{7}{3} j_x, \quad q_y^{eq} = -\frac{7}{3} j_y, \quad q_z^{eq} = -\frac{7}{3} j_z, \tag{11}$$

$$p_{xx}^{eq} = \frac{1}{3\rho_0}\left[2j_x^2 - \left(j_y^2 + j_z^2\right)\right], \quad p_w w^{eq} = \frac{1}{\rho_0}\left[j_y^2 - j_z^2\right], \tag{12}$$

$$p_{xy}^{eq} = \frac{1}{\rho_0} j_x j_y, \quad p_{yz}^{eq} = \frac{1}{\rho_0} j_y j_z, \quad p_{xz}^{eq} = \frac{1}{\rho_0} j_x j_z, \tag{13}$$

$$m_{xyz}^{eq} = 0. \tag{14}$$

In the MRT D3Q19 model the physical viscosity is only applied to the moments m_9, m_{11}, m_{13}, m_{14} and m_{15} and thus the relaxation times read

$$S = diag\left(0,\ 1.19,\ 1.4,\ 0,\ 1.2,\ 0,\ 1.2,\ 0,\ 1.2,\ \nu,\ 1.4,\ \nu,\ 1.4,\ \nu,\ \nu,\ \nu,\ 1.98,\ 1.98,\ 1.98\right). \tag{15}$$

The relaxation times for the conserved moments ρ_0 and j_i are set to zero. The transformation matrix $M_{\alpha\beta}$ consisting of orthogonal vectors is given in Appendix A. An extensive description of the MRT-LBM can be found *e.g.* in D'Humières *et al.* [4].

II.B. LES-LBM Approach

As already mentioned, turbulence modeling is performed with an explicit SGS model based on the original Smagorinsky approach [11]- [15]. The main idea is a superposition of the molecular kinematic viscosity ν and a turbulent viscosity ν_{turb} related to the filter length scale or lattice size Δ_x

$$\nu_{turb} = \left(C_s \Delta_x\right)^2 \bar{\Pi}, \tag{16}$$

where $C_s = 0.1$ is the Smagorinsky constant and $\bar{\Pi} = \sqrt{\Pi_{ij}\Pi_{ji}}$ the second-order moment of the non-equilibrium term of the distribution functions, hence the shear rate norm. A major advantage of this formulation is the direct evaluation of the shear rate from the distribution functions instead of using a FDM formulation as used in other implementations of the LBM method. The effective viscosity becomes

$$\nu_{eff} = \nu_{turb} + \nu_{mol} \tag{17}$$

where ν_{turb} describes the turbulent viscosity.
Since the molecular viscosity within the LBM framework is expressed by

$$\nu_{mol} = (\tau_{mol} - 0.5)\,\frac{1}{3} \tag{18}$$

the effective collision time

$$\tau_{eff} = \tau_{mol} + \tau_{turb} \tag{19}$$

can be used to express the effective viscosity in the LBM theory. The turbulent collision time in equation [19] is obtained by

$$\tau_{turb} = 0.5\left(\sqrt{\tau_{mol}^2 + \left((C_s\Delta_x)^2\,\frac{\Delta_t}{c_s}4\sqrt{2}\tau_{eff}\bar{\Pi}\right)} - \tau_{mol}\right) \tag{20}$$

according to Yu et al. [14].

II.C. Modeling geometries of complex shape

An interpolation technique proposed by Bouzidi *et al.* [30] is used to represent domain boundaries of arbitrary shape. The main issue of using interpolation techniques in LBM to represent arbitrary surfaces is to evaluate the post-propagation state of fluid nodes next to a solid wall within the discrete time step. This is necessary since post-collision information from nodes within the boundary are needed. This problem is illustrated in figure 1. To reconstruct the information at fluid node A, a linear interpolation technique is proposed,

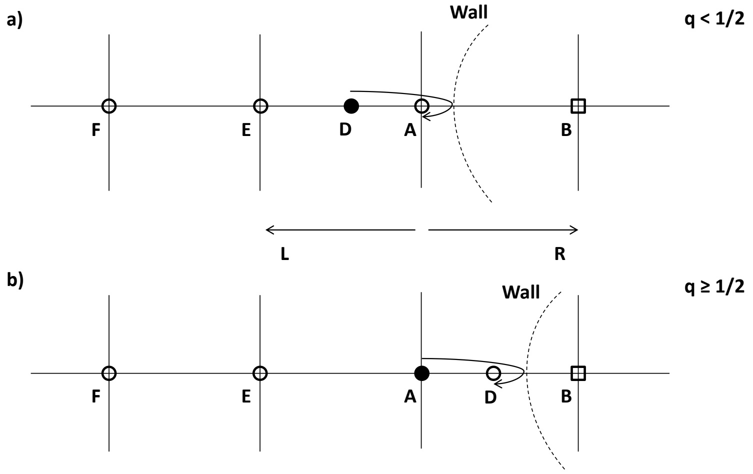

Figure 1: Fluid node state reconstruction based on the distance of the solid boundary to fluid nodes, from [30]; *a*) normalized distance q less than $\frac{1}{2}$; *b*) normalized distance q higher than $\frac{1}{2}$.

$$f_{i'}\left(r_{i,L}, t+1\right) = \begin{cases} 2qf_i^c\left(r_{i,L}, t\right) + (1-2q)\,f_i^c\left(r_{i,L} - c_i, t\right) & ,for\ q < 1/2 \\ \frac{1}{2q}f_i^c\left(r_{i,L}, t\right) + \frac{2q-1}{2q}f_i^c\left(r_i, t\right) & ,for\ q \geq 1/2, \end{cases} \tag{21}$$

where $f_{i'}\left(r_{i,L}, t+1\right)$ is the post-collision and post-propagation state and the right-hand side of equation (21) is the post-collision and pre-propagation step. The factor $q = \frac{x_B - x_A}{\Delta_{lattice}}$ in equation (21) describes the ratio of the distance between the wall and the nearest fluid cell to the lattice size. This technique is a combination of the well known bounce-back scheme and an interpolation which is second-order accurate.

The proposed linear interpolation technique by Bouzidi is implemented in the open source LBM code *OpenLB* by Kratzke and Krause [37] and will be coupled with the introduced MRT-LBM approach and the LES Smagorinsky model.

II.D. Modeling of moving boundaries

In the section II.C, the solid boundary treatment for non-moving boundaries was introduced. The interpolation technique can be extended for moving boundaries by adding a simple expression proposed by [30]. In case of an linear interpolation the right-hand side of equation [21] is modified with

$$f_{i'}\left(r_{i,L},t+1\right)=\begin{cases} 2qf_i^c\left(r_{i,L},t\right)+\left(1-2q\right)f_i^c\left(r_{i,L}-c_i,t\right)+\delta f_{i'} & ,\ for\ q<1/2 \\ \frac{1}{2q}f_i^c\left(r_{i,L},t\right)+\frac{2q-1}{2q}f_i^c\left(r_i,t\right)+\delta f_{i'} & ,\ for\ q\geq 1/2 \end{cases} \tag{22}$$

where

$$\delta f_{i'}=\begin{cases} 2\omega_\alpha e_{\alpha i}u_i^b & ,\ for\ q<1/2 \\ \frac{1}{q}\omega_\alpha e_{\alpha i}u_i^b & ,\ for\ q\geq 1/2. \end{cases} \tag{23}$$

With this simple extension the distribution functions for complex moving boundaries in vicinity of the wall can be reconstructed.

III. Results of the validation test cases

All simulations are performed with the open source LBM code *OpenLB*. So far the MRT scheme and the interpolation scheme by Bouzidi for complex boundary treatment were implemented separately. The proposed LES approach was coupled with the MRT scheme and validated using generic flow cases such as the double-shear layer and the Taylor-Green vortex.

III.A. Results for the MRT scheme

A common validation test case for CFD codes is the temporal development of the dissipation rate of a three-dimensional Taylor-Green vortex [33]. The investigation of the dissipation rate of the kinetic energy ϵ is a standard benchmark to determine the code's properties and its ability to resolve turbulent scales of motion. In a three-dimensional, $2\pi-$periodic box a two-dimensional velocity field

$$u_i^0=\begin{bmatrix} \frac{2}{\sqrt{3}}sin\left(\frac{2}{3}\pi\right)sin\left(x\right)cos\left(y\right)cos\left(z\right) \\ \frac{2}{\sqrt{3}}sin\left(-\frac{2}{3}\pi\right)cos\left(x\right)sin\left(y\right)cos\left(z\right) \\ 0 \end{bmatrix} \tag{24}$$

is initialized. When integrating in time a three-dimensional vortex field is generated. The mean dissipation rate is obtained by

$$\begin{aligned} \epsilon=\frac{1}{Re}\frac{1}{n_xn_yn_z}\sum_{n_xn_yn_z}\Bigg[&\left(\frac{\partial u}{\partial x}\right)^2+\left(\frac{\partial u}{\partial y}\right)^2+\left(\frac{\partial u}{\partial z}\right)^2+ \\ &\left(\frac{\partial v}{\partial x}\right)^2+\left(\frac{\partial v}{\partial y}\right)^2+\left(\frac{\partial v}{\partial z}\right)^2+ \\ &\left(\frac{\partial w}{\partial x}\right)^2+\left(\frac{\partial w}{\partial y}\right)^2+\left(\frac{\partial w}{\partial z}\right)^2\Bigg]+\epsilon_{sgs} \end{aligned} \tag{25}$$

where n_x, n_y and n_z represents the spatial resolution and $\epsilon_{sgs}=\left(C_s*\Delta_x\right)^2\bar{\Pi}^3$ is the subgrid dissipation provided by the explicit LES model.

In figure 2 the development of the dissipation rate ϵ is shown for different solver settings. As clearly recognizable all three LBM approaches do not differ in their prediciton of the time-dependent dissipation rate. Thus the MRT and the SRT scheme predict the same flow characteristics as has been expected for this test case. The MRT scheme with enabled turbulence model shows the same results as without turbulence

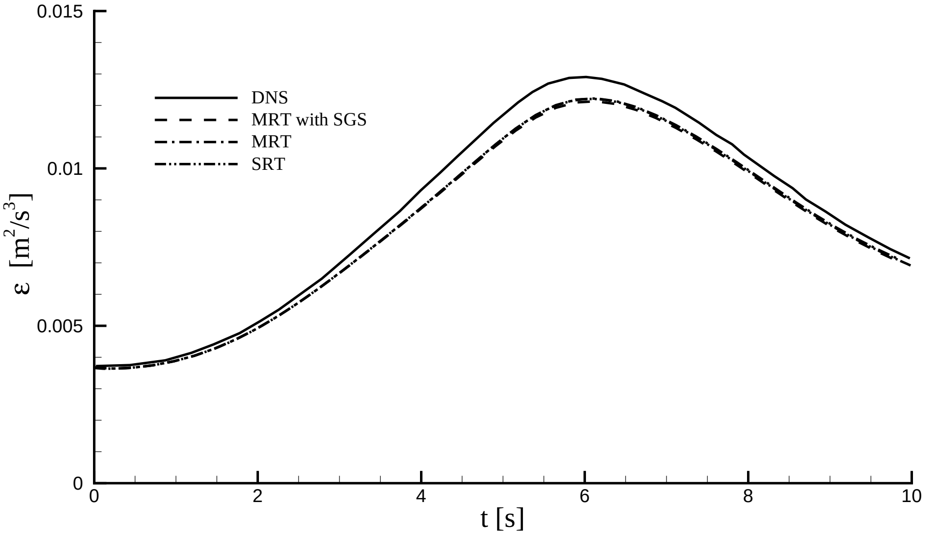

Figure 2: Dissipation rate for a Taylor-Green vortex as predicted by the SRT, MRT and MRT-LES approach compared to DNS data of Brachet *et al.* at [33], $Re = 200$.

modeling since all scales are resolved which leads to the conclusion, that the SGS models does not interfere in the simulation and produces no or very little artificial dissipation for a resolved flow setup. The Reynolds number was set to $Re = 200$ for all cases and the spatial resolution for the SRT, MRT, MRT-SGS was 128^3 cells. The DNS was performed with a spectral scheme employing 256^3 cells.

The MRT scheme detailed above was investigated by Dellar [5] and applied to a two-dimensional double shear layer with an initial velocity field

$$u_x^0 = \begin{cases} tanh\left(80 * (y - 1/4)\right), & for\ y \le 1/2 \\ tanh\left(80 * (3/4 - y)\right), & for\ y > 1/2 \end{cases} \tag{26}$$

and

$$u_y^0 = 0.05 * sin\left(2\pi\left(x + 1/4\right)\right) \tag{27}$$

in a double periodic box of the size 2π and a spatial resolution of $n_x = n_y = 128$ voxels. Dellar observed an increased stability with the MRT scheme for a Reynolds number of $Re = 10,000$ compared to the SRT technique. With *OpenLB* the same observations were made, even for higher Reynolds numbers up to $Re \approx 10^5 - 10^6$. While with the SRT approach strong oscillations and diverging simulations at Reynolds numbers of this range were found, the applied MRT scheme showed a smooth shear layer without any oscillations.

III.B. Validation of the MRT-LES model combined with solid boundary treatment: Flow around a 2D square cylinder

In order to validate the implementation of the solid boundary treament the two-dimensional-dimensional flows around a square cylinder were investigated at different Reynolds numbers covering laminar as well as turbulent flow regimes.

The results obtained for the laminar flow setup were compared to those of Breuer et al. [38]. *Breuer et al.* showed results of the averaged drag coefficient in a channel with the height of $L_y = 8D$, where D is the length of the cylinder investigated. The domain length was $L_x = 50D$ and different numerical approaches were applied. At the inlet a laminar velocity profile was imposed while at the outlet the pressure was prescribed.

Upper and lower walls were handled as bounce-back walls.
In the present investigation the drag coefficient was obtained via a momentum-exchange method, which is an intrinsic way of evaluating the forces on solid boundaries within LBM. For moving boundaries, one has to keep in mind, that due to the non-galilean invariance of the momentum-exchange method, this term has to be modified by second-order terms, see [44].

In figure 3 the results obtained with *OpenLB* are compared to those of *Breuer et al.* who employed a Finite Volume Method (FVM) and LBM approach. The results with *OpenLB* were obtained using the MRT scheme combined with the complex boundary treatment introduced above. The spatial resolution of the square cylinder was for all three numerical simulations similar. While both LBM approches represented the square cylinder with 40 voxels in length and height the FVM simulation represented the obstacle with 42 cells.

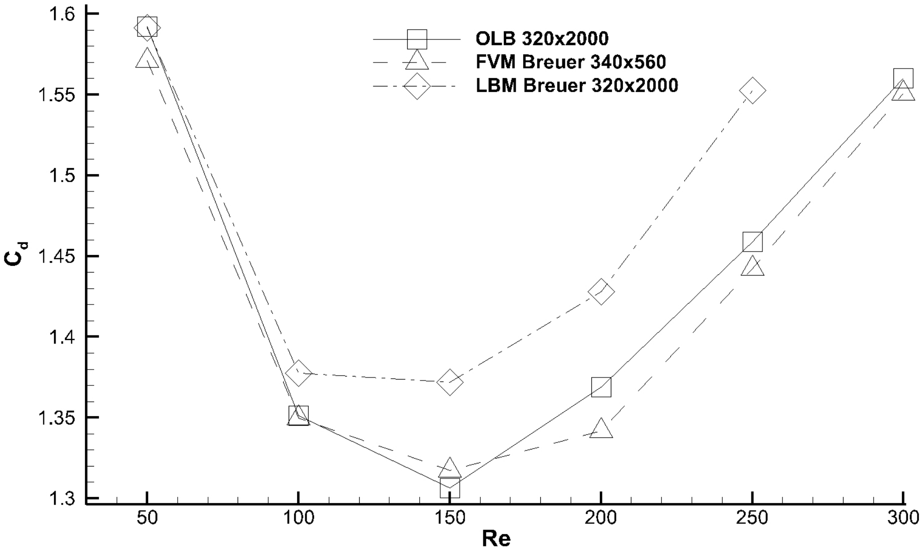

Figure 3: Drag coefficient of a square cylinder as function of Reynolds number.

Results obtained with *OpenLB* match the reference data of Breuer et al. using the FVM better than a standard LB method at all Reynolds numbers considered. This confirms the significantly improved accuracy of the solid boundary treatment introduced by Bouzidi et al. [30].

The turbulent flow around a two-dimensional square cylinder at a Reynolds number of $Re = 21,400$ was investigated experimentally by Lyn, Rodi and numerically by Murakami and Mochida [34]- [35]. The investigated setup was the reference for the numerical simulations of Wienken [39] and Bouris and Bergeles [41] who performed three-dimensional simulations. The data obtained in these investigations were taken as reference for the two-dimensional numerical studies with *OpenLB*.

The boundary conditions for the simulations with *OpenLB* were set as follows: At the inlet a uniform velocity profile with $u = 1m/s$ was imposed. The top and the bottom walls were set to a free-slip boundary condition and at the outlet the pressure was prescribed in combination with a convection boundary condition based on Yang [40].

The reference length was set to the diameter of the square $D = 1$ and the channel width was set to $14D$. The length of the domain was set to $48D$ and the obstacle was positioned $12D$ from the inlet. The obstacle was represented using the two-dimensional interpolation technique. Two different mesh resolutions were investigated and compared to experimental [34] and numerical results [39, 41]. The coarse simulation consists of 100 voxels per reference length and the finer simulation of 200 voxels, respectively. This results in a non-dimensional wall distance of $\frac{\Delta_x}{D} = 0.000625$ and $\frac{\Delta_x}{D} = 0.0003125$, respectively. Comparing the mesh of Bouris [41], who used in his finest simulation an ratio of $\frac{\Delta_x}{D} = 0.00125$ for the two-dimensional simulation and $\frac{\Delta_x}{D} = 0.0004$ for the three-dimensional one, the resolution in the current investigation is considered suitable to capture major flow characteristics. Wienken on the other hand used in his studies a cell size of $\Delta_x = \frac{D}{20}$, which is comparably coarse.

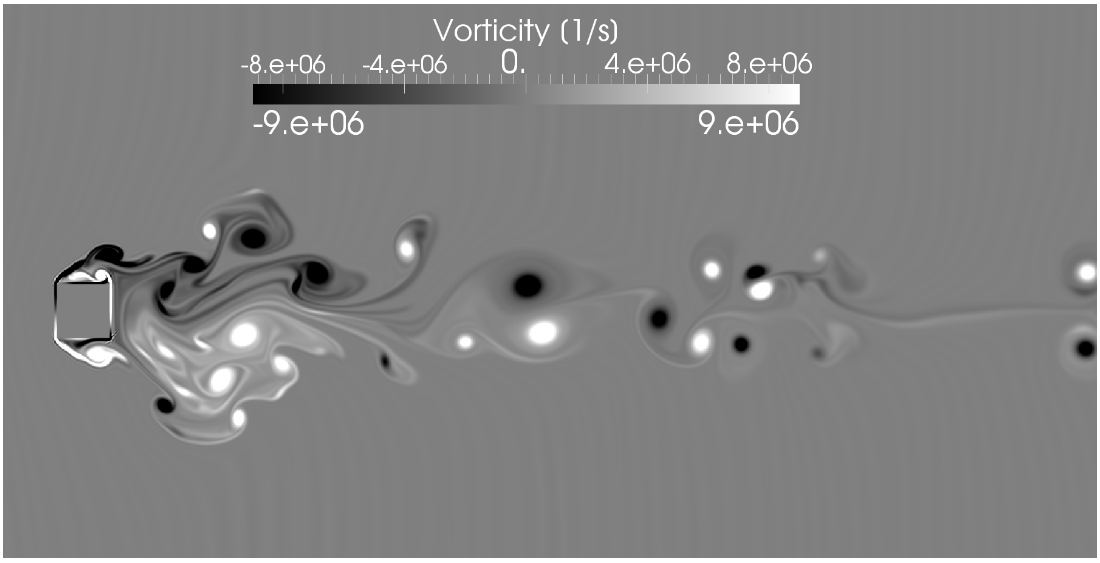

Figure 4: Unsteady vortex field in the wake of the square cylinder for $Re = 21,400$ and a spatial resolution of $\frac{\Delta_x}{D} = 0.000625$.

For $Re = 21,400$ the unsteady vortex field predicted by *OpenLB* is shown in figure 4. The obtained drag coefficients and Strouhal numbers are presented in table 1.

Case	Drag	Sr
OpenLB$(N = 100)$	1.472	0.124
OpenLB$(N = 200)$	1.590	0.129
Experiment [34]	2.1	0.132
Wienken [39]	2.28	0.128
Bouris [41]	2.28	0.134

Table 1: Drag coefficients and Strouhal numbers for the flow around the 2D square cylinder at $Re = 21,400$.

For the Reynolds number of $Re = 21,400$ the Strouhal number predicted by the experiments was $Sr = 0.132$. The simulation with the coarse resolution underestimates the Strouhal number by approximately 6% and the computation with the higher resolution underestimates the Strouhal number only by 3%. While the obtained Strouhal number agrees well with the reference data, the predicted drag is not yet sufficiently accurate.

This might result from potential deficiencies within the momentum-exchange computation for determining te drag coefficient, as well as potential shortcomings of the SGS turbulence modeling for wall-bounded flows. Both issues are currently under investigation.

Since the drag was not predicted sufficiently, the velocity in free-stream direction along the centerline was compared with experimental and numerical results of Lyn and Murakami [34, 35], see figure 5. As can be recognized, the mean velocity field predicted by *OpenLB* is in significantly better agreement with the experimental data than results of the RANS and RSE computations. *OpenLB* underestimates the recirculation zone in the wake of the obstacle, which leads to a decreased average drag value. Consequently,

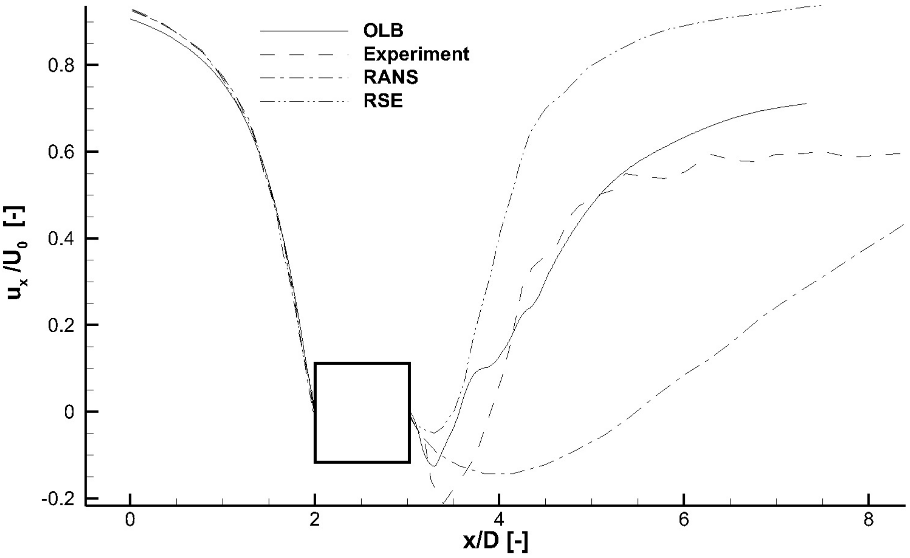

Figure 5: Comparison of the time-averaged streamwise velocity at the centerline for a $2D$ square cylinder as predicted by *OpenLB*, RANS, Reynolds-Stress-Equation (RSE) and Experiments at $Re = 21,400$.

further investigation of the drag evaluation with the momentum exchange has to be considered.

IV. Rotating geometries

Based on the results of Kang et al. [42] the implementation of rotating geometries in *OpenLB* has been validated for the flow setup of a rotating cylinder at a Reynolds number of $Re = 100$ and a rotational speed of $\alpha = \frac{\Theta D}{2U_\infty} = 1$. Here, Θ is defined as the angular velocity of the cylinder.
Additionally the results obtained by Mittal and Kumar [43] for the flow around a rotating cylinder at a Reynolds number of $Re = 200$ are taken as reference. For both test cases a two-dimensional flow was considered.
Kang et al. performed their simulations employing a body fitted rotationally symmetric grid. In the present LBM simulation the two-dimensional cylinder was placed in a rectangular domain. The height of the domain was $L_y = 16D$, where D is the diameter of the cylinder. The length was chosen to be $L_x = 50D$. This setup gives a blockage ratio of the cylinder to the width of the domain of $b_r = \frac{D}{L_y} = \frac{1}{16}$ in order to avoid effects occuring from pressure drops due to suction between domain boundary and solid boundary. A uniform block profile was imposed at the inlet, the upper and lower boundary were modeled with a free slip-boundary condition and at the outlet the pressure was prescribed. Four different spatial resolutions were investigated to determine grid independence for the LBM simulation with rotating solid boundaries. The cylinder diameter D was resolved by $N = 20$, 37.5, 50 and 100 voxels, respectively.

In table 2 the results obtained are compared to the reference simulation by Kang et al. The lift coefficient is in good agreement with the reference data. However, the drag has been overestimated by approximately 20% compared to the data of Kang et al. Also when using the corrected momentum-exchange method of Lorenz et al. [44] the results could not be improved substantially.
Similar results were found for the laminar testcase proposed by Mittal et al. [43]. A rotating cylinder at a Reynolds number of $Re = 200$ and $\alpha = 1$ is considered and the same domain size as for the test case of Kang et al. were applied. The results for the drag and lift coefficient obtained with *OpenLB* are shown in

table 3. Again, the lift has been determined with reasonable accuracy of 5%, while for the drag coefficient the numerical results obtained with *OpenLB* deviate by 16% from the reference data. A comparison of the flows around rotating cylinders at $Re = 100$ and $Re = 200$ predicted by *OpenLB* are shown in figure 6.

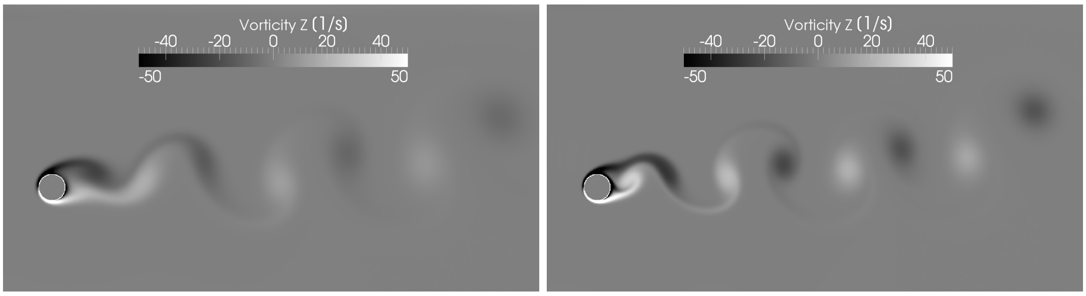

(a) $Re = 100$ (b) $Re = 200$

Figure 6: Vorticity predicted by *OpenLB* for both investigated Reynolds numbers around a rotating cylinder with $\alpha = 1$.

In view of the results shown in table 2 and 3 and the presented results above the following can be concluded: First, the drag was not predicted sufficiently accurate for turbulent flow setups and second, for laminar flow cases the predicted drag and lift coefficient is not sufficiently reproduced only in the case of rotating boundaries. This leads to the assumption, that the implemented momentum-exchange method exhibit deficiencies for these cases and need further investigations.

As part of additional validations the flow around a rotating cylinder with $\alpha = 2$ at a Reynolds number of $Re = 3,800$ will be presented. Comparison between the results obtained with *OpenLB* and the reference

Case	Drag	Lift
OpenLB$(N = 20)$	1.3630	−2.9801
OpenLB$(N = 37.5)$	1.3130	−2.6930
OpenLB$(N = 50)$	1.302	−2.7101
OpenLB$(N = 100)$	1.334	−2.8501
Kang et al. [42]	1.1040	−2.4881
OpenLB$(N = 50)$Corrected	1.362	−2.7410

Table 2: Drag and lift coefficients for a rotating cylinder at $Re = 100$ and $\alpha = 1$.

Computation	Drag	Lift
OpenLB$(N = 20)$	1.295	−2.720
OpenLB$(N = 37.5)$	1.227	−2.462
OpenLB$(N = 50)$	1.218	−2.420
OpenLB$(N = 100)$	1.303	−2.643
Mittal et al.	1.080	−2.424
OpenLB$(N = 20)$Corrected	1.286	−2.729
OpenLB$(N = 37.5)$Corrected	1.228	−2.667
OpenLB$(N = 50)$Corrected	1.256	−2.649

Table 3: Drag and lift coefficients for a rotating cylinder at $Re = 200$ and $\alpha = 1$.

case of Nair et al. [45], will be given. The two-dimensional numerical reference test case is based on the previous investigation of Mittal et al. [46] who performed an analysis of the temporal evolution of the drag and lift coefficient.

The domain size based on the cylinder diameter D was $L_x = 50D$ in streamwise direction and $L_y = 16D$ in latereal direction, respectively. At the inlet a uniform block profile was imposed, the lower and upper wall were modeled with an free slip boundary condition and at the outlet a convection boundary condition was given. Due to the higher Reynolds number and the doubled angular velocity of the obstacle, the resolution of the cylinder diameter was increased to $N = 200$. The streamlines do agree well with the numerical experiment of Nair et al., see figure 7. The streamlines are shown for the same physical simulation time $t = 5.5s$

Differences regarding the position of the detached vortex result from differences in the simulation initialization: Nair et al [45] prescribed constant inflow velocities at start of the simulation, whereas for *OpenLB* inlet velocity has been ramped up to the desired value. This causes already convective transport although the simulation has not reached the desired inflow conditions yet.

The averaged lift coefficient, shown in table 4, is in reasonable agreement with the reference data. The drag was overestimated by 21%, while the lift was underestimated by 8%.

Computation	Drag	Lift
OpenLB$(N = 200)$	0.760	-4.721
Nair et al.	0.625	-5.111

Table 4: Drag and lift coefficients of the flow around a rotating cylinder at $Re = 3,800$ for $\alpha = 2$.

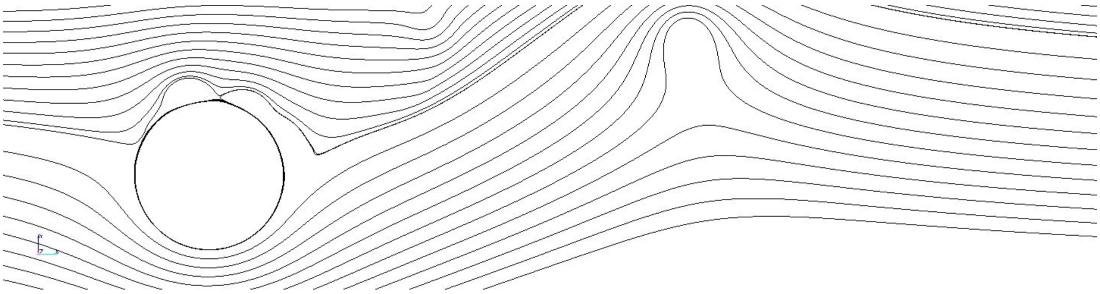

(a) Streamlines predicted by *OpenLB*

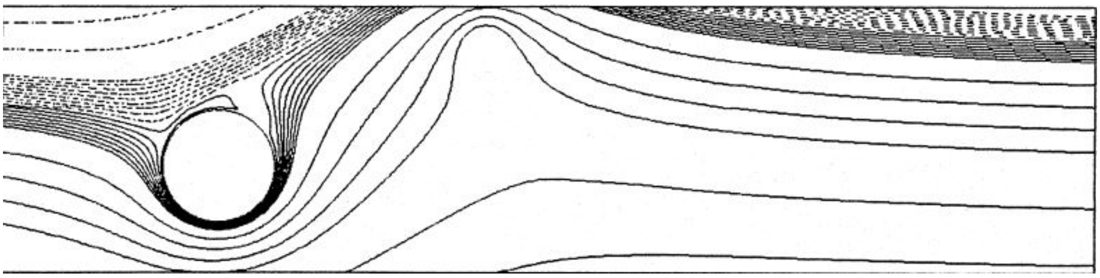

(b) Streamlines predicted by *Nair et al.*

Figure 7: Visualization of the streamlines at $t = 5.5$.

IV.A. Three-dimensional test case: Turbulent flow around a three-dimensional rotating cylinder

Finally, a rotating three-dimensional cylinder was simulated at a Reynolds number of $Re = 5,000$ based on its diamter D. The angular velocity of the counterclockwise rotating cylinder was chosen in such way that

$\alpha = 1$. The lateral extension of the cylinder was $L_y = \frac{D}{3}$.

The size of the computational domain was $10D$ in streamwise, $4D$ in transversal and $5D$ in lateral direction respectively. The rotating obstacle was resolved with 70 voxels, which leads on a equidistant mesh to 68mio. voxels. At the inlet a uniform velocity profile was imposed. The lower, upper, left and right boundary were modeled as free slip condition while at the outlet the pressure was prescribed and a convection boundary condition was given. The simulation was performed on the SuperMUC cluster of the *Leibniz-Rechenzentrum* in Munich. The simulation took $15h$ on 1024 cores for the simulation of $300,000$ timesteps.

In figure 8 a part of the computational domain is shown and as recognizable the flow structures in the wake are turbulent. two-dimensional flows at this Reynolds number do not provide such regimes but due to the small thickness of the cylinder affect a strong mixing behind the rotating cylinder occurs as around real wheels.

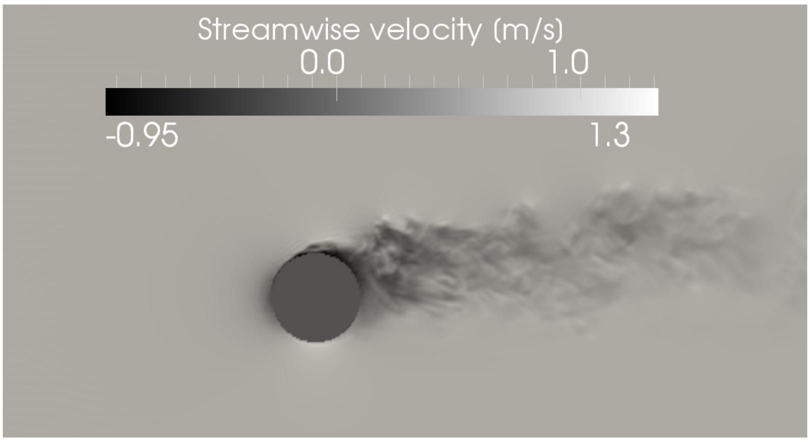

Figure 8: Instantaneous streamwise velocity snapshot in the wake of the rotating wheel at $Re = 5,000$.

To underline this turbulent mixing figure 9 shows the instantaneous isosurfaces of the normalized lateral velocity component. In the wake of the obstacle a mixing between the downstream detaching vortices is visible. Since turbulent structures around a rotating cylinder were simulated at a Reynolds number of $Re = 5,000$ without any numerical instabilities occuring, *OpenLB* showed its applicability for such complex flow setups.

V. Conclusions and outlook

In this paper the systematic evolution of the open source LBM code *OpenLB* as a numerical tool for the simulation of turbulent flows around moving boundaries of arbitrary shape was presented.

First, the implemented MRT method was valdiated for two- and three-dimensional test cases, such as the double-shear layer and the Taylor-Green vortex. The results obtained were in excellent agreement with the reference data for laminar setups. Beyond this a remarkable increase in stability was found for pseudo-turbulence in two-dimensional double-shear layer flows using the MRT scheme.

Afterwards the explicit SGS model was coupled with the MRT method and applied to the Taylor-Green vortex and compared with reference data. For the low Reynolds number case no contribution of the SGS model was found to the dissipation rate. The SGS model was then tested for the turbulent flow around a two-dimensional square cylinder at a Reynolds number of $Re = 21,400$. Although the drag was not predicted accuratly the estimated flow field in the wake of the body was in very good agreement with experimental data. The improved prediction of the drag using the momentum-exchange method will be part of the future work.

After implementing the interpolation scheme proposed by Bouzidi [30] and merging it with the MRT-LES scheme, the two-dimensional laminar and turbulent flow around rotating cylinders has been simulated. In the laminar case the predicted drag was not sufficiently accurate, while the lift was estimated reasonable. The same results were found for the turbulent test case proposed by Nair and Mittal [45, 46].

Finally the three-dimensional flow around a rotating cylinder was simulated. A very satisfactoring nu-

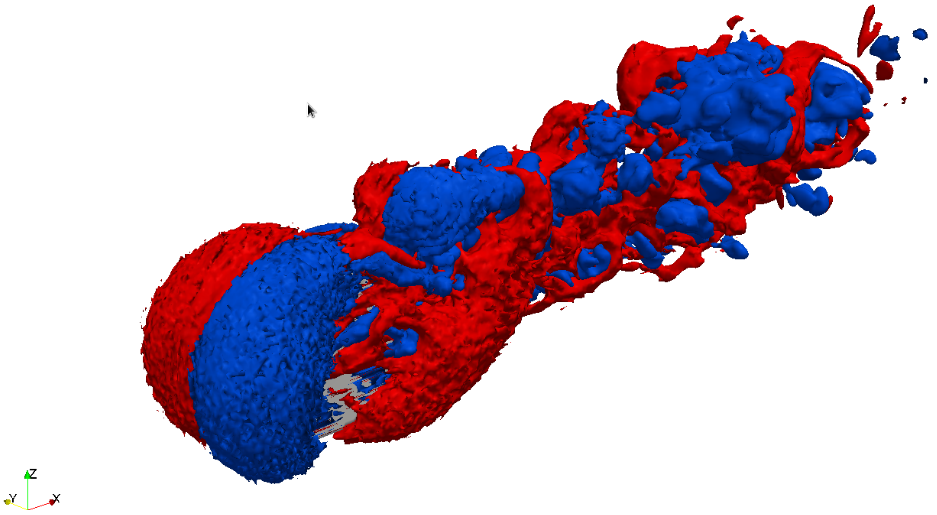

Figure 9: Instantaneous isosurfaces of the normalized lateral velocity magnitude, with $v = -0.1$ (blue) and $v = 0.1$ (red).

merical stability of the method has been found. Also characteristic flow structures in the wake of rotating geometries, *e.g.* wheels of passenger cars, can be identified in the obtained flow field.

Future work will be focussed on the correct estimation of drag and lift coefficients for rotating and for turbulent flows and on advanced turbulence modeling, thus near-wall flows can be predicted more correctly. Beyond this, grid refinement techniques will be implemented to enhance efficiency and to allow for a more detailed analysis of flows with practical relevance.

Appendix

The transformation matrix from velocity to momentum space is given with

$$M = \begin{bmatrix}
1 & 1 & 1 & 1 & 1 & 1 & 1 & 1 & 1 & 1 & 1 & 1 & 1 & 1 & 1 & 1 & 1 & 1 & 1 \\
-30 & -11 & -11 & -11 & 8 & 8 & 8 & 8 & 8 & 8 & -11 & -11 & -11 & 8 & 8 & 8 & 8 & 8 & 8 \\
12 & -4 & -4 & -4 & 1 & 1 & 1 & 1 & 1 & 1 & -4 & -4 & -4 & 1 & 1 & 1 & 1 & 1 & 1 \\
0 & -1 & 0 & 0 & -1 & -1 & -1 & -1 & 0 & 0 & 1 & 0 & 0 & 1 & 1 & 1 & 1 & 0 & 0 \\
0 & 4 & 0 & 0 & -1 & -1 & -1 & -1 & 0 & 0 & -4 & 0 & 0 & 1 & 1 & 1 & 1 & 0 & 0 \\
0 & 0 & -1 & 0 & -1 & 1 & 0 & 0 & -1 & -1 & 0 & 1 & 0 & 1 & -1 & 0 & 0 & 1 & 1 \\
0 & 0 & 4 & 0 & -1 & 1 & 0 & 0 & -1 & -1 & 0 & -4 & 0 & 1 & -1 & 0 & 0 & 1 & 1 \\
0 & 0 & 0 & -1 & 0 & 0 & -1 & 1 & -1 & 1 & 0 & 0 & 1 & 0 & 0 & 1 & -1 & 1 & -1 \\
0 & 0 & 0 & 4 & 0 & 0 & -1 & 1 & -1 & 1 & 0 & 0 & -4 & 0 & 0 & 1 & -1 & 1 & -1 \\
0 & 2 & -1 & -1 & 1 & 1 & 1 & 1 & -2 & -2 & 2 & -1 & -1 & 1 & 1 & 1 & 1 & -2 & -2 \\
0 & -4 & 2 & 2 & 1 & 1 & 1 & 1 & -2 & -2 & -4 & 2 & 2 & 1 & 1 & 1 & 1 & -2 & -2 \\
0 & 0 & 1 & -1 & 1 & 1 & -1 & -1 & 0 & 0 & 0 & 1 & -1 & 1 & 1 & -1 & -1 & 0 & 0 \\
0 & 0 & -2 & 2 & 1 & 1 & -1 & -1 & 0 & 0 & 0 & -2 & 2 & 1 & 1 & -1 & -1 & 0 & 0 \\
0 & 0 & 0 & 0 & 1 & -1 & 0 & 0 & 0 & 0 & 0 & 0 & 0 & 1 & -1 & 0 & 0 & 0 & 0 \\
0 & 0 & 0 & 0 & 0 & 0 & 0 & 0 & 1 & -1 & 0 & 0 & 0 & 0 & 0 & 0 & 0 & 1 & -1 \\
0 & 0 & 0 & 0 & 0 & 0 & 1 & -1 & 0 & 0 & 0 & 0 & 0 & 0 & 0 & 1 & -1 & 0 & 0 \\
0 & 0 & 0 & 0 & -1 & -1 & 1 & 1 & 0 & 0 & 0 & 0 & 0 & 1 & 1 & -1 & -1 & 0 & 0 \\
0 & 0 & 0 & 0 & 1 & -1 & 0 & 0 & -1 & -1 & 0 & 0 & 0 & -1 & 1 & 0 & 0 & 1 & 1 \\
0 & 0 & 0 & 0 & 0 & 0 & -1 & 1 & 1 & -1 & 0 & 0 & 0 & 0 & 0 & 1 & -1 & -1 & 1
\end{bmatrix} \tag{28}$$

References

[1] Chen, S. and Doolen, G. D., *Lattice Boltzmann for Fluid Flows*, Annu. Rev. Fluid Mech. 30:329-364, 1998.

[2] Succi, S. *The Lattice Boltzmann Equation*, Oxford Science Publications, 2^{nd} edition 2009.

[3] Bhatnagar P.L., Gross E.P., Krook M., *A model for collision processes in gases. I. Small aplitude processes in charged and neutral one component systems*, Phys. Rev. 94:511-525, 1954.

[4] D'Humières, D., Ginzburg, I., Krafczyk, M., Lallemand, P., Luo, L-S., *Multiple-relaxation-time lattice Boltzmann models*

in three dimensions, Phil. Trans. R. Soc. Lond. 360:437-451, 2002.

[5] Dellar, P., *Incompressible limits of lattice Boltzmann equations using multiple relaxation times*, J. Comput. Phys. Vol. 190 Issue 2:351-370, 2003.

[6] Du, R., Chen, X., *Multi-relaxation-time lattice Boltzmann model for incompressible flow*, Physical Letters A 359:564-572, 2006.

[7] Succi, S., Amati, G., Benzi, R., *Challanges in Lattice Boltzmann Computing*, Journal of Statistical Physics 81:5-16, 1995.

[8] Fares, E., *Unsteady flow simulation of the Ahmed reference body using a lattice Boltzmann approach*, Computers & Fluids 35:950-950, 2006.

[9] Filippova, O., Succi, S., Mazzocco, F., Arrighetti, C., Bella, G., Hänel, D., *Multiscal eLattice Boltzmann Schemes with Turbulence modelling*, Journal of Computational Physics 170:812-829, 2001.

[10] Chen, H., Kandasamy, S., Orszag, S., Shock, R., Succi, S., Yakhot, V., *Extended Boltzmann Kinetic Equation for Turbulent Flows*, Science Vol 301:633-636, 2003.

[11] Krafczyk, M., T¨olke, J., Luo, L-S., *Large Eddy Simulation with a Multiple-Relaxation-Time LBE Model*, International Journal of Modern Physics B Vol. 17:33-39, 2003.

[12] Yu, H., Luo, L-S., Girimaji, S., *LES of turbulent square jet flow using an MRT lattice Boltzmann model*, Computers & Fluids 35:957-965, 2006.

[13] Yu, H., Girimaji, S., *Near-field turbulent simulations of rectangular jets using lattice Boltzmann method*, Phys. Fluids 17, 2005.

[14] Yu, H., Girimaji, S., Luo, L-S., *DNS and LES of decaying isotropic turbulence with and without frame rotation using lattice Boltzmann method*, Journal of Computational Physics 209:599-616, 2005.

[15] Hou, S., Sterling, J., Chen, S., Doolen, G. D., *A Lattice Boltzmann Subgrid Model for High Reynolds Number Flows*, J. Comput. Phys. 209:599-616, 2005.

[16] He, X., Luo, L-S., Dembo, M., *Some progress in lattice Boltzmann method, Part 1. Non-uniform grids*, J. Comput. Phys. 129:357-363, 1996.

[17] He, X., Doolen, G., *Lattice Boltzmann method on a curvlinear coordinate system: vortex shedding behind a circular cylinder*, Phys. Rev. E 56:434-440, 1997.

[18] He, X., Doolen, G., *Lattice Boltzmann method on curvlinear coordinates system: flow around a circular cylinder*, J. Comput. Phys. 134:306-315, 1996.

[19] Inamuro, T., *Lattice Boltzmann methods for moving boundary flows*, Fluid Dyn. Res. 44, 2012.

[20] Shu, C., Wu., J., *A new Immersed Boundary-Lattice Boltzmann Method and its Application to Incompressible Flows*, Modern Physics Letters B Vol 23:261-264, 2009.

[21] Niu, X. D., Shu, C., Peng, Y., *A momentum exchange-based immersed boundary-lattice Boltzmann mehtod for simulating incompressible viscous flows*, Physics Letters A 354:173-182, 2006.

[22] Zhu, L., He, G., Wang, S., Miller, L., Zhang, X., You, Q., Fang, S., *A An immersed boundray method byy the lattice Boltzmann approach in three dimensions with application*, Computer & Mathematics with Applications Vol. 61 Issue 12:3506-3518, 2011.

[23] Feng, Z-G., Michaelides, E. E., *The immersed boundary-lattice Boltzmann method for solving fluid-particles interaction problems*, J. Comput. Phys. 195:602-628, 2004.

[24] Zu, Y. Q., Yan, Y. Y., Shi, W. P., Ren, L. Q., *International Journal of Numerical Methods for Heat & Fluid Flow*, International Journal of Numerical Methods for Heat & FLuid Flow Vol. 18 No. 6:766-782, 2007.

[25] Lallemand, P., Luo, L-S., *Lattice Boltzmann method for moving boundaries*, J. Comput. Phys. 184:406-421, 2002.

[26] Guo, Z., Zheng, C., Shi, B., *An extrapolation method for boundary conditions in lattice Boltzmann method*, Phys. Fluids 14, 2007

[27] Mei, R., Luo, L-S., Shyy, W., *An Accurate Curved Boundary Treatment in the Lattice Boltzmann Method*, ICASE Report No.2000-6, 2000.

[28] Mei, R., Shyy, W., Yu, D., Luo, L-S., *Lattice Boltzmann Method for 3-D Flows with Curved Boundary*, ICASE Report No.2002-17, 2002.

[29] Mei, R., Yu, D., Shyy, W., *Force Evaluation in the Lattice Boltzmann Method Involving Curved Geometry*, ICASE Report No.2002-22, 2002.

[30] Bouzidi, M., Firdaouss, M., Lallemand, P., *Momentum transfer of a Boltzmann-lattice fluid with boundaries*, ICASE Report No.2002-22, 2002.

[31] Kao, P. H., Yang, R. J., *An investigation into curved and moving boundary treatments in the lattice Boltzmann method*, J. Comput. Phys. 227:5671-5690, 2008.

[32] Krause, M. J., *Fluid Flow Simulation and Optimisation with Lattice Boltzmann Methods on High Performance Computers: Application to the Human Respiratory System*, PhD Thesis, Karlsruhe Institute of Technologies, Karlsruhe, Germany, 2010.

[33] Brachet, M., Meiron, D. I., Orszag, S. A., Nickel, B. G., Morf, R. H., Frisch, U., *Small-scale structure of the Taylor Green vortey*, J. Fluid Mech. 130: 411-452, 1983.

[34] Lyn, D. A., Rodi, W., *The flapping shear layer formed by flow seperation from the forward corner of a square cylinder*, J. Fluid Mech. 267: 353-376, 1994.

[35] Murakami, S., Mochida, A., *On turbulent vortex shedding flow past 2D square cylinder predicted by CFD*, J. of Wind Engineering and Industrial Aerodynamics 54/55: 353-376, 1995.

[36] Le, H., Moin, P., Kim, J., *Direct numerical simulation of turbulent flow over a backward-facing step*, J. Fluid Mech. 130: 349-374, 1997.

[37] Kratzke, J., *Accurate Momentum Transfer at Curved Boundaries with Lattice Boltzmann: Design of a Vritual Wind Tunnel*, Diploma Thesis, Karlsruhe Institute of Technologies, Karlsruhe, Germany, 2012.

[38] Breuer, M., Bernsdorf, J., Zeiser, T., Durst, F., *Accurate computations of the laminar flow past a square cylinder based on two different methods: lattice-Boltmann and finite-volume*, International Journal of Heat and Fluid Flow 21(2):186-196, 2000.

[39] Wienken, W., *Die Large Eddy Simulation mittels der Finite-Elemente-Methode zur Bestimmung des Kavitationsbeginns*, PhD Thesis, Technische Universitaet Dresden, Dresden, Germany, 2003.

[40] Yang, Z., *Lattice Boltzmann outflow treatments: Convective conditions and others*, Comp. and Math. with Applications 65: 160-171, 2013.

[41] Bouris, D., Bergeles, G., *2D LES of vortex shedding from a square cylinder*, J. of Wind Eng. and Indust. Aerodynamics 80: 31-46, 1999.

[42] Kang, S., Choi, H., Lee, S.,*Laminar flow past a rotating cylinder*, Phys. of Fluids 11: 3311-3321, 1999.

[43] Mittal, S., Kumar, B.,*Flow past a rotating cylinder*, J. Fluid Mech. 476: 303-334, 2003.

[44] Lorenz, E., Caiazzo, A., Hoekstra, G.,*Corrected momentum exchange method for lattice Boltzmann simulations of suspension flow*, Phys. Rev. 79:036705, 2009.

[45] Nair, M. T., Sengupta, T. K., Chauhan, U. S.,*Flow past rotating cylinders at high Reynolds numbers using high order upwind schemes*, Computers & Fluids 27 (1): 47-70, 1998.

[46] Mittal, S., Nair, M. T., Sengupta, T. K.,*Numerical Simulation of Flow past rotating and translating circular cylinder*, 7^{th}, Asian congress of Fluid Mechanics, 1997.

C.2. WALL ADAPTION FOR TURBULENCE MODELS IN THE LBM FRAMEWORK

International Symposium
On Turbulence and Shear Flow
Phenomena (TSFP-9)
June 30 - July 3, 2015 *Melbourne, Australia*

TOWARDS WALL-ADAPTION OF TURBULENCE MODELS WITHIN THE LATTICE BOLTZMANN FRAMEWORK

Patrick Nathen
Institute for Aerodynamics and Fluid Mechanics
Technische Universität München
Boltzmannstr. 15, 85748 Garching bei München, Germany
patrick.nathen@aer.mw.tum.de

Daniel Gaudlitz[1] **and Nikolaus Adams**[2]
Institute for Aerodynamics and Fluid Mechanics
Technische Universität München
Boltzmannstr. 15, 85748 Garching bei München, Germany

ABSTRACT

This paper presents the development towards wall adaptive explicit filters for the simulation of turbulent wall bounded flows in the framework of the lattice Boltzmann method (LBM). First, we show the effect of different collision models on the characteristics of turbulent flow simulations by employing the Taylor-Green vortex as a numerical testcase. Second, an extension of the approximate deconvolution method (ADM), see Malaspinas & Sagaut (2012), Malaspinas & Sagaut (2011) and Sagaut (2010) for the simulation of wall-bounded turbulent flows is presented. A temporal dissipation relaxation is applied for explicit filtering, in order to suppress filtering in regions, where the flow is resolved and to adapt filtering in underresolved regions in such way, that the energy drain in the scales is physically motivated and consistent with the kinetic theory of turbulence. We apply the extended ADM for the simulation of a turbulent channel flow at $Re_\tau = 180$ and $Re_\tau = 395$ to demonstrate, that the ADM method of Malaspinas & Sagaut (2011) with selective viscosity filters is strictly dissipative for low-order filters. Hence, especially for wall-bounded flows the application of the proposed adaptive relaxation of the filter can be beneficial.

The lattice-Boltzmann method

LBM solves a set of kinetic equations in terms of discrete velocity distribution functions $f_\alpha(t,\boldsymbol{x})$ numerically. The discrete Boltzmann equations can be written as

$$f_\alpha(t+\Delta t, \boldsymbol{x}+\boldsymbol{c}_\alpha \Delta t) = f_\alpha(t,\boldsymbol{x}) + \Omega_\alpha(f_\alpha(t,\boldsymbol{x})) \quad (1)$$

where $\Omega_\alpha(f_\alpha(t,\boldsymbol{x}))$ is the collision operator, which represents non-linear and viscous effects of the Navier Stokes equations and $\boldsymbol{c}_\alpha$ is the discrete velocity set of the lattice applied. Macroscopic moments are reconstructed with a Gauss-Hermite quadrature based on the Hermite Polynomial expansion on a discrete lattice. The first two moments of the velocity distribution functions are the conserved moments ρ and the momentum $\rho\boldsymbol{u}$, which read

$$\rho = \sum_\alpha f_\alpha, \; \rho\boldsymbol{u} = \sum_\alpha \boldsymbol{c}_\alpha f_\alpha \quad (2)$$

while the momentum flux is the second-order off-equilibrium moment of the velocity distribution functions

$$\boldsymbol{\Pi} = \sum_\alpha f_\alpha^{neq} \boldsymbol{c}_\alpha \boldsymbol{c}_\alpha \quad (3)$$

In order to reconstruct the macroscopic equations of fluid motion, a Chapman Enskog expansion is used. The interested reader can refer to Chen & Doolen (1998) among others.

To close equation (1) the collision term needs to be modeled. One well-known approach is the linearization around small perturbations of the thermodynamic equilibrium. This approach is called the Bhatnagar-Gross-Krook (BGK) ansatz, see He & Luo (1997); Guo *et al.* (2000); Guo & Shu (2013) or Sukop & Thorne (2006) among others, which represents the collision term as a linear relaxation towards a maxwellian equilibrium

$$\begin{aligned}\Omega_\alpha(f_\alpha(t,\boldsymbol{x})) &= f_\alpha(t+\Delta t, \boldsymbol{x}+\boldsymbol{c}_\alpha\Delta t) - f_\alpha(t,\boldsymbol{x}) \\ &= -\frac{1}{\tau}\left(f_\alpha(t,\boldsymbol{x}) - f_\alpha^{eq}(t,\boldsymbol{x})\right).\end{aligned} \quad (4)$$

$f_\alpha^{eq}(t,\boldsymbol{x})$ is a low Mach number truncated Maxwell-Boltzmann distribution, which is adjusted in such a way, that equation (3) is fulfilled and mass and momentum are conserved. A widely used formulation for f_α^{eq} is given by

$$f_\alpha^{eq} = \rho\omega_\alpha \left[1 + \frac{\boldsymbol{c}_\alpha \boldsymbol{u}}{c_s^2} + \frac{1}{2c_s^4}(\boldsymbol{u}\boldsymbol{u} - c_s^2\boldsymbol{\delta})\boldsymbol{u}\boldsymbol{u}\right]. \quad (5)$$

ω_α are the weights to satisfy the exact Gauss-Hermite quadrature of the lattice, c_s is the lattice speed of sound and

---

[1] daniel.gaudlitz@aer.mw.tum.de
[2] nikolaus.adams@tum.de

$\boldsymbol{\delta}$ is the Kronecker delta. Although, the BGK approach has been applied to many flow problems, see Hänel (2004) and Waldrow (2000), it has been found to suffer from instabilities at high Reynolds numbers, which have its origins in unphysical moments of f_α. To remedy this shortcoming, the Multi-Relaxation-Time (MRT) scheme was developed by D'Humiéres *et al.* (2002). The main idea is to transform the collision step into the momentum space and to relax each moment separately in order to reduce the instabilities arising from the temporal growth of these unphysical moments. Thus, the single relaxation time from the BGK model is replaced by a relaxation time matrix $\boldsymbol{S}$, which relaxes each moment $m_\alpha = \boldsymbol{M} f_\alpha$ independently. The matrix $\boldsymbol{M}$ is a linear transformation matrix and the corresponding algorithm for the MRT scheme reads

$$\begin{aligned} & f_\alpha(t+\Delta t, \boldsymbol{x}+\boldsymbol{c}_\alpha \Delta t) - f_\alpha(t,\boldsymbol{x}) \\ & = -\boldsymbol{M}^{-1}\boldsymbol{S}(m_\alpha(t,\boldsymbol{x}) - m_\alpha^{eq}(t,\boldsymbol{x})) \end{aligned} \tag{6}$$

The MRT model increases the stability of the LBM method substantially. Yet, e.g. due to inconsistent derivation of boundary conditions for stresses on domain boundaries, where velocities are prescribed, instabilities arise in the MRT model for Reynolds numbers larger than approx. 5000 for three dimensional flows, see Freitas *et al.* (2011). In order to suppress these exponentially growing disturbances, Latt (see Latt & Chopard (2006) and Latt (2007)) proposed a regularization of the classical BGK algorithm, employing an approximation of the first-order multiscale expansion term

$$f_\alpha^{neq} = f_\alpha - f_\alpha^{eq} \approx f_\alpha^{(1)} = -\frac{\Delta t}{\omega c_s^2} \omega_\alpha \boldsymbol{Q}_\alpha \partial_i \rho \boldsymbol{u}. \tag{7}$$

Here, $\boldsymbol{Q}_\alpha$ is the first-order non equilibrium moment $\boldsymbol{Q}_\alpha = \sum \boldsymbol{c}\boldsymbol{c} f_\alpha^{neq}$. The non-equilibrium distribution function f_α^{neq} is used to approximate the first-order multiscale expansion term. This term is included in the BGK model, thus the regularized BGK algorithm reads

$$f_\alpha(t+\Delta t, \boldsymbol{x}+\boldsymbol{c}_\alpha \Delta t) = f_\alpha(t,\boldsymbol{x}) + (1-\omega) f_\alpha^{(1)}(t,\boldsymbol{x}) \tag{8}$$

This regularization operation is not only necessary for the flow field, but also for the boundaries. The main issue with respect to boundary conditions in the RLB is the proper reconstruction of the unknown distribution functions propagating into the flow domain. Since for the regularization the discrete velocity information is needed, a proper approximation of the non-equilibrium part $f_\alpha^{(1)}$ in equation (7) is required. Different approaches to model $f_\alpha^{(1)}$ at domain boundaries are proposed in Latt (2007) and Latt *et al.* (2008). In the present investigation the interpolated boundary approximation of the strain rate is considered for wall-bounded flows only.

The approximate deconvolution method (ADM) for LBM

The turbulence model investigated in this paper, which is adapted for wall-bounded flows, is the approximate deconvolution method (ADM) of Stolz & Adams (1999), Adams & Stolz (2002) and Stolz *et al.* (2001). The concept of ADM is a generalization of the scale-similarity model for Large-Eddy simulation based subgrid-scale models. The consecutive steps of explicit filtering and subsequent deconvolution of the macroscopic equations for fluid motions was adopted by Sagaut (2010) and Malaspinas & Sagaut (2011) in the LBM framework using a selective viscosity filter, see Tam *et al.* (1993). Applying a homogeneous low-pass filter kernel G on equation (1) one receives

$$\frac{\overline{Df_\alpha(t,\boldsymbol{x})}}{Dt} = \overline{\Omega_\alpha(f_\alpha(t,\boldsymbol{x}))} \tag{9}$$

which is equal to

$$\begin{aligned} & \frac{\overline{Df_\alpha(t,\boldsymbol{x})}}{Dt} - \Omega_\alpha(\overline{f}_\alpha(t,\boldsymbol{x})) \\ & = G * \Omega_\alpha(f_\alpha(t,\boldsymbol{x})) - \Omega_\alpha(\overline{f}_\alpha(t,\boldsymbol{x})) = \sigma_{sgs} \end{aligned} \tag{10}$$

where σ_{sgs} is the subgrid stress term emerging from the discrepancy between exact convolution and computabale terms. In general two approaches are followed at this point, which can be easily shown by re-writing the right-hand side of equation (10) as

$$\begin{aligned} & \left[G * \Omega_\alpha(\hat{f}_\alpha(t,\boldsymbol{x})) - \Omega_\alpha(\overline{f}_\alpha(t,\boldsymbol{x}))\right] \\ & + \left[G * \Omega_\alpha(f_\alpha(t,\boldsymbol{x})) - \Omega_\alpha(\hat{f}_\alpha(t,\boldsymbol{x}))\right] \\ & = \sigma_{sgs} = \sigma_{sgs}^1 + \sigma_{sgs}^2 \end{aligned} \tag{11}$$

where σ_{sgs}^1 is the known term and σ_{sgs}^2 is the unknown term which needs to be modeled and $\hat{f}_\alpha(t,\boldsymbol{x}))$ is the approximate deconvolution of the distribution function. At this point either the term σ_{sgs}^2 is modeled as demonstrated in Sagaut (2010) and Malaspinas & Sagaut (2011), or the simplified version of Stolz, Adams and additionally Mathew Mathew *et al.* (2003), is applied where the exact distribution function is replaced by it's approximate inverse $G * \Omega_\alpha(f_\alpha(t,\boldsymbol{x})) \approx G * \Omega_\alpha(\hat{f}_\alpha(t,\boldsymbol{x}))$. This simplification is valid for $\hat{f}_\alpha \approx \overline{f}_\alpha$ and has a tremendous effect on the required filter properties, since the discretization scheme in LBM is fixed and thus the ADM-LES approach itself is decoupled from the filter operation in the LBM framework. In earlier work, see Pruett & Adams (2000), the authors showed that indeed the underlying LES model cannot be chosen independently from the applied filter. Thus, if the filter operation is decoupled from our discretization scheme and the subgrid-scale model, the filter procedure can be adjsuted in such way to act only on the scales intended. Using the simplified procedure, equation (11) reduces to

$$\begin{aligned} & \frac{\overline{Df_\alpha(t,\boldsymbol{x})}}{Dt} - \Omega_\alpha(\overline{f}_\alpha(t,\boldsymbol{x})) \\ & = G * \Omega_\alpha(\hat{f}_\alpha(t,\boldsymbol{x})) - \Omega_\alpha(\overline{f}_\alpha(t,\boldsymbol{x})) = \sigma_{sgs}^1. \end{aligned} \tag{12}$$

The simplified approach given in equation (12) is the underlying approach in the current investigation. An inverse filter operation is performed with a deconvolution operator $\hat{\phi} = G^{-1} * \overline{\phi} = Q * \overline{\phi}$. The quality of an inverse filter operation is described with the transfer function $\hat{G}(\xi)$ in spectral space, where ξ is the wavenumber. In the work of Stolz

& Adams (1999), Adams & Stolz (2002) and Stolz *et al.* (2001), a Padé filter was applied and the deconvoluted solution is obtained by the Van Cittert iterative method. The authors showed, that a high-order deconvolution can be provided up to the cut-off wavenumber of the applied filter. Sagaut (2010) and Malaspinas & Sagaut (2011) used a class of selective viscosity filters up to order $N = 4$. In Tam *et al.* (1993), the stencil properties were derived and compared to each other. These filters damp high-wavenumber parts of an arbitrary signal, employing a damping approach, which reads

$$\hat{f}_{\alpha}^{out}(t,\boldsymbol{x}) = \overline{f}_{\alpha}^{in}(t,\boldsymbol{x}) - \sigma \sum_{n=-j}^{j} d_n \overline{f}_{\alpha}^{in}(t,\boldsymbol{x}+e_i n) \tag{13}$$

where the filter strength σ is related to an artifical viscosity and d_n is the weighting coefficient. In figure 1 the filters used for ADM by Malaspinas & Sagaut (2011) are shown in terms of the transfer function. It is visible, that even for the highest orders of the viscosity filters, the damping is quite strong. Hence, the underlying assumption $\hat{f}_\alpha \approx \overline{f}_\alpha$ for applying an explicit filter shown in figure 1 in the framework of the simplified procedure is questionable. A very high filter stencil is necessary in order to be consistent with the underlying assumptions made in this context. This is not desirable for the LBM, since it's algorithm is executed locally and any non-local operation drains the computational efficiency dramatically. Especially, if one considers an inverse convolution of each discrete lattice velocity would render the LBM algorithm inappropriate for flow problems.

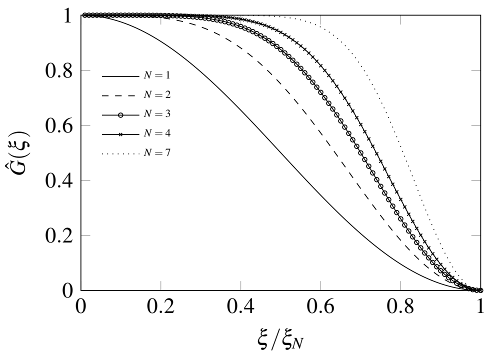

Figure 1: Transfer functions of the filters used by Malaspinas & Sagaut (2011) for the ADM $N = 1..4$ and an additional high-order viscosity filter $N = 7$ from Tam *et al.* (1993). The wavenumber is normalized with the Nyquist wavenumber ξ_N

From a computational point of view, we focus on the deconvolution of the macroscopic moments and aim to modify the strength of the filter σ as a function of space and time $\sigma(\boldsymbol{x},t)$ instead of leaving it constant. Thus, we cannot increase the order, and subsequently the steepness of the transferfunction, but the scales on which the filter operation will be applied. Therefore we aim to develop a selective viscosity filter, where the filter strength is adjusted in such way, that even low filter orders operate on large wavenumber only scales and thus $\hat{f}_\alpha \approx \overline{f}_\alpha$ is satisfied. With this approach, filtering is adopted to the mesh resolution automatically in terms of the resolved scales.

Our approach is based on the idea of the shear-improved Smagorinsky model of Lèveque *et al.* (2007). This model is based on the idea, that resolved turbulent scales in terms of the resolved strain-rate relax towards an average strain-rate and thus the fluctuating part of the strain-rate is significant at scales of filter size Δ_x. In flow regions, where the fluctuating part of the strain-rate is larger than the average strain rate, the turbulent flow can be considered as homogeneous and the standard Smagorinsky model is reconstructed. This approach was adopted earlier by Jafari & Rahnama (2011) for the MRT-based lattice Boltzmann, but the application was only limited to low Reynolds numbers. Also as shown by Malaspinas & Sagaut (2012), the modification of the effective relaxation rate does not inevitably lead to the filtered equations of fluid motions, namely the filtered Navier-Stokes equations. We apply a relaxation of the filter strength in terms of the temporal averaged resolved strain-rate. Without loss of generalization, a temporal averaging procedure is used since in statistically steady flows, like the converged turbulent channel flow, the efficiency increases (local operation), the spatial averaged statistics are reconstructed as well (ergodic system) and it is also suitable for the application to complex flows, with arbitrary flow seperations. The filter strength is computed as

$$\sigma(t,\boldsymbol{x}) = \frac{(|S|_{ij}(t,\boldsymbol{x}) - \langle|S|_{ij}(\boldsymbol{x})\rangle)\Delta_t}{(\rho + \langle\delta\rho\rangle)} \frac{\nu}{2} \left(\frac{\omega}{c_s^2}\right)^2 \tag{14}$$

where $\langle|S|_{ij}\rangle$ is the time averaged resolved strain-rate and Δ_t the physical time step. Averaging is perfomed as soon as the flows achieves a statistically steady state in terms of an autocorrelation function.

$$\eta = \frac{\langle u_x(\boldsymbol{x},t) u_x(\boldsymbol{x},t+\tau)\rangle}{\langle u_x(\boldsymbol{x},t) u_x(\boldsymbol{x},t)\rangle} \tag{15}$$

For flows with strong unsteady effects as they appear in external aerodynamics, a phase-averging procedure is the straight forward extension of this adaptive explicit filtering step. Despite the fact, that a time correlation needs to be estimated, the computational costs are very low compared with other approaches like the dynamic Smagorinsky model. Although we have a non-local filter approach, which reduces the computational efficiency, this approach is consistent with the macroscopic limit of the filtered equations of fluid motion. The filter-subgrid-scale model coupling and no loss of generalization in terms of Reynolds number and mesh requirements is present.

Beyond this, any amplification of unphysical moments are suppressed, since non-physical strain rates are only locally apparent and damped by our temporal adapted explicit filtering step. It is worth to mention, that the amplification of unphysical moments in terms of the strain-rate lead to an overpredicted eddy-viscosity for standard approaches in the LBM framework since the strain-rate and thus the non-equilibrium part of the velocity distribution function is directly linked to the turbulent relaxation time. This is a promising step towards BGK based simulation for high

Reynolds number flows where the stabilization is consistent with a physically motivated energy drain.

Analysis of the discrete lattice schemes for the simulation of turbulent flows

In order to investigate the properties of the different collision models, we employ the well-known Taylor-Green vortex and analyze the intergral dissipation rate. It will be outlined, why the BGK collision model is our model of choice. Prior analysis showed, that the BGK and MRT model have a oppositioned behavior: While the BGK scheme tends to be unstable if the Reynolds number is increased at a fixed mesh resolution, the MRT scheme showed no mesh convergence at a fixed mach number if the mesh resolution is increased at a fixed Reynolds number. This is exemplified for the Reynolds number $Re = 3000$ and two different mesh resolutions, $N = 64$ and $N = 256$, in figure 2.

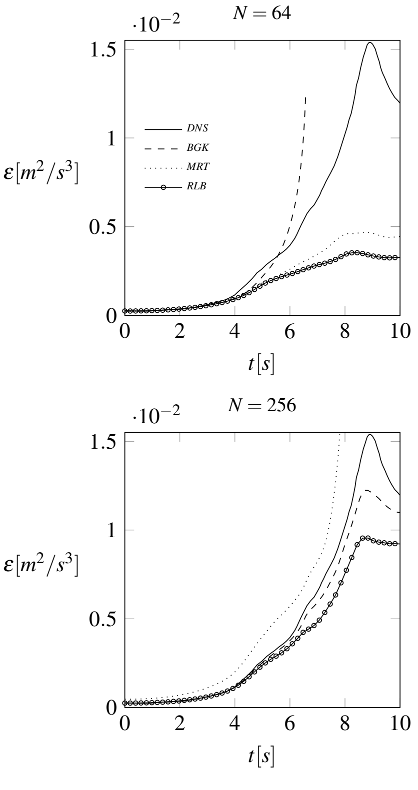

Figure 2: Temporal evolution of the dissipation rate of the Taylor-Green vortex predicted by the BGK, MRT and RLB scheme at $Re = 3000$ for the resolutions $N = 64$ and 256.

While the BGK scheme diverged for the lowest resolution which corresponds to the findings of others, see Lallemand & Luo (2000) and He & Luo (1997), the MRT scheme showed no convergence if the mesh resolution was increased to $N = 256$.

Beyond this, it was found that the RLB collision model is unconditionally stable at all resolutions and Reynolds numbers, but it suffers from a rather strong additional numerical viscosity. In order to represent the same range of turbulent scales for a given Reynolds number with the RLB scheme, additional computational effort has to be taken into account in terms of an increased resolution.

Based on these investigations, the BGK collision model was chosen for all further investigations, since mesh convergence was proven and the instabilities at high Reynolds numbers and low resolutions can be damped by our new model.

The turbulent channel flow

The aim of this work is to provide an extension of the ADM in the framework of the LBM. The model should adapt automatically the filtering strength to the local resolved scales. In regions where turbulence is resolved, filtering is suppressed by an energy drain balance, while in regions where the flow is underresolved, explicit filtering is adapted in such way, that the energy drain caused by filtering corresponds to a physically motivated viscosity model. The test case chosen is based on the work of Bespalko (2011). The domain had the extensions of $L_x = 12H$, $L_y = 4H$ and $L_z = 2H$ for the streamwise, lateral and wall normal direction respectively, where H is the channel half width. In streamwise and lateral direction, periodic boundary conditions were applied. Constant forcing in streamwise direction was applied as in Bespalko (2011). At the bottom and the top of the domain a halfway bounce-back rule, combined with a non-linear finite-difference regularization was applied, see Latt *et al.* (2008). In order to investigate the general sensitivity of the ADM for wall-bounded flows, we first apply the ADM with different filter stencils (2*nd* and 3*rd* order) and filter strengths ($\sigma = 0.001$ and $\sigma = 0.005$) to the turbulent channel flow at $Re_\tau = 180$. This is the smallest Reynolds numbers for turbulent scales in a turbulent channel flow. DNS reference data is taken from Kim *et al.* (1987) and Moser *et al.* (1999). In figure 3 the influence of the pure filtering on the turbulent velocity field is shown.

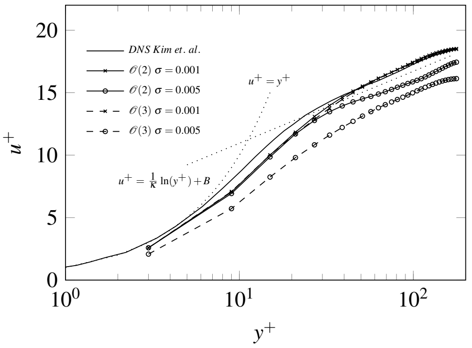

Figure 3: Mean velocity profiles of turbulent channel flow at $Re_\tau = 180$. Comparison of reference DNS of Kim *et al.* (1987) to the underresolved simulations with the BGK-based ADM model.

As it is clearly recognizable, the influence of the order of the filter is inferior to the applied filter strength, since the difference in the predicted velocity profiles by the BGK-based ADM is rather small for the lower filter strength compared with the DNS data. For the higher filter strength both filters underpredict velocity field, especially in the log-region of the flow. In previous investigations, it has been shown that the BGK model without any turbulence model has a good agreement with the DNS data for $y^+ < 30$, but in the bulk regions the average flow field was overpredicted. In the current study, the influence of explicit filtering leads a ”shift-down” of the average velocity field, which indicates the necessity of selective filtering. This ”shift-down” is also marginally influenced by the constant forcing as shown later.

The proposed model should filter mainly in the bulk region, while the wall-nearest region should be unaffected by the filtering procedure. The Reynolds numbers $Re_\tau = 185$ and $Re_\tau = 395$ were investigated with the adaptive ADM, at two resolutions $N = 31$ and $N = 71$.

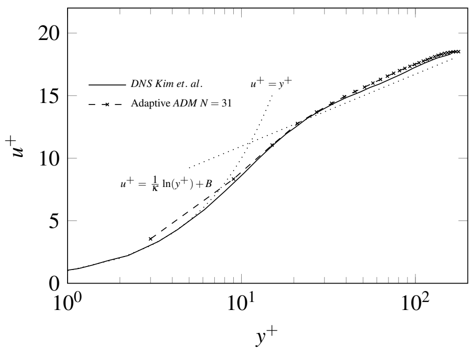

Figure 4: Mean velocity profiles of turbulent channel flow at $Re_\tau = 180$. Comparison of reference DNS of Kim *et al.* (1987) to the underresolved simulations with the BGK-based adaptive ADM model.

In figure 4 the averaged velocity profiles for $Re_\tau = 180$, predicted by the adaptive ADM model is presented and compared to the DNS of Kim *et al.* (1987). The setup with $N = 31$ cells per half-width is underresolved since $\Delta y^+ \approx 6$. Due to the applied bounce-back rule, the first fluid node is at $\Delta y^+ \approx 3$. Nevertheless, the log-law region of the flow was predicted very well and only in vicinity of the wall the velocity was slightly overpredicted. Increasing the resolution to $N = 71$ cells did not influence the results significantly.

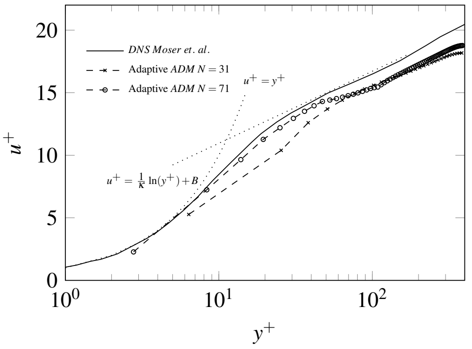

Figure 5: Mean velocity profiles of turbulent channel flow at $Re_\tau = 395$. Comparison of reference DNS of Moser *et al.* (1999) to the underresolved simulations with the BGK-based adaptive ADM model.

In figure 5 the results for $Re_\tau = 395$ when employing the adaptive ADM are shown, for two resolutions of the channel half-width $N = 31$ and $N = 71$, which corresponds to a normalized resolution of $\Delta y^+ \approx 12.8$ and $\Delta y^+ \approx 5.6$ respectively. It is visible, that for the lower resolution $N = 31$ the velocity is generally underpredicted compared to the reference DNS data, while the results for the higher resolution are in good agreement with the DNS for $y^+ < 30$. Although for $N = 71$ the log-law region is slightly underpredicted as well, the adaptive nature of the filtering can be recognized. While the wall nearest region is unaffected by filtering, the scales in the bulk flow are underpredicted and thus, the filter step has an influence on the flow field in the log-law. The bulk flow is underpredicted by both resolutions in the same order of magnitude and it appears, that the constant forcing approach used here is not suitable for the adaptive ADM. Since adaptive filtering is only performed in the log-law region, the damping causes an underprediction of the velocity field, using a constant driving force for the turbulent channel flow. This was also shown for constant filter strengths, see figure 3.

Conclusion

In this paper the lattice Boltzmann method (LBM) was applied to predict turbulent fluid flows. Different collision models were investigated and the single relaxation time scheme was found to be the least dissipative collision model while allowing grid convergence at increasing resolutions. Beyond this it was shown, that the classical approximate deconvolution method (ADM) approach is not suitable for the simulation of wall-bounded flows. This is because the filter strength is chosen quite arbitrary as in Ricot *et al.* (2009) and Ricot *et al.* (2002), and the selective viscosity damping stencils are very dissipative on their own. Thus, a selective filtering approach was presented based on the scales resolved. This approach connects mesh resolution and Reynolds number in terms of a physically motivated energy drain. Although the method is quite dissipative for marginally resolved setups ($N = 31$) at lower Reynolds numbers ($Re_\tau = 180$ and $Re_\tau = 395$), it shows promising results for LES like setups ($N = 71$). Further work is done on dynamic forcing, in order to keep the mass flow constant and not the absolute volume force. The proposed model is a consistent turbulence model in the framework of the hydrodynamic limit of the filtered Navier-Stokes equations. The explicit filtering step can be extended for complex geometries since a local temporal average is taken into account for the scales resolved.

REFERENCES

Adams, N. A. & Stolz, S. 2002 A subgrid-scale deconvolution approach for shock capturing. *J. Comp. Phys.* **178**, 391–426.

Bespalko, D. J. 2011 Validation of the lattice boltzmann method for direct numerical simulation of wall-bounded turbulent flows. dissertation, Queen's University.

Chen, S. & Doolen, G. D. 1998 Lattice boltzmann method for fluid flows. *Annu. Rev. Fluid Mech.* **30**, 329–364.

D'Humiéres, D., Ginzburg, I., Krafczyk, M., Lallemand, P. & Luo, L.-S. 2002 Multiple-relaxation-time lattice boltzmann models in three dimensions. *Phil. Trans. R. Soc. Lond. A* **361**, 437–451.

Freitas, R. K., Henze, A., Meinke, M. & Schröder, W. 2011 Anaysis of lattice-boltzmann methods for internal flows. *Comp. Fl.* **47**, 115–121.

Guo, Z., Baochang, S. & Nengchao, W. 2000 Lattice bgk model for incompressible navier stokes equation. *J. Comp. Ph.* **165**, 288–306.

Guo, Z. & Shu, S. 2013 *Lattice Boltzmann Method and its Applications in Engineering*. World Scientific.

Hänel, D. 2004 *Molekulare Gasdynamik*. Springer-Verlag.

He, X. & Luo, L.-S. 1997 Lattice boltzmann model for the incompressible navier stokes equation. *J. Stat. Phys.* **88**, 927–944.

Jafari, S. & Rahnama, M. 2011 Shear-improved smagorinsky modeling of turbulent channel flow using generalized lattice boltzmann equation. *Int. J. Numer. Meth. Fluids* **67**, 700–712.

Kim, J., Moin, P. & Moser, R. 1987 Turbulence statistics in fully-developed channel flow at low reynolds-number. *J. Fluid Mech.* **177**, 133–166.

Lallemand, P. & Luo, L. S. 2000 Theory of the lattice boltzmann method: Dispersion, dissipation, isotropy, galilean invariance, and stability. *Phys. Rev. E* **61**, 6546.

Latt, J. 2007 Hydrodynamic limit of lattice boltzmann equations. dissertation, Université de Genève.

Latt, J. & Chopard, B. 2006 Lattice boltzmann method with regularized non-equilirbium distribution functions. *Mathematics and Computer in Simulation* **72**, 165–168.

Latt, J, Chopard, B., Malaspinas, O., Deville, M. & Michler, A. 2008 Straight velocity boundaries in the lattice boltzmann method. *Phys. Rev. E* **77**, 056703.

Lèveque, E., Toschi, F., Shao, L. & Bertoglio, J. P. 2007 Shear-improved smagorinsky model for large-eddy simulation of wall-bounded turbulent flows. *J. Fl. Mech.* **570**, 491–502.

Malaspinas, O. & Sagaut, P. 2011 Advanced large-eddy simulation for lattice boltzmann methods: The approximate deconvolution model. *Phys. Fluids* **23**, 105103.

Malaspinas, O. & Sagaut, P. 2012 Consistent subgrid scal modelling for lattice boltzmann methods. *J. Fluid Mech.* **700**, 514–542.

Mathew, J., Lechner, R., Foysi, H., Sesterhenn, J. & Friedrich, R. 2003 An explicit filtering method for large eddy simulation of compressible flows. *Phys. Fluids* **15**, 2279.

Moser, R. D., Kim, J. & Mansour, N. N. 1999 Direct numerical simulation of turbulent channel flow up to $re_\tau = 590$. *Phys. Fl.* **11**, 943–945.

Pruett, C. D. & Adams, N. A. 2000 A priori analyses of three subgrid-scale models for one-parameter families of filters. *Phys. Fl.* **12**, 1133–1142.

Ricot, D., Maillar, V. & Bailly, C. 2002 Numerical simulation of unsteady cavity flow using lattice boltzmann method. In *8th AIAA/CEAS Aeroacoustics Conference & Exhibit*.

Ricot, D., Marie, S., Sagaut, P. & Bailly, C. 2009 Lattice boltzmann method with selective viscosity filter. *J. Comp. Phys* **228**, 4478–4490.

Sagaut, P. 2010 Toward advanced subgrid models for lattice-boltzmann-based large-eddy simulation: Theoretical formulations. *Computers and Mathematics with Applications* **59**, 2194–2199.

Stolz, S. & Adams, N. A. 1999 An approximate deconvolution procedure for large-eddy simulation. *Phys. Fluids* **11**, 1699.

Stolz, S., Adams, N. A. & Kleiser, L. 2001 An approximate deconvolution model for large-eddy simulation with application to incompressible wall-bounded flows. *Phys. Fluids* **13**, 997.

Sukop, M. C. & Thorne, D. T. 2006 *Lattice Boltzmann Modeling*. Springer-Verlag.

Tam, C. K. W., C., Webb J. & Dong, Zhong 1993 A study of the short wave components in computational acoustics. *J. Comp. Acous.* **1**, 133–166.

Waldrow, D. A. 2000 *Lattice-Gas Cellular Automata and Lattice Boltzmann Models: An Introduction*. Springer-Verlag.

APPENDIX D

Implementation of the MRT model

The linear transformation matrix $\boldsymbol{M}$ from velocity space $\mathbb{V}$ to momentum space $\mathbb{M}$ is given by

$$M = \begin{bmatrix}
1 & 1 & 1 & 1 & 1 & 1 & 1 & 1 & 1 & 1 & 1 & 1 & 1 & 1 & 1 & 1 & 1 & 1 & 1 \\
-30 & -11 & -11 & -11 & 8 & 8 & 8 & 8 & 8 & 8 & -11 & -11 & -11 & 8 & 8 & 8 & 8 & 8 & 8 \\
12 & -4 & -4 & -4 & 1 & 1 & 1 & 1 & 1 & 1 & -4 & -4 & -4 & 1 & 1 & 1 & 1 & 1 & 1 \\
0 & -1 & 0 & 0 & -1 & -1 & -1 & -1 & 0 & 0 & 1 & 0 & 0 & 1 & 1 & 1 & 1 & 0 & 0 \\
0 & 4 & 0 & 0 & -1 & -1 & -1 & -1 & 0 & 0 & -4 & 0 & 0 & 1 & 1 & 1 & 1 & 0 & 0 \\
0 & 0 & -1 & 0 & -1 & 1 & 0 & 0 & -1 & -1 & 0 & 1 & 0 & 1 & -1 & 0 & 0 & 1 & 1 \\
0 & 0 & 4 & 0 & -1 & 1 & 0 & 0 & -1 & -1 & 0 & -4 & 0 & 1 & -1 & 0 & 0 & 1 & 1 \\
0 & 0 & 0 & -1 & 0 & 0 & -1 & 1 & -1 & 1 & 0 & 0 & 1 & 0 & 0 & 1 & -1 & 1 & -1 \\
0 & 0 & 0 & 4 & 0 & 0 & -1 & 1 & -1 & 1 & 0 & 0 & -4 & 0 & 0 & 1 & -1 & 1 & -1 \\
0 & 2 & -1 & -1 & 1 & 1 & 1 & 1 & -2 & -2 & 2 & -1 & -1 & 1 & 1 & 1 & 1 & -2 & -2 \\
0 & -4 & 2 & 2 & 1 & 1 & 1 & 1 & -2 & -2 & -4 & 2 & 2 & 1 & 1 & 1 & 1 & -2 & -2 \\
0 & 0 & 1 & -1 & 1 & 1 & -1 & -1 & 0 & 0 & 0 & 1 & -1 & 1 & 1 & -1 & -1 & 0 & 0 \\
0 & 0 & -2 & 2 & 1 & 1 & -1 & -1 & 0 & 0 & 0 & -2 & 2 & 1 & 1 & -1 & -1 & 0 & 0 \\
0 & 0 & 0 & 0 & 1 & -1 & 0 & 0 & 0 & 0 & 0 & 0 & 0 & 1 & -1 & 0 & 0 & 0 & 0 \\
0 & 0 & 0 & 0 & 0 & 0 & 0 & 0 & 1 & -1 & 0 & 0 & 0 & 0 & 0 & 0 & 0 & 1 & -1 \\
0 & 0 & 0 & 0 & 0 & 0 & 1 & -1 & 0 & 0 & 0 & 0 & 0 & 0 & 0 & 1 & -1 & 0 & 0 \\
0 & 0 & 0 & 0 & -1 & -1 & 1 & 1 & 0 & 0 & 0 & 0 & 0 & 1 & 1 & -1 & -1 & 0 & 0 \\
0 & 0 & 0 & 0 & 1 & -1 & 0 & 0 & -1 & -1 & 0 & 0 & 0 & -1 & 1 & 0 & 0 & 1 & 1 \\
0 & 0 & 0 & 0 & 0 & 0 & -1 & 1 & 1 & -1 & 0 & 0 & 0 & 0 & 0 & 1 & -1 & -1 & 1
\end{bmatrix} \tag{D.1}$$

The relaxation time parameters of $\boldsymbol{\Lambda}$ are given in equation D.2

$$\boldsymbol{\Lambda} = (0, 1.19, 1.4, 0, 1.2, 0, 1.2, 0, 1.2, \lambda_\nu, \lambda_\nu, \lambda_\nu, \lambda_\nu, \lambda_\nu, 1.4, 1.4, 1.98., 1.98, 1.98) \tag{D.2}$$

In Equation (D.2), λ_ν is related to the viscosity. The moment equilibrium functions are given in Equations (D.3a)-(D.3s) as

$$m_0^{eq} = \rho = m_0 \tag{D.3a}$$

$$m_1^{eq} = e^{eq} = 11m_0 - 19\left(\frac{m_3^2 + m_5^2 + m_3^2}{m_0}\right) \tag{D.3b}$$

$$m_2^{eq} = \lambda^{eq} = -\frac{475}{63}\left(m_0 + \frac{m_3^2 + m_5^2 + m_3^2}{m_0}\right) \tag{D.3c}$$

$$m_3^{eq} = j_x = m_3 \tag{D.3d}$$

$$m_4^{eq} = q_x^{eq} = \frac{2}{3}m_3 \tag{D.3e}$$

$$m_5^{eq} = j_y = m_5 \tag{D.3f}$$

$$m_6^{eq} = q_y^{eq} = \frac{2}{3}m_5 \tag{D.3g}$$

$$m_7^{eq} = j_z = m_7 \tag{D.3h}$$

$$m_8^{eq} = q_z^{eq} = \frac{2}{3}m_7 \tag{D.3i}$$

$$m_9^{eq} = S_{xx}^{eq} = \frac{2m_3^2 - (m_5^2 + m_7^2)}{m_0} \tag{D.3j}$$

$$m_{10}^{eq} = S_{zz}^{eq} = \frac{m_5^2 - m_7^2}{m_0} \tag{D.3k}$$

$$m_{11}^{eq} = S_{xy}^{eq} = \frac{m_3 m_5}{m_0} \tag{D.3l}$$

$$m_{12}^{eq} = S_{xz}^{eq} = \frac{m_3 m_7}{m_0} \tag{D.3m}$$

$$m_{13}^{eq} = S_{yz}^{eq} = \frac{m_5 m_7}{m_0} \tag{D.3n}$$

$$m_{14}^{eq} = Q_1^{eq} = -\omega_Q \frac{-2m_3^2 + m_5^2 + m_7^2}{m_0} \tag{D.3o}$$

$$m_{15}^{eq} = Q_1^{eq} = \omega_Q \frac{m_5^2 - m_7^2}{m_0} \tag{D.3p}$$

$$m_{16}^{eq} = h_x^{eq} = 0 \tag{D.3q}$$

$$m_{17}^{eq} = h_y^{eq} = 0 \tag{D.3r}$$

$$m_{18}^{eq} = h_z^{eq} = 0 \tag{D.3s}$$

with $\omega_Q = 0$.

APPENDIX E

Bibliography

N. A. Adams. A stochastic extension of the approximate deconvolution method. *Phys. Fl.*, 23:055103, 2011.

N. A. Adams and S. Stolz. A Subgrid-Scale Deconvolution Approach for Shock Capturing. *J. Comp. Phys.*, 178:391–426, 2002.

S. Ansumali and I. V. Karlin. Stabilization of the lattice Boltzmann method by the H-theorem: A numerical test. *Phys. Rev. E*, 62:7999–8003, 2000.

S. Ansumali and I. V. Karlin. Single relaxation time model for entropic lattice Boltzmann methods. *Phys. Rev. E*, 65:056312, 2002.

D. J. Bespalko. *Validation of the Lattice Boltzmann Method for Direct Numerical Simulation of Wall-Bounded Turbulent Flows.* dissertation, Queen's University, 2011. URL `http://qspace.library.queensu.ca/dspace/bitstream/1974/6729/1/Bespalko_Dustin_J_201109_PhD.pdf`.

P. L. Bhatangar, E. P. Gross, and M. Krook. A Model for Collision Processes in Gases. I. Small Amplitude Processes in Charged and Neutral One-Component Systems. *Phys. Rev.*, 94:511–525, 1954.

B. M. Boghosian, J. Yepez, P. V. Coveney, and A. Wager. Entropic lattice Boltzmann methods. *Proceedings of the Royal Society of London A: Mathematical, Physical and Engineering Sciences*, 457(2007):717–766, 2001.

B. M. Boghosian, P. J. Love, P. V. Coveney, I. V. Karlin, S. Succi, and J. Yepez. Galilean-invariant lattice-Boltzmann models with H-theorem. *Phys. Rev. E*, 68:025103, 2003.

F. M. Bouzidi, M. Firdaouss, and P. Lallemand. Momentum transfer of a lattice-Boltzmann fluid with boundaries. *Phys. Fl.*, 13:3452–3459, 2002.

M. Bouzidi, D. d'Humiéres, P. Lallemand, and L. L. S. Lattice Boltzmann equation on a two dimensional rectangular grid. *J. Computat. Phys.*, 172:704–717, 2001.

M. Breuer, J. Bernsdorf, T. Zeiser, and F. Durst. Accurate computations of the laminar flow past a square cylinder based on two different methods: lattice-Boltzmann and finite-volume. *Inter. J. Heat and Fluid Flow* , 21:186–196, 2000.

C. Cercignani. *The Boltzmann Equation and Its Applications.* Springer-Verlag, 1988.

S. Chen and G. D. Doolen. Lattice Boltzmann Method For Fluid Flows. *Annu. Rev. Fluid Mech.*, 30:329–364, 1998.

S. S. Chikaarla and I. V. Karlin. Entropic lattice Boltzmann method for turbulent flow simulations: Boundary conditions. *Physica A: Statistical Mechanics and its Applications*, 392:1925–1930, 2013.

D. K. Clarke, H. Hassan, and M. Salas. Euler calculations for multielement airfoils using Cartesian grids. *AIAA Journal*, 24:353–358, 1986.

D. d'Humiéres, I. Ginzburg, M. Krafczyk, P. Lallemand, and L.-S. Luo. Multiple-relaxation-time lattice Boltzmann models in three dimensions. *Phil. Trans. R. Soc. Lond. A*, 361:437–451, 2002.

Y. H. Dong and P. Sagaut. A study of time correlation in lattice Boltzmann-based large-eddy simulation of isotropic turbulence. *Phys. Fluids*, 20:035105, 2008.

Y. H. Dong, P. Sagaut, and S. Marie. Inertial consistent subgrid model for large-eddy simlation based on the lattice Boltzmann method. *Phys. Fluids*, 20:035104, 2008.

B. Dorschner, F. Bösch, S. S. Chikatamarla, K. Boulouchos, and I. V. Karlin. Entropic multi-relaxation time lattice Boltzmann model for complex flows. *J. Fluid Mech.*, 801: 623–651, 2016a.

B. Dorschner, N. Frapolli, S. S. Chikatamarla, and I. V. Karlin. Grid refinement for entropic lattice Boltzmann models. *Phys. Rev. E*, 94:053311, 2016b.

R. Du, B. Shi, and X. Chen. Multi-relaxation-time lattice Boltzmann model for incompressible flow. *Phys. Letters A*, 359:564–572, 2006.

D. Fauconnier, C. Bogey, and E. Dick. On the performance of relaxation filtering for large-eddy simulation. *Journal of Turbulence*, 14:22–49, 2013.

Z. G. Feng and E. E. Michaelidis. The immersed boundary-lattice Boltzmann method for solving fluid-particles interaction problems. *J. Comp. Phys.* , 195:602–628 , 2004.

Z. G. Feng and E. E. Michaelidis. Proteus: a direct forcing method in the simulations of particulate flows. *J. Comp. Phys.* , 202:20–51, 2005.

J. H. Ferziger and M. Peric. *Computational Methods for Fluid Dynamics.* Springer-Verlag, 2002.

O. Filippova, S. Succi, F. Mazzoccoc, C. Arrighettic, G. Bellad, and D. Hänel. Multiscale Lattice Boltzmann Schemes with Turbulence Modeling. *J. Comp. Phys.*, 170:812–829, 2002.

R. K. Freitas, A. Henze, M. Meinke, and W. Schröder. Anaysis of Lattice-Boltzmann methods for internal flows. *Comp. Fl.*, 47:115–121, 2011.

M. Geier, M. Schoenherr, A. Pasquali, and M. Krafczyk. The Cumulant Lattice Boltzmann Equation in three dimensions: theory and validation. *Computers and Mathematics with Applications*, 70:507, 2015.

M. C. Geier. *Ab Initio Derivation of the cascaded lattice Boltzmann automaton*. dissertation, Albert-Ludwigs-Universität Freiburg, 2006. URL `http://www.freidok.uni-freiburg.de/volltexte/2860/pdf/thesisGeierLast.pdf`.

S. Geller, S. Uphoff, and M. Krafczyk. Turbulent jet computations based on MRT and Cascaded Lattice Boltzmann models. *Comp. Math. Appl.*, 65:956–1966, 2013.

I. Ginzburg, F. Verhaeghe, and D. D'Humiéres. Two-relaxation-time Lattice Boltzmann scheme: About parametrization, velocity, pressure and mixed boundary conditions. *Comm. Comp. Phys.*, 3:427–478, 2008.

H. Grad. Note on the N-dimensional Hermite polynomials. *Commun. Pure Appl. Maths*, 9:325, 1949a.

H. Grad. On the kinetic theory of rareed gases. *Commun. Pure Appl. Maths*, 9:331, 1949b.

Z. Guo and S. Shu. *Lattice Boltzmann Method and its Applications in Engineering*. World Scientific, 2013.

Z. Guo, S. Baochang, and W. Nengchao. Lattice BGK Model for Incompressible Navier-Stokes Equation. *J. Comp. Ph.*, 165:288–306, 2000.

X. He and L.-S. Luo. Lattice Boltzmann Model for the Incompressible Navier-Stokes Equation. *J. Stat. Phys.*, 88:927–944, 1997.

S. Hou, J. Sterling, S. Chen, and G. Doolen. A lattice Boltzmann subgrid model for high Reynolds number flows. *Fields Institute Communications*, 6:151–166, 1996.

D. Hänel. *Molekulare Gasdynamik*. Springer-Verlag, 2004.

R. Illnera and M. Pulvirentib. A derivation of the BBGKY-hierarchy for hard sphere particle systems. *Transport Theory and Statistical Physics*, 16:997–1112, 1987.

T. Inamoru. Lattice Boltzmann methods for moving boundary flows. *Fluid Dyn. Res.*, 44:1–22, 2012.

S. Kang, H. Choi, and S. Lee. Laminar flow past a rotating cylinder. *Phys. Fl.*, 11: 3311–3321, 1999.

I. V. Karlin, F. Bösch, and S. S. Chikatamarla. Gibbs' principle for the lattice-kinetic theory of fluid dynamics. *Phys. Rev. E*, 90:031302, 2014.

M. J. Krause, G. Thäter, and V. Heuveline. Adjoint-based fluid flow control and optimisation with lattice Boltzmann methods. *Computers and Mathematics with Applications*, 65:945–960, 2013.

P. Lallemand and L.-S. Luo. Theory of the lattice Boltzmann method: Dispersion, dissipation, isotropy, Galilean invariance, and stability. *Phys. Rev. E*, 61:6546, 2000.

P. Lallemand and L. S. Luo. Lattice Boltzmann method for moving boundaries. *J. Comput. Phys.*, 184:406–421, 2003.

P. Lammers. *Direkte numerische Simulationen wandgebundener Strömungen kleiner Reynoldszahlen mit dem lattice Boltzmann Verfahren.* dissertation, Friedrich-Alexander-Universität Erlangen-Nürnber, 2004. URL `https://opus4.kobv.de/opus4-fau/frontdoor/index/index/docId/144`.

P. Lammers, K. N. Bernonov, R. Volkert, G. Brenner, and F. Durst. Lattice BGK direct numerical simulation of fully developed turbulence in incompressible plane channel flow. *Comp. Fl.*, 35:1137–1153, 2006.

J. Latt. *Hydrodynamic Limit of Lattice Boltzmann Equations.* dissertation, Université de Genève, 2007. URL `http://archive-ouverte.unige.ch/unige:464`.

J. Latt and B. Chopard. Lattice Boltzmann Method with regularized non-equilirbium distribution functions. *Mathematics and Computer in Simulation*, 72:165–168, 2006.

J. Latt, B. Chopard, O. Malaspinas, M. Deville, and A. Michler. Straight velocity boundaries in the lattice Boltzmann method. *Phys. Rev. E*, 77:056703, 2008.

W. J. Layton. *Approximate Deconvolution Models of Turbulence: Analysis, Phenomenology and Numerical Analysis.* Springer-Verlag, 1st edition, 2010.

E. Lèveque, F. Toschi, L. Shao, and J. P. Bertoglio. Shear-improved Smagorinsky model for large-eddy simulation of wall-bounded turbulent flows. *J. Fl. Mech.*, 570:491–502, 2007.

O. Malaspinas. Increasing stability and accuracy of the lattice Boltzmann scheme: recursivity and regularization. *arXiv preprint arXiv:1505.06900*, 2015.

O. Malaspinas and P. Sagaut. Advanced large-eddy simulation for lattice Boltzmann methods: The approximate deconvolution model. *Phys. Fluids*, 23:105103, 2011.

O. Malaspinas and P. Sagaut. Consistent subgrid scale modeling for lattice Boltzmann methods. *J. Fluid Mech.*, 700:514–542, 2012.

S. Marié and X. Gloerfelt. Adaptive filtering for the lattice Boltzmann method. *Journal of Computational Physics*, 333:212–226, 2017.

R. Mittal and G. Iaccarino. IMMERSED BOUNDARY METHODS. *Annu. Rev. Fluid Mech.*, 37:239–261, 2005.

S. Mittal and B. Kumar. Laminar flow past a rotating cylinder. *J. Fluid Mech.*, 476: 303–334, 2003.

M. T. Nair, T. K. Sengupta, and U. S. Chauhan. Flow past rotating cylinders at high Reynolds numbers using high order upwind schemes. *Comp. Fl.*, 27:47–70, 1998.

P. Nathen, J. K. D. Gaudlitz, and M. J. Krause. Adaptive filtering for the lattice Boltzmann method. 21^{st} *AIAA Computational Fluid Dynamics Conference*, June 24 - 27: San Diego, CA, USA, 2013.

P. Nathen, D. Gaudlitz, and N. A. Adams. Towards wall-adaption of turbulence models within the Lattice-Boltzmann framework. *The* 9^{th} Symposium on Turbulence and Shear Flow Phenomena (TSFP-9), June 30 - July 3:Melbourne, Australia, 2015.

P. Nathen, D. Gaudlitz, M. Krause, and N. Adams. On the Stability and Accuracy of the BGK, MRT and RLB Boltzmann Schemes for the Simulation of Turbulent Flows. *J. Comm. Comp. Phys.*, 23:846 –876, 2018a.

P. Nathen, M. Haussmann, M. Krause, and N. Adams. Adaptive Filtering for the Simulation of Turbulent Flows with Lattice Boltzmann Methods. *Computers & Fluids*, Accepted in Press:XXX, 2018b.

C. Peng. *The Lattice Boltzmann Method for Fluid Dynamics: Theory and Applications.* dissertation, École Polytechnique, 2014. URL `http://dii-sm.epfl.ch/files/content/sites/cmcs/files/People/Peng%20Chen/LBM.pdf`.

C. S. Peskin. *Flow Patterns Around Heart Valves: A Digital Computer Method for Solving the Equations of Motion.* dissertation, Albert Einstein College of Medicine of Yeshiva University, 1972. URL `http://www.umi.com/en-US/products/dissertations/disexpress.shtml`.

K. N. Premnath, M. J. Pattisona, and S. Banerjee. Dynamic subgrid scale modeling of turbulent flows using lattice-Boltzmann method. *Physica A: Stat. Mech. Appl.s*, 388: 2640–2658, 2009.

K. N. Premnath, J. Abraham, and S. Banerjee. DISCRETE LATTICE BGK BOLTZMANN EQUATION COMPUTATIONS OF TRANSIENT INCOMPRESSIBLE TURBULENT JETS. *Int. J. Mod. Phys. C*, 15:699–719, 2014.

D. Ricot, V. Maillar, and C. Bailly. Numerical Simulation of Unsteady Cavity Flow Using Lattice Boltzmann Method. In *8th AIAA/CEAS Aeroacoustic's Conference & Exhibit*, 2002.

D. Ricot, S. Marie, P. Sagaut, and C. Bailly. Lattice Boltzmann method with selective viscosity filter. *J. Comp. Phys*, 228:4478–4490, 2009.

P. Sagaut. Toward advanced subgrid models for Lattice-Boltzmann-based Large-eddy simulation: Theoretical formulations. *Computers and Mathematics with Applications*, 59:2194–2199, 2010.

F. Schwabl. *Statistische Mechanik.* Springer-Verlag, 3rd edition, 2006.

C. Shu and J. Wu. A new immersed boundary-lattice Boltzmann method and its application to incompressible flows. *Modern Phys. Letters B*, 23:261–264, 2009.

J. Smagorinsky. General Circlation Experiments with the Primitive Equations. *Mon. Weath. Rev.*, 91:99–164, 1963.

S. Stolz and N. A. Adams. An approximate deconvolution procedure for large-eddy simulation. *Phys. Fluids*, 11:1699, 1999.

S. Stolz, N. A. Adams, and L. Kleiser. An approximate deconvolution model for large-eddy simulation with application to incompressible wall-bounded flows. *Phys. Fluids*, 13:997, 2001.

S. Succi. *The Lattice Boltzmann Equation for Fluid Dynamics and Beyond.* Oxford Science Publications, 2001.

M. C. Sukop and D. T. Thorne. *Lattice Boltzmann Modeling.* Springer-Verlag, 2006.

C. K. W. Tam, W. J. C., and Z. Dong. A STUDY OF THE SHORT WAVE COMPONENTS IN COMPUTATIONAL ACOUSTICS. *J. Comp. Acous.*, 1:133–166, 1993.

H. Udaykumar, R. Mittal, P. Rampunggoon, and A. Khanna. A Sharp Interface Cartesian Grid Method for Simulating Flows with Complex Moving Boundaries. *J. Comp. Phys.* , 174:345–380, 2001.

H. Versteeg and W. Malalasekra. *An Introduction to Computational Fluid Dynamics: The Finite Volume Method.* Pearson, 2007.

D. A. Waldrow. *Lattice-Gas Cellular Automata and Lattice Boltzmann Models: An Introduction.* Springer-Verlag, 2000.

M. Weickert, G. Teike, S. O., and M. Sommerfeld. Investigation of the LES WALE turbulence model within the lattice Boltzmann framework. *Computers and Mathematics with Applications*, 59:2200–2214, 2010.

H. Yu and S. S. Girimaji. Near-field turbulent simulations of rectangular jets using lattice Boltzmann method. *Phys. Fluids.*, 17:125106, 2005.

H. Yu, S. S. Girimaji, and L. S. Luo. DNS and LES of decaying isotropic turbulence with and without frame rotation using lattice Boltzmann method. *J. Comp. Phys.*, 209: 599–616, 2005.

H. Yu, L.-S. Luo, and S. S. Girimaji. LES of turbulent square jet flow using an MRT lattice Boltzmann model. *Comp. Fl.*, 35:957–965, 2006.

R. Zhang, X. Shan, and H. Chen. Efficient kinetic method for fluid simulation beyond the Navier-Stokes equation. *Phys. Rev. E*, 74:046703, 2006.